



Structural performance of geopolymer concrete

Shear and flexural behavior of a prestressed girder with cast in-situ topping under short-term loading

J.E. Paredes Pineda

DELFT UNIVERSITY OF TECHNOLOGY

Jose Eduardo Paredes Pineda

Student number 5022290

**STRUCTURAL PERFORMANCE OF GEOPOLYMER CONCRETE:
SHEAR AND FLEXURAL BEHAVIOR OF A PRESTRESSED GIRDER
WITH CAST IN-SITU TOPPING UNDER SHORT-TERM LOADING**

MASTER THESIS

Master of Science Civil Engineering

Structural Engineering – Concrete Structures

Thesis Committee

Dr.ir. M. (Mladena) Lukovic (Chair and daily supervisor) TU Delft Concrete Structures

Dr.ir. E.O.L. (Eva) Lantsoght TU Delft Concrete Structures

Universidad San Francisco de Quito

Dr.ir. G. (Guang) Ye TU Delft Materials and Environment

Ir. Z. (Zhenxu) Qian TU Delft Concrete Structures

Date of public defense: August 15th, 2022

Faculty of Civil Engineering and Geosciences

Stevinweg 1, Delft

Preface

The present document is the deliverable of months of research in the upscaling of two geopolymer concrete mixtures in structural elements consisting of an individual prestressed girder with a topping layer cast in-situ. The study addresses how to deal with the material differences, of this more sustainable alternative to conventional concrete, for applying current methods of analysis for conventional concrete structures and to what extent they are appropriate for the analysis of geopolymer concrete structures.

I would like to extend my gratitude to Delft University of Technology and the Justus en Louise van Effen Foundation for giving me the opportunity to pursue the MSc in Structural Engineering, one of the most renowned programmes in the world. I am grateful for the challenge over the past 2 years. I have acquired knowledge, gained understating and become more passionate about civil engineering.

I would like to acknowledge the persons who supported me during this research. Eva Lantsoght is one of the main reasons for me being able to write these words today. I will be forever grateful to her for introducing me to the project, her exceptional efficiency for reviewing my work, the input throughout the research process and her guidance over the years. Mladena Lukovic for engaging me in the project ever since the start and motivating me to move forward. I always felt welcome to talk to her and I appreciate the time she spent on making things clear for me when I found difficulties along the way. Zhenxu Qian for her thorough review of my progress and her pressuring for delivering written results which eased the writing process of the final report. Guang Ye, the Microlab and Shizhe Zhang for the material test results, their openness to address my questions and the time shared during the project. Yitao Huang for assisting me in the testing of the elastic modulus samples. Mauro Poliotti and Shozab Mustafa for their support with the finite element modelling.

Furthermore, I am thankful for all the people I have met during my studies. Brilliant students and great friends that contributed greatly to my learning process and have accompanied me during my time in Delft. To U-BASE for the friendships and unforgettable memories.

Lastly, I want to express my gratitude to my parents. Their everlasting love and support have set the foundation for achieving my dreams.

Jose Eduardo Paredes Pineda

Delft, August 2022

Abstract

Structural performance of geopolymer concrete: Shear and flexural behavior of a prestressed girder with cast in-situ topping under short-term loading

By Jose Eduardo Paredes Pineda

The future expectations of a circular economy require alternative materials to satisfy the continuously increasing demand for infrastructure in a sustainable way. Geopolymer concrete is engineered from the technological use of by-products to minimize the energy consumption, raw materials depletion and CO₂ emissions. The chemical structure of the binder phase in geopolymer concrete mixtures and the material properties are dependent on the choice of constituent materials (precursors and alkali-activators) and the curing conditions. The resulting wide range of different geopolymer concrete mixtures and the lack of predictive models and standards for application limit the use of the material in real world applications. Moreover, the time-dependent material properties (e.g. elastic modulus, creep and shrinkage) of geopolymer concrete may pose an impediment for the generalized applicability of the material in prestressed structures since studies report higher creep and shrinkage, and a decrease of the elastic modulus over time, as compared to conventional concrete, which could influence adversely the load carrying capacity, cracking resistance, deflections and prestress losses.

This document presents the upscaling of two geopolymer concrete mixtures in structural elements consisting of an individual prestressed girder with a reinforced topping layer. The self-compacting geopolymer concrete (SCGC) mixture of the precast girder is based on ground granulated blast furnace slag (GGBFS) as precursor alkali-activated by sodium hydroxide and sodium silicate solutions and the topping layer is cast by a ready-mix geopolymer concrete provider. The precast girder is prestressed 2.5 days after casting and the topping layer is cast in-situ 28 days after the casting date of the girder. The objective is to study the different material properties, determine their impact in the structural performance and define the extent of applicability of current methods of analysis for conventional concrete structures, as defined in EN 1992-1-1 and the Rijkswaterstaat's Guidelines for NLFEA, for geopolymer concrete. The structural performance of the elements subjected to flexural and shear mechanical tests is studied by analytical methods and 2D plane stress nonlinear finite element analyses, which are further compared to experimental results in terms of deformations, load-deflection response, principal strains, normal stresses, damage evolution, cracking stages, maximum load and failure mechanism. The shear behavior of the elements is studied at an age of 28 days after casting of the topping, whereas the flexural behavior is assessed at this age and after 9 months to analyze the effect of the long-term material properties of the geopolymer concrete mixtures in the prestressing losses, cracking load and maximum load carrying capacity.

The reduction of the elastic modulus in both geopolymer concrete mixtures that were used in this study seems to be intrinsically related to the drying process. It appears more or less stable over time for standard curing (20°C, RH>95%) but decreases 10% at 28 days when exposed to drying after 14 days of standard curing and in air-exposed samples a decrease between 7 and 26% is reported at 56 days. The elastic modulus of the ready-mix geopolymer concrete mixture samples exposed to drying at early ages (≤ 7 days) seems to stabilize after 30 days but the initial stiffness is lower than samples exposed to drying at later stages. The elastic modulus of both geopolymer concrete mixtures is lower (for standard curing and when exposed to drying after 7 or 14 days of standard curing) than the estimates from EN 1992-1-1 for OPC concrete of the same strength class. The empirical relation from EN 1992-1-1 for

estimating the elastic modulus from the compressive strength is not applicable and neither are the empirical relations suggested from literature studies because of the difference on the constituent materials and curing conditions. The increase of creep and shrinkage between 30 and 60 days suggest a pronounced viscous mechanical response of geopolymer concrete probably caused by the rearrangement of the C-A-S-H gel structure as indicated by other researchers. The prediction models to determine the material properties from the 28-day compressive strength as defined in EN 1992-1-1 [22] for conventional concrete do not capture the long-term material properties (e.g. elastic modulus, creep and shrinkage) of the geopolymer concrete mixtures from this study. The isotropic elasticity-based prediction models underestimate considerably the creep coefficient and shrinkage strains leading to unsafe design assumptions.

The linear elastic behavior of the specimen is accurately described by the analytical model and the numerical simulation for both short-term tests but the numerical model does not capture the experimental results of the flexural test after 9 months as the specimen was cracked prior to the test the cyclic loading at high load levels in the experiment causes stiffness degradation. The short-term flexural resistance is higher (8% by analytical model and 3% for the numerical simulation) than the maximum load attained during testing. The stress distributions at characteristic phases and the cracking load (3% higher than the experiment) are practically equal from the analytical and numerical model. The measured concrete strains at midspan at the levels of steel reinforcement are accurately described by the numerical simulation. The cracking pattern in the topping in the NLFEA shows more cracks at smaller spacing because higher stresses transfer from the precast girder due to perfect bonded. The short-term shear resistance was 12% higher from the numerical simulation and 16% lower from the analytical model, as compared to the experiment. The cross-section of the numerical simulation is stiffer and fully composite since the precast girder and the topping are perfectly bonded, whereas in the experiment debonding occurred. The shear failure was characterized by a shear critical crack in the topping; the position and orientation of the shear critical crack from the NLFEA was consistent with the DIC observations.

The long-term material properties of the geopolymer concrete mixtures influence the structural performance of the specimens. The camber of the SCGC girders continues to increase over time (2.5 to 7 days) as the elastic modulus and creep do not stabilize but in concrete girders with similar geometry and prestressing layout the camber is more or less constant. The prestress losses at 28 days are higher than for conventional concrete and increase from 26% after 28 days to 38% after 270 days due to the larger shrinkage strains and creep deformations over time. The variation in the elastic modulus at 28 days due to different curing conditions has a marginal effect in the short-term load – deflection response to the flexural test. The cracking load is decreased significantly (15%) in the specimen after 9 months but the creep and shrinkage deformations do not appear to stabilize after this period, hence the prestress losses will continue to increase over time and the cracking resistance will continue to decrease which is critical for the performance over the service lifetime of the structure. The design criteria of conventional concrete structures based on estimating the material properties from the 28-day compressive strength result in non-conservative estimates of the cracking resistance and flexural load carrying capacity of prestressed geopolymer concrete members which can lead to an unsafe design. The flexural resistance after 9 months is overestimated by 5% in the numerical simulation as compared to the experimental results. The truss model for shear resistance, the bilinear compressive stress block for flexural resistance and the 2D plane stress analysis with total strain based orthogonal rotating crack model with exponential tension softening and parabolic compressive relation can be used to estimate the structural performance of the prestressed girder with reinforced cast in-situ topping built in geopolymer concrete with the adequate long-term material properties as input.

Symbols and abbreviations

Symbols

Latin upper case letters

A_{ct}	Area of the gross transformed composite cross-section
$A_{c,cr}$	Area of the cracked composite section
A_g	Area of the girder
A_{gt}	Area of the gross transformed girder cross-section
$A_{g,cr}$	Area of the cracked girder
A_p	Equivalent area of prestressing tendons
A_{pt}	Transformed area of prestressing tendons
A_{sgt}	Transformed area of reinforcement steel in the girder
A_{si}	Area of layer of longitudinal reinforcement $i = 1, 2, 3$ and 4
A_{stt}	Transformed area of reinforcement steel in topping
A_{sw}	Area of shear reinforcement
A_t	Area of the topping
A_{tt}	Transformed area of topping

E_c	Elastic modulus of concrete
E_{cm}	Secant modulus of elasticity of concrete
E_p	Elastic modulus of prestressing steel
E_s	Elastic modulus of reinforcement steel
EI	Bending stiffness
F	Fictitious topping force
G_F	Fracture energy
G_C	Compressive fracture energy
I	Second moment of area
I_{ct}	Second moment of area of the gross transformed composite cross-section
$I_{c,cr}$	Second moment of area of the cracked composite section
I_g	Second moment of area of the girder
I_{gt}	Second moment of area of the gross transformed girder cross-section
$I_{g,cr}$	Second moment of area of the cracked girder
I_t	Second moment of area of the topping
L	Span length
L_f	Final length
L_0	Initial length
M_{cr}	Cracking moment
M_{dec}	Decompression moment
M_{ext}	Externally applied bending moment
M_{Gc}	Moment caused by self-weight of the girder
M_{Gr}	Moment caused by service loads
M_{Gt}	Moment caused by self-weight of the topping
N_{cu}	Concrete compressive force
N_{si}	Axial force in each layer of reinforcement steel $i = 1, 2, 3$ and 4
P_e	Equivalent axial force in composite section
P_m	Prestressing force
P_{max}	Maximum theoretical prestressing force applied in tendons
P_{mi}	Prestressing force after elastic losses
P_{m0}	Initial prestressing force after instantaneous losses

P_{mt}	Prestressing force after losses at t days
Q_{cr}	Externally applied cracking load
Q_{ext}	Maximum load for 4-point load test
S	First moment of area above and about the centroidal axis
V_{Rd}	Design shear resistance
$V_{Rd,c}$	Design shear resistance of members not requiring shear reinforcement
$V_{Rd,s}$	Design shear resistance of members requiring shear reinforcement
V_{Rm}	Average shear resistance
$V_{Rm,g}$	Average shear resistance of the girder
$V_{Rm,s,g}$	Average shear resistance of the shear reinforcement in the girder
$V_{Rm,t}$	Average shear resistance of the topping
$V_{Rm,s,t}$	Average shear resistance of the shear reinforcement in the topping
W_{cb}	Bottom section modulus of the composite section
W_{ct}	Top section modulus of the composite section
W_{gb}	Bottom section modulus of the girder
W_{gt}	Top section modulus of the girder

Latin lower case letters

a	Lever arm of each axial force acting on the composite section
b	Width of the composite section
b_w	Smallest width of the cross-section in the tensile area
d	Effective depth of the cross-section
e_p	Eccentricity of the tendon group
e_{pe}	Eccentricity of P_e from the n.a.
d_{si}	Distance to the layer of reinforcement from the top
f_{bpt}	Bond strength of concrete
f_c	Compressive strength of concrete
f_{cd}	Design compressive strength of concrete
f_{ck}	Characteristic compressive strength of concrete
$f_{ck}(t)$	Characteristic compressive strength at time t
f_{cm}	Mean compressive strength of concrete
$f_{cm,cube}$	Mean compressive strength of 150x150x150 mm ³ cubic samples

$f_{cm}(t)$	Mean compressive strength of concrete at time t
f_{ct}	Tensile strength of concrete
f_{ctm}	Mean tensile strength of concrete
$f_{ctm,f}$	Mean flexural tensile strength of concrete
f_p	Tensile strength of prestressing steel
$f_{p0.1}$	0.1% proof-stress of prestressing steel
f_{si}	Stress in each layer of reinforcement steel $i = 1, 2, 3$ and 4
f_y	Yield stress of reinforcement steel
f_{ywd}	Yield strength of stirrups
h_c	Height of the composite section
h_g	Height of the girder
h_0	Notional size of the girder
k_h	Coefficient depending on the notional size
k_n	Normal stiffness of interface elements
k_t	Tangential stiffness of interface elements
l_{pt}	Transmission length
p	Prestressing losses (in %)
q_g	Self-weight load
q_{Gc}	Self-weight of the girder as a uniformly distributed load
q_{Gt}	Self-weight of the topping as a uniformly distributed load
q_q	Variable load
s	Spacing of stirrups
t_s	Age of the concrete (days) at the beginning of drying shrinkage (or swelling).
t_0	Immediately after prestressing
$t_{2.5}$	Age at prestressing (2.5 days)
t_{30}	Age of 30 days after prestressing
t_{60}	Age of 60 days after prestressing
u	Exposed perimeter of the girder
v_1	Strength reduction factor for concrete cracked in shear
x_u	Height of the compression zone
y	Distance P_e is moved from uncracked to cracked section

z	Internal lever arm
z_{cb}	Distance to the centroid of the composite section from the bottom
z_{ctb}	Distance to the centroid of the gross transformed composite cross-section from the bottom
$z_{c,cr}$	Distance to the centroid of the cracked composite section from the bottom
z_{gb}	Distance to the centroid of the girder from the bottom
z_{gtb}	Distance to the centroid of the gross transformed girder cross-section from the bottom
$z_{g,cr}$	Distance to the centroid of the cracked girder from the bottom
z_{scb}	Distance to the centroid of reinforcement steel in the topping from the bottom
$z_{s gb}$	Distance to the centroid of reinforcement steel in the girder from the bottom
z_{tb}	Distance to the centroid of the topping from the bottom
<i>Greek letters</i>	
α	Angle of tensile ties.
α_{cw}	Coefficient taking into account the stress state in the compression chord
δ_{Gc}	Deformation caused by self-weight of the girder
δ_{Gt}	Deformation caused by self-weight of the topping
δ_P	Deformation caused by prestressing
δ_{Pt_0}	Deformation after prestressing
δ_t	Total deformation at t days
$\delta_{\phi,t}$	Creep deformation at t days
Δ_{el}	Elastic deformation
ΔL	Change in length
ΔP	Total prestressing losses
ΔP_{el}	Elastic losses
ΔP_{pr}	Prestressing losses
$\Delta \sigma$	Total prestressing losses
$\Delta \sigma_c$	Creep losses
$\Delta \sigma_{pr}$	Relaxation losses
$\Delta \sigma_s$	Shrinkage losses
ε	Strain
ε_b	Strain bottom fiber of the composite section

$\varepsilon_{ca}(t)$	Autogenous shrinkage at time t
$\varepsilon_{cc}(t)$	Total strain of concrete at time t
$\varepsilon_{cc}(t_0)$	Instantaneous elastic strain
$\varepsilon_{cc}(t, t_0)$	Creep strain of concrete specimens at time t
$\varepsilon_{cd}(t)$	Drying shrinkage strain at time t
$\varepsilon_{cd,0}$	Nominal unrestrained shrinkage strain of concrete
ε_{cs}	Total shrinkage strain
$\varepsilon_{cs}(t, t_0)$	Shrinkage strain of concrete specimens at time t
ε_{ps}	Strain of prestressing tendons at centroid level
$\varepsilon_{p0.1}$	0.1% plastic strain
ε_{si}	Strain of reinforcement steel $i = 1, 2, 3$ and 4
ε_t	Strain top fiber of the composite section
ε_u	Strain of prestressing steel at maximum load
η	Modular ratio girder to topping concrete
η_p	Modular ratio prestressing steel to concrete
η_{p1}	Coefficient that takes into account the type of tendon and the bond situation at release
η_s	Modular ratio reinforcement steel to concrete
η_t	Modular ratio topping to girder concrete
η_1	Coefficient for bond conditions
θ	Angle of the compression struts
κ	Curvature
$\kappa_{c,cr}$	Curvature of the cracked composite section
κ_{cr}	Curvature at cracking of the bottom fiber
κ_{dec}	Curvature at decompression of the bottom fiber
κ_{Gc}	Curvature caused by self-weight of the girder
κ_{Gt}	Curvature caused by self-weight of the topping
κ_p	Curvature caused by prestressing
κ_u	Curvature at maximum load
μ	Ratio of initial prestressing to tensile strength of prestressing steel
ν	Poisson ratio
ρ	Density

ρ_c	Density of concrete
ρ_l	Reinforcement ratio
ρ_{1000}	Value of relaxation loss (in %), at 1000 hours after tensioning and at a mean temperature of 20°C
ϕ	Reinforcement bar diameter
$\phi(t, t_0)$	Creep coefficient at time t
σ_b	Stress in the bottom fibre of the composite section
σ_{bgt}	Stress bottom fibre of the gross transformed girder cross-section
σ_{cp}	Average axial stress in the concrete cross-section
σ_{gb}	Stress bottom fibre girder due to P_{m60} and M_G
$\sigma_{gb,cr}$	Stress bottom fibre girder due to M_{cr}
$\sigma_{gb,dec}$	Stress bottom fibre girder due to M_{dec}
σ_{Gt}	Stress caused by self-weight of the topping
σ_{gt}	Stress top fibre girder due to P_{m60} and M_G
$\sigma_{gt,cr}$	Stress top fibre girder due to M_{cr}
$\sigma_{gt,dec}$	Stress top fibre girder due to M_{dec}
σ_{max}	Maximum theoretical prestress applied in tendon
$\sigma_{p,max}$	Maximum stress applied in tendon
σ_{mi}	Initial prestressing
σ_{pmi}	Prestressing after elastic losses
σ_{pm0}	Initial prestressing after instantaneous losses
$\sigma_{pm0}(x)$	Stress in the tendon immediately after tensioning or transfer
σ_{pmt}	Prestressing after losses at t days
σ_{ps}	Stress at centroid of the tendon group
σ_t	Stress in the top fibre of the composite section
$\sigma_{tb,cr}$	Stress bottom fibre topping due to M_{cr}
$\sigma_{tb,dec}$	Stress bottom fibre topping due to M_{dec}
σ_{tgt}	Stress top fibre of the gross transformed girder cross-section
$\sigma_{tt,dec}$	Stress top fibre topping due to M_{dec}
$\sigma_{tt,cr}$	Stress top fibre topping due to M_{cr}
$\sigma_{1,2}$	Maximum and minimum principal strains

Abbreviations

AAM	Alkali-activated material
ADTM	Autogenous deformation testing machine
BFS	Blast Furnace Slag
BWWA	Brisbane West Wellcamp Airport
DIC	Digital image correlation
DOF	Degree of freedom
EFC	Earth Friendly Concrete
FBG	Fibre Bragg grating
FE	Finite element
FEA	Finite element analysis
FEM	Finite element model
FOS	Fibre Optic Sensors
GGBFS	Ground granulated blast-furnace slag
GWP	Global Warming Potential
LCA	Life Cycle Assessment
LFEA	Linear finite element analysis
LVDT	Linear variable differential transformers
NLFEA	Non-linear finite element analysis
OPC	Ordinary Portland cement
RH	Relative humidity
RQ	Research question
SCGC	Self-compacting geopolymer concrete
SCM	Supplementary cementitious material
USD	United States Dollars

Table of contents

1. Introduction.....	1
1.1 Background.....	1
1.2 Problem statement.....	3
1.3 Research question and objectives	5
1.3.1 Research Question 1 (RQ1).....	5
1.3.2 Research Question 2 (RQ2).....	5
1.4 Outline	6
2. Literature review	8
2.1 Alkali-activated concrete	8
2.1.1 History	8
2.1.2 Definitions.....	9
2.1.3 Classification.....	9
2.1.4 Constituents.....	10
2.2 Material properties of geopolymer concrete	11
2.2.1 Preliminaries and selected studies.....	11
2.2.2 Mechanical properties.....	14
2.2.3 Volume stability.....	19
2.3 Structural tests of geopolymer concrete members	21
2.3.1 Reinforced geopolymer concrete members.....	21
2.3.2 Prestressed geopolymer concrete members.....	23
2.4 Numerical studies of geopolymer concrete members.....	23
2.5 Geopolymer concrete in the contemporary context	25
2.5.1 Existing standards for geopolymer concrete	25
2.5.2 Applications in structural geopolymer concrete	27

2.6	Advantages and limitations to the application of geopolymer concrete.....	30
2.6.1	Advantages.....	30
2.6.2	Limitations	31
2.7	Conclusions	32
3.	Case study and experimental results	34
3.1	General.....	35
3.2	Construction details	35
3.2.1	Mix requirements	35
3.2.2	Construction sequence	35
3.2.3	Geometry.....	37
3.3	Material properties of geopolymer concrete mixtures	39
3.3.1	Experimental program for mechanical properties	39
3.3.2	Compressive strength	39
3.3.3	Elastic modulus.....	39
3.3.4	Volume stability properties.....	44
3.3.5	Calculation values.....	49
3.4	Material properties of prestressing and reinforcement steel	50
3.4.1	Prestressing steel	50
3.4.2	Reinforcement steel.....	50
3.5	Experimental setup of mechanical tests	50
3.5.1	Prestressing stage measurements.....	50
3.5.2	Test setup of mechanical tests.....	50
3.6	Experimental results on composite girders.....	55
3.6.1	Prestressing.....	55
3.6.2	Time dependent deformation	57
3.6.3	Flexural test	58
3.6.4	Shear test	60
3.6.5	Flexural test after 9 months.....	63
4.	Flexural and shear capacity by analytical and numerical methods	65
4.1	Analytical analysis.....	65
4.1.1	Principles of prestressing.....	65
4.1.2	Stage I: Prestressing (2.5 days).....	67
4.1.3	Stage II: Cast in-situ topping (30 days)	70
4.1.4	Stage III: Composite section (60 days).....	70
4.1.5	Magnel diagram	71
4.1.6	Flexure.....	72
4.1.7	Ultimate Limit State: Shear	79

4.2	Finite element model.....	85
4.2.1	Geometry.....	85
4.2.2	Material models and parameters.....	87
4.2.3	Element types and finite element mesh.....	89
4.2.4	Boundary conditions	90
4.2.5	Phased analysis and loading	90
4.2.6	Load increments and convergence criteria.....	91
4.3	Linear finite element analysis.....	92
4.4	Nonlinear finite element analysis.....	93
4.4.1	Composite section	93
4.4.2	Flexural test	93
4.4.3	Shear test	99
5.	Comparison of experimental, analytical and FEA results.....	106
5.1	Prestressing.....	106
5.1.1	Deformations	106
5.1.2	Concrete stresses at midspan.....	107
5.1.3	Transmission length.....	107
5.2	Short-term flexural behavior	108
5.2.1	Load – deflection	108
5.2.2	Concrete stresses at midspan.....	110
5.2.3	Load – strains at midspan	111
5.2.4	Maximum principal strains and crack widths	112
5.3	Sensitivity analysis.....	114
5.4	Short-term shear behavior	117
5.4.1	Load – deflection	117
5.4.2	Failure mode.....	119
5.5	Long-term flexural behavior (after 9 months).....	119
6.	Conclusions and future work	123
6.1	Conclusions	123
6.2	Future work.....	129
	References	130
	Appendix A: Construction drawings.....	135
	Appendix B: Inspection certificates of prestressing strands.....	141
	Appendix C: Analytical calculations.....	143

List of figures

Figure 1.1. Basic composition of alkali-activated and OPC concretes	2
Figure 1.2. Global cement and energy production and global CO ₂ emissions from cement production [5].....	2
Figure 1.3. MSc Thesis Outline	7
Figure 2.1. Classification of SCMs	11
Figure 2.2. Stress-strain response of slag-based geopolymer concrete activated with Ca(OH) ₂ and w/b<30% as reported by Yang, et al. [36].....	14
Figure 2.3. Variation of compressive strength of geopolymer concrete to GGBFS to fly ash proportion [33].....	15
Figure 2.4. Correlation of flexural strength and compressive strength of geopolymer concrete at 28 days	16
Figure 2.5. Flexural strength of geopolymer concrete at different ages for ambient and high temperature curing [16].....	17
Figure 2.6. Correlation of elastic modulus and compressive strength of geopolymer concrete at 28 days	18
Figure 2.7. Elastic modulus of geopolymer concrete for different compressive strengths	19
Figure 2.8. Drying shrinkage vs RH for different mortar mixes [17].....	20
Figure 2.9. Geopolymer concrete projects in Russia and China [4]	27
Figure 2.10. Geopolymer concrete projects in Australia [8]	28
Figure 3.1. Casting operation of precast girders in Haitsma Beton	36
Figure 3.2. Casting operation of the topping over a girder specimen in Ghent University	36
Figure 3.3. Cross-section dimensions and prestressing layout of prestressed girder	37
Figure 3.4. Longitudinal and shear reinforcement of prestressed girder	37
Figure 3.5. Shear reinforcement layout at prestressed girder ends	38

Figure 3.6. Cross-section of composite section and reinforcement layout of cast in-situ topping	38
Figure 3.7. Shear reinforcement layout of cast in-situ topping	38
Figure 3.8. Elastic modulus development over time of Haitsma Beton - TU Delft SCGC mixture	40
Figure 3.9. Elastic modulus testing.....	40
Figure 3.10. Elastic modulus development over time of ready-mix geopolymer concrete mixture	41
Figure 3.11. Elastic modulus values according to different methods	43
Figure 3.12. Autogenous shrinkage of Haitsma Beton - TU Delft SCGC mixture	44
Figure 3.13. Total strain of Haitsma Beton - TU Delft SCGC mixture	44
Figure 3.14. $\beta_{as}(t)$	45
Figure 3.15. $\beta_{ds}(t, t_s)$	45
Figure 3.16. Creep coefficient for concrete under normal environmental conditions (Figure 3.1 EN 1992-1-1 [22])	46
Figure 3.17. Autogenous shrinkage from geopolymer concrete samples and calculation model as EN 1992-1-1.....	47
Figure 3.18. Volume stability properties according to different methods	48
Figure 3.19. Flexural test setup [61]	51
Figure 3.20. Flexural test measurement devices [61]	51
Figure 3.21. Strain stirrups in flexural test [61]	52
Figure 3.22. Applied load as measured by load cells (Flexural test)	52
Figure 3.23. Shear test setup [61]	53
Figure 3.24. Shear test measurement devices [61]	53
Figure 3.25. Applied load as measured by load cells (Shear test)	54
Figure 3.26. Applied load as measured by load cells (Flexural test after 9 months)	54
Figure 3.27. Strain change measured by FBG sensors along the length of the specimen [62]	55
Figure 3.28. Camber of prestressed girders with SCGC and conventional concrete C60/75	56
Figure 3.29. Strain at midspan of the precast girder from casting (0 days) to before test (60 days) [62].....	57
Figure 3.30. Comparison of strains: FBG monitoring and material test results [62]	57
Figure 3.31. Load-deflection diagram (Flexural test)	58
Figure 3.32. Concrete strains at midspan (Flexural test)	59
Figure 3.33. Cracking pattern in the constant moment region at different load levels (Flexural test) [61].....	60
Figure 3.34. Load-deflection diagram (Shear test)	60
Figure 3.35. Development of cracks and crack width in side surface (Flexural test) [60]	61
Figure 3.36. Cracking pattern after failure (Shear test) [61]	62
Figure 3.37. Development of cracks in side surface (Shear test) [60].....	63
Figure 3.38. Load-deflection diagram (Flexural test after 9 months).....	63
Figure 3.39. Failure of specimen subjected to flexural test after 9 months [61].....	64
Figure 4.1. Stresses in the midspan of a statically determinate beam subjected to prestressing (P_m), permanent (q_g) and variable loading (q_q) [68].....	66
Figure 4.2. Pre-tensioning process.....	66
Figure 4.3. Pre-tensioning of concrete: a) before and b) after tensioning [68]	67
Figure 4.4. Stage I: Stress distribution	68
Figure 4.5. Transfer of prestressing force.....	69
Figure 4.6. Deformation due to prestressing (red), self-weight (blue) and total (black) at 2.5 days	69
Figure 4.7. Stresses after losses at midspan t_{60}	71

Figure 4.8. Magnel diagram	72
Figure 4.9. Stress and strain distribution at midspan for decompression moment	73
Figure 4.10. Stress and strain distribution at midspan for decompression moment	73
Figure 4.11. Analysis of transformed composite cross-section	74
Figure 4.12. Analysis of cracked composite cross-section	75
Figure 4.13. Stress-strain relationship in compression (ULS) [68]	76
Figure 4.14 Idealized stress-strain relationships in tension and compression [22].....	76
Figure 4.15. Forces and strain distribution (ULS)	77
Figure 4.16. Prestressing steel stresses and strains (ULS)	78
Figure 4.17. Stress and strain distributions at midspan (ULS)	78
Figure 4.18. Moment curvature diagram.....	78
Figure 4.19. Truss model [68]	79
Figure 4.20. Dimensions of compression strut in truss model [68].....	80
Figure 4.21. Coefficient for the stress state in the compressive strut.....	81
Figure 4.22. Influence of prestressing force in the shear capacity of a prestressed member without shear reinforcement [68]	82
Figure 4.23. Two members for calculation of shear resistance (blue: precast girder, red: cast in-situ topping)	83
Figure 4.24. Inclined stirrups in cast in-situ topping.....	84
Figure 4.25. Impression of FE model	85
Figure 4.26. Discretization of cross-section.....	86
Figure 4.27. Stress-strain curves for geopolymere concrete	88
Figure 4.28. Stress-strain curves for reinforcement and prestressing steel	88
Figure 4.29. Traction-displacement curves for the interface	89
Figure 4.30. Mesh of plane stress elements.....	89
Figure 4.31. Mesh of embedded reinforcement elements longitudinal reinforcement (red), shear reinforcement (blue), prestressing tendons (green)	89
Figure 4.32. Boundary conditions.....	90
Figure 4.33. Analysis phases	91
Figure 4.34. Deformation after prestressing (Scale factor: 10)	92
Figure 4.35. Stress and strain distributions after prestressing at midspan	92
Figure 4.36. Vertical reaction forces.....	93
Figure 4.37. Evolution of convergence norms and number of iterations per load step.....	93
Figure 4.38. Evolution of the relative energy variation	94
Figure 4.39. Load - deflection curve NLFEA.....	94
Figure 4.40. Deformed meshes at different load steps (Scale factor: 10)	95
Figure 4.41. Stress distribution at midspan at different load steps.....	95
Figure 4.42. Maximum principal strains in the topping at 199, 222, 250, 276 and 345 kN ...	96
Figure 4.43. Maximum principal strains in the precast girder at 199, 222, 250, 276 and 345 kN	97
Figure 4.44. Minimum principal strains at 199, 222, 250, 276 and 345 kN.....	97
Figure 4.45. Concrete strains at midspan NLFEA	98
Figure 4.46. Node localization for extraction of concrete strains.....	98
Figure 4.47. Longitudinal reinforcement strains at 236, 276 and 345 kN	99
Figure 4.48. Shear reinforcement strains at 236, 276 and 345 kN.....	99
Figure 4.49. Prestressing tendons strains at 345 and 399 kN	99
Figure 4.50. Evolution of convergence norms and number of iterations per load step.....	100
Figure 4.51. Evolution of the relative energy variation	100
Figure 4.52. Load - deflection curve NLFEA.....	101
Figure 4.53. Deformed meshes at different load steps (Scale factor: 10)	102
Figure 4.54. Maximum principal strains in concrete at 446, 593, 638, 814 and 184 kN	103

Figure 4.55. Minimum principal strains in concrete at 446, 593, 801, 814 and 184 kN	104
Figure 4.56. Shear reinforcement strains at 493, 568, 638 and 814 kN.....	104
Figure 4.57. Longitudinal reinforcement strains at 493, 540, 638 and 814 kN	105
Figure 5.1. Deformations after prestressing (Experimental vs analytical vs LFEA)	107
Figure 5.2. Stress and strain distributions after prestressing at midspan (Analytical vs LFEA)	107
Figure 5.3. Transmission length	108
Figure 5.4. Microcracking in the cast in-situ topping at the onset of cracking (Load step 7: 64 kN).....	108
Figure 5.5. Load - deflection curve during flexural test (Experimental vs NLFEA)	109
Figure 5.6. Characteristic load levels (Experimental vs analytical vs NLFEA)	109
Figure 5.7. Stress distribution at midspan at different load steps (Analytical vs NLFEA) ...	110
Figure 5.8. Concrete strains at midspan (Experimental vs NLFEA)	111
Figure 5.9. Maximum principal strains from DIC measurements and NLFEA at different load levels	113
Figure 5.10. Maximum crack widths in precast girder (Experimental vs NLFEA)	114
Figure 5.11. Maximum crack widths in cast in-situ topping (Experimental vs NLFEA)	114
Figure 5.12. Prestressing of precast girders at different ages for geopolymer concrete under different curing conditions and OPC concrete	115
Figure 5.13. Sensitivity analysis Load - deflection curves.....	116
Figure 5.14. Load - deflection curve during shear test (Experimental vs NLFEA)	117
Figure 5.15. Maximum deformation under point of application of loading	118
Figure 5.16. Shear capacity	118
Figure 5.17. Line interfaces in 2D plane stress model.....	118
Figure 5.18. Cracking pattern at failure from NLFEA and DIC measurements.....	119
Figure 5.19. Comparison of forces flexural test vs flexural test after 9 months (NLFEA) ...	121
Figure 5.20. Load - deflection curve during flexural test after 9 months (Experimental vs NLFEA).....	121
Figure 5.21. Load - deflection curve during flexural test and flexural test after 9 months (Experimental vs NLFEA).....	122

List of tables

Table 2.1. Summary of satisfactory combinations of solid precursors and alkaline activators [4].....	11
Table 2.2. Summary of studies on the material properties of geopolymer concrete	12
Table 2.3. Summary of studies on the material properties of geopolymer concrete (cont.)..	13
Table 2.4. Summary of studies on structural tests on geopolymer concrete girders	22
Table 2.5. Summary of studies on FE modelling of geopolymer concrete girders subjected to 4-point load tests.....	24
Table 2.6. Standards including alkali-activated materials throughout the world	26
Table 2.7. Examples of application of structural geopolymer concrete	29
Table 3.1. Overview of casting operations.....	36
Table 3.2. Number of samples for mechanical tests according to the casting date.....	39
Table 3.3. Overview of mechanical tests for material properties of geopolymer concrete mixtures	39
Table 3.4. Compressive strength of the geopolymer concrete mixtures [MPa]	39
Table 3.5. Curing regimes of Elastic modulus samples of ready-mix geopolymer concrete mixture	40
Table 3.6. Expressions for elastic modulus and tensile strength	42
Table 3.7. Elastic modulus of geopolymer concrete [MPa]	42
Table 3.8. Nominal unrestrained drying shrinkage values $\epsilon_{cd,0}$ [% ₀] for concrete (Table 3.2 EN 1992-1-1 [22])	46
Table 3.9. Volume stability properties of SCGC mixture of precast girder according to EN 1992-1-1	46
Table 3.10. Volume stability properties of geopolymer concrete.....	47
Table 3.11. Mechanical properties of geopolymer concrete mixtures	49

Table 3.12. Summary of volume stability properties of Haitsma Beton - TU Delft SCGC mixture	49
Table 3.13. Mechanical properties of prestressing steel.....	50
Table 3.14. Measured deformations of precast girders after prestressing	55
Table 3.15. Deformation of precast girders of similar dimensions and prestress configuration produced by Haitsma Beton with conventional concrete C60/75	56
Table 3.16. Maximum crack width in the constant moment region at different load steps from DIC measurements	59
Table 4.1. Equilibrium of horizontal forces (ULS)	77
Table 4.2. Conservative assumptions of truss models.....	80
Table 4.3. Discretization of real geometry for plane stress FE model	86
Table 4.4. Longitudinal reinforcement	86
Table 4.5. Material parameters of geopolymer concrete.....	87
Table 4.6. Finite element type and mesh details	90
Table 4.7. Analysis phases	91
Table 4.8. Convergence criteria	92
Table 4.9. Maximum crack width in the constant moment region at different load steps from NLFEA	96
Table 5.1. Parameters sensitivity analysis.....	115
Table 5.2. Parameters analysis flexural test after 9 months	120

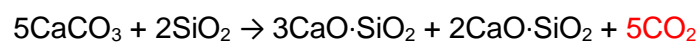
1

Introduction

1.1 Background

For the last century, the development of technology around binding systems for construction application has been primarily focused on Ordinary Portland Cement (OPC) concrete [1]. Concrete is an assembly of granular particles held together by a fluid binder phase which hardens over time. The binder phase is formed by the chemical reaction triggered by the hydration of OPC with the addition of water (Figure 1.1). The versatile initial fluid phase allows for freedom of form and is easy to use, whereas the hardened phase displays good functional performance regarding strength and durability. Furthermore, concrete is an inexpensive solution for application in the construction sector due to the broad availability and low cost of its constituent materials, making concrete the second-most-used substance in the world after water and the most widespread construction material [2]. The demand for worldwide cement production is currently increasing around 30% per decade as a result of a growing worldwide population paired with the increasing demand for infrastructure, particularly in developing nations [3].

However, this conventional binder system has some drawbacks. OPC concrete, as the largest volume manufactured material in the world, is a significant source of greenhouse gases. Carbon dioxide (CO₂) is released from the burning of fossil fuel for energy generation in the synthesis of high calcium content minerals and from the decarbonation of limestone in the kiln during manufacturing [1]:



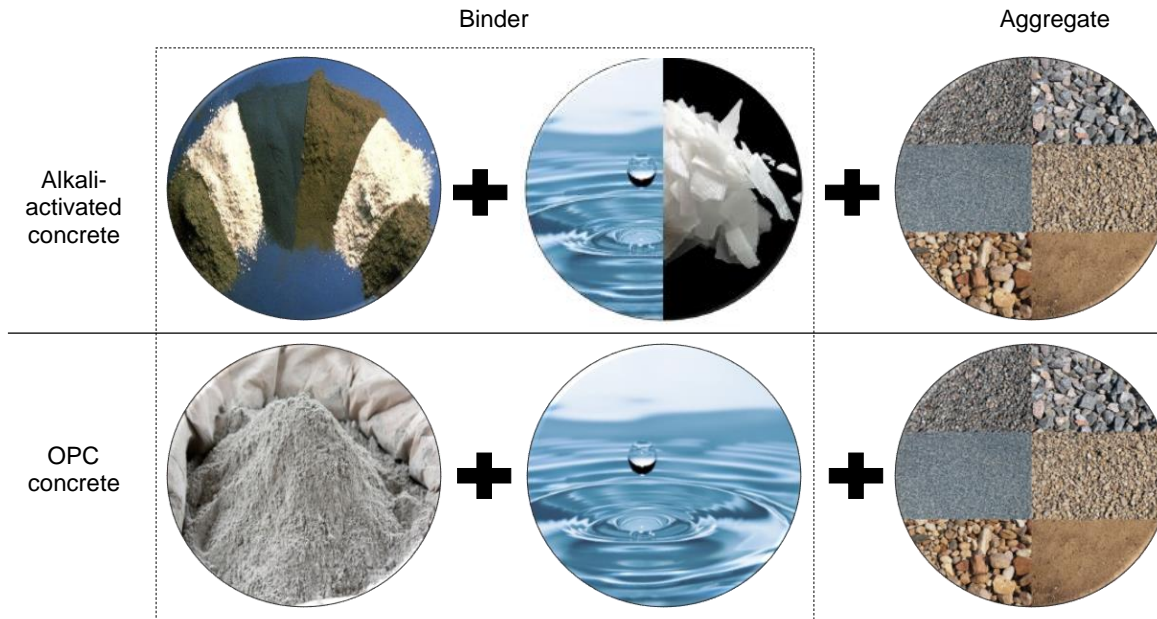


Figure 1.1. Basic composition of alkali-activated and OPC concretes

The global production of OPC and the associated CO₂ emissions have been increasing steadily since the 1940s (Figure 1.2) and the production of 1 ton of OPC can account for up to 1 ton of CO₂. OPC production contributes 5-8% to the worldwide anthropogenic CO₂ emissions [4] and the industry ranks as the 4th largest contributor only behind the petroleum, coal and natural gas industries [3].

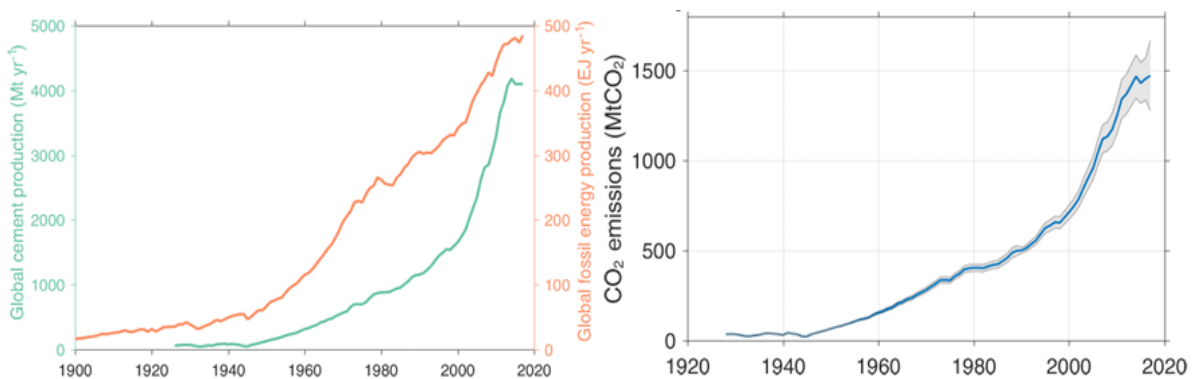


Figure 1.2. Global cement and energy production and global CO₂ emissions from cement production [5]

In most of the developed world, replacement of OPC by Supplementary Cementitious Materials (SCMs) has been a generalized practice for decades in the production of alternative binders with a lesser impact on CO₂ emissions, depletion of finite natural resources and energy consumption. The most common SCMs are industry by-products such as fly ash, Blast Furnace Slag (BFS) and silica fume, which are obtained from coal-powered thermal plants, and the production of iron and metal alloys, respectively. Natural pozzolans and incinerated clays are also used to a certain extent as SCMs. In Europe, EN 197-1 [6] establishes blended cement types with partial replacement (up to 95%) of OPC by other constituents. On the other hand, developing countries requiring new industrial developments may be reluctant to implement new technologies as the initial capital for a new cement factory, producing 1 million tons per year, ranges between 75-240 million USD, and the investment is recovered by production and commercialization of cement [3].

Nowadays, the environmental impact is a crucial design criterion in engineering practice and the industry needs to adapt to satisfy the continuously increasing demand for infrastructure in a sustainable way with the implementation of alternative materials. Consequently, in the past years the term alkali-activated concrete has become more popular as a technological innovation and sustainable design strategy for achieving a “cement-free” construction sector. Alkali-activated concrete is reported to be a low-environmental-impact alternative to OPC concrete where the binder phase results from the reaction of an alkali activator, previously dissolved in water, with a solid precursor containing alumina and silica (Figure 1.1). An independent study by Habert and Ouellet-Plamondon [7], from the Life-Cycle Assessment (LCA) research area, concluded that alkali-activated concrete contributes to less than 5% of the Global Warming Potential (GWP) and achieves an overall reduction of CO₂ emissions of 80% compared to OPC concrete.

The development of knowledge around alkali-activated materials dates back to the early 20th century; with extensive theoretical research, standardization and full-scale precast and cast in-situ applications in the former Soviet Union and China after the 1950s [4]. Nowadays, alkali-activated concrete has increased interest due to the sustainability considerations aforementioned. Past projects [4] and successful commercial operations in Australia, in pavements, slabs, walls, water tanks, bridge decks and tunnel segments [8, 9], demonstrate that standard construction practices for OPC concrete structures are applicable to a certain extent for alkali-activated concrete. Additionally, the functional requirements can be fulfilled on a project-scale basis as alkali-activated concrete is a versatile material, locally adaptable and achievable with numerous possible combinations from a wide range of precursors and activators [8]. In general, it is reported that alkali-activated concrete has good fire resistance, high early strength [4], low carbonation depths [1], resistance to sulfate attack, acid and chloride ingress [9], low susceptibility to alkali-silica reaction and the high alkalinity which seems to be favorable for the protection of embedded steel reinforcement [10]. Conversely, the material properties are dependent of the chemical structure of the binder phase according to the choice of constituents and the lack of predictive models and standards for application limit the use of alkali-activated concrete in real world applications [9]. The development of strength is comparable to OPC concretes but curing conditions influence significantly the development of stiffness and strength of the binder phase [11, 12].

Conferring to future expectations of our society, the Dutch government is collaborating along knowledge institutions, entrepreneurs, industry, trade unions, and environmental, financial, public organizations to close the raw material cycles and achieve a complete circular economy by 2050 with a reduction to half of the consumption of primary raw materials by 2030 [13, 14]. The Fryslan project is a joint venture between Delft University of Technology, Ghent University, Haitsma Beton and the Province of Fryslan to execute a cement free bridge for road traffic. The objective of the project is to replace the bridge of the Kowebrege Jouswier with a more sustainable alternative, a bridge built with alkali-activated concrete. For large-scale application of alkali-activated concrete in this bridge, structural elements consisting of an individual prestressed girder with a compression layer on top are studied to demonstrate compliance with criteria regarding performance and safety.

1.2 Problem statement

Future construction materials will have to satisfy functional performance requirements over an intended service life with the application of renewable/recyclable building materials and the provision of an added value to the environment. Alkali-activated or geopolymers concrete appears to satisfy the latter part of the requirements but the functional performance still needs to be guaranteed before large-scale application of this (not so) new material.

The key performance indicator of conventional concrete structures is the 28-day compressive strength. This property sets the basis of concrete codes and most of the material properties can be derived from the compressive strength with empirical correlations. In general, geopolymer concrete exhibits similar development of strength at 28 days [11] and stress-strain relationship in compression [15], to conventional concrete. However, the correlations to estimate the remaining material properties of conventional concrete do not seem to hold for geopolymer concrete. Specifically, several studies indicate that in geopolymer concrete the elastic modulus, creep coefficient and shrinkage strains are different than in conventional concrete. The elastic modulus is a parameter determining the in-service performance of a geopolymer concrete structure and indicates the response against elastic deformation when a force is applied. The prediction formulas for conventional concrete may overestimate this property as the elastic modulus of geopolymer concrete is highly sensible to drying and is lower than conventional concrete; no general remarks to the development of the elastic modulus in different types of geopolymer concrete mixtures as function of the compressive strength are available [3, 11, 16]. Geopolymer concrete displays a highly viscous response over time as the deformations associated with the reorganization of the microstructure are irreversible [17] and literature [3, 18] indicates higher creep for slag-based geopolymer concrete and lower creep for fly ash-based geopolymer concrete, than conventional concrete; the same tendency is followed by the shrinkage behavior. The implications of the different material properties pose a critical impediment for the generalized applicability of geopolymer concrete since a lower stiffness and higher shrinkage strains and creep deformations could reduce the buckling capacity of axial members, result in larger deflections in slender structures, higher prestress losses and different creep behavior of prestressed structures.

The differences in material properties puts in doubt the structural performance of geopolymer concrete structures and the structural upscaling of geopolymer concrete mixtures needs to be investigated. According to Sanjayan [3], the average number of publications per year with “geopolymer” in the keywords, title or abstract in the Scopus database was 3 per year in 1990 with a rise to 450 in 2015. Nevertheless, the research gap is still evident because the majority of studies in 2015 focus on the chemistry and microscopic structures; only 10% report aspects regarding structural engineering or construction. For small scale tests, many studies have been performed to study the influence of a wide range of parameters. In contrast just a few structural scale tests have been conducted and most of the studies are focused on fly ash-based alkali-activated concrete [19]. Furthermore, from the limited number of studies at structural level, prestressed geopolymer concrete structures are even more exceptional, hence further research is imperative for structural application of geopolymer concrete. Sonal, et al. [20] investigates the flexural response of prestressed and non-prestressed (geopolymer and OPC concrete) girders without conventional reinforcement to 4-point load tests. The deflections and cracking load for prestressed geopolymer concrete girders are higher than OPC concrete girders and the load capacity is similar regardless of the concrete type [20].

The applicability of geopolymer concrete as a standard construction practice is limited by the lack of a legal and technical framework for manufacturing, specification, design, analysis and construction [9]. Standardization is a response to the necessities of the prevalent construction practice [8] and performance-based standards are required at each jurisdiction in a project-level basis but also internationally to set the foundation of a widespread business practice [1]. The construction sector and engineering practice require the knowledge from the research in numerical models, empirical equations, appropriate assumptions and safety factors, to produce safe, durable and economic designs according to the expectations of clients and society [21]. A universal mix design methodology and predictive models need to be made available for compliance with performance specifications from design [10]. Real-world applications supported by laboratory testing are paramount to build confidence of the public

and industry in a new technology. The conformity of existing design provisions for conventional reinforced and prestressed concrete structures shall be evaluated to determine the feasibility of applying these criteria for alkali-activated concrete structures [21].

This study intends to contribute towards the introduction of geopolymer concrete as a construction material. The focus is on the upscaling of two geopolymer concrete mixtures in structural elements consisting of an individual prestressed girder with a reinforced topping layer cast in-situ. The main objectives are to study how these material properties differ with conventional concrete, determine their impact in the structural performance and define the extent of applicability of current methods of analysis for conventional concrete structures, as defined in EN 1992-1-1 and the Rijkswaterstaat's Guidelines for NLFEA, for geopolymer concrete. The structural performance of the elements subjected to flexural and shear mechanical tests is studied by analytical methods and 2D plane stress nonlinear finite element analyses, which are further compared to experimental results in terms of deformations, load-deflection response, principal strains, normal stresses, damage evolution, cracking stages, maximum load and failure mechanism.

1.3 Research question and objectives

The main research questions and sub-questions of the present study are:

1.3.1 Research Question 1 (RQ1)

How different are the time-dependent material properties (e.g. elastic modulus, creep and shrinkage) of the two geopolymer concrete mixtures compared to conventional concrete of similar strength class? What is their influence in the response of a prestressed girder with reinforced cast in-situ topping to prestressing and mechanical tests?

1. How do the curing conditions affect the development of stiffness of the two geopolymer concrete mixtures used in the precast girder and cast in-situ topping?
2. What are the differences in the elastic modulus, creep and shrinkage of the two geopolymer concrete mixtures, with the properties estimated with EN 1992-1-1 [22] for conventional concrete and empirical relations for geopolymer concrete from literature?
3. What is the effect of the elastic modulus, creep and shrinkage of the two geopolymer concrete mixtures on the camber, prestressing force, flexural behavior and load-deflection response of the prestressed girder with reinforced cast in-situ topping?

1.3.2 Research Question 2 (RQ2)

To what extent are the methods of analysis for conventional concrete structures, from EN 1992-1-1 [22] and the Rijkswaterstaat's Guidelines for NLFEA [23], applicable to estimate the flexural and shear capacity of the test specimen consisting of a prestressed girder with reinforced cast in-situ topping built with geopolymer concrete?

4. To what extent are the analytical models from EN 1992-1-1 [22] and the numerical models developed according Rijkswaterstaat's Guidelines for NLFEA [23] applicable to simulate the prestressing stage and construction sequence of the test specimen?
5. To what extent are the analytical models from EN 1992-1-1 [22] applicable to estimate the resistance of the test specimen subjected to flexural and shear tests?
6. To what extent are the numerical models, assumptions and modelling choices (material constitutive models, element types, boundary conditions, loading and interaction between different materials) from Rijkswaterstaat's Guidelines for NLFEA [23] applicable to estimate the response of the test specimen to flexural and shear tests?

1.4 Outline

This study is divided in six chapters and the relationships between each other and the research questions are displayed graphically in the outline (Figure 1.3).

Chapter 1 frameworks the background, motivation, scope, main objectives and research questions of the present thesis. Chapter 2 starts with a literature review of the material properties, with respect to the choice of the constituent materials and curing conditions, and a comparison with conventional concrete. Furthermore, studies on the structural behavior of reinforced and prestressed alkali-activated concrete flexural members are analyzed. Next, the current stage of development, representative real-world applications, advantages and limitations of alkali-activated concrete in the construction sector are examined. Chapter 3 describes the application of geopolymer concrete in structural scale with the construction and testing of the structural performance of a prestressed girder with cast in-situ topping. The development of the elastic modulus over time of the geopolymer mixtures employed in the construction of the prototype specimens for different curing conditions is analyzed (sub-question 1), and compared to the estimates from EN 1992-1-1 for conventional concrete and from the empirical relations from the studies in Chapter 2; the comparison is further done for the creep coefficient and shrinkage strains (sub-question 2). Afterwards, the experimental results of 4-point bending and 3-point load mechanical tests for assessing the flexural and shear capacity of the specimens are included. Chapter 4 contains the analytical analysis according to EN 1992-1-1 and the 2D plane stress linear and nonlinear phased analysis in FE software DIANA, of the aforementioned structural tests (sub-questions 4, 5 and 6) with the necessary modifications where deviations of the properties of geopolymer and conventional concrete are identified (sub-question 2). Chapter 5 contains a comparison between the experimental, analytical and FEM results with regards to deformations, load-deflection response, principal strains, normal stresses, damage evolution, cracking stages, maximum load and failure mechanism (sub-questions 4, 5 and 6). Additionally, the analysis of the long-term creep and shrinkage behavior and a sensitivity analysis (influence of the different elastic modulus according to the curing conditions), with the respective variation in the prestressing force, are performed to assess the influence in the flexural behavior (sub-question 3). Finally, Chapter 6 gives conclusions and recommendations from the results and observations of the present study.

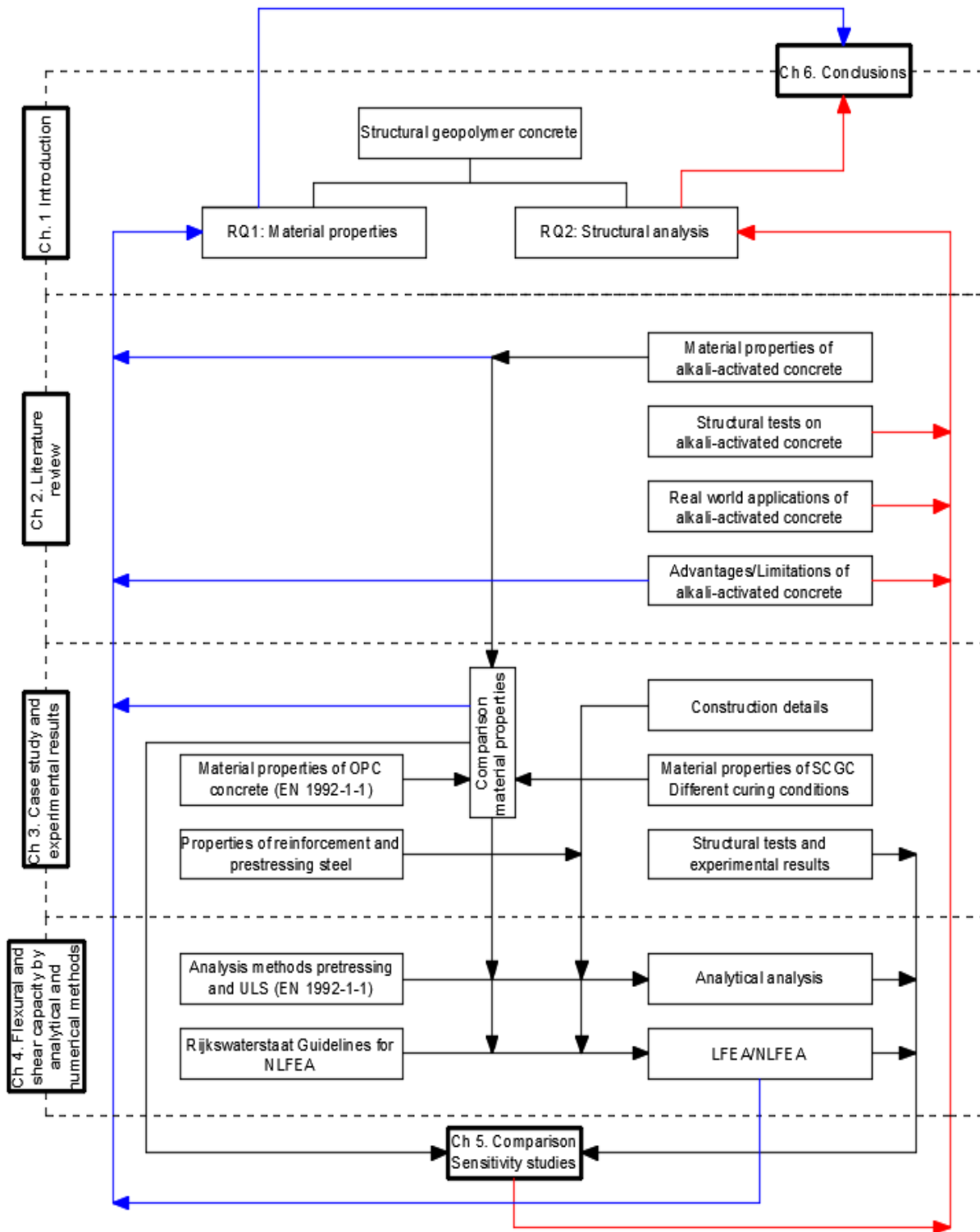


Figure 1.3. MSc Thesis Outline

2

Literature review

This chapter provides a description of alkali-activated concrete from existing literature. The sequence of development of the material through history is summarized; followed by formal definitions of alkali-activated and geopolymer concretes, classifications and descriptions of the different constituent materials. The material properties with regards to the choice of the constituent materials and curing conditions are described and compared to the material properties of OPC concrete. The insights from experimental studies and numerical simulations on the structural behavior of alkali-activated concrete structures are presented. Finally, the current stage of development in standards, representative real-world applications, potential advantages and limitations of alkali-activated concrete in the construction sector are analyzed.

2.1 Alkali-activated concrete

2.1.1 History

According to J. L. Provis et al. [4], some ancient Roman concretes resulted from the activation of pozzolanic materials, in particular volcanic ashes with high alkali content, triggered by the reaction of calcium compounds, specifically lime. Evidently, insights of the durability of concrete can be derived from the analysis of ancient Roman materials as several structures remain intact after centuries and modern cement repairs have rarely been as durable as ancient cements under similar exposure conditions. Furthermore, the inspection of ancient mortars after two millennia, indicates the presence of zeolites [4]. Similarly, the research in alternative construction materials by Glukhovskiy in Kiev around the 1950s, as a response to the cement shortages in the Soviet Union and China, identified zeolitic materials containing alkalis as the hydration products of the basic rock-forming materials in the Earth's crust, while the hydration products of OPC are calcium silicate hydrate (C-S-H) and portlandite [1].

The formal knowledge around alkali-activated materials (AAMs) started in the early 20th century when German scientist Hans K uhl patented a solid material from the reaction of a precursor containing silica and alumina with an alkali source in 1908. In the 1940s, Belgian engineer Purdon experimented alkali-activation of different blast furnace slags with sodium hydroxide solutions and already noted that slag-alkali cements presented low heat evolution, and higher flexural and tensile strengths than OPC concretes of similar compressive strength [4]. The term geopolymer was first used in the 1980s by French chemist Davidovits with his development in alkali-activation of metakaolin where the binder forms a Si-O-Al inorganic polymer which exhibited good fire resistance and high early strength [1, 3].

In the following decades, the use of by-products, such as fly ash and GGBFS, as precursors in alkali-activated concrete was mainly substituted by the generalized practice of partial replacement of OPC in blended cement types [8]. In general, the use of by-products as SCMs is positive for environmental considerations but also improves the fresh and hardened properties of concrete. Specifically, EN 197-1 [6] establishes blended cement types with limits for the alkali, fly ash and GGBFS content (CEM III/C allows up to 95% GGBFS and 5% clinker). Nowadays, the use of alternative binders to achieve a “cement-free” building sector due to sustainability considerations is the main driver for the development of knowledge around alkali-activated concrete.

2.1.2 Definitions

Alkali-activation: is the generic term for the production of a hardened binder by the chemical reaction of a solid aluminosilicate precursor under alkaline conditions caused by an alkaline-activator (solid or dissolved). Cement blends are not encompassed by the definition if Portland cement is the principal source of alkalinity [10].

Alkali-activated material (AAM): is the broadest classification that includes any binder derived from alkali-activation [4].

Geopolymer: a subset of AAMs where an inorganic sodium aluminosilicate (zeolite type of polymer) binder phase (N-A-S-H gel) [21] results from the synthesis of an aluminosilicate-rich reacting component containing low-calcium content [4], such as metakaolin, fly ash, metallurgical slag or natural pozzolan [8], with an alkali metal hydroxide or silicate activator.

Strictly speaking, geopolymer does not encompass precursors with high-calcium content, such as GGBFS, as the main binder phase is a calcium-silicate hydrate (C-A-S-H gel) with lower Ca/Si ratio compared to OPC concrete [21]. In this study, the use of the term geopolymer will be used in a broad sense to include any alkaline-activated cement. Even though this is not strictly accurate, the definition is used due to the wide applicability of the term geopolymer concrete in current practice. Other names such as inorganic geopolymer concrete and geocement may be used to denominate a material synthesized with the same chemistry [8].

2.1.3 Classification

According to Roy [10], geopolymer concrete can be classified according to the production route of the binder:

1. One-part mix: the activator and precursor are mixed as dry powder and the chemical reaction occurs by addition of water. The potential of production and distribution as bagged material is of particular interest for upscaling at industrial level.
2. Two-part mix: is the main production route of geopolymer concrete by the combination of a liquid activator solution with solid precursors. More suitable for precast production at industrial scale with precise dosage control of the activator.

Krivenko [24] defines two main categories of overlapping composition fields according to the basic composition of the binder phase:

$\text{Me}_2\text{O} \cdot \text{Me}_2\text{O}_3 \cdot \text{SiO}_2 \cdot \text{H}_2\text{O}$: Alkaline zeolitic type minerals

$\text{Me}_2\text{O} \cdot \text{MeO} \cdot \text{Me}_2\text{O}_3 \cdot \text{SiO}_2 \cdot \text{H}_2\text{O}$: Mixed alkali-alkaline earth zeolites, calcium hydrosilicates and carbonates

Furthermore, Krivenko [24] further describes five categories of geopolymer based on the composition of the precursors:

1. Alkali-activated slag cements
2. Alkali-activated Portland blended cement
3. Alkali-activated pozzolan cements
4. Alkali-activated lime-pozzolan/slag cements
5. Alkali-activated calcium aluminate blended cement

2.1.4 Constituents

In the most general sense, concrete is a composite material of granular materials bonded by a hardened binder phase. The granular materials are aggregates such as sand, gravel or crushed stone [25] which are used indistinctively both for OPC and geopolymer concretes. On the other hand, the binder phase results from alkali-activation of a precursor and activator or hydration of cement with water, for geopolymer or OPC concretes, respectively.

The alkali source is any solution that supplies alkalinity to the mixture to accelerate the dissolution of the solid precursor [4]. According to Fernandez-Jimenez, et al. [26], the six categories of alkali-activators according to their chemical composition, as defined by Glukhovsky, are:

1. Caustic alkalies: MOH
2. Non-silicate weak acid salts: M_2CO_3 , M_2SO_3 , M_3PO_4 , MF , etc.
3. Silicates: $\text{M}_2\text{O} \cdot n\text{SiO}_2$
4. Aluminates: $\text{M}_2\text{O} \cdot n\text{Al}_2\text{O}_3$
5. Aluminosilicates: $\text{M}_2\text{O} \cdot \text{Al}_2\text{O}_3 \cdot (2-6)\text{SiO}_2$
6. Non-silicate strong acid salts: M_2SO_4

where M is either Na or K. The most common activators are sodium hydroxide (NaOH) and sodium silicate $\text{Na}_2\text{O} \cdot \text{SiO}_2$. For high calcium precursors, such as GGBFS, Na_2CO_3 and Na_2SO_4 are also effective [10].

In theory, alkali-activation is possible with any solid material rich in silica and alumina. Figure 2.1 displays the classification of supplementary cementitious materials (SCMs) with potential use as precursors for geopolymer concrete. Aluminosilicate-rich materials as industrial by-products (fly ash, blast furnace slag), incinerated materials (metakaolin) and natural pozzolans are already used as partial replacement for Portland cement in blended cements [10]. Additionally, recycled aluminosilicates, ferric clays, ferrous and non-ferrous slags, glass and organic waste are potential precursors without the demand for production of blended cements. Furthermore, alkali-activation can be used on a unique precursor or combination of precursors.

Nevertheless, geopolymer concrete is far from a one-size-fits-all solution as a wide range of precursors and activators are available and the selection depends upon availability, reactivity, costs and environmental considerations [10]. Extensive research from literature regarding adequate combinations of precursors with alkali-activators is presented by Provis, et al. [4] and is summarized in Table 2.1.

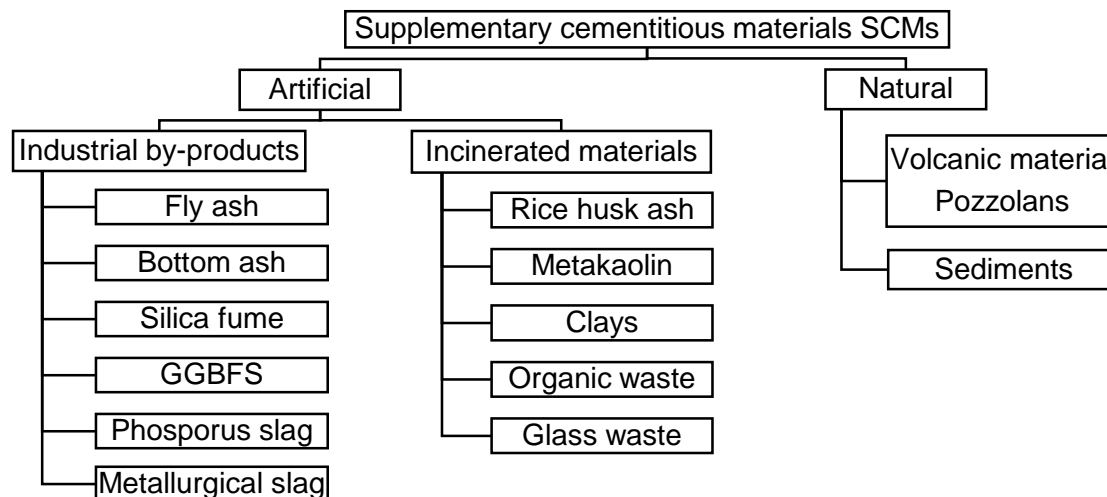


Figure 2.1. Classification of SCMs

Table 2.1. Summary of satisfactory combinations of solid precursors and alkaline activators [4]

Precursor	MOH	$M_2O \cdot nSiO_2$	M_2CO_3	M_2SO_4
Blast furnace slag	Acceptable	Desirable	Good	Acceptable
Fly ash	Desirable	Desirable	Poor	With clinker
Calcined clays	Acceptable	Desirable	Poor	With clinker
Natural pozzolans	Acceptable	Desirable	-	-
Steel/phosphorus slag	-	Desirable	-	-
Copper slag	-	Acceptable	-	-
Red mud	-	Acceptable	-	-
Incinerated solid waste	-	Acceptable	-	-

2.2 Material properties of geopolymer concrete

2.2.1 Preliminaries and selected studies

The concrete codes are primarily based on the 28-day compressive strength as key performance indicator for the design and analysis of conventional concrete structures. The compressive behavior of geopolymer concrete is similar to OPC concrete in terms of development of strength at 28 days [11] and stress-strain relationship [15]. Nevertheless, as will be described in this section, the behavior of the binder phase in geopolymer concrete depends upon a wide range of factors such as choice (and combination) of precursors (type, reactivity and quality) and activators, and curing conditions. Therefore, there is an intrinsic variability in the material properties within different types of geopolymer concretes but also with respect to OPC concrete. Specifically, the prediction models from conventional concrete codes cannot be taken as a concluding framework for determining the material properties of geopolymer concrete since it can result in non-conservative estimates which will lead to an unsafe design.

This section provides a description of the development of mechanical and volume stability properties (elastic modulus, creep, shrinkage, and compressive, tensile, flexural and bond strengths) of alkali-activated low-calcium and high-calcium precursors. The study is limited to binders based on fly ash, GGBFS or a combination of both. This investigation is based on selected studies (Table 2.2 and Table 2.3), in combination with several other sources, that describe the effects of the type of activator, GGBFS to fly ash proportions and curing regimes on the development of the material properties of geopolymer concrete, and compare to OPC concrete control samples or estimates from OPC concrete based codes.

Reference	Precursor		Activator	Control sample	Description of study
	GGBFS	Fly ash			
Castel, et al. [28]	14.8%	85.2%	NaOH and Na ₂ SiO ₃	-	Creep and shrinkage of geopolymer concrete for curing conditions at elevated temperature (40 or 80°C) and compared to EN1992-1-1 predictions. Compressive strength and elastic modulus also tested at 28 days.
Humad, et al. [29]	100% high MgO BFS	0%	10% weight Na ₂ CO ₃ and Na ₂ SiO ₃	-	Compressive strength at 3, 7, 28, 180 and 360 days. Drying shrinkage of unsealed samples after final setting (1 day for heat curing, 2-3 days lab conditions) and creep tests of sealed samples for 28 days. Samples tested at 20°C±2°C and 40%±7% RH.
Li, et al. [30]	100% 50%	0% 50%	NaOH and Na ₂ SiO ₃	CEM I 52.5N CEM III/A 42.5LA CEM III/B 42.5HSR LA	Elastic modulus, compressive and tensile splitting strengths at 1, 3, 7, 28 days. Measurement of autogenous shrinkage and restrained autogenous shrinkage.
Li, et al. [31]	50%	50%	NaOH and Na ₂ SiO ₃	CEM I 52.5R	Measurement of setting time, autogenous shrinkage (7 days), shrinkage under saturated condition, chemical shrinkage and internal RH and characterization of the microstructure. Monitoring of elastic modulus from casting to 7 days.
Ma & Dehn [32]	100%	0%	NaOH and Na ₂ SiO ₃	CEM I 32.5R concrete	Autogenous shrinkage at 65% RH of sealed GGBFS-based geopolymer and OPC concretes, compressive creep of sealed and unsealed specimens. Comparison to fib Model Code 2020 [27].
Nath & Sarker [11]	0%	100%	NaOH and Na ₂ SiO ₃	2 OPC mixtures (ACI 211.1-91)	11 mixtures. Additives (GGBFS, OPC and calcium hydroxide in small varying proportions) are used to improve the setting properties. Compressive strength, flexural strength and elastic modulus at 28 and 90 days.
Parthiban, et al. [33]	100 to 0%	0 to 100%	NaOH and Na ₂ SiO ₃	-	12 mixtures with a design characteristic compressive strength of 40 MPa at 28 days. Samples unmolded after 24 h, cured at ambient conditions and tested at 28 days.

Table 2.2: Summary of studies on the material properties of geopolymer concrete

Table 2.3. Summary of studies on the material properties of geopolymer concrete (cont.)

Reference	Precursor		Activator	Binder of control sample	Description of study
	GGBFS	Fly ash			
Prinsse, et al. [34]	100% 50%	0% 50%	NaOH and Na ₂ SiO ₃	-	Development of material properties (compressive strength, flexural strength, tensile splitting strength, elastic modulus) over time (up to around 2 years).
Puertas, et al. [35]	100% 70% 50% 0%	0% 30% 50% 100%	NaOH (2 and 10 M)	-	Influence of activator concentration, curing temperature and GGBFS to fly ash proportion in the strength and hydration products of geopolymer mortar. Compressive strength at 1, 7, 28 and 90 days, curing at 25 or 65°C for 5 h and then exposed to ambient temperature and 98% RH.
Sofi, et al. [15]	Varying	Principal	NaOH, Na ₂ SiO ₃ and Na ₂ CO ₃	-	6 mixtures. Influence in the mechanical properties when including coarse aggregate and GGBFS. Samples cured at 30-35°C and 80% RH, unmolded after 24 h and then cured at 23°C until testing for elastic modulus, compressive, tensile splitting and flexural strength at 28 days.
Yang, et al [36]	100%	0%	Primary: Ca(OH) ₂ Auxiliary: Na ₂ SiO ₃ and	-	12 mixtures. Evaluate the effect of the water to binder ratio (25 to 60%) in the 28-day mechanical properties (compressive strength, stress-strain relation, elastic modulus, direct tensile strength, modulus of rupture, shear stress-strain relation, bond stress-slip diagram)
Ye & Radlinska [37]	100%	0%	NaOH	Type I Portland cement	Shrinkage of GGBFS-based geopolymer concrete exposed to four different RH (70, 50, 30 and 11%) and 23±0.5°C for up to 70 days. Also characterization of the microstructure is studied.
Ye, et al. [17]	100%	0%	NaOH and Na ₂ SiO ₃	Type I Portland cement	Shrinkage behavior of four GGBFS-based mortars exposed to drying after 7 days at 23±0.5°C and different RH (85, 70, 50, and 30%) directly (constant RH level) or stepwise (RH level dropped after equilibrium) and for different proportion of activators. Elastic modulus also tested at 28 days.

2.2.2 Mechanical properties

2.2.2.1 Compressive strength

The 28-day average compressive strength of geopolymer concrete is close to the design strength of OPC concrete of similar density [15] and a similar stress-strain relation in compression to OPC concrete is achieved with the same aggregate type [11]. Yang, et al. [36] conclude that higher compressive strengths are obtained by a decreasing the water to binder ratio, as in conventional concrete, which reduces the porosity of the hardened binder and the microcracks with the aggregate particles. Furthermore, the authors report similar increasing rate of strength to OPC concrete and compare the stress-strain relationships in compression of GGBFS-based geopolymer concrete ($w/b < 30\%$) with predictions by CEB/fib and the modified Hognestad's model (Figure 2.2) [36]. The stress-strain relationship as defined in EN 1992-1-1 [22] is omitted since it presents a more brittle descending branch. The behavior of the geopolymer concrete mixture shows good agreement with the modified Hognestad's model whereas it displays lower stiffness and slower drop of strength in the descending branch as compared to the CEB/fib model. In general, the initial stiffness and peaks load increases with the compressive strength which is similar to the behavior of OPC concrete.

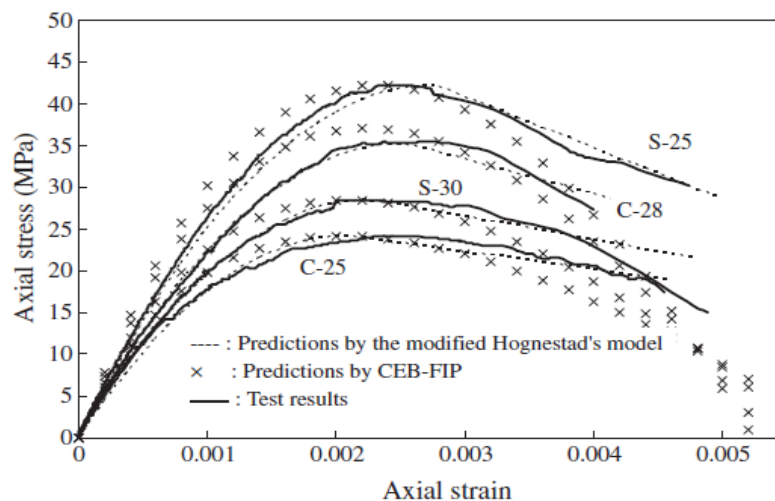


Figure 2.2. Stress-strain response of slag-based geopolymer concrete activated with $\text{Ca}(\text{OH})_2$ and $w/b < 30\%$ as reported by Yang, et al. [36]

Some ambient cured geopolymer concrete samples continue to develop strength after 28 days as the compressive strength at 28 days (25-46 MPa) increased at 90 days (33-53 MPa) [11]. The assessment of cylindrical samples from a GGBFS-based geopolymer concrete storehouse in Poland after 25 years, compared to the 28-day strength (further details provided in 2.5.2), also suggests that the compressive strength of geopolymer concrete appears to increase significantly over time [4]. On the other hand, a 17% decrease of the compressive strength is reported between 56 days and 1 year in GGBFS-based geopolymer concrete samples exposed to 50% RH (Relative Humidity) and 23°C after unmolding [12]. Therefore, the 28-day strength, generalized design criteria for OPC concrete structures, may not be an accurate indicator of the performance over the service lifetime of a geopolymer concrete structure, even though similar 28-day compressive strength to OPC concrete is achievable with geopolymer concrete.

The early-age strength of geopolymer concrete is intrinsically related to curing conditions and the structure of the binder phase according to the calcium content of the precursors. In fly ash-based binders the early-age strength is lower than OPC concrete as the polymerization reaction at ambient conditions is slower in mixtures with precursors with low-calcium content

[35]. For such reason, Aldred & Day [8], suggest heat curing to improve the development of strength at early ages. Puertas, et al. [35] reports that the 1-day strength is higher for binders with higher proportion of GGBFS, as GGBFS-based binders develop similar early-age strength to OPC concrete at ambient temperature [38] because of the presence of C-S-H gel in addition to the polymeric structure. The higher initial curing temperature has a positive effect on the early-age (1 day) strength, conversely lower temperature during the first 5 h gives higher strengths at later ages [35].

The reported higher early strength of geopolymer concrete with GGBFS and high temperature curing is especially relevant for prestressed structures as higher initial prestressing may be attained [39] which could increase the load-carrying capacity or decrease the material quantities, i.e. more slender design for a certain application. Nevertheless, the long-term performance would need to be checked as the presented studies remark that high-temperature curing at early ages reduces the strength over time. Finally, Provis [10] mentions that sealed curing is highly desirable as the strength development can be restricted if the activator leaches from the binder phase in submerged curing. On the other hand, Collins & Sanjayan [38] report increasing compressive strength for immersed cured samples until 400 days while sealed samples did not gain significant strength after 91 days. Both studies agree on a decrease in compressive strength due microcracking of air-exposed samples.

In combined systems of fly ash and GGBFS, the 7 and 28-day strength increases with increase in GGBFS content when cured in ambient conditions (Figure 2.3) [33]. Similarly, the compressive strength is lower for geopolymer concrete mixtures with replacement of GGBFS by fly ash [11, 30]. The influence of the GGBFS to fly ash proportion and the concentration of alkali-activator solution are more significant than the curing temperature in the development of strength; highest strengths are reached for 10 M activator concentration and increases with the content of GGBFS, regardless of the age [35]. Similarly, Yang, et al. [36] remark that the 28-day compressive strength is minimally affected by the curing conditions regardless of the choice of alkali-activator in GGBFS-based geopolymer concrete. On the other hand, in fly ash-based geopolymer concrete heat curing increases the 28-day strength significantly [28].

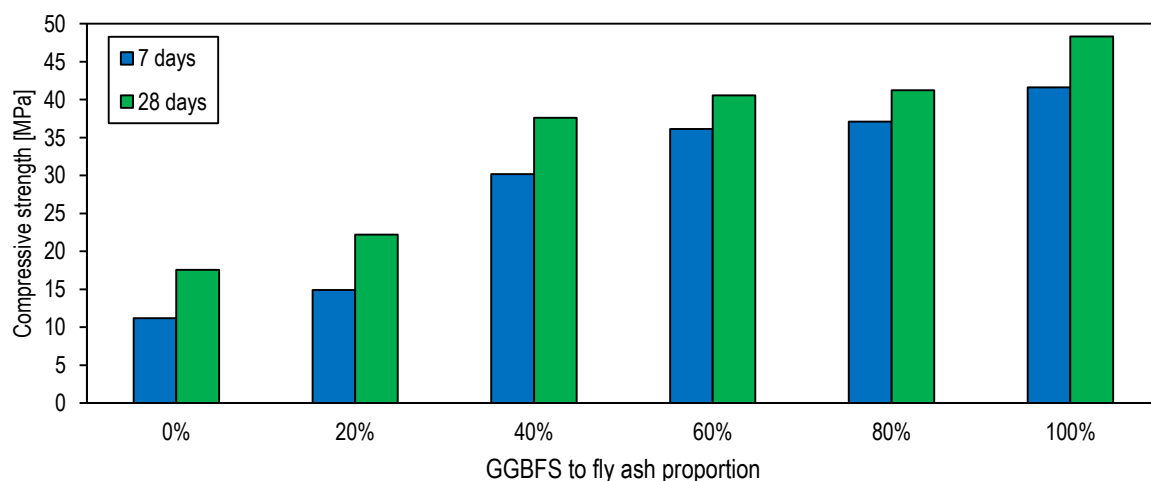


Figure 2.3. Variation of compressive strength of geopolymer concrete to GGBFS to fly ash proportion [33]

The compressive strength of GGBFS-based geopolymer with the choice of calcium hydroxide as activator is lower than OPC concrete with similar water to binder ratios due to a lower intensity of C-S-H gels that contribute to hardening and strength [36]. On the other hand, also for GGBFS-based geopolymer concrete, a combination of sodium carbonate and sodium silicate as activators provide a higher compressive strength than a mixture activated exclusively by sodium carbonate [29].

2.2.2.2 Flexural and tensile strength

The tensile strength of concrete allows to estimate the loads that cause cracking in a structure and achieve a satisfactory design regarding durability and performance. The tensile strength of concrete can be indirectly derived from the tensile splitting strength or the flexural strength but the findings regarding geopolymer concrete are not fully in agreement.

The tensile splitting strength of geopolymer concrete is found higher than the EN 1992-1 [22] and AS 3600 provisions for OPC concrete of a similar strength class [15]. The empirical relation for OPC concrete from EN 1992-1-1 [22] underestimates the tensile strength of geopolymer concrete due to a superior interfacial transition zone (ITZ) in geopolymer concrete caused by a denser ITZ with a similar microstructure to the bulk binder region [3]. The tensile splitting strength of geopolymer concrete (GGBFS and fly ash-based) and the tensile to compressive strength ratios are also lower; the commonly used ratio of 0.1 to estimate the tensile strength from the compressive strength is not applicable [30].

Different authors [11, 16, 36] propose empirical correlations to determine the tensile strength of geopolymer concrete (Figure 2.4). The flexural strength of fly ash-based geopolymer concrete is higher than for OPC concrete of similar strength class for both ambient and high temperature curing, and generally higher than estimates from OPC concrete codes AS 3600 and ACI 318 (Figure 2.4) [11, 16]. On the other hand, the fib Model Code 2010 [27] provisions are higher than the tensile strength of GGBFS-based geopolymer concrete but with an increasing rate against the compressive strength like OPC concrete (Figure 2.4) [36].

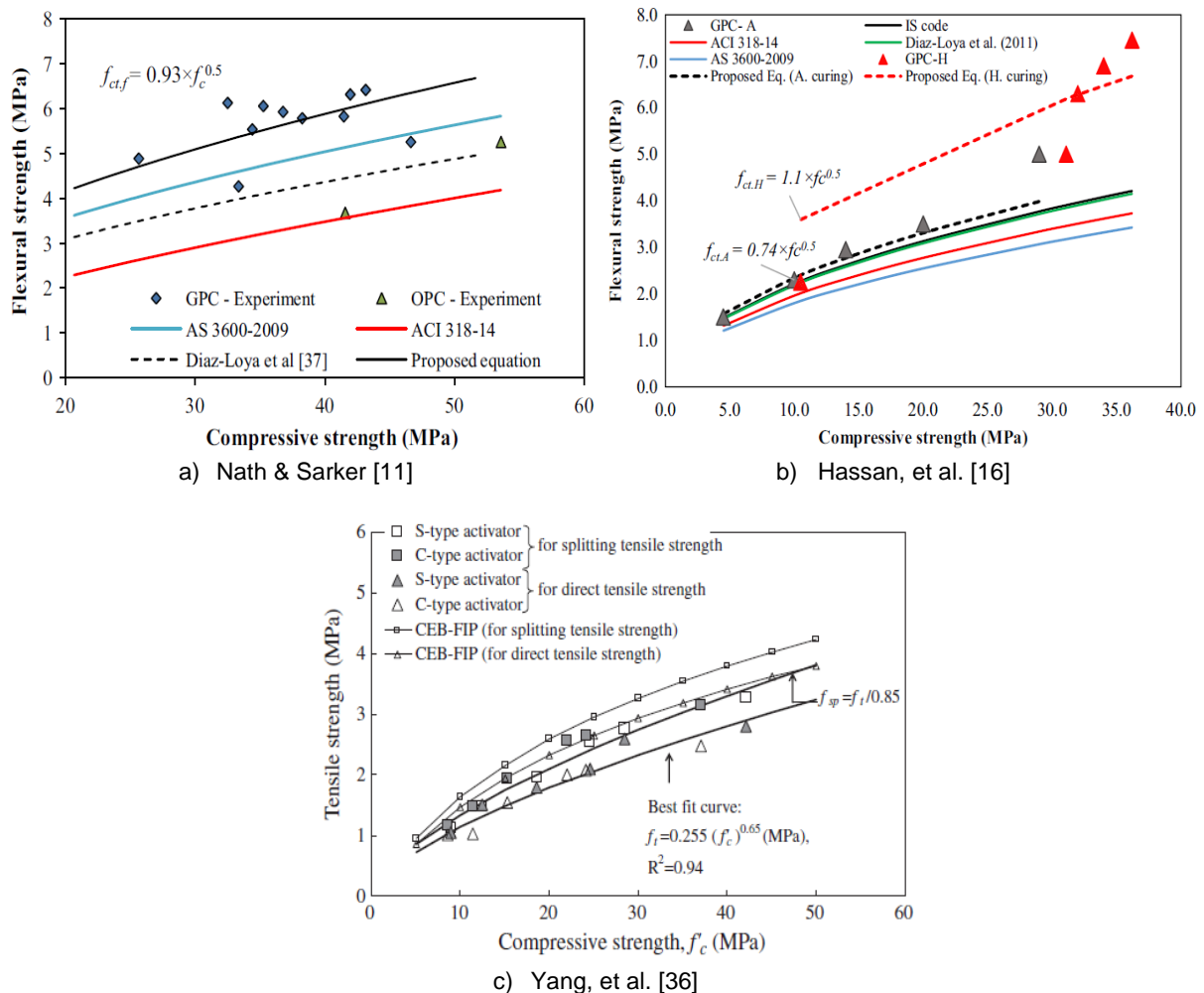


Figure 2.4. Correlation of flexural strength and compressive strength of geopolymer concrete at 28 days

The development of the flexural strength of ambient-cured geopolymer concrete follows the trend as the development of the compressive strength, the flexural strength increases with a higher proportion of GGBFS, OPC or calcium hydroxide in the mixture [11]. Nevertheless, this increase is reported only until a certain limit of high-calcium precursor content as the percentage of C-S-H gel also increases to a level that the tensile strength of the geopolymer binder is closer to the OPC concrete of similar grade. The flexural strength increases over time but the strength of ambient-cured geopolymer concrete is lower than heat-cured samples (Figure 2.5) [16].

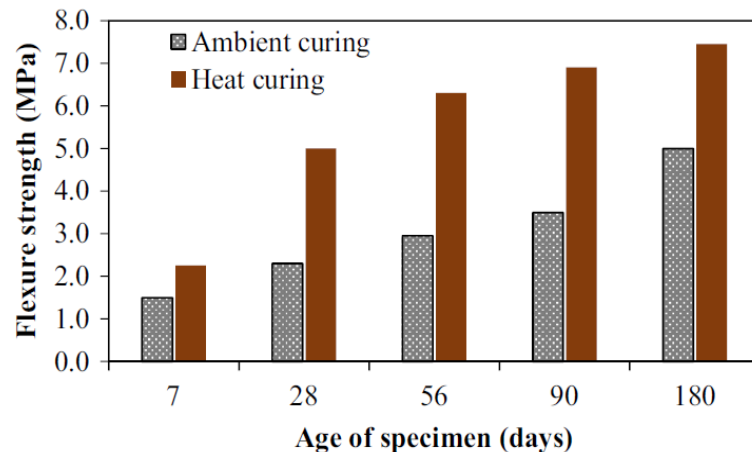


Figure 2.5. Flexural strength of geopolymer concrete at different ages for ambient and high temperature curing [16]

2.2.2.3 Elastic modulus

The elastic modulus is a parameter determining the in-service performance of a geopolymer concrete structure and indicates the response against elastic deformation when a force is applied. In general, the elastic modulus increases for a higher compressive strength as prescribed by the prediction models for OPC concrete.

The elastic modulus of ambient cured geopolymer concrete is lower than OPC concrete of similar strength class and is overestimated by standards and empirical equations from OPC concrete codes [11, 16, 30, 36] (Figure 2.6). In particular, the experimental results of the elastic modulus are lower than the estimates with ACI 318-19 [40], fib Model Code [27] and EN 1992-1-1 [22]. The elastic modulus of geopolymer concrete at 28 and 90 days are 25-30% and 22-31% lower than OPC concrete, respectively. According to Sanjayan [3], Hardito, et al. (2005) report 23% lower elastic modulus of fly ash geopolymer concrete samples compared to OPC concrete. Similarly, Nath & Sarker [11], summarize the findings on pulverized fuel ash mortars by Puertas, et al. [41] and mentions that the geopolymer samples attained lower elastic modulus than OPC mortar. Therefore, the prediction formulas for OPC concrete result in non-conservative estimates. The implications of the lower elastic modulus pose a critical impediment for the generalized applicability of geopolymer concrete since a lower stiffness is accompanied by larger deflections in slender structures, can reduce the buckling capacity of axial members and influences the prestress losses and creep behavior of prestressed structures.

Different authors [11, 16, 36] and several others like Lee & Lee (2013), Diaz-Loya, et al. (2011) and Hardito, et al. (2005) propose empirical relations between the compressive strength and the elastic modulus, as shown in Figure 2.6. Nevertheless, these equations are not universally applicable to geopolymer concrete as the differences in the proposed relations are due to variation of types of fly ash, mixture compositions, curing conditions and aggregate type.

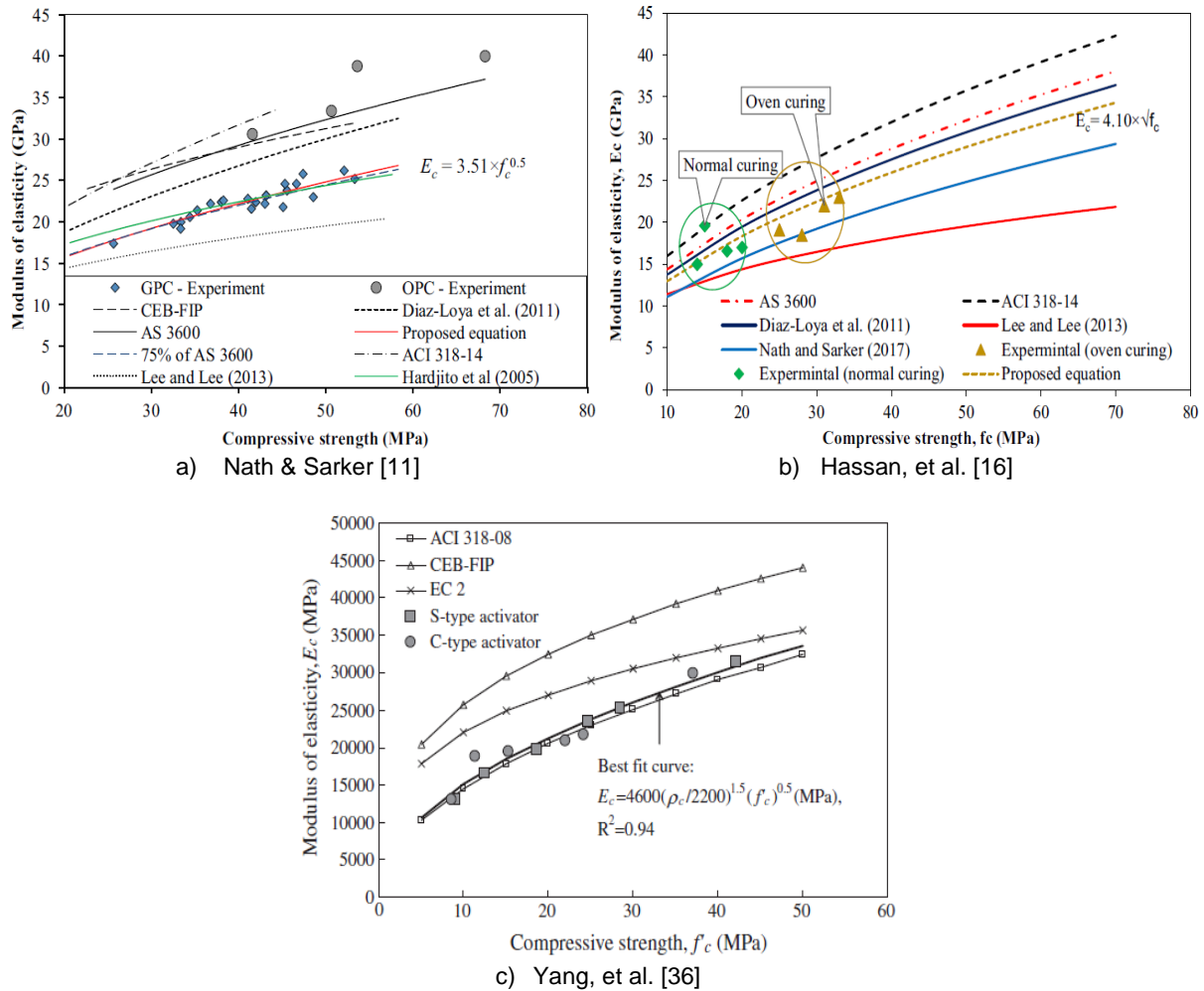


Figure 2.6. Correlation of elastic modulus and compressive strength of geopolymer concrete at 28 days

However, there is agreement that the elastic modulus increases for higher compressive strengths [3, 11, 16] (Figure 2.7). The compressive strength of geopolymer concrete increases with the content of GGBFS and for higher compressive strength the elastic modulus increases but remains lower than the estimates with OPC concrete codes. Likewise, it is reported that the elastic modulus is higher when GGBFS is the choice of precursor as compared to fly ash due to a denser pore structure [31]. Furthermore, the elastic modulus is around 35% lower when the mixture is alkali-activated exclusively with sodium hydroxide as compared to a combination of sodium hydroxide and sodium silicate, which results in similar values to OPC concrete [17].

The elastic modulus of fly ash-based geopolymer concrete is increased with heat curing (80°C), as the compressive strength, for 1 day and increasing the curing time beyond has little effect [28]. The effect of the curing conditions are shown in Figure 2.7.a), heat-cured and ambient-cured samples follow the trend of increasing modulus of elasticity with increasing compressive strength. The scatter of data for the samples with design compressive strengths of 50 MPa show that similar modulus of elasticity can be attained regardless of curing conditions, even when curing at ambient temperature causes a lower early-age strength. Nevertheless, the elastic modulus of geopolymer concrete starts to decrease after 7 days due to the microcracking [30] caused by the shrinkage process which will be explained in detail in the following Chapter.

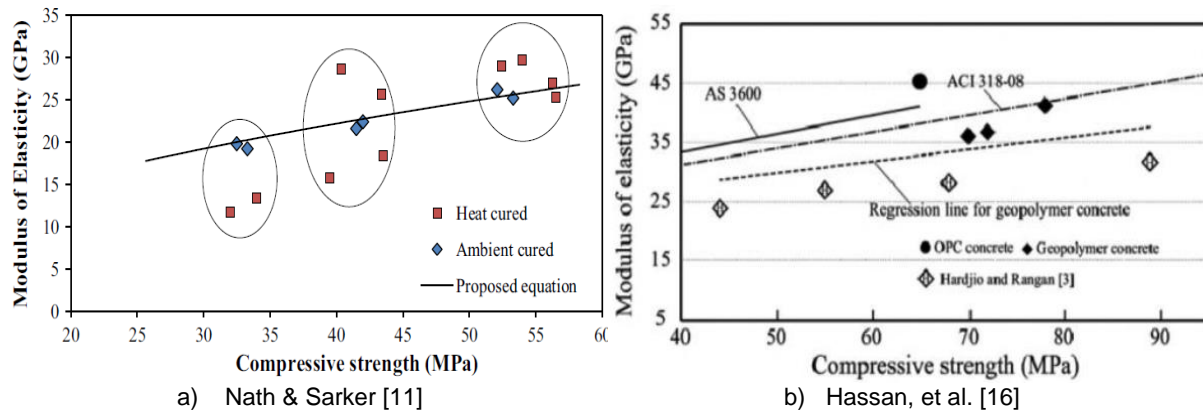


Figure 2.7. Elastic modulus of geopolymer concrete for different compressive strengths

2.2.2.4 Rebar-concrete bond strength

The bond mechanism between the binder phase and the reinforcement influences the load-carrying capacity and cracking behavior (opening and spacing) of structural members by the transfer length. Mo, et al. [21] summarizes up to 10 different studies on the bond strength of geopolymer concrete mixtures with varying constituents, bar diameters, strength class, curing conditions and coating of reinforcement. Furthermore, the test methods of the studies include direct pull-out, beam-end and splice tests. In general, the results show that the bond strength is higher for geopolymer concrete than OPC concrete. Similarly, the estimates from AS 3600, ACI 318-19 [40] and EN 1992-1-1 [22] give conservative predictions of bond strength. The bond strength reported by Yang, et al. [36] is consistently higher than the estimate from EN 1992-1-1 [22] regardless of the compressive strength but the difference is larger as the compressive strength increases; the bond strength is lower than the estimate from CEB/fib for compressive strengths smaller than 25 MPa. The repercussions of a higher bond strength are beneficial for modelling as the assumption of perfect bond between geopolymer concrete and reinforcement is even more realistic than for OPC concrete structures.

2.2.3 Volume stability

2.2.3.1 Shrinkage

Shrinkage in concrete can be decomposed in autogenous, drying, chemical and carbonation shrinkage. Drying shrinkage is the volume change due to moisture loss to the environment due to the difference of the internal relative humidity of concrete and a lower relative humidity of the environment. Autogenous shrinkage is the external volume change of concrete under constant temperature without moisture exchange with the environment and the driving mechanisms are the hydration of the cementitious materials and self-desiccation of the hardened paste. Some authors [18] associate the high shrinkage in GGBFS-based geopolymer concrete with the pore size distribution, which is reduced by incorporating fly ash with heat curing. The behavior is similar to OPC concrete where shrinkage and creep are lower for denser concrete and a higher proportion of GGBFS increases the compressive strength and elastic modulus as discussed beforehand.

On the other hand, Ye, et al. [37] attribute the large magnitude of shrinkage to the mechanical response of the solid binder phase rather than a higher driving force caused by the capillary pores. In general, GGBFS-based geopolymer concrete exhibits a considerably larger drying shrinkage and moisture loss than OPC concrete regardless of the exposure conditions and the higher shrinkage rate occurs at the same time when the samples are exposed to drying

[37]. The shrinkage mechanism in GGBFS-based geopolymer concrete is characterized by a pronounced viscous behavior as the shrinkage dramatically increases despite the moisture loss remaining constant and is caused by the rearrangement and reorganization of the C-A-S-H gel which occurs at high RH, hence the shrinkage kinetics are strongly dependent on the RH. Most of the shrinkage associated with the reorganization of the microstructure is irreversible. The drying shrinkage behavior is dependent upon the drying rate and history as the total shrinkage, also indicating a pronounced viscoelastic behavior at high RH. The relation between RH and shrinkage for OPC concrete is linear but the behavior of GGBFS-based geopolymer concrete, alkali-activated by NaOH or NaOH and water glass solutions, is parabolic with the largest shrinkage not corresponding to the lowest RH (Figure 2.8) [17]. The magnitude of the shrinkage is larger when exposed directly to higher RH, contrary to the behavior of OPC concrete which undergoes highest shrinkage at lower RH [37, 42].

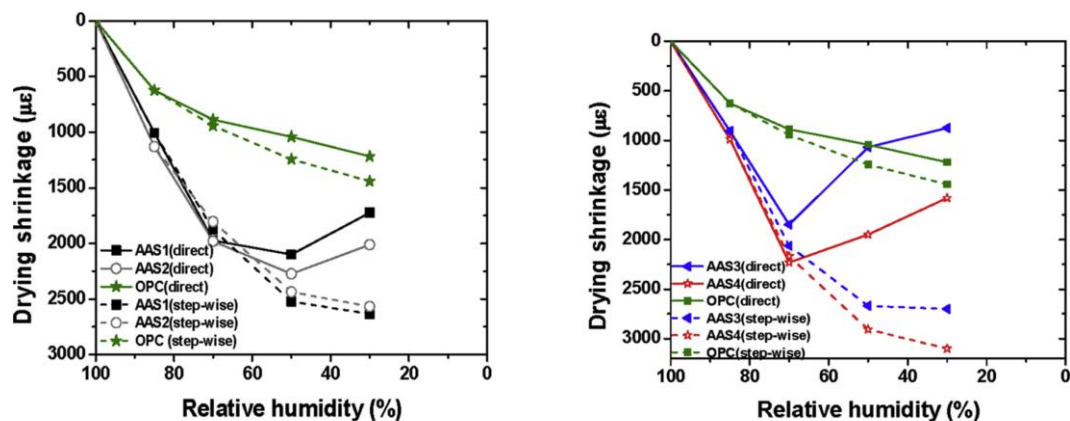


Figure 2.8. Drying shrinkage vs RH for different mortar mixes [17]

The drying shrinkage and mass loss of GGBFS-based geopolymer concrete is larger than OPC concrete independent of the RH, whether the samples are exposed directly or step-wise to drying [17]. Specifically, the drying shrinkage in GGBFS-based geopolymer concrete cured at 23°C and 50% RH is about three times higher than OPC concrete samples [18] and also compared to OPC concrete at 60 days [43]. Furthermore, the drying shrinkage of GGBFS-based geopolymer concrete samples cured at 40°C and measured after 24h are also 3 times higher than the prediction model of EN 1992-1-1 [22] for OPC concrete, whereas similar values are obtained for samples cured at the same temperature for 3 days or at elevated temperature (80°C) for 1 day (extending the elevated temperature curing time has little effect in reducing the shrinkage) [28]. For high MgO BFS-based geopolymer concrete, the highest drying shrinkage occurs for alkali-activation with sodium silicate and the lowest for sodium carbonate [29]. The drying shrinkage is higher for GGBFS-based mortars activated only with a sodium hydroxide solution as compared to a combination of sodium hydroxide and sodium silicate [17]. Furthermore, GGBFS-based geopolymer mortars alkali-activated by sodium hydroxide and sodium silicate is 3 and 6 times higher than OPC mortars, respectively; whereas for sodium carbonate the shrinkage is lower or similar to OPC mortars [44].

The autogenous shrinkage of geopolymer concrete, disregarding the choice of precursor, is higher than for OPC concrete but is higher for GGBFS than for fly ash-based binders [30]. Moreover, according to Ma & Dehn [32] the prediction model from fib Model Code 2010 [27] is not applicable to estimate the autogenous shrinkage of GGBFS-based geopolymer concrete since it lasts for a longer time and has a higher ultimate value than OPC concrete. The autogenous shrinkage of ambient-cured geopolymer concrete is 40% lower for fly ash (1700 µm/m at 1 day and 3700 µm/m at 7 days) precursor as compared to GGBFS (3560 µm/m at 1 day and 6600 µm/m at 7 days). Nevertheless, the autogenous shrinkage in fly ash-based geopolymer concrete is still 6 times larger than for OPC concrete [31].

2.2.3.2 Creep

The creep coefficient of GGBFS-based geopolymer concrete determined experimentally is higher than the prediction model from fib Model Code 2010 [27, 32]. Creep coefficients for high MgO BFS-based are nearly identical regardless of heat curing and choice of alkali-activator [29]. Heat-cured fly ash-based geopolymer concrete undergoes low creep and the prediction model from EN 1992-1-1 [22] gives a similar estimate to the creep coefficient for specimens cured for 3 days at 40°C [28]. Similar to the shrinkage behavior, previously explained in detail, creep is also related to the rearrangement and reorganization of the C-A-S-H structure which results in a highly viscous response and the deformation associated with the reorganization of the microstructure is irreversible. The relevance of this observation lies in the fact that isotropic elasticity-based prediction models for OPC concrete are not valid to predict the visco-elastic/viscoplastic material response both for creep and shrinkage of geopolymer concrete [17].

2.3 Structural tests of geopolymer concrete members

As mentioned in 1.2, most of the studies are around the material properties of geopolymer concrete and only limited number focus on structural elements, design, and application. Table 2.4 provides a summary of studies of reinforced and prestressed geopolymer concrete girders.

2.3.1 Reinforced geopolymer concrete members

2.3.1.1 Flexure

The behavior of under-reinforced concrete girders, from fly ash-based geopolymer concrete and steam cured after 3 days, is qualitatively similar to OPC concrete girders in terms of cracking load, crack-width, flexural stiffness, load-deflection response, ultimate load and failure mode when subjected to flexural loading [45]. Du, et al. [46] analyze the moment-curvature, ductility, cracking evolution and failure mode of ambient-cured fly ash-based geopolymer concrete girder and their OPC concrete counterparts. The moment curvature diagrams, failure mode (conventional flexural failure with crushing of the cover in the compression zone) and ductility are similar for ambient-cured geopolymer and OPC concrete specimens, but geopolymer concrete girders display larger crack widths with less number of cracks. On the other hand, Prinsse, et al. [34] report that the crack spacing and crack pattern is similar for moist-cured geopolymer and OPC concrete girders. Sonal, et al. [20] report that the midspan deflection and failure mode are similar for both ambient-cured non-prestressed geopolymer and OPC concrete girders, but geopolymer concrete members show a lower load-carrying capacity. The ultimate moments of ambient-cured fly ash-based geopolymer concrete girders is only 1, 4 and 8% higher than the OPC concrete counterparts for compressive strengths of 30, 50 and 70 MPa, respectively. However, the elastic modulus of geopolymer concrete is 18-19% lower than OPC concrete but the initial flexural stiffness only decreased between 2 and 9% for the different strength classes, hence the discrepancy in the flexural stiffness is less significant even though the elastic modulus is much lower [46]. Prinsse, et al. [34] also mention that the effect of the decrease of material properties on structural behavior of reinforced geopolymer concrete girders is marginal. Yost, et al. [47] report that the elastic behavior, strength and failure mode of under-reinforced fly ash-based geopolymer concrete girders ($f_c = 54.8$ MPa) is identical to the OPC concrete counterparts ($f_c = 48.3$ MPa). On the other hand, the behavior of over-reinforced girders is completely linear until sudden failure in comparison to the OPC counterpart which showed a slight nonlinear response closer to the maximum load and the crushing strain is higher for fly-ash geopolymer than for the OPC counterpart [47].

Reference	Precursor	Activator	Varying parameters	Description
Du, et al. [46]	Fly ash	NaOH and Na ₂ CO ₃	Concrete strength: 30, 50 and 70 MPa Reinforcement ratio: 0.66, 1.61, 1.63, 2.71% Shear span to depth ratio: 2.67 and 3.43 Ambient curing.	Investigate the flexural response of 12 geopolymer and 3 OPC concrete girders to 4-point load tests. Shear reinforcement provided to prevent shear failure.
Prinsse, et al. [34]	GGBFS and fly ash	NaOH and Na ₂ SiO ₃	GGBFS to Fly ash proportion: 100:0 and 50:50 Unmolded after 1 day and cured at 20°C and 95% RH for 28 days, later some specimens kept in moisture and others 20°C and 55% RH.	Development of material properties over time (up to around 2 years) and the response to 4-point load tests of reinforced beams with 0.61% reinforcement ratio.
Sonal, et al. [20]	50% GGBFS 50% Fly ash	NaOH and Na ₂ SiO ₃	Prestressed and non-prestressed girders in OPC and geopolymer concrete. Ambient cured for 28 days before testing.	Investigate the flexural response of 8 prestressed and non-prestressed (geopolymer and OPC concrete) girders without reinforcement to 4-point load tests.
Sumajow, et al. [45]	Fly ash	NaOH and Na ₂ SiO ₃	Compressive strength: 34, 42 and 46 MPa Reinforcement ratio: 0.64, 1.18, 1.84, 2.69% Ambient cured 3 days, then steam cured (60°C for 1 day), demolded and ambient cured.	Investigate the flexural response of 6 under-reinforced geopolymer concrete girders to 4-point load tests.
Visintin, et al. [48]	Fly ash	NaOH and Na ₂ SiO ₃	Compressive strength: 21, 24 and 33 MPa Reinforcement ratio: 0.89, 1.07 and 1.34% Shear span-to-depth ratio: 2.0, 2.5, 3.0 and 3.5 Sealed for 3 days, then ambient cured.	Determine the contribution to the shear capacity of 8 geopolymer concrete in girders without stirrups.
Wu, et al. [49]	GGBFS	NaOH and Na ₂ SiO ₃	Concrete strength: 40, 60, or 80 MPa Reinforcement ratio: 1.82, 2.54, or 2.72% Longitudinal bar strength: 400 or 600 MPa Shear span-to-depth ratio: 1.5, 2.5, or 4 Beam depth: 300 or 400 mm	Investigate the response of 18 GGBFS-based geopolymer concrete and 3 OPC concrete girders with shear and longitudinal reinforcement to 4-point load tests.
Yost, et al. [47]	Fly ash	NaOH and Na ₂ SiO ₃	Binder: OPC and fly ash Under-reinforced, over-reinforced and shear critical design Reinforcement ratio and shear span	Establish how accurately existing design and analysis procedures for OPC apply to the estimating the response of fly ash-based geopolymer concrete girders.

Table 2.4. Summary of studies on structural tests on geopolymer concrete girders

2.3.1.2 Shear

The girders without shear reinforcement fail suddenly in shear by sliding along a critical shear crack. The shear capacity is estimated according to the fib Model Code 2010 Level II approach [27] and a mechanics based approach (segmental approach). The estimates from the fib Model Code 2010 underestimate the shear capacity of geopolymer concrete girders but the segmental approach, in combination with the shear-friction relationships for OPC concrete, predict accurately the ultimate shear capacity of the girders without stirrups [48].

The crack distribution and failure mode of geopolymer concrete girders with shear reinforcement are similar to OPC concrete girders. The girders failed by a diagonal shear crack or by yielding of reinforcement and crushing of the cover in the compression zone (flexural or flexural shear failure). The change of shear failure to flexural failure is due to the contribution of high strength geopolymer concrete to the shear capacity, which is a similar behavior to OPC concrete structures. Furthermore, the shear strength and yield stiffness of geopolymer concrete girder is 94% and 99% of its OPC concrete counterpart, respectively. The loads at which the maximum crack widths (of the flexural cracks at the bottom of the specimens) reached 0.2 and 0.3 mm are lower for geopolymer than OPC concrete girders. Finally, the load of the test results showing shear failure were compared to the predicted shear strength of ACI 318-19 [40], EN 1992-1-1 [22] and fib Model Code 2010 Level III [27]. The shear capacity according to ACI 318-19 is the sum of the concrete and stirrups contributions, whereas for EN 1992-1-1 the contribution of concrete is neglected in structures with shear reinforcement and Level III consists on the highest level prediction which will give the most accurate results. ACI 318-19 and EN 1992-1-1 underestimated the test results (78% and 59%, respectively) and fib Model Code Level III gave the better approximation (97%) [49].

2.3.2 Prestressed geopolymer concrete members

According to Sonal, et al. [20] the deflections and cracking load for prestressed geopolymer concrete girders are higher than OPC prestressed concrete girders. Nevertheless, the load capacity is similar regardless of the concrete type. Prestressed geopolymer concrete members display higher deflections and lower bending stiffness which may be related to a lower elastic modulus. The cracking load in geopolymer are higher than for OPC concrete girders [20].

2.4 Numerical studies of geopolymer concrete members

The state-of-the-art by Mo, et al. [21] observes some successful numerical studies of geopolymer concrete structural members with commercial FE packages ANSYS and Abaqus. Table 2.5 gives an overview of selected studies on numerical modelling of geopolymer concrete specimens subjected to 4-point flexural testing.

Neupane et al. [39] conducted numerical simulations in Abaqus of geopolymer concrete with input material properties from testing. The material samples are sealed cured until testing. The load-deflection responses from the numerical simulation show that, for both spans, the cracking and maximum loads are around 20% and 10% higher in the geopolymer concrete girders, respectively. Nevertheless, similar 28-day elastic modulus between geopolymer and OPC concretes are reported, whereas 2.2.2.3 indicates that the elastic modulus of geopolymer concrete is consistently lower than for OPC concrete for ambient cured samples. Validation with experimental results is required to determine the applicability of the modelling choices in this study since higher maximum loads are reported when the experiments described before suggest similar capacities for geopolymer and OPC girders in flexure.

Table 2.5. Summary of studies on FE modelling of geopolymer concrete girders subjected to 4-point load tests

Reference	Element description	Finite element modelling	Description
Neupane et al. [39]	<p>One part (powder-activated): 50% fly ash 32% GGBFS 18% activator blended in the power Curing: Sealed at 23°C until testing</p> <p>Cross-section: 300x400 mm² or 350x700 mm² Span: 5 or 10 m Reinforcement: 3 or 4 ϕ16 mm in tension, 2ϕ12 mm in compression and ϕ8 mm stirrups @ 225 mm Shear span: 1.75 or 3.8 m</p>	<p>Package: Abaqus Geopolymer: Damage plasticity model (Hognestad curve in compression and Carreira & Chu in tension), C3D8R 3D 8-node brick elements with reduced integration. Reinforcement: Embedded 3D beam elements B31 Bond: Perfect bond for geopolymer-reinforcement and surface-to-surface contact with traction separation law for concrete-tendons</p>	Material properties of geopolymer concrete and OPC control samples properties are obtained from material testing and used as input for four numerical models of reinforced geopolymer and OPC concrete girders.
Nguyen, et al. [50]	<p>Precursor: Fly ash Activator: sodium hydroxide Curing: 60°C for 4h</p> <p>Cross-section: 100x200 mm² Span: 1.5 m Reinforcement: 2ϕ10 mm in tension, 2ϕ8 mm in compression and ϕ8 mm stirrups @ 150 mm Shear span: 0.375 m</p>	<p>Package: Abaqus Geopolymer: C3D8R 3D 8-node brick element with reduced integration and hourglass control. Reinforcement: T3D2 2-node linear 3D truss element.</p>	Experimental and numerical study reinforced geopolymer concrete girders to evaluate the behavior under 4-point load flexural tests. Stress-strain relation, elastic modulus and Poisson ratio determined from testing of cylinder samples.
El-Sayed & Algash [51]	<p>Precursor: Recycled wheat straw ash Activator: sodium meta-silicate and sodium hydroxide Curing: Ambient curing for 28 days</p> <p>Cross-section: 300x150 mm² Span: 1.6 m Reinforcement: 2ϕ12 mm in tension, 2ϕ10 mm in compression & 12ϕ8 mm as stirrups Shear span: 0.65 m</p>	<p>Package: ANSYS 2019-R1 Geopolymer concrete: Solid 65 Reinforcement: Link 180</p>	NLFEA to verify the high strength and ultra-high strength geopolymer concrete beams reinforced with GFRP-bars with the experimental results. Compressive strength, elastic modulus and tensile strength obtained from material testing.

Nguyen, et al. [50] conducted a numerical study in Abaqus of the flexural response of ambient-cured reinforced geopolymer concrete girders and compared to experimental results. The modelling choices are similar to Neupane et al. [39] but reinforcement is modelled only as truss-elements with axial stiffness and no contribution to the strength by bending as the beam elements. The authors report that the load – deflection curve and cracking pattern from the experiment and numerical simulation are in good agreement whereas the deflections are slightly different due to the support conditions. El-Sayed & Algash [51] carried out NLFEAs in ANSYS 2019-R1 of high strength and ultra-high strength geopolymer concrete beams reinforced with GFRP-bars and compared to experimental results of ambient cured specimens. The ultimate loads with the numerical simulation are within 89 to 93% of the experimental values. Additionally, the cracking pattern and load – deflection curves showed good agreement with the experiment. In both studies, the models are constructed with the material properties obtained from testing.

The set of modelling assumptions of each study are intrinsic to the choice of software package. For example, in Abaqus the concrete damaged plasticity model describes the nonlinear response of concrete with tensile cracking and compressive crushing as the two main failure mechanisms [52] whereas in ANSYS the SOLID65 elements allows the addition of cracking and crushing capabilities [53]. Furthermore, different constitutive relations for interfaces, bond behavior, reinforcement steel, concrete in tension and compression are available for numerical modelling. Consequently, the modelling choices of the selected studies do not imply that alternative formulations for modelling are not valid but intend to demonstrate that modelling of geopolymer concrete structures is satisfactory with commercial FE packages with material models for OPC concrete. In the Netherlands, Rijkswaterstaat's Guidelines for NLFEA of Concrete Structures [23] and software package DIANA are the suggested practice for concrete structures and their applicability for geopolymer concrete is studied in the present document.

2.5 Geopolymer concrete in the contemporary context

2.5.1 Existing standards for geopolymer concrete

The existing concrete and cement standards define terminology and specifications, prescribe methods of testing, and recommend practices for OPC or blended cements. The standards are a response to the necessities of the market to regulate generic products of widespread use in the industry to satisfy the needs and expectations of both customers and manufacturers. The customers expect high quality materials meeting a minimum set of requirements and manufacturers produce, compete and innovate the technology within this minimum set of performance specifications. Concrete and cement standards undergo reviewing and amendment every few years but the modifications are based on the properties of the material manufactured and used according to the standard. To create a new standard or modifying existing ones, that have been developed based on the performance of another material, for a new material is a long process [4].

Geopolymer concrete does not comply with most of the prescriptive cement standards due to the difference in the composition, chemistry and hydration products. The large variety of possibilities for producing geopolymer concrete (2.1) is an impediment to formulate a new class of materials in the same prescriptive approach as adopted for OPC. The conceptual and innovation phases of geopolymer concrete are in development since the early 20th century and are now firmly supported with extensive research at laboratory scale for mix design based on fresh and hardened properties and durability. Therefore, current research and future standards for geopolymer concrete should be derived as much as possible from existing standards when possible.

The generalized use of geopolymer concrete does not necessarily require the development of a completely new body of knowledge but it can be supported by the current practices for OPC concrete. In fact, the following European standards for OPC concrete are already used for manufacturing and testing of geopolymer concrete:

- Specifications of raw materials (precursors)
- EN 12350 series: Fresh properties
- EN 12390 series: Hardened properties
- EN 934 and EN 480: Use of admixtures (even though the effectiveness of admixtures for OPC concrete in geopolymer concrete needs to be studied)

On the other hand, the mixing procedure is different to a certain extent for geopolymer concrete due to the different components but the equipment and technology is comparable to OPC concrete mixing. Furthermore, additional safety requirements are associated to the use of geopolymer concrete due to the high alkalinity.

Nowadays, examples of pilot and industrial applications at structural scale can be found throughout the world, and the market penetration phase with commercial-scale production in several countries is imminent. Therefore, some countries and organizations are already moving towards standardization in existing concrete standards or in exclusive standards and are summarized in Table 2.6. The standards below mostly address the replacement of OPC concrete by SCMs, only the cases of Australia (job-to-job basis) and Ukraine (and former USSR) encompass the application of geopolymer concrete at structural level.

Table 2.6. Standards including alkali-activated materials throughout the world

Country	Standard	Description
Australia	VicRoads Section 610, 703, 701, 705, 711.	State authority specifications for the use of alkali-activated materials for corrosion and chemical resistant applications, paving and on a job-by-job basis for structural concrete [10].
Canada	CSA A3004-E	SCMs others than GGBFS, fly ash and silica fume suitable for use in concretes [4].
China	GB/T 29423-2012	Use of alkali-activated materials for corrosion and chemical resistant applications [10].
Ukraine and former USSR	Over 60 standards (1961-2007)	Constituent raw materials, cement compositions, concrete mix design, manufacturing, structures and design, recommendations on use in special field [4].
United Kingdom	BSI PAS 8820:2016	Performance-based specification for AAMs with aluminosilicate main constituents and an alkali-activator [3].
Switzerland	SIA Merkblatt 2049:2014	Encompasses the use of alkali-activated slag.
International	ASTM C1157	Cements for general and special applications, classified in 6 categories (performance requirements). Geopolymer concrete complies if the performance requirement is met. Acceptance in only in 5 states as of 2014 [4].
International	ASTM WK68966	Work Item document. Flexible framework to implement geopolymer concrete in a job-to-job basis [54].

2.5.2 Applications in structural geopolymer concrete

The former Soviet Union and China have a longstanding history in the research, standardization and application of geopolymer concrete both precast and cast in-situ. Furthermore, cement types such as F-cement in Finland, Purdocement in Belgium, Pyrament in North America indicate early commercial ventures of alkali-activation in the construction industry [10]. According to Roy [1], geopolymer concrete applications include cast in-situ and precast heavy-duty pavements, acid-resistant floor slabs, foundations, storage buildings, residential buildings and irrigation systems. Table 2.7 summarizes a set of pilot and commercial-scale projects of geopolymer concrete in structural applications. The projects presented are relevant for their size, use, age and construction process. In particular, the detailed description of the projects in the next paragraphs, demonstrate that standard practices, equipment and labor for mixing, casting and curing of OPC concrete structures are applicable to a certain extent to geopolymer concrete.

According to Provis, et al. [4] the projects in China and Russia (Figure 2.9) have not presented durability issues during their service lifetime; more interesting is the testing of cylinder samples from the storehouse in Poland after 25 years which indicate a significant increase in the compressive strength compared to 28 days and an average rate of carbonation of less than 0.5 mm/year in all samples.



Figure 2.9. Geopolymer concrete projects in Russia and China [4]

Aldred & Day [8] and Glasby, et al. [9], report the use of trademarked alkali-activated GGBFS-fly ash-based, Earth Friendly Concrete (EFC) from Wagners in a variety of projects in Australia ranging from pavements, slabs, walls, water tanks, bridge decks and tunnel segments both precast and cast in-situ (Figure 2.10). The Brisbane West Wellcamp Airport (BWWA) is the largest modern project in geopolymer concrete which was used to build the pavement of the turning node and apron areas, an entry bridge, culverts, footings, sewer tanks and barriers. The most remarkable aspect of this project is the installation at the project location of a twin mobile wet mix batch plant with modifications for allocating the activators. One water tank was cast with EFC and another with a blended cement (80% Portland cement and 20% fly ash) to explore the self-healing behavior and water tightness of geopolymer concrete. It is reported that through cracks in the EFC tank healed rapidly by gel swelling mechanism.



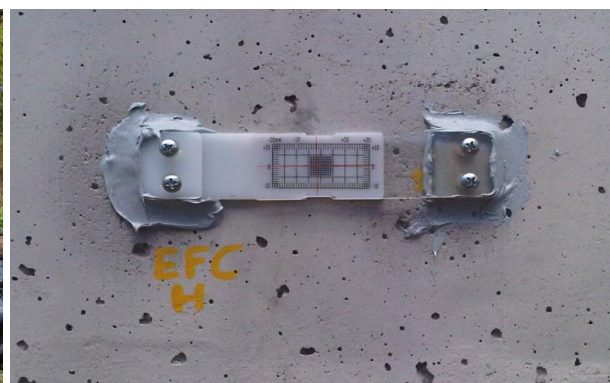
a) Global Change Institute: precast floor elements



b) BWWA: airport pavement



c) BWWA: twin mix batch plant



d) Water tank and gauge measurement after healing

Figure 2.10. Geopolymer concrete projects in Australia [8]

Table 2.7. Examples of application of structural geopolymer concrete

Description	Area/Storeys	Location	Year	Design requirements	Precursor	Activator	Precast	Cast in-situ
Storehouse [4]	-	Krakov, Poland	1947	-	BFS	Na ₂ CO ₃	Heating tunnel (70°C, 6h) floor slabs and wall panels	-
Office and retail building [4]	6 storeys 8.6x31.5 m ²	Yinshan County, China	1988	$f_c = 20$ MPa $f_{cm} = 24.1$ MPa w: b = 0.44 30-50 mm slump	Portland cement-BFS-steel slag	Na ₂ SO ₄	-	Mixed in-situ
Precast girders and columns [4]	Columns: 400x400 mm ² Girders: 350x450 mm ²	Yinshan County, China	1988	$f_c = 30$ MPa $f_{cm} = 35.9$ MPa w: b = 0.50	Portland cement-BFS-steel slag	Na ₂ SO ₄	Precast in building site	-
3 high-rise residential buildings [4]	20+ storeys	Lipetsk, Russia	1994	$f_c = 25$ MPa w: b = 0.35	BFS	Alkali-activated	Steam cured floor slabs and stairways	Temperature cured exterior walls
Bridge [8]	Bridge deck	Murrarie, Australia	2009	$f_c = 40$ MPa	Earth Friendly Concrete EFC® Alkali-activation of GGBFS and fly ash		Deck delivered to site	-
Boat ramp [8]	Ramp and approach slab	Bundaberg, Australia	2011	$f_c = 40$ MPa			Precast planks	One-part mix activated in-situ
Global Change Institute [8]	33 floor slabs 10.8x2.4 m ²	Brisbane, Australia	2013	$f_c = 40$ MPa			Precast floor slabs	-
Brisbane West Wellcamp Airport [9]	40000 m ³	Brisbane, Australia	2014	$f_{ct} = 4.8$ MPa $\epsilon_{cd} = 450$ μm/m			Details in main text	

2.6 Advantages and limitations to the application of geopolymer concrete

This section presents potential advantages and limitations of the generalized use of geopolymer concrete in the construction sector, aside the observations on the material properties discussed in 2.2.

2.6.1 Advantages

2.6.1.1 Environmental considerations

The classic design approach of structural concrete is based mainly on the functional performance regarding fresh and hardened properties, durability and costs. The future expectations of a sustainable society relies on environmentally friendly materials engineered from the technological use of substantial amounts of waste and by-products to minimize energy consumption, waste generation and toxic emissions [1]. Geopolymer concrete has been promoted as an alternative to OPC concrete with reduced embodied energy and CO₂ emissions [55]. In particular, the estimated CO₂ savings from LCA studies comparing geopolymer and OPC concretes range from 30% to 80% [4].

2.6.1.2 Adaptability and potential for upscale production

The possible combinations of the large variety of precursors and activators makes geopolymer concrete resourceful for satisfying the functional requirements for a specific application and locally adaptable depending on the availability of the components. Developing countries with an increasing demand for urban development like India and China, which are also dependent on coal-fired power plants, expose ideal conditions for high value use of fly ash for satisfying the demand of construction materials in a sustainable manner as fly ash does not require grinding. According to Provis [10], clays, lateritic and volcanic soils, from which precursors can be obtained, are stored in significantly larger quantities than the global demand for construction materials in the foreseeable future. Clays are available worldwide, lateritic soils are found mainly in tropical regions and volcanic resources are abundant in the Andes, Middle East and southern Europe. Regarding the activators, the source of alkali metals is sodium chloride, obtained from seawater and converted to sodium carbonate (Na₂CO₃) by the Solvay process or to sodium hydroxide (NaOH) by the chlor-alkali process. Sodium carbonate production is scalable in regions with natural mineral resources like United States, Turkey, Mexico, Botswana, etc. [4].

The production of geopolymer concrete does not require the development of new processes. The mixing and casting procedures employ the same technology that has been perfected for decades in the concrete industry. Slight modifications for dosing and storing of activators need to be implemented for upscale production in industrial plants. Nevertheless, geopolymer concrete is considered more suitable for precast applications under stricter levels of quality control for safety, curing and mix proportioning [10]. Furthermore, the most widely used precursors (GGBFS and fly ash) and activators are produced with existing technologies and well defined processes. Successful commercial operations, particularly in Australia [8], demonstrate that geopolymer concrete with locally-sourced precursors and activators in low dosages are a cost effective alternative to OPC concrete.

2.6.1.3 Energy requirements

The energy requirements are drastically reduced since the rotary kilns for Portland cement production are not required and the thermal processes associated with activator production arise at moderate temperatures which can be reached with alternative sources to fossil energy [10]

2.6.1.4 Durability

The microstructure of the geopolymer matrix appears to be durable as the reaction products seem stable over time [1]. As consequent, several authors report enhanced durability of some geopolymer concrete mixtures compared to OPC concrete. For example, geopolymer concrete can present relatively low carbonation depths, no micro cracks after prolonged service [1] and resistance to sulfate attack, acid and chloride ingress [9]. Additionally, the susceptibility to alkali-silica reaction is not large and the high alkalinity seems to be favorable for the protection of embedded steel reinforcement [10]. Finally, Provis, et al. [4] reports dense binder structures, well-protected steel reinforcement and higher strength than design criteria in a limited number of studies of in-service geopolymer concretes in structures or structural components after decades.

2.6.2 Limitations

2.6.2.1 Availability of constituents

The availability of precursors and alkali-activators is determined by the local context and depends upon technical considerations, as having a developed industry with the available technology and capacity for manufacturing of constituent materials in the sufficient amounts, and economic drivers as the demand for the same materials for different applications. The production of chemical activators in remote and poor regions is not possible due to technical limitations [10]. In much of the developed world, the stock of GGBFS and other precursors is required to fulfill the demand for the production of blended cements [10] due to the enhanced properties when combined with Portland cement. On the other hand, in other countries GGBFS is a waste material requiring valorization [4]. Furthermore, energy production from coal is a widespread practice in some countries but some others are dependent on other sources, hence an uneven distribution of the stock of fly ash across the world.

2.6.2.2 LCA methodology

A consistent Life Cycle Assessment (LCA) methodology is required to provide scientific arguments to support the endorsement of geopolymer concrete as a standard practice in the construction sector. Furthermore, the effects across other environmental impact categories shall be accounted for as alkali-activation discharges non-Greenhouse gas emissions like SO_x, NO_x, phosphate and others [4]. For example, Habert, et al. [56] report unfavorable outcomes in terms of environmental toxicity with the production of the alkali-activator (sodium silicate) with a rather inefficient process. The functional unit for the LCA analysis also requires a proper performance-based definition which can be comparable to a reference Portland cement-based concrete of similar properties and cost for the particular location and application. The local availability is a determinant factor in the LCA calculation due to the transportation requirements of bulk constituents which can govern the emissions if the transportation distances are too long [10]. Additionally, the source and dosage of the activator, and the energy involved in the production of components shall be specified for the specific application and location.

2.6.2.3 Safety

Safety training and suitable personal equipment is required for handling geopolymer concrete as the alkaline-activators are corrosive and irritant [10].

2.6.2.4 Use of admixtures

The current mix designs of geopolymer concrete do not encompass the use of admixtures designed for OPC concretes because they are ineffective. For example, naphthalene or PCE-based superplasticizers, often used with OPC, have little effect on geopolymer concrete [32]. Further research is required for finding admixtures specifically for enhancing the properties of geopolymer concrete.

2.6.2.5 Durability

Testing durability of geopolymer concrete consists of exposing samples to extreme conditions for short periods of time under controlled laboratory conditions [4]. The results shall be taken as a measurement of the expected performance but not as definitive proof as the test methods have proved satisfactory for concrete structures but not necessarily will resemble the behavior of geopolymer concrete during its service lifetime. Even though, structures in geopolymer concrete, exposed to environmental conditions and inspected after decades indicate no issues with durability. Nevertheless, the same holds for modern cements as durability has not yet been assessed in real world applications after long periods of time.

2.6.2.6 Standardization and policy

The applicability of geopolymer concrete as a standard construction practice is limited by the lack of a legal and technical framework for manufacturing, specification, design, analysis and construction [9]. Each jurisdiction requires standards for the application in a project-level basis but international performance-based standards will set the basis for construction in geopolymer concrete to be a widespread business practice in the globalized world [1]. In particular, a universal mix design methodology is required due to the variability in chemistry, mineralogy and availability of the constituents. Furthermore, a systematic methodology and predictive databases need to be made available for optimal pairing of precursors and activators for compliance with performance specifications from design [10].

2.7 Conclusions

The stress-strain relation in compression and the 28-day compressive strength of geopolymer concrete are similar to those of OPC concrete; the design compressive strength can be achieved with geopolymer concrete of similar density and same aggregates as in OPC concrete. Nevertheless, the development of strength in geopolymer concrete depends upon the microstructure of the binder phase (choice of precursors and activators) and the curing conditions. In particular, the early age strength for ambient cured samples is higher for high-calcium content systems (GGBFS-based) as the C-S-H gel is more abundant than in low-calcium systems (fly ash-based). On the other hand, higher initial strength is achieved with heat curing in low-calcium systems but afterwards it decreases over time. Air-exposed samples can show a decrease of the compressive strength due to microcracking caused by moisture loss. The 28-day strength, generalized design criteria for OPC concrete structures, may not be an accurate indicator of the performance over the service lifetime of a geopolymer concrete structure as studies report both a decrease or increase in the compressive strength of geopolymer concrete after 28-days.

The elastic modulus, creep and shrinkage of geopolymer concrete also evidence an intrinsic relationship with the constituent materials and curing conditions. The empirical relations to determine the material properties of OPC concrete from the 28-day compressive strength, as defined in conventional concrete codes, could not be generally applicable for geopolymer concrete as they result in non-conservative estimates. The variability is apparent within different mixtures of geopolymer concretes but also with respect to OPC concrete. The elastic modulus increases with the compressive strength as in OPC concrete but is lower than OPC concrete of similar strength class and is overestimated by standards and empirical equations from OPC concrete codes. Similar to the compressive strength, the elastic modulus is higher for increasing calcium-content in the binder phase and for low-calcium systems it can be increased with 1-day heat curing. Furthermore, the elastic modulus is increased with the use of both sodium silicate and sodium hydroxide as when alkali-activation occurs only with the latter. The bond strength is higher for geopolymer concrete than OPC concrete and estimates from EN 1992-1-1 [22] give conservative predictions of bond strength. The assumption of perfect bond between geopolymer concrete and reinforcement for modelling can be more realistic than for OPC concrete structures. The behavior of the binder phase is characterized by a viscous response associated with the rearrangement of the C-A-S-H gel at high RH which causes irreversible deformation. The driving mechanism of shrinkage may be a mechanical response caused by the changing microstructure as the shrinkage increases despite the moisture loss remaining constant. Furthermore, the relation between RH and shrinkage is parabolic as opposed to the linear relation in OPC concrete. The autogenous shrinkage of geopolymer concrete, disregarding the choice of precursor, is higher than for OPC concrete but is higher for GGBFS than for fly ash-based binders. The creep coefficient of GGBFS-based geopolymer concrete determined experimentally is higher than the prediction model. Based on the literature study, the isotropic elasticity-based prediction models for OPC concrete are not valid to predict the visco-elastic/viscoplastic material response both for creep and shrinkage.

The structural performance of geopolymer concrete is assessed by analyzing reported shear and flexural tests in reinforced geopolymer concrete girders. The varying parameters in the selected studies are: compressive strength, proportion of GGBFS to fly ash, reinforcement ratio, shear span-to-depth ratio and curing regime. Furthermore, some studies also compare the structural behavior to OPC concrete counterparts. The flexural behavior of fly-ash based reinforced geopolymer concrete girders, steam or ambient cured, is similar to the OPC concrete counterparts in terms of elastic behavior, cracking load, load – deflection response, ultimate load and failure mode. Conversely, some studies suggest similar crack pattern but others report larger crack widths with less number of cracks. The flexural capacity of prestressed geopolymer concrete members is similar to OPC concrete but display higher deflections and lower flexural stiffness. The shear behavior of geopolymer concrete girders with shear reinforcement indicates that the crack pattern and failure mode are similar to OPC concrete girders. ACI 318–19 and EN 1992-1-1 underestimate the shear capacity but fib Model Code Level III gives the better approximation. Numerical simulations of mechanical tests in Abaqus and ANSYS of reinforced geopolymer concrete girders, with material properties derived from testing, indicate a good resemblance in terms of load-deflection response. The similarity in the flexural behavior with OPC concrete counterparts when testing after 28 days, as well as the acceptable results of numerical simulations with experimental results, indicate that the mechanical models and finite element modelling choices for OPC concrete can be used to accurately estimate the short-term flexural capacity of reinforced geopolymer concrete girders. In the case of numerical modelling, the set of assumptions is related to the choice of software but the background theory is generalized, hence the use of other software packages with different modelling choices is possible.

Case study and experimental results

In recent times, several geopolymer concrete mixtures display satisfactory workability, mechanical properties and durability while improving sustainability considerations in comparison to conventional concrete. Nevertheless, for large-scale application of geopolymer concrete it has to be demonstrated that it satisfies criteria regarding performance, durability and safety during its intended service life in structural scale. Extensive testing on both material and structural level is required due to the inherent challenges for implementing a new material in the construction sector since the design criteria for structural application are not defined in standards and there are several knowledge gaps regarding the structural behavior.

The objective of the Fryslan project is to replace the bridge of the Kowebrege Jouswier with a more sustainable alternative, a bridge built with geopolymer concrete. In particular, the target is to safely upscale a two geopolymer concrete mixtures to structural level by guaranteeing appropriate material performance, feasibility for large scale industrial production and satisfactory structural capacity in prestressed structures. This chapter describes the application of geopolymer concrete in structural scale with the construction and testing of the structural performance of a bridge prototype concept. The prestressed girder is precast in a factory with a SCGC mixture developed by TU Delft. The reinforced topping is cast in-situ by a ready-mix geopolymer concrete provider. The details with respect to the geometry, construction phases and mechanical tests are defined. The development of the mechanical properties and volume stability over time of the two mixtures employed in the construction of the prototype specimens are analyzed. Finally, the experimental results of 4-point bending and 3-point load mechanical tests for assessing the flexural and shear capacity of the specimens are included. The shear behavior of the elements is studied at an age of 28 days, whereas the flexural behavior is assessed at this age and after 9 months to analyze the effect of the long-term material properties of the geopolymer concrete mixtures in the prestressing losses, cracking load and maximum load carrying capacity.

3.1 General

In total eight HKO-300 prestressed girders are prefabricated by Haitsma Beton with a geopolymer mix design developed at Delft University of Technology. The precast girders are delivered to Magnel Laboratory in Ghent University where the construction is completed with the casting of the in-situ topping by a ready-mix concrete provider and the mechanical tests are executed. Five specimens consisting of an individual precast girder with cast in-situ topping and a mock-up bridge deck of three precast girders with cast in-situ topping are constructed. The individual specimens are tested for (1) short-term flexural capacity by 4-point bending test, (2) short-term shear capacity by 3-point load test and (1) sustained loading for 9 months followed by flexural test and (1) loaded by self-weight for 9-months followed by flexural test. The mock-up bridge is tested for cyclic loading followed by loading in the flexure and shear critical positions. Furthermore, material samples are obtained during each casting operation for the execution of material tests to assess the fresh properties, mechanical properties, volume stability and durability. The content to follow focuses in the individual specimens tested for short-term flexural and shear capacity, and loaded by self-weight for 9 months followed by flexural test, but general aspects of the project are described as well.

The mix design, material properties, test setup, measurement devices, loading protocols and experimental results are as described in:

- Testing Report on Phase I : Development of a self-compacting geopolymer concrete (C45/55) [57]
- Testing Report on Phase I – Part 2: Durability and volume stability of the self-compacting geopolymer concrete (C45/55) [58]
- Testing Report on Phase II – Industrial production of pre-cast bridge girders using the self-compacting geopolymer concrete (C45/55) [59]
- Additional Testing Report on Phase III – Full-scale tests on girders and deck – Part I [60]
- Test Report Jul '22: Loading tests on prestressed precast bridge deck members in AAM concrete, by UGhent [61]
- Monitoring of Prestressed Geopolymer Concrete Girders using Smart Aggregates and Fibre Optic Sensors [62]

3.2 Construction details

3.2.1 Mix requirements

The SCGC mixture used for the precast girders satisfies the following requirements:

- Use of local aggregate and alkali-activator.
- Strength class at least C45/55 with 1-day strength higher than 30 MPa.
- Fresh properties: Slump flow class (SF2), viscosity class (VS1), segregation resistance class (SR1<23%) and slump retention (45 min > 580-640 mm SF1).

The geopolymer concrete mixture used for the in-situ casting of the topping is delivered by a ready-mix truck and satisfies the strength class requirements C30/37.

3.2.2 Construction sequence

The precast girders are cast in three dates in Haitsma Beton (Figure 3.1 b)). The girders are demolded and prestressed at an age of 2.5 days (Figure 3.1 c)) and consequently covered with wet burlaps and sealed with plastic to prevent moisture loss. The precast girders are delivered after 14 days to Ghent University and the curing conditions were maintained. The

casting operations of the topping were executed 30 days after the casting date of the girders (Figure 3.2). An overview of the casting operations is shown in Table 3.1. The burlaps and plastic sheets are removed between 7 and 14 days before the casting of the topping to install the sensors, build the reinforcement cage and set-up the formwork. Hence, the precast girders are exposed to drying at an age of 21 days. The specimens from casting operation 2 are covered with wet burlaps and plastic after the casting operations of the topping until the age of testing, the specimens from casting operation 1 are only covered with plastic (sealed). The author assisted the casting operations and assembly of the reinforcement cage of some specimens.

Table 3.1. Overview of casting operations

Casting operation	Haitsma Beton		Ghent University	
	# of girders	Casting date	Casting date	Description
1	2	27/08/2021	27/09/2021	2 specimens for sustained loading
2	3	10/09/2021	11/10/2021	Mock-up bridge deck
3	3	17/09/2021	18/10/2021	3 specimens for flexural and shear tests



a) Preparation of activator



b) Casting of girders



c) Prestressing and demolding

Figure 3.1. Casting operation of precast girders in Haitsma Beton



Figure 3.2. Casting operation of the topping over a girder specimen in Ghent University

3.2.3 Geometry

The construction sequence presented above is executed according to the drawings of the cross-sections of the HKO-300 girders of Haitsma Beton and the cast in-situ topping, presented below and in Appendix A. Likewise, the prestressing, longitudinal and shear reinforcement layout presented is as executed during the construction stages.

The precast prestressed girders have a total length of 7350 mm, nominal length of 7000 mm, width of 990 mm and height of 300 mm. The prestressing tendon layout consists of a total of 16 FeP1860 tendons with a nominal diameter of 12.9 mm and a cross-sectional area of 100 mm². The tendons are distributed in a bottom layer of 12 tendons and a top layer of 4 tendons. Four prestressing tendons in the bottom layer are detached over 1000 mm on each end. The cross-section dimensions and layout of the prestressing tendons is shown in Figure 3.3.

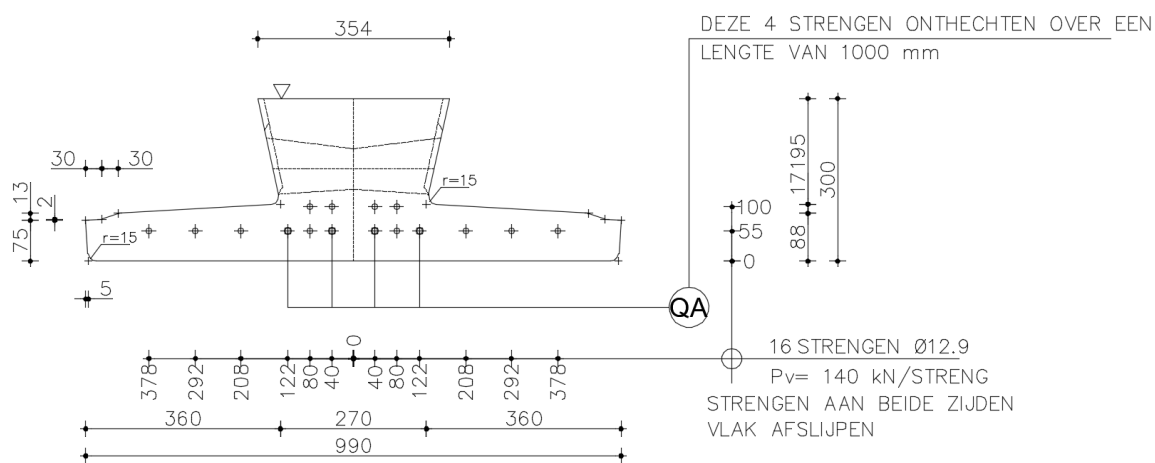


Figure 3.3. Cross-section dimensions and prestressing layout of prestressed girder

The geometrical properties of the cross-section are as follows:

A_g	=	156219.1	mm ²	I_g	=	1.20E+09	mm ⁴
u	=	2577	mm	Z_{gb}	=	110.5	mm
h_0	=	121	mm	W_{gb}	=	1.08E+07	mm ³
				W_{gt}	=	6.31E+06	mm ³

The longitudinal and shear reinforcement is built with B500B bars. The longitudinal reinforcement consists of four bars in the bottom flange and two in the top of the web, with a nominal diameter of 10 mm. Furthermore, the shear reinforcement consists of two-legged stirrups with a nominal diameter of 8 mm. The reinforcement layout is presented in Figure 3.4.

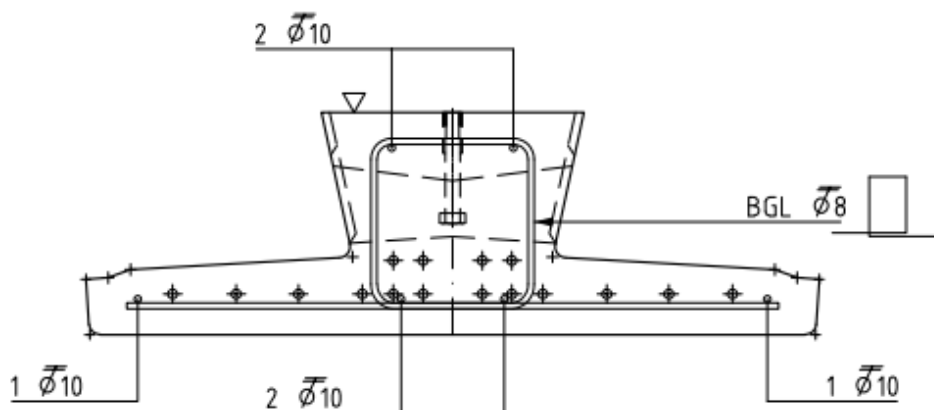


Figure 3.4. Longitudinal and shear reinforcement of prestressed girder

A total of 15 stirrups are spread at variable spacing lengths over the first 1350 mm at each end (Figure 3.5) whereas a total of 18 stirrups are spread in the midspan with a uniform spacing of 250 mm over a length of 4250 mm.

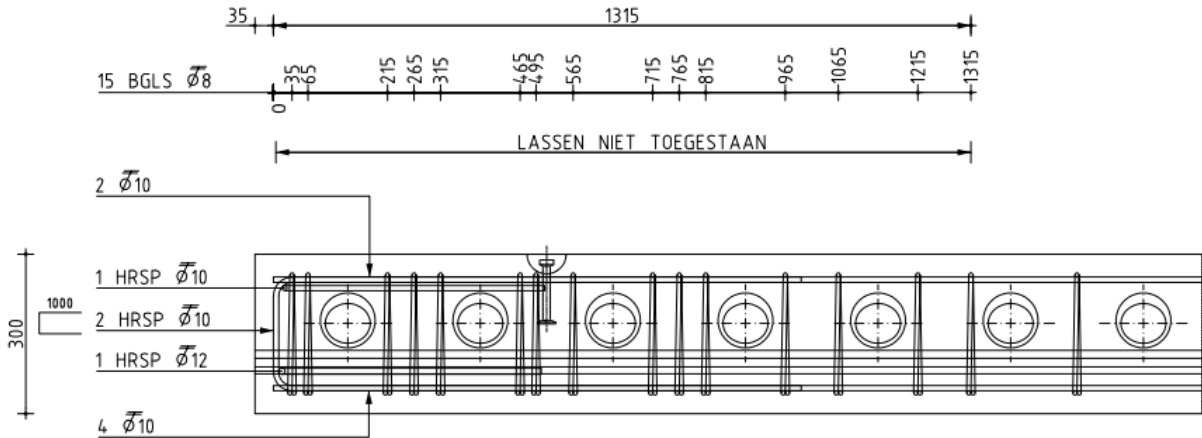


Figure 3.5. Shear reinforcement layout at prestressed girder ends

The composite cross-section is built up with the in-situ casting operation of the deck. The width of the composite section is increased to 1100 mm and the height of the topping is 120 mm over the top of the web of the precast girder, reaching a total height of 420 mm for the composite section. The longitudinal and shear reinforcement is built with B500B bars. The longitudinal reinforcement consists of four bars ($\phi 16\text{mm}$) in the bottom and 8 bars ($\phi 12\text{mm}$) in the top of the cast in-situ topping (Figure 3.6).

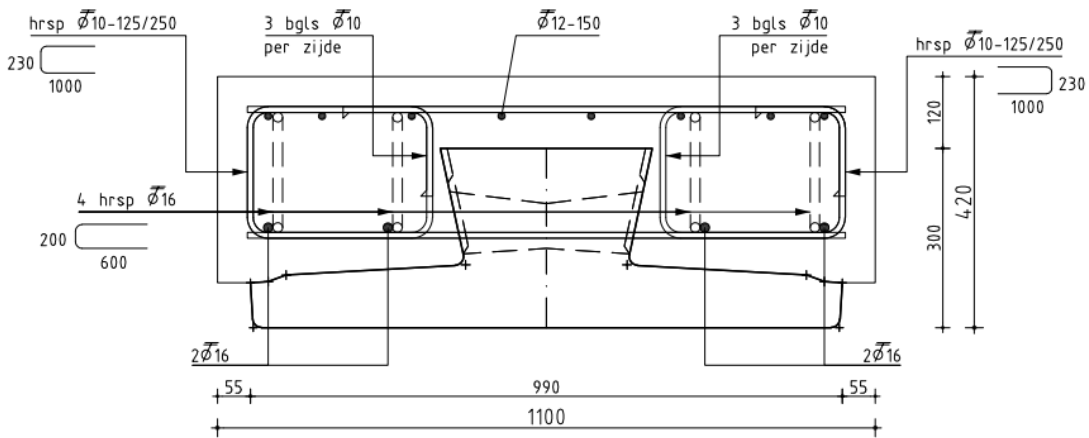


Figure 3.6. Cross-section of composite section and reinforcement layout of cast in-situ topping

The shear reinforcement consists of 29 pairs per side of slightly inclined one-legged stirrups ($\phi 10\text{ mm}$) with a spacing of 250 mm spanning over the nominal length of 7000 mm. Furthermore, three vertical one-legged stirrups with a spacing of 250 mm are provided at each end. The shear reinforcement layout of the cast in-situ topping is displayed in Figure 3.7.

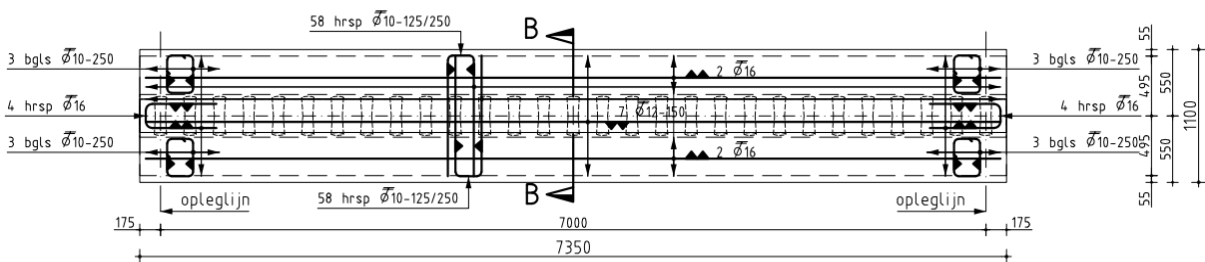


Figure 3.7. Shear reinforcement layout of cast in-situ topping

3.3 Material properties of geopolymer concrete mixtures

This section describes the material properties of the geopolymer concrete mixtures to be used in the calculation of the flexural and shear capacity of the specimen consisting of an individual precast prestressed girder with reinforced topping layer cast in-situ.

3.3.1 Experimental program for mechanical properties

Cubic samples 150x150x150 mm³ and prismatic samples 100x100x400 mm³ are collected in every casting operation for testing of the mechanical properties (Table 3.2). Table 3.3 presents an overview of the mechanical tests performed on the samples collected at each casting date.

Table 3.2. Number of samples for mechanical tests according to the casting date

Samples	Haitsma Beton			Ghent University		
	27/08/21	10/09/21	17/09/21	27/09/21	11/10/21	18/10/21
Cubes	20	20	20	16	16	16
Prisms	2	2	2	2	2	3

Table 3.3. Overview of mechanical tests for material properties of geopolymer concrete mixtures

Mixture	Cube samples	Prisms
Precast girder	f_c at 2.5, 7, 28 and 56 days	E_c at 2.5, 28 and 56 days
Cast in-situ topping	f_c at 1, 7, 28 and 91 days	E_c at 7, 15, 30 and 60 (or 81) days

3.3.2 Compressive strength

The samples of the SCGC mixture of the precast girders are heat-cured under 25°C for 1 day meanwhile the samples of the ready-mix geopolymer concrete mixture of the topping are demolded after 24 h and covered in plastic until testing. All the samples are moisture-cured in standard conditions 20°C, RH>95% and the compressive strength is determined at different ages according to EN12390-3 [63]. The results of the compressive strength at different ages of the mixtures from the different casting dates are summarized in Table 3.4 [59].

Table 3.4. Compressive strength of the geopolymer concrete mixtures [MPa]

Age [days]	Precast			Ready-mix		
	27/08/21	10/09/21	17/09/21	27/09/21	11/10/21	18/10/21
1	-	-	-	25	25	25
2.5	47.5	50.6	49.6	-	-	-
7	53.4	53.7	53.5	35	42	45
28	63.6	63.4	59.4	45	55	55
267	-	-	-	59	-	-

3.3.3 Elastic modulus

3.3.3.1 Experimental results

The development of stiffness and lower elastic modulus of the geopolymer concrete mixtures is a key aspect influencing the structural performance of prestressed members and are intrinsically related to the curing conditions, as discussed in 2.2.2.3. The prismatic samples obtained from the casting operations are exposed to different curing conditions to study the development of stiffness. The elastic modulus is tested in agreement with ISO 1920-10:2010 [64] and EN 12390-13 [65].

The samples corresponding to the SCGC mixture of the precast girders are subjected to heat-curing under 25°C for 1 day, followed by moisture-curing in standard conditions 20°C, RH>95% for 7, 14 or 28 days and finally exposed to drying 20°C, RH=50%. The development of the elastic modulus over time is illustrated in Figure 3.8 [57].

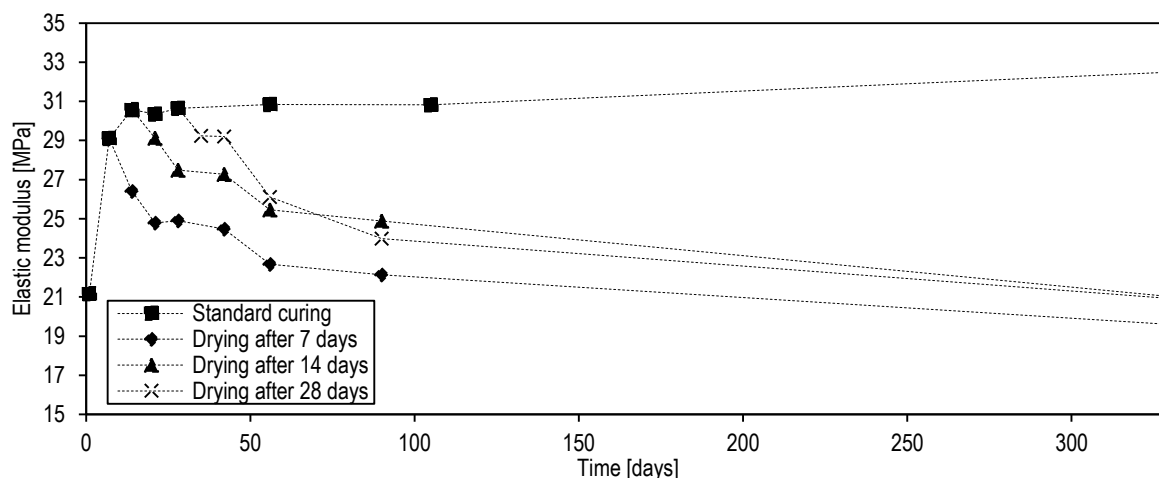


Figure 3.8. Elastic modulus development over time of Haitsma Beton - TU Delft SCGC mixture

A detailed study on the influence of curing conditions on the development of stiffness is conducted by the author with the samples corresponding to the ready-mix mixture of the topping (Figure 3.9). In particular, samples are exposed to seven different curing conditions (Table 3.5), and the elastic modulus is tested up to 60 or 81 days, depending on the casting date. The development of the elastic modulus over time is illustrated in Figure 3.10.

Table 3.5. Curing regimes of Elastic modulus samples of ready-mix geopolymer concrete mixture

Casting date	Sample	Curing regime
Sep 27	1	Standard curing (20°C, RH>95%)
	2	Standard curing 30 days → Drying (20°C, RH=50%)
Oct 11	1	Standard curing 14 days → Drying
	2	Sealed 14 days → Drying
Oct 19	1	Standard curing 7 days → Drying
	2	Sealed 7 days → Drying
	3	Sealed 3 days → Drying



Figure 3.9. Elastic modulus testing

As described in 2.2.2.3, the elastic modulus increases with the compressive strength for heat-cured and ambient-cured samples. Furthermore, from 2.2.2.1 the compressive strength of air-exposed samples decreases due to microcracking in the surface due to the moisture loss. Therefore, it can be expected that compressive strength and hence the elastic modulus decrease for samples exposed to drying. The development of the elastic modulus of the Haitsma Beton – TU Delft SCGC mixture (Figure 3.8) demonstrates this behavior as the elastic modulus decreases after exposed to drying, in contrast to the sample kept under standard curing for which the elastic modulus appears to be stable over time after 14 days. For this SCGC mixture the samples exposed to drying earlier report a higher decrease in the elastic modulus over time and the decrease ranges between 15-26% at 56 days. The ready-mix geopolymer (Figure 3.10 a)) also displays this behavior, as the sample exposed to drying shows a decrease in the elastic modulus of 7% at 60 days. The drop in the elastic modulus is similar for both mixtures when comparing the samples kept under standard curing with the samples exposed to drying after 14 days, 10% decrease at 28 days for both mixtures. Moreover, from 2.2.2.3 it is also stated that a similar modulus of elasticity can be attained for concrete compressive strength of around 50 MPa whether the sample is heat-cured or ambient-cured in early stages. A similar observation seems to describe the trend of the samples exposed to drying in early stages (Figure 3.10 c)). Even though, the initial exposure to drying is accompanied by a lower stiffness, the elastic modulus of the three samples seems to stabilize and reach a similar value after 30 days regardless of the time of exposure to drying.

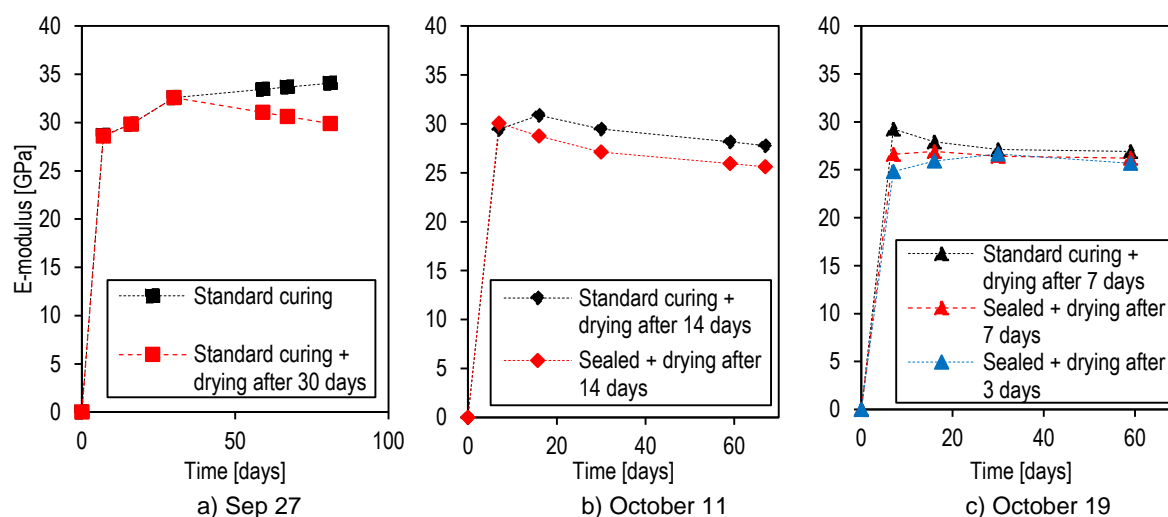


Figure 3.10. Elastic modulus development over time of ready-mix geopolymer concrete mixture

3.3.3.2 Elastic modulus according to EN 1992-1-1 and literature

The elastic modulus is calculated according the empirical relations from EN 1992-1-1 [22] for conventional concrete and the experimentally derived expressions for geopolymer concrete as suggested from literature in 2.2. An overview of the expressions is presented in Table 3.6. The expression for the elastic modulus of OPC concrete from EN 1992-1-1 [22] is fundamentally different to the empirical expressions for geopolymer concrete from different studies. The empirical expressions for the elastic modulus of geopolymer concrete are obtained by curve fitting of the experimental data, using the commonly used term of the square root of the compressive strength of concrete with a scalar factor. The expression for the elastic modulus of OPC concrete in ACI 318-19 [40] is also based on the square root of the compressive strength of concrete. The expression by Yang, et al. [36] also includes a dependency on the density if geopolymer concrete.

Table 3.6. Expressions for elastic modulus and tensile strength

Reference	Elastic modulus
EN 1992-1-1 [22]	$E_{cm} = 22000(f_{cm}/10)^{0.3}$
Yang, et al. [36]	$E_c = 4600(\rho_c/2200)^{1.5}f_c^{0.5}$
Nath & Sarker [11]	$E_c = 3510f_c^{0.5}$
Hassan, et al. [16]	$E_c = 4100f_c^{0.5}$

3.3.3.3 Comparison of experimental results and estimates

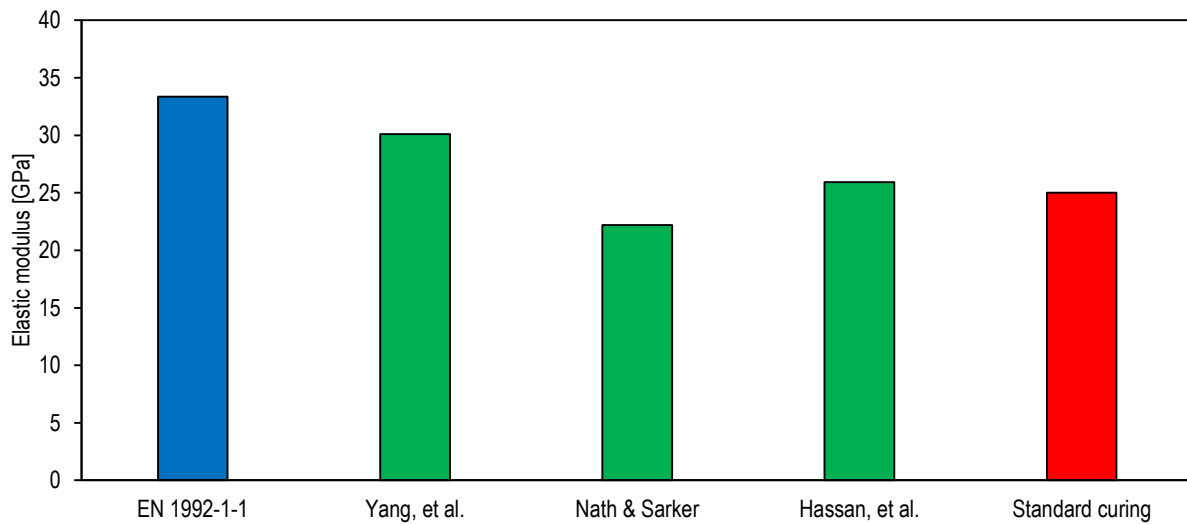
The elastic modulus obtained from material tests of the geopolymer concrete mixtures, the calculated estimates for the elastic modulus from the empirical relations as defined in EN 1992-1-1 [22] for conventional concrete and the experimentally derived expressions for geopolymer concrete as suggested from literature in 2.2. are summarized in Table 3.7 and visually represented in Figure 3.11.

Table 3.7. Elastic modulus of geopolymer concrete [MPa]

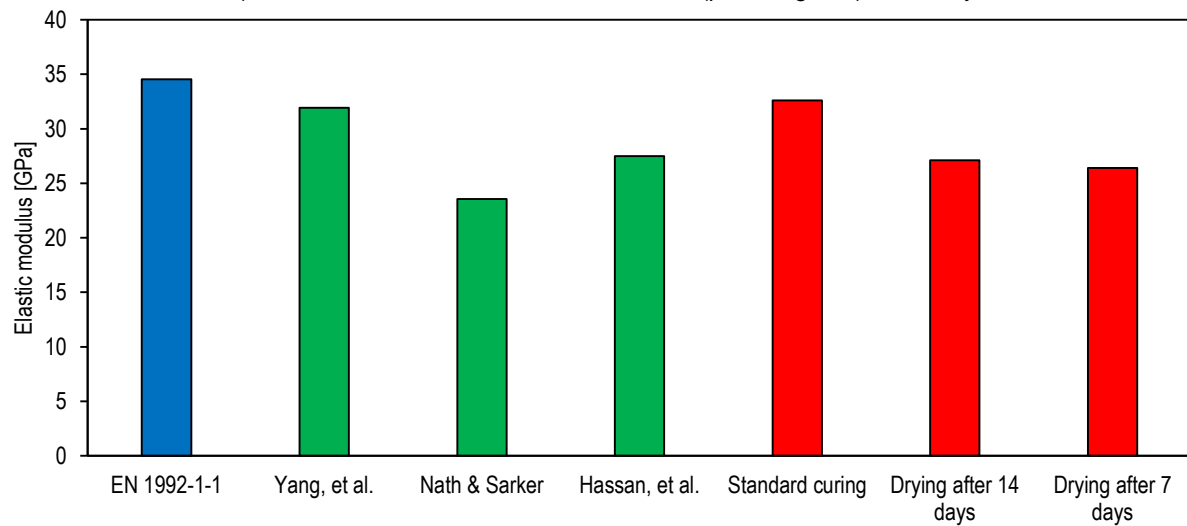
Reference	Precast 2.5 days	Ready-mix 30 days	Precast 30 days
EN 1992-1-1 [22]	33.35	34.55	35.65
Yang, et al. [36]	30.09	31.92	33.64
Nath & Sarker [11]	22.20	23.55	24.82
Hassan, et al. [16]	25.93	27.50	28.99
Standard curing	25.00	32.60	30.65
Drying after 14 days	-	27.10	27.50
Drying after 7 days	-	26.40	24.90

The first noticeable aspect is that the prediction formula for OPC concrete in EN 1992-1-1 [22] overestimates the elastic modulus of geopolymer concrete at 2.5 and 30 days, regardless of the curing condition and strength class. The empirical relation suggested by Yang, et al. [36] for ambient cured slag-based geopolymer concrete activated with calcium hydroxide estimates the highest values but are still lower than the estimates from EN 1992-1-1 [22]. The geopolymer concrete mixtures are also slag-based but the activator is sodium hydroxide and sodium silicate. On the other hand, the empirical relation from Nath & Sarker [11] for ambient-cured fly ash-based geopolymer concrete activated with sodium hydroxide and sodium silicate gives the lowest estimates. Finally, the empirical relation from Hassan, et al. [16] gives the closest predictions to the elastic modulus. Nevertheless, this study is conducted on fly ash-based geopolymer concrete with early age heat-curing and ambient curing.

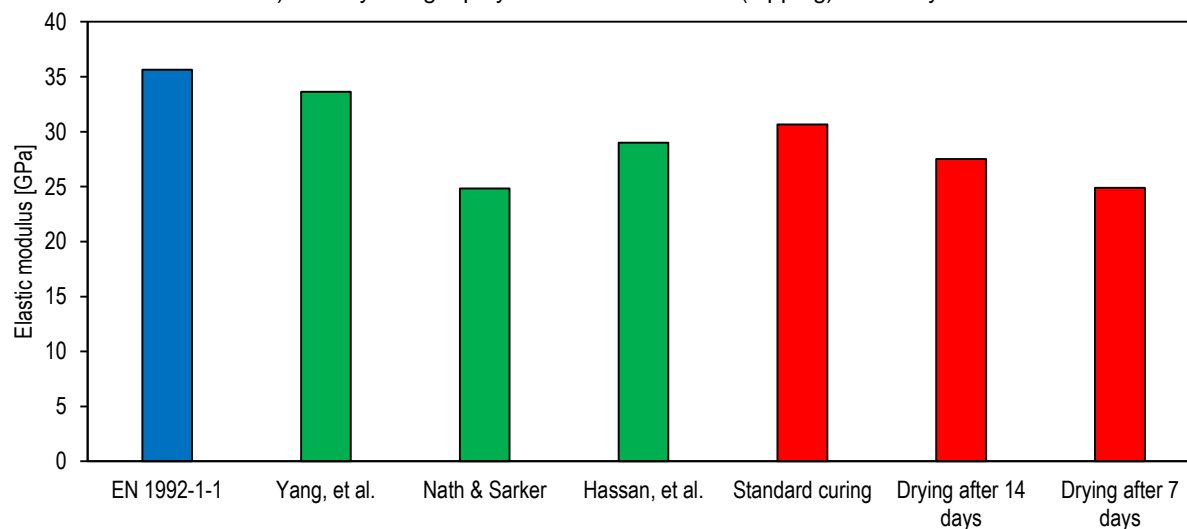
From 2.2.2.3 it was expected that the elastic modulus of ambient cured geopolymer concrete at 28 days would be 25-30% lower than OPC concrete and that the prediction formulas for OPC concrete result in non-conservative estimates of the elastic modulus. Similar results are reported since the elastic modulus at 30 days of the samples of the two geopolymer concrete mixtures are 22-30% lower when exposed to drying and 6-14% lower for standard curing. As discussed in detail in the preceding section, the elastic modulus decreases for samples exposed to drying which is observed from the 30-day results of the samples exposed to drying at different times. As described in 2.2.2.1, slag-based binders develop similar strength to OPC concrete because of the presence of C-S-H gel in addition to the polymeric structure caused by the higher calcium content as compared to low-calcium (fly ash) based geopolymer. Therefore, the higher amount of calcium due to the choice of activator explains why the prediction formula from Yang, et al. [36] is closer to the behavior of OPC concrete as compared to the experimental results for the samples regardless of the curing conditions.



a) Haitsma Beton - TU Delft SCGC mixture (precast girder) at 2.5 days



b) Ready-mix geopolymer concrete mixture (topping) at 30 days



c) Haitsma Beton - TU Delft SCGC mixture (precast girder) at 30 days

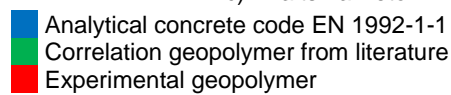


Figure 3.11. Elastic modulus values according to different methods

As described in 2.2.2.1, the compressive strength of ambient cured samples increases for higher slag content in combined systems of GGBFS and fly ash [11, 33, 35] and from 2.2.2.3, the elastic modulus increases with the compressive strength for heat-cured and ambient-cured samples. Therefore, the lowest estimates from the empirical relation by Nath & Sarker [11] can be due to the choice of fly ash as precursor of the geopolymer concrete mix and its influence in the compressive strength.

The elastic modulus of geopolymer concrete is lower than OPC concrete estimates but a conclusive framework for calculating the elastic modulus from the compressive strength is unavailable because the empirical relations presented beforehand are intrinsically dependent in the choice of activators, composition of the precursors and curing conditions.

3.3.4 Volume stability properties

3.3.4.1 Experimental results

The autogenous shrinkage (Figure 3.12) was measured with an autogenous deformation testing machine (ADTM) for samples cured at 25°C for 1 day and 20°C until 28 days.

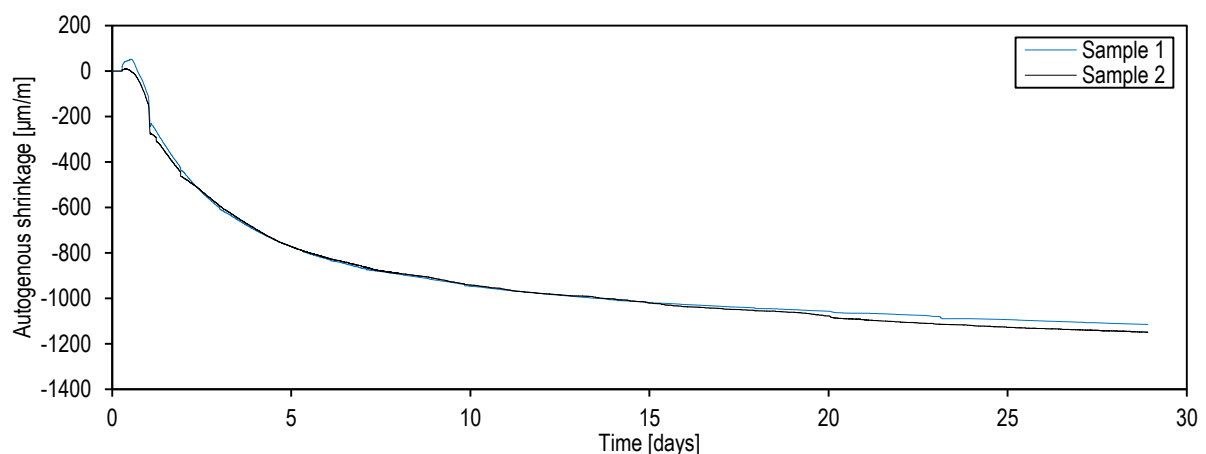


Figure 3.12. Autogenous shrinkage of Haitsma Beton - TU Delft SCGC mixture

The creep behavior is measured according to EN 12390-17 [66] with prismatic samples of 100x100x400 mm³. The samples were cured for 2.75 days and then subjected to a stress of 17 MPa. Figure 3.13 displays the results of the total deformation, shrinkage, autogenous shrinkage, elastic deformation and creep deformation.

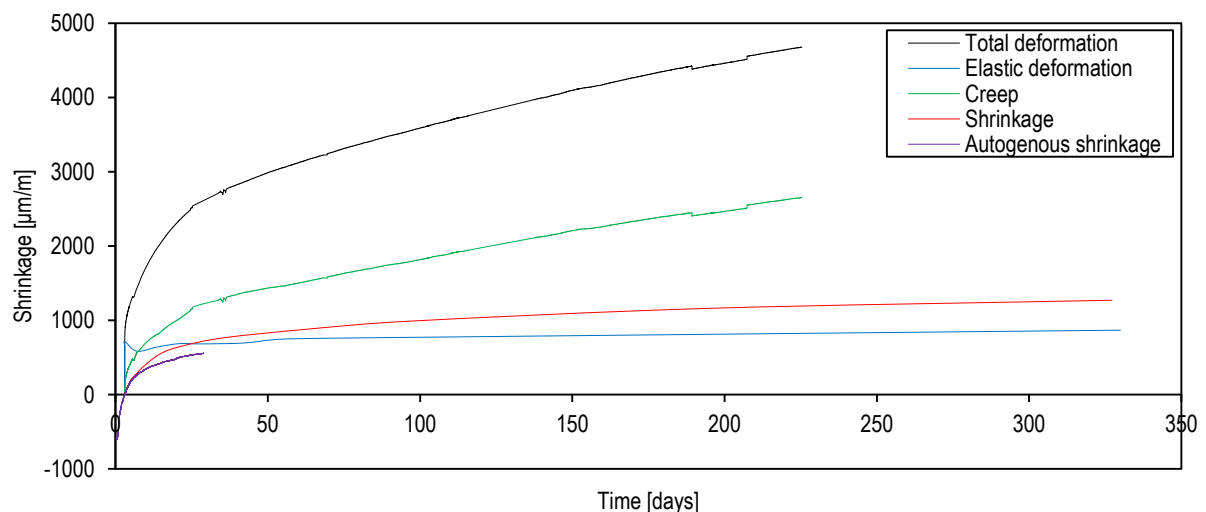


Figure 3.13. Total strain of Haitsma Beton - TU Delft SCGC mixture

In order to obtain the curves in Figure 3.13, first the elastic strain is subtracted from the total strain. The resultant strain is the total creep and shrinkage strains. The total creep strain is obtained by subtracting the shrinkage strain which is obtained from tests on shrinkage specimens. Therefore, the total creep at any time is given by the following expression:

$$\varepsilon_{cc}(t, t_0) = \varepsilon_{cc}(t) - [\varepsilon_{cs}(t, t_0) + \varepsilon_{cc}(t_0)]$$

The drying shrinkage is obtained by subtracting the autogenous from the total shrinkage.

The strain due to restrained autogenous shrinkage is determined by subtracting the strain at $t \rightarrow \infty$ from the strain at the age of prestressing, both values are obtained from Figure 3.12.

$$\varepsilon_{ca} = \varepsilon_{ca}(t_{30}) - \varepsilon_{ca}(t_{2.5}) = 1140 - 590 = 550 \mu\text{m/m}$$

The strain due to drying shrinkage ε_{cd} at 30, 60 and 270 days is determined from Figure 3.13, by subtracting the total shrinkage from the autogenous shrinkage, and is equal to 153, 332 and 674 $\mu\text{m/m}$, respectively.

Finally, the creep coefficient $\phi(t, t_0)$ at 30, 60 and 270 days is calculated from Figure 3.13 with the ratio of the creep strain at the corresponding age to the initial elastic deformation:

$$\phi(t_{30}, t_0) = \frac{1214}{664} = 1.83 \quad \phi(t_{60}, t_0) = \frac{1500}{664} = 2.26 \quad \phi(t_{270}, t_0) = \frac{2652}{664} = 3.99$$

3.3.4.2 Volume stability properties according to EN 1992-1-1

According to EN 1992-1-1 3.1.4 (6) [22] the total shrinkage ε_{cs} strain is composed by the autogenous ε_{ca} and drying ε_{cd} shrinkage strains. The autogenous shrinkage develops primarily during the early days after casting. The final autogenous shrinkage strain $\varepsilon_{ca}(\infty)$ is a linear function of the concrete compressive strength. The development of the autogenous shrinkage over time is given by the exponential function $\beta_{as}(t)$ (Figure 3.14). The drying shrinkage develops slowly as it depends on the moisture loss through the hardened concrete and is obtained by multiplying the nominal unrestrained shrinkage $\varepsilon_{cd,0}$ by coefficient k_h and rational function $\beta_{ds}(t, t_s)$ (Figure 3.15).

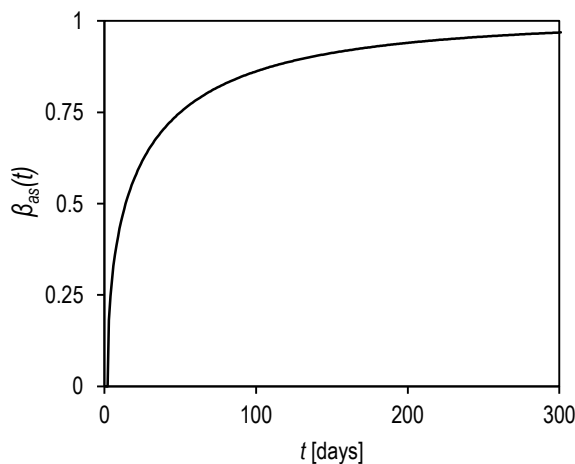


Figure 3.14. $\beta_{as}(t)$

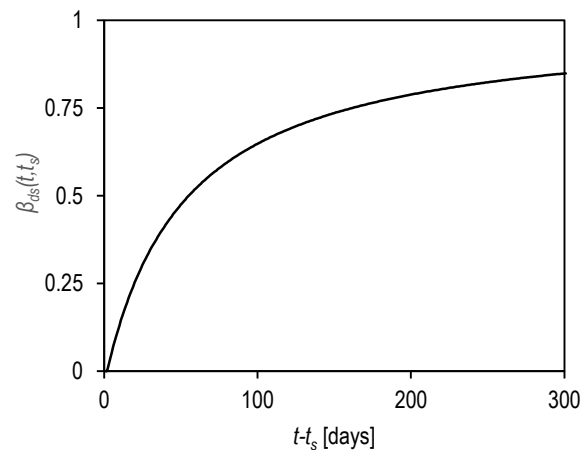


Figure 3.15. $\beta_{ds}(t, t_s)$

The autogenous and drying shrinkage strains at time t are given by:

$$\begin{aligned} \varepsilon_{ca}(\infty) &= 2.5(f_{ck} - 10) \\ \beta_{as}(t) &= 1 - e^{-0.2t^{0.5}} \\ \varepsilon_{ca}(t) &= \beta_{as}(t)\varepsilon_{ca}(\infty) \end{aligned}$$

$$\begin{aligned} \beta_{ds}(t, t_s) &= \frac{t - t_s}{(t - t_s) + 0.04\sqrt{h_0^3}} \\ \varepsilon_{cd}(t) &= \beta_{ds}(t, t_s)k_h\varepsilon_{cd,0} \end{aligned}$$

The design concrete strength class of the girder is C45/55. The maximum autogenous shrinkage is $\varepsilon_{ca}(\infty) = 87.5 \mu\text{m}/\text{m}$. The value of k_h is dependent on the notional size of the member and is equal to 1.0 for $h_0 = 100$ and 0.85 for $h_0 = 200$ (for $h_0 = 121$, $k_h = 0.97$ by linear interpolation). $\varepsilon_{cd,0}$ is obtained by linear interpolation from Table 3.8, for both the strength class (C45/55) and RH (50%). For the calculation of $\beta_{ds}(t, t_s)$, the age at the beginning of drying shrinkage t_s is obtained from Figure 3.13 when the shrinkage and autogenous shrinkage curves start to separate (7 days). The creep coefficient $\phi(t, t_0)$ is determined from Figure 3.16.

Table 3.8. Nominal unrestrained drying shrinkage values $\varepsilon_{cd,0}$ [‰] for concrete (Table 3.2 EN 1992-1-1 [22])

$f_{ck}/f_{ck,cube}$ (MPa)	Relative Humidity (in ‰)					
	20	40	60	80	90	100
20/25	0.62	0.58	0.49	0.30	0.17	0.00
40/50	0.48	0.46	0.38	0.24	0.13	0.00
60/75	0.38	0.36	0.30	0.19	0.10	0.00
80/95	0.30	0.28	0.24	0.15	0.08	0.00
90/105	0.27	0.25	0.21	0.13	0.07	0.00

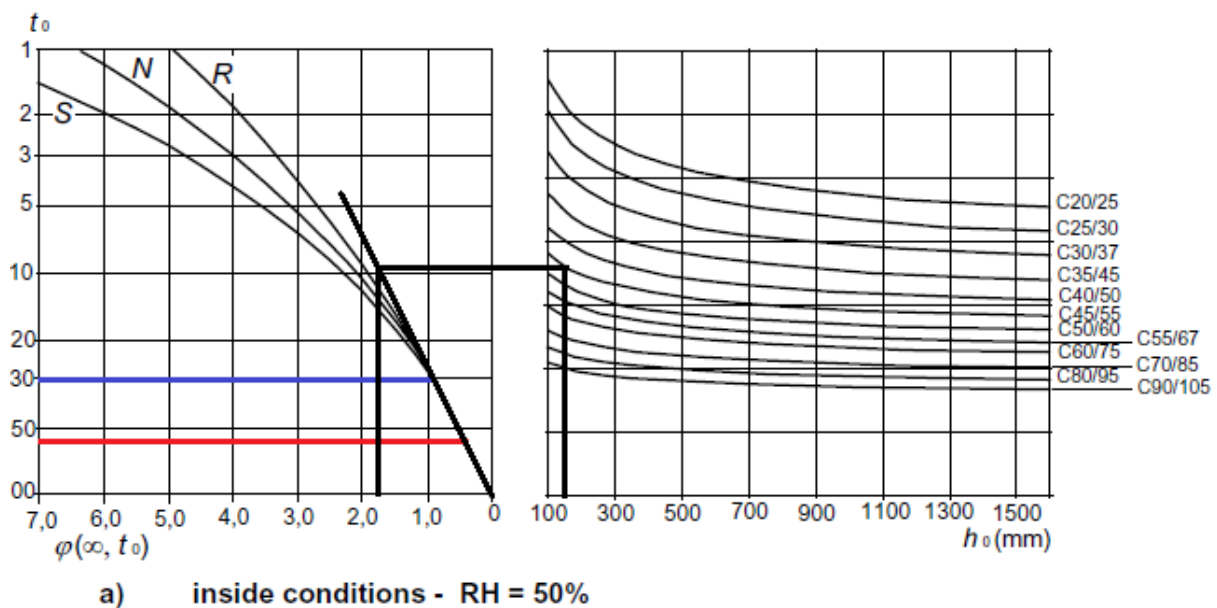


Figure 3.16. Creep coefficient for concrete under normal environmental conditions (Figure 3.1 EN 1992-1-1 [22])

The volume stability material properties calculated with the methods for OPC concrete as defined in EN 1992-1-1 [22] are summarized in Table 3.9.

Table 3.9. Volume stability properties of SCGC mixture of precast girder according to EN 1992-1-1

t [days]	$\varepsilon_{ca}(\infty)$ [$\mu\text{m}/\text{m}$]	$\beta_{as}(t)$	$\varepsilon_{ca}(t)$ [$\mu\text{m}/\text{m}$]	$\varepsilon_{cd,0}$ [$\mu\text{m}/\text{m}$]	$\beta_{ds}(t, t_s)$	ε_{cd} [$\mu\text{m}/\text{m}$]	$\phi(t, t_0)$
2.5	87.5	0.270	23.6	397.5	0	-	-
30	87.5	0.666	58.2	397.5	0.302	116.3	1.73
60	87.5	0.788	68.9	397.5	0.499	192.4	1.73
270	87.5	0.963	84.2	397.5	0.835	322.1	1.73

3.3.4.3 Comparison of experimental results and estimates

The estimated creep coefficient and the measured autogenous and drying shrinkage at different ages, from material tests of the SCGC mixture of the precast girder, and the estimated volume stability properties according to EN 1992-1-1 [22] are summarized in Table 3.10 and visually represented in Figure 3.18.

Table 3.10. Volume stability properties of geopolymer concrete

t [days]	EN 1992-1-1 [22]			Experimental results		
	ε_{ca} [$\mu\text{m}/\text{m}$]	ε_{cd} [$\mu\text{m}/\text{m}$]	$\phi(t, t_0)$	ε_{ca} [$\mu\text{m}/\text{m}$]	ε_{cd} [$\mu\text{m}/\text{m}$]	$\phi(t, t_0)$
2.5	23.6	-	-	590	-	-
30	58.2	116.3	1.73	1140	153	1.83
60	68.9	192.4	1.73	1144	332	2.26
270	84.2	322.1	1.73	1144	674	3.99

From Figure 3.13, the autogenous shrinkage mainly develops during early-age and an exponential function to describe the development of the autogenous shrinkage could be suitable for geopolymer concrete as well. In fact, Figure 3.17 displays the measured autogenous shrinkage and the exponential calculation model from EN 1992-1-1 [22] until 28 days, but with a modified value for $\varepsilon_{ca}(\infty)$ determined by curve-fitting and is equal to 1745 $\mu\text{m}/\text{m}$. It was described beforehand that in EN 1992-1-1 3.1.4 (6) [22] $\varepsilon_{ca}(\infty)$ is related linearly to the compressive strength of concrete and was equal to 87.5 $\mu\text{m}/\text{m}$ for C45/55. Therefore, even though the exponential model may be suitable (Figure 3.18 a)), the linear prediction of the final autogenous shrinkage is definitely not applicable since the autogenous shrinkage of geopolymer concrete is significantly higher (an order of magnitude) than for OPC concrete.

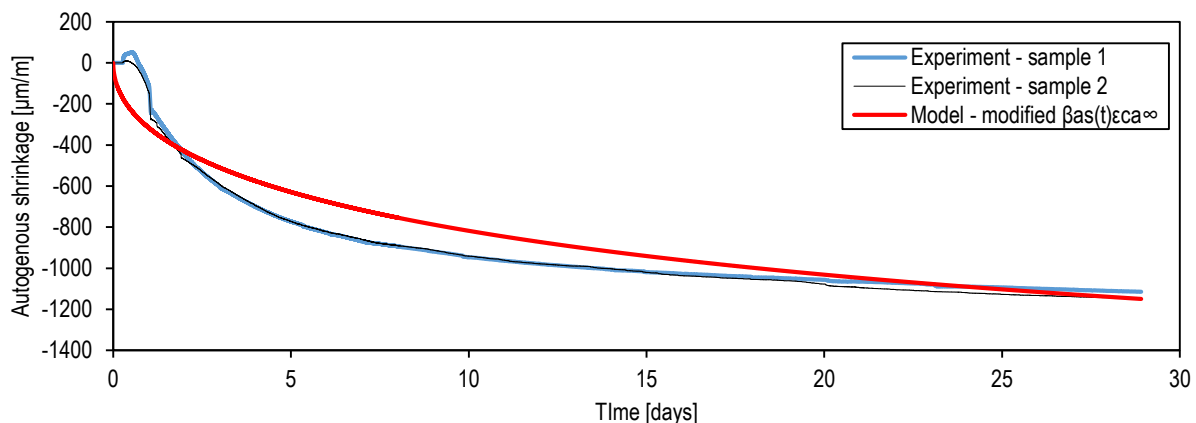
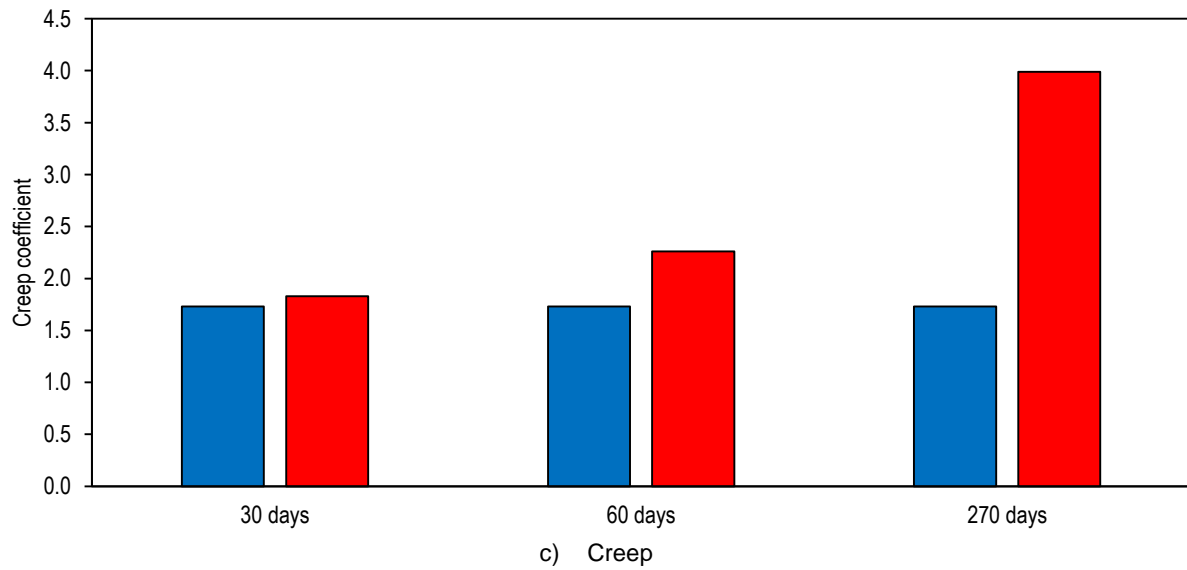
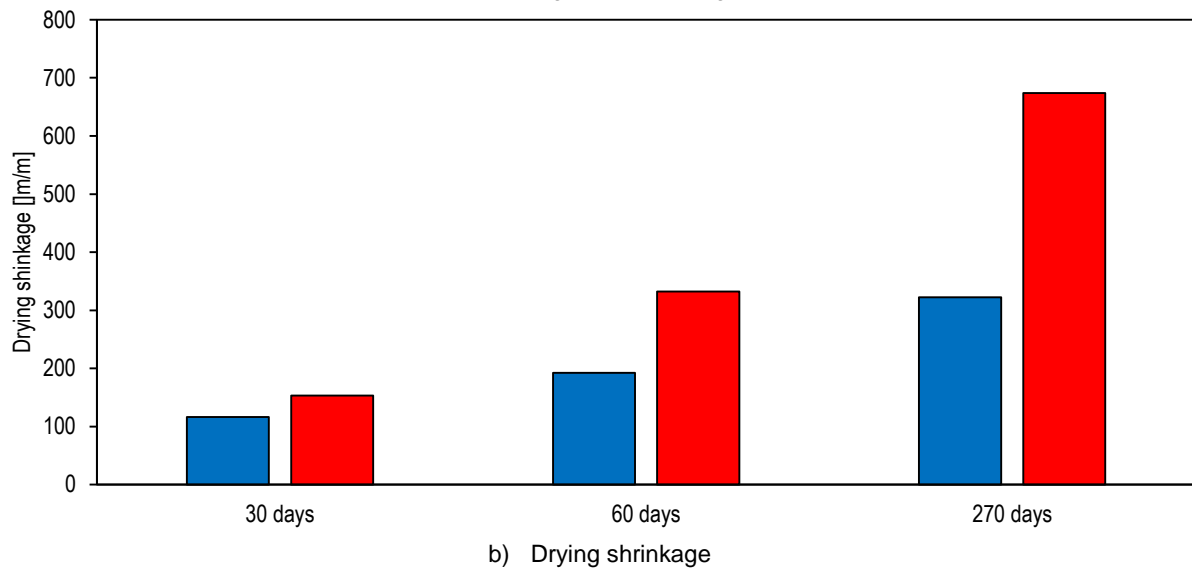
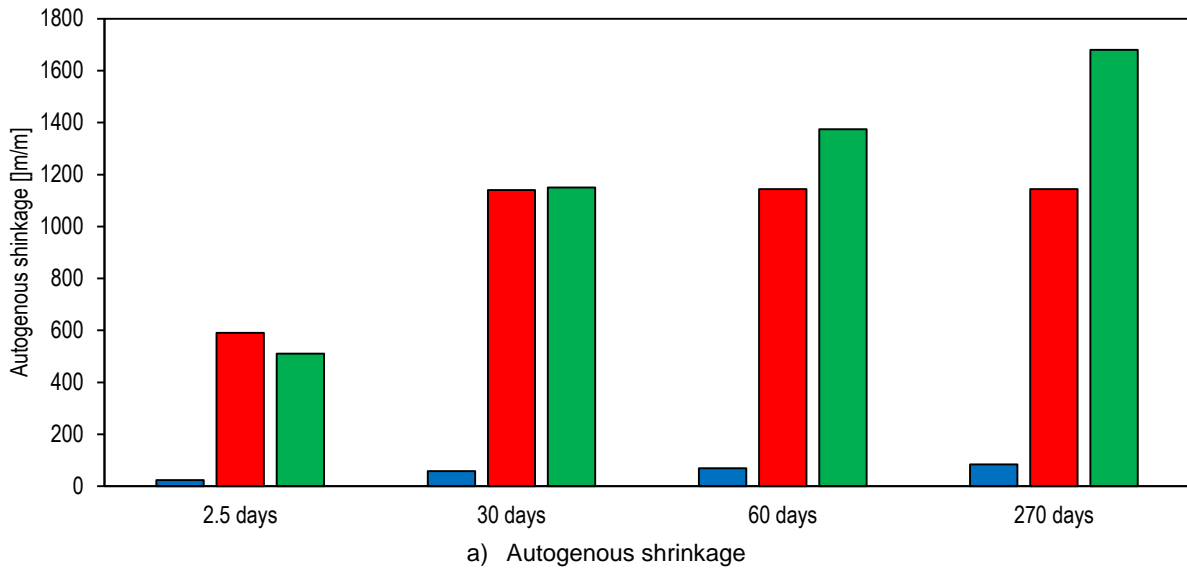


Figure 3.17. Autogenous shrinkage from geopolymer concrete samples and calculation model as EN 1992-1-1

The drying shrinkage of SCGC at 30 days is higher than the estimate from EN 1992-1-1 [22] for OPC concrete (32% higher) but the difference is increased with time (73% and 110% higher at 60 and 270 days, respectively). This is lower than difference reported in 2.2.3.1, which states that the drying shrinkage of GGBFS-based geopolymer concrete is around 3 times higher than OPC concrete for different exposure conditions. The drying shrinkage at 60 and 270 days compared to 30 days, is 2.2 and 4.4 times higher for SCGC whereas it is only 1.7 and 2.8 times higher for OPC concrete. As discussed in 2.2.3.1, the driving force of shrinkage in geopolymer concrete can also be due to the viscoelastic behavior since the shrinkage continues to increase for a constant moisture loss. The difference may be further explained as the relation between RH and shrinkage for OPC concrete is linear but the parabolic relation for GGBFS-based geopolymer concrete is caused by the rearrangement of the C-A-S-H gel structure dependent on the drying rate and history.



■ Analytical concrete code EN 1992-1-1
■ Experimental geopolymer
■ Modified expression from EN 1992-1-1

Figure 3.18. Volume stability properties according to different methods

A higher creep coefficient was expected since the observations from 2.2.3.2 indicate that the prediction model from fib Model Code 2010 [27] also underestimates the creep coefficient of GGBFS-based geopolymer concrete. The creep coefficient of SCGC at 30 days is almost the same as the prediction model from EN 1992-1-1 [22] for OPC concrete. On the other hand, at 60 and 270 days the creep coefficient increases for SCGC whereas for OPC it remains constant. The visco-elastic/viscoplastic material response of geopolymer concrete explains the higher creep since the deformation associated with the reorganization of the microstructure is irreversible. The creep coefficient at 270 days is significantly larger than at 30 days, indicating considerable creep deformations.

3.3.5 Calculation values

As described in 3.2.2, the specimens are covered with wet burlaps and sealed with plastic for the longer possible time but curing takes place in an open space exposed to the environment. Therefore, the structure is subjected to the drying process. The decrease in the elastic modulus needs to be considered since higher elastic deformations will lead to higher prestressing losses and modify the stress distributions assumed for design. In particular, the elastic modulus under three curing conditions are selected to analyze the best fit to the real conditions. Scenario 2 is the default option for the calculations in the next sections as the combination of standard curing and drying resemble the exposure conditions of the structure.

- 1) Standard curing 20°C, RH>95%¹
- 2) Drying after 14 days: Standard curing 20°C, RH>95% for 14 days, drying 20°C, RH=50%²
- 3) Drying after 7 days: Standard curing 20°C, RH>95% for 7 days, drying 20°C, RH=50%³

The compressive strength is taken from the cubic samples subject to standard curing conditions for the casting dates of September 17 and October 19 (casting dates of individual specimens for flexural and shear tests) and the Poisson ratio and density are taken as standard values for conventional concrete. The material properties are obtained from the experimental results from prior sections and are summarized in Table 3.11 and Table 3.12.

Table 3.11. Mechanical properties of geopolymer concrete mixtures

Quantity	Units	Precast		Ready-mix
		2.5 days	30 days	30 days
E_c^1	MPa	25000	30650	32600
E_c^2	MPa		27500	27100
E_c^3	MPa		24900	26400
ν	-	0.2		
ρ	kg/m ³	2550		
$f_{cm,cube}$	MPa	50	60	55
f_{cm}	MPa	40	50	45
f_{ctm}	MPa	2.8	3.6	3.0

Table 3.12. Summary of volume stability properties of Haitsma Beton - TU Delft SCGC mixture

Age [days]	ϵ_{ca} [$\mu\text{m}/\text{m}$]	ϵ_{cd} [$\mu\text{m}/\text{m}$]	$\phi(t, t_0)$
2.5	590	-	-
30	1140	153	1.83
60	1144	332	2.26
270	1144	674	3.99

3.4 Material properties of prestressing and reinforcement steel

3.4.1 Prestressing steel

The material properties of the prestressing tendons are obtained from the Inspection certificate EN 10204:2004 Type 3.1 provided to Haitsma Beton as part of the contract requirements from the manufacturer. Two certificates were issued for the EN 3868:2001 FeP1860-12.9-7S tendons and are provided in Appendix B and the data is summarized in Table 3.13. The material properties to be used in calculations are selected from sample 1 since it has the lowest resistance and ductility of both samples.

Table 3.13. Mechanical properties of prestressing steel

Quantity	Units	Sample 1	Sample 2
E_p	GPa	192.49	192.88
f_p	MPa	1915	1927
$f_{p0.1}$	MPa	1694	1675
$\varepsilon_{p0.1}$	%	1-1.1	1-1.1
ε_u	%	5.95	6.64

3.4.2 Reinforcement steel

The material properties of the B500B reinforcement steel are: $E_s = 200$ GPa and $f_y = 500$ MPa.

3.5 Experimental setup of mechanical tests

The following section describes the test setup, measurement devices and loading protocols of the flexural test (4-point bending), shear test (3-point load) and flexural test (4-point bending) after 9 months subjected to self-weight performed on the individual girder specimens in Magnel Laboratory in Ghent University in 15 November 2021, 17 of November 2021 and 20 June 2022, respectively [60, 61, 62].

3.5.1 Prestressing stage measurements

The midspan deformations and length change of the precast girders are measured manually after prestressing (2.75 \approx 3 days) and at 7 days. Fibre optic sensors (FOS) are employed in the precast girder for monitoring the early age deformation and detect the transmission length. Strain and temperature Fibre Bragg grating (FBG) sensors are applied to measure the mechanical strains and compensate for thermal strains. The sensors for monitoring early deformation and temperature are fixed on the prestressing strands. The accuracy of strain and temperature measurements are $\pm 1 \mu\epsilon$ and $\pm 0.1^\circ\text{C}$, respectively. Measurements are performed before/after casting of the girders, before/after application of the prestressing force, before/after casting of the topping layer and before the mechanical tests.

3.5.2 Test setup of mechanical tests

The specimen is simply supported at the two ends by a hinge and roller support. The support plates (350 mm x 280 mm, thickness of 30 mm) act directly over steel roller bearings with a nominal diameter of 40 mm. One of the roller bearings is blocked to act as a hinge support meanwhile the other remains free. The specimen is settled over the support plates by a mortar layer between the steel and the bottom face of the precast girder.

3.5.2.1 Flexural test (15 Nov 2021)

The 4-point bending test setup is shown in Figure 3.19. The load is applied by two hydraulic loading jacks at a distance of 2300 mm from the supports. The nominal capacity of each loading jack is 500 kN and stroke of 125 mm. Load transferring occurs via spreader beams (HEM600) which span over the full width and rest over a 10 mm thick mortar bed.

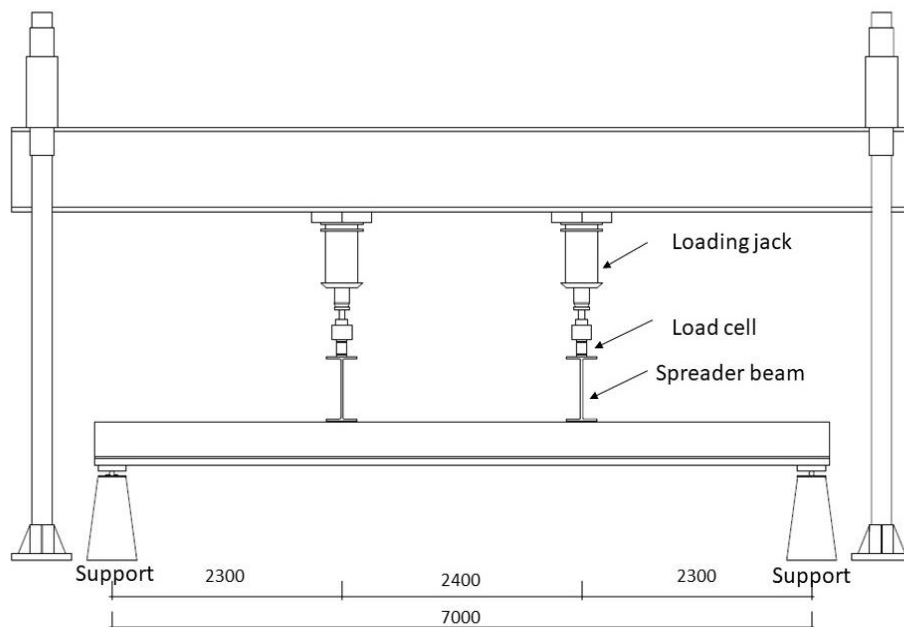


Figure 3.19. Flexural test setup [61]

The instrumentation layout for data acquisition during the flexural test is displayed in Figure 3.20. The applied load is monitored by load cells placed between the loading jacks and spreader beams. Vertical displacements are measured using 5 LVDTs, at the top of the specimen over the supports and at the bottom of the specimen at midspan and under the points of application of loading. Concrete strains are measured in the constant moment region by 8 strain stirrups with gauge length of 200 mm (Figure 3.21), and monitor the compressive strain near the top of the specimen and the tensile strains at the level of the prestressing tendons of the precast girder and the longitudinal reinforcement of the topping. Furthermore, visual inspection of crack formation, manual measurement of crack openings with a crack microscope and DIC measurements are performed during testing.

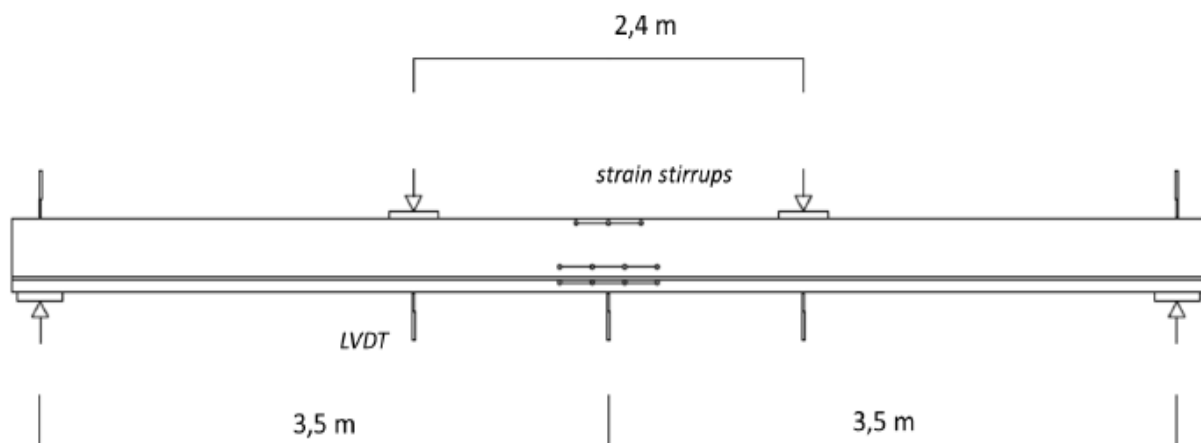


Figure 3.20. Flexural test measurement devices [61]

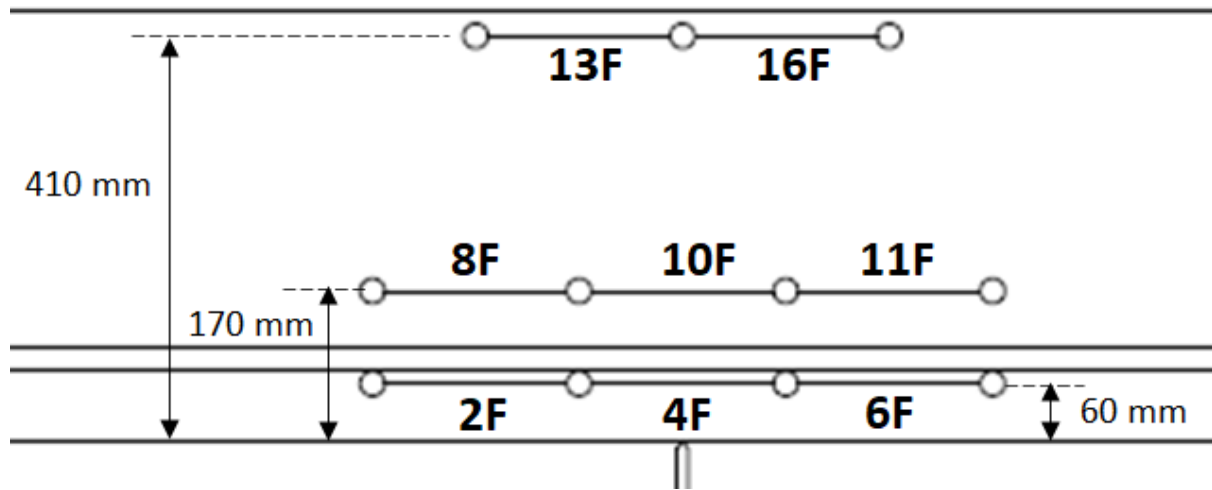


Figure 3.21. Strain stirrups in flexural test [61]

The loading scheme for the flexural test as measured by the loading cells is displayed in Figure 3.22. Initially, the load is applied by load control at a speed of 10 kN/min. The load is increased to 10 kN and then unloaded for an initial check of the test setup. Subsequently, the load is increased until 130 kN with intermediate stops at 40 kN, 70 kN and 100 kN for measurements, followed by unloading. Afterwards, the load is increased until 280 kN with stops at 130 kN, 160 kN, 190 kN, 220 kN and 250 kN. At this point, the load is switched to displacement control at a speed of 2 mm/min and the load is increased to 360 kN with intermediate stops at 300 kN and 330 kN. The speed rate is increased to 4 mm/min and the load is increased until the maximum stroke is reached.

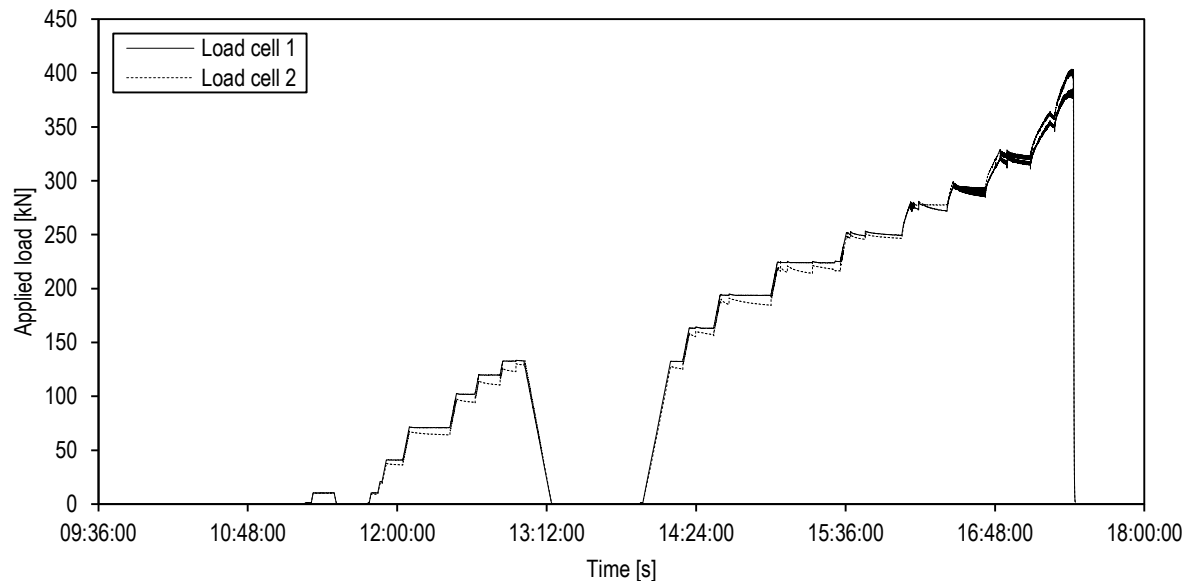


Figure 3.22. Applied load as measured by load cells (Flexural test)

3.5.2.2 Shear test (17 Nov 2021)

The 3-point load test setup is shown in Figure 3.23. The load is applied by two hydraulic loading jacks connected in parallel at a distance of 1200 mm from the hinge support. The hinge support end is placed closest to the point of application of loading. The nominal capacity of each loading jack is 500 kN. Load transferring occurs via a spreader beam (HEM600) which spans over the full width and rest over a 10 mm thick mortar bed.

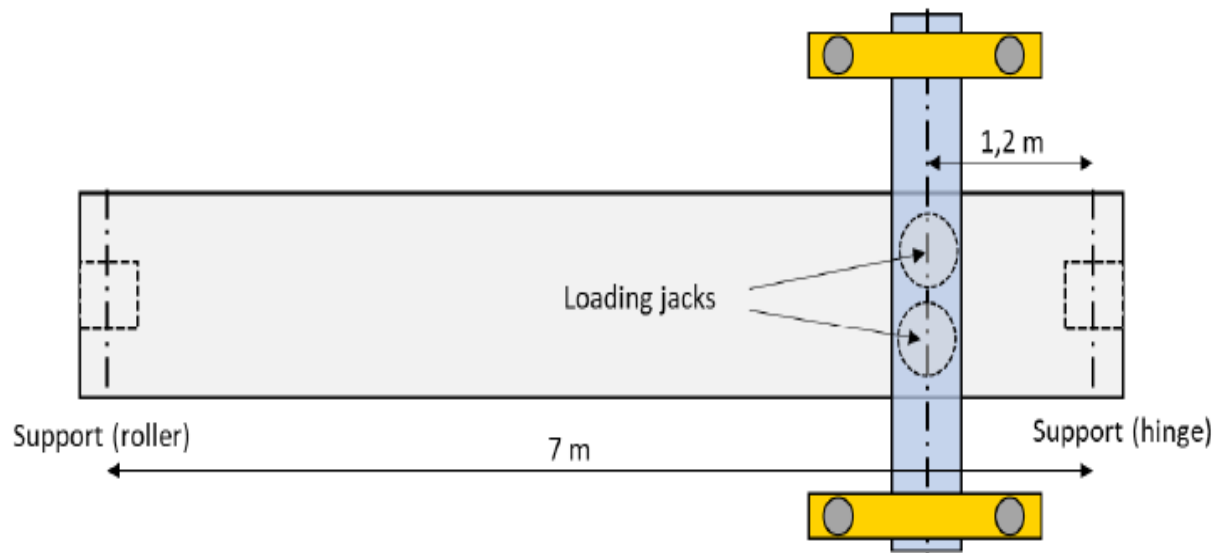


Figure 3.23. Shear test setup [61]

The instrumentation layout for data acquisition during the flexural test is displayed in Figure 3.24. The applied load is monitored by load cells placed between the loading jacks and spreader beam. The total applied load is the sum of the two load cells. Vertical displacements are measured using 3 LVDTs, at the top of the specimen over the supports and at the bottom of the specimen at the point of application of loading. Furthermore, visual inspection of crack formation and DIC measurements are performed during testing.

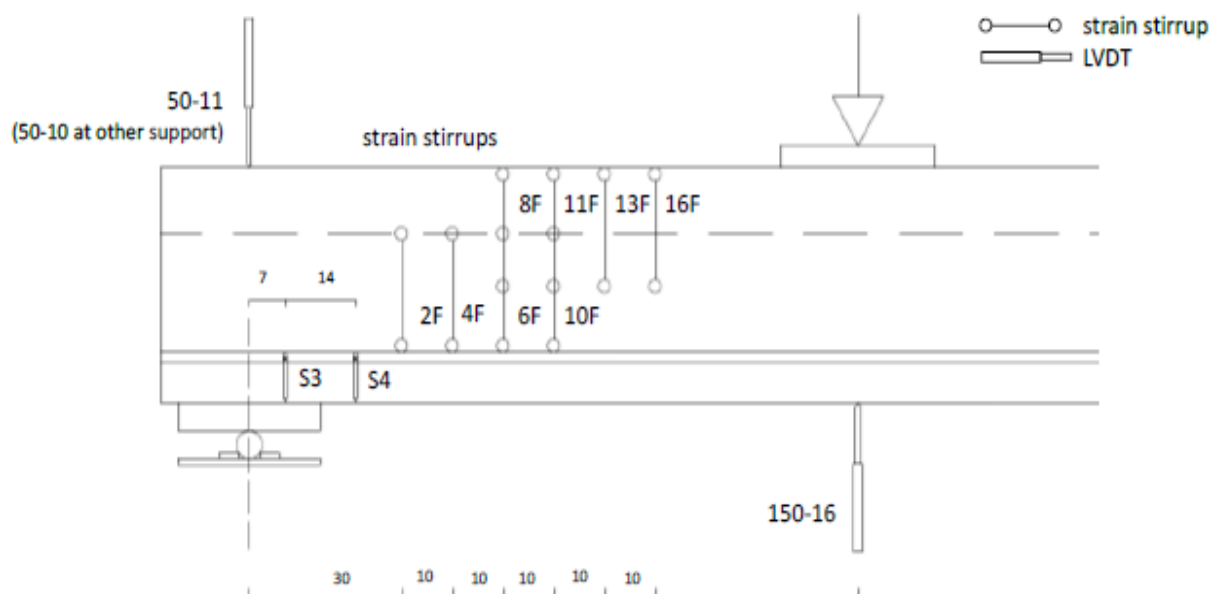


Figure 3.24. Shear test measurement devices [61]

The loading scheme for the shear test as measured by the loading cells is displayed in Figure 3.25. Initially, the load is applied by displacement control at a speed of 0.5 mm/min. The load is increased to 10 kN, then unloaded for an initial check of the test setup and then preloaded to 10 kN. Subsequently, the load is increased until 300 kN and maintained constant. At 310 kN the load rate is increased to 1 mm/min and the load is increased until failure.

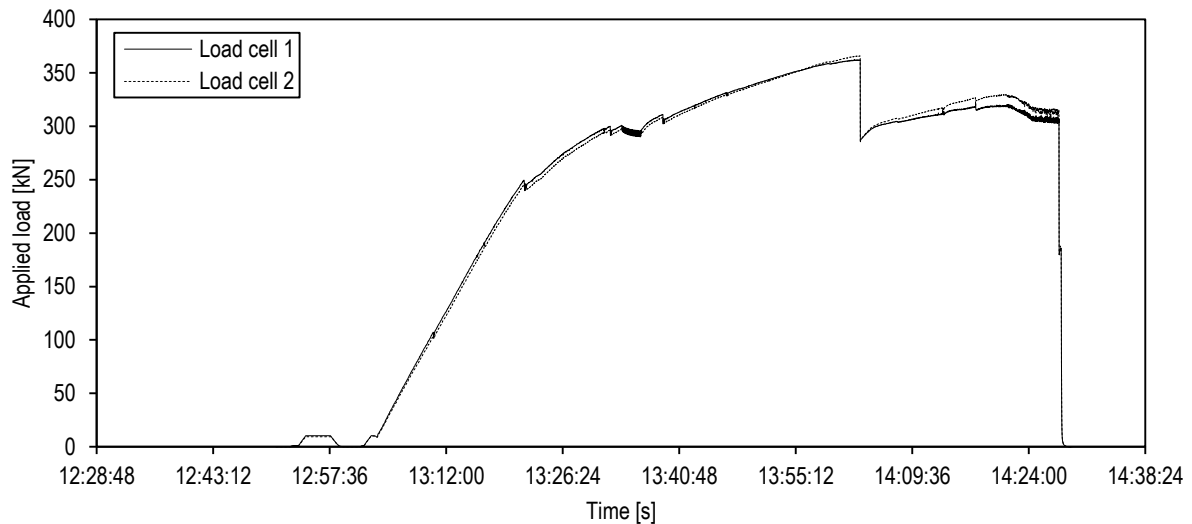


Figure 3.25. Applied load as measured by load cells (Shear test)

3.5.2.3 Flexural test after 9 months (20 Jun 2022)

The topping of the specimen is casted on its supports on 27 September 2021 and left without any additional load for almost 9 months until 15 June 2022. The fluctuation of the temperature and RH in the main test hall is recorded. The average temperature is 19°C (min: 12°C, max: 26°C) and the average RH is 50% (min: 26%, max: 79%). The instrumentation layout for data acquisition during the flexural test and test itself is executed as stated in 3.5.2.1 but loading jacks with a stroke of 250 mm are used, as contrary to the 125 mm stroke from the previous flexural test.

The loading scheme for the flexural test after 9 months as measured by the loading cells is displayed in Figure 3.26. Initially, the load is applied by load control at a speed of 10 kN/min or 20 kN/min for the last two load cycles. The specimen is preloaded to 5 kN, the load is increased to 190 kN and then unloaded to 5 kN. Subsequently, the load is increased to 250 kN and 300 kN in the next two load cycles, each followed by unloading to 5 kN. Finally, in the last cycle the load is increased to 300 kN followed by force application by displacement control at a speed of 6mm/min until failure.

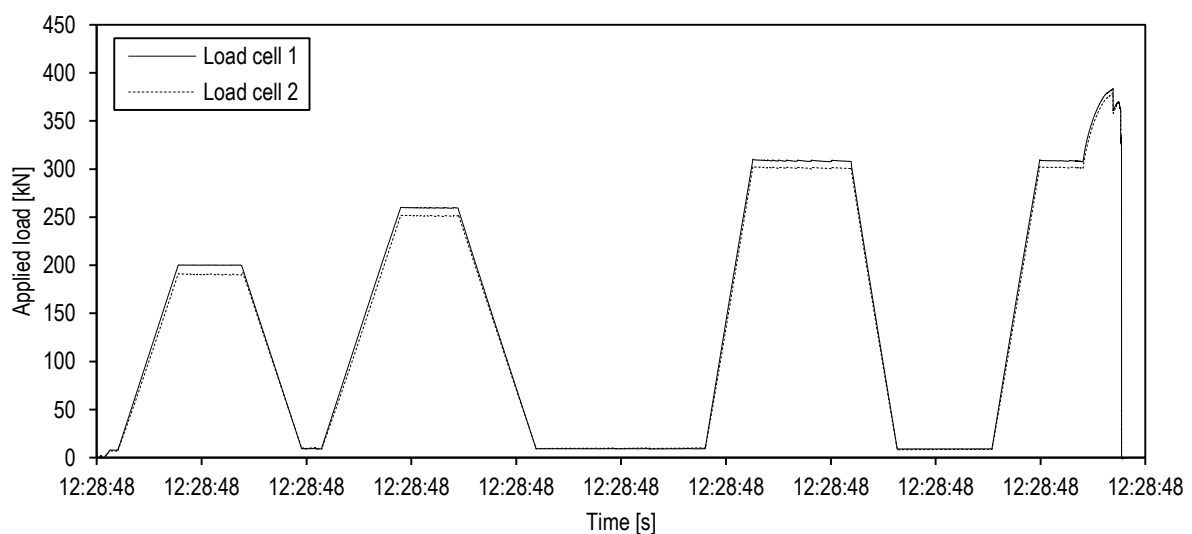


Figure 3.26. Applied load as measured by load cells (Flexural test after 9 months)

3.6 Experimental results on composite girders

3.6.1 Prestressing

3.6.1.1 Strains in prestressing strands

The length from the end of the prestressing strand to the point where the effective stress is developed, as the stress is gradually transferred from the steel to the surrounding concrete, is the transmission length. The relative strains measured by the FBG sensors along the length of the specimen for the shear test are displayed in Figure 3.27, the end of the specimens are selected as reference points. The transmission length, based on the comparison with the analytically determined concrete strains after prestressing (at the transmission length the steel and concrete fully coupled and the strains shall be equal), is included in Chapter 5.

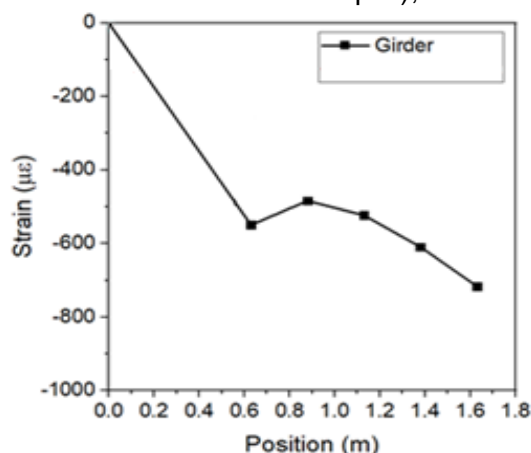


Figure 3.27. Strain change measured by FBG sensors along the length of the specimen [62]

3.6.1.2 Deformation at midspan

The prestressing force is applied to the precast girder by releasing of the tendons at an age of 2.5 days. The length change and camber is measured at an age of 3 and 7 days. The length change is composed by three components: 1) elastic deformation due to prestressing, 2) autogenous and drying shrinkage, and 3) creep behavior under stresses caused by prestressing. The measurements of the camber are displayed in Table 3.14 and were performed by Haitsma Beton for the specimens from September, 17 2021 [59].

Table 3.14. Measured deformations of precast girders after prestressing

Quantity	Units	Specimen 1		Specimen 2		Specimen 3	
		3 days	7 days	3 days	7 days	3 days	7 days
L_0	mm	7355		7355		7350	
L_f	mm	7344	7342	7340	7340	7341	7340
ΔL	mm	11	13	15	15	9	10
ε	$\mu\varepsilon$	1496	1768	2039	2039	1224	1361
Camber	mm	11	17	11	17	13	18

Table 3.15 summarizes the deformations of precast girders produced by Haitsma Beton with conventional concrete of strength class C60/75. The specimens, selected from the database of Haitsma Beton, are similar in type (HKO-300), length (7351 mm) and prestressing layout (16 tendons) to the precast girders in SCGC. Figure 3.28 displays the average values of the measured camber of the aforementioned prestressed girders in OPC concrete at ages 1 and 28 days and the camber of the three specimens in SCGC at ages 3 and 7 days.

Table 3.15. Deformation of precast girders of similar dimensions and prestress configuration produced by Haitsma Beton with conventional concrete C60/75

Type	Mold no.	Casting date	Length [mm]	Camber after demolding			Camber after 28 days				
				Calculated value [mm]	Measuring date	Measured [mm]	Deviation [mm]	Calculated value [mm]	Measuring date	Measured [mm]	Deviation [mm]
HKO	3	04/01/2021	7351	13.8	05/01/2021	11	-2.8	22.6	24/02/2021	12	-10.6
HKO	4	04/01/2021	7351	13.8	05/01/2021	10	-3.8	22.6	24/02/2021	13	-9.6
HKO	4	05/01/2021	7351	13.8	06/01/2021	7	-6.8	22.6	24/02/2021	12	-10.6
HKO	3	05/01/2021	7351	13.8	06/01/2021	9	-4.8	22.6	24/02/2021	12	-10.6
HKO	4	06/01/2021	7351	13.8	07/01/2021	7	-6.8	22.6	24/02/2021	11	-11.6
HKO	3	06/01/2021	7351	13.8	07/01/2021	7	-6.8	22.6	24/02/2021	12	-10.6
HKO	3	07/01/2021	7351	13.8	08/01/2021	10	-3.8	22.6	24/02/2021	13	-9.6
HKO	4	07/01/2021	7351	13.8	08/01/2021	10	-3.8	22.6	24/02/2021	13	-9.6

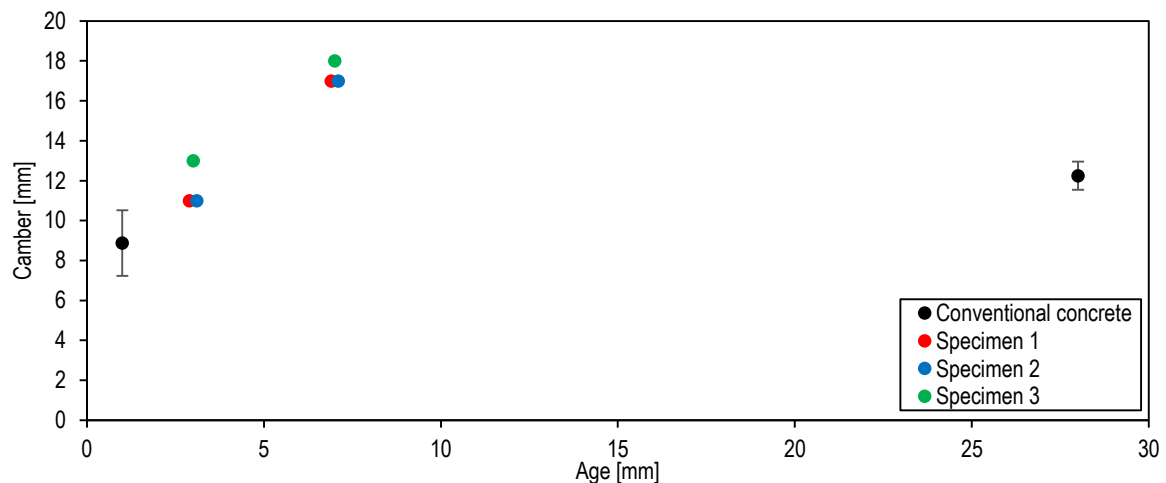


Figure 3.28. Camber of prestressed girders with SCGC and conventional concrete C60/75

The precast girder behavior is elastic during the prestressing stage and the camber is inversely proportional to the bending stiffness. As described in 3.3.3, the elastic modulus is lower for SCGC than for OPC concrete of the same strength class (OPC concrete girders are C60/75-even higher elastic modulus), hence also lower bending stiffness as the girders have the same cross-section. Therefore, the elastic component of the deformation is higher for the girders in SCGC as can be seen from the measurements at 3 days (Figure 3.28). Moreover, the creep deformation of OPC concrete is proportional to the elastic deformation, even though this may not hold for SCGC, and the creep coefficient for SCGC is also higher than for OPC concrete (3.3.4.3). Additionally, 3.3.3 reported a decrease of the elastic modulus over time for the SCGC mixture. Therefore, a higher creep deformation and lower bending stiffness explain why the camber 7 days after prestressing is higher than the 1 day and 28 day measurements for OPC concrete girders. Furthermore, as described in 2.2.3 geopolymer concrete undergoes a rearrangement of the C-A-S-H structure with increasing irreversible deformations under constant moisture loss. The visco-elastic/viscoplastic response of geopolymer concrete explains why the camber of geopolymer concrete girders continues to increase over time whereas it stabilizes for OPC concrete girders.

3.6.2 Time dependent deformation

The evolution of the internal strain in the precast girder is obtained from the FBG measurements before the mechanical tests. The sensors measure strain change and the first measurement after installation of the sensors before casting is the baseline for calibration.

The monitoring results (after temperature compensation) of the girder subjected to flexural test is shown in Figure 3.29. In between casting of the girder (0 days) and prestressing (2.5 days) an increase in strain is noticeable and corresponds to autogenous shrinkage since the mold is sealed during this period. A large deformation occurs after prestressing due to the elastic deformation of the specimen and at 30 days a decrease in strain is observed due to the weight of the fresh topping geopolymer concrete cast in-situ. The specimen undergoes shrinkage deformation which seems to stabilize after 60 days.

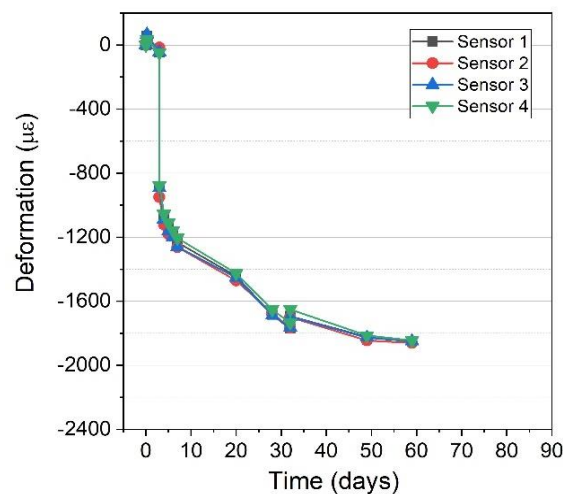


Figure 3.29. Strain at midspan of the precast girder from casting (0 days) to before test (60 days) [62]

Figure 3.30 presents a comparison of the strain measured with FBGs in the precast girder and the strain measurements from material tests as presented in Figure 3.13 (3.3.4.1). Considering that the FBGs strain measurements stabilize after 60 days, the total deformation is overestimated if the findings based on material scale samples are used at structural level. The drying behavior of the SCGC girder is not sufficiently captured by the material tests as larger structures undergo less shrinkage-induced microcracking due to the size effect on drying.

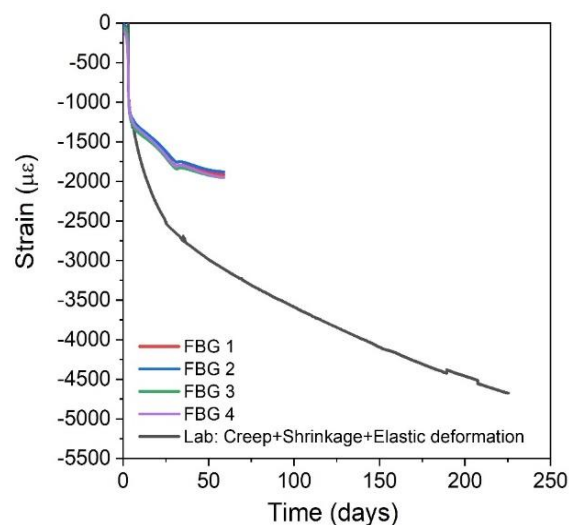


Figure 3.30. Comparison of strains: FBG monitoring and material test results [62]

3.6.3 Flexural test

3.6.3.1 Load – deflection behavior

Figure 3.31 displays the measured deflections under the points of application of loading and midspan to the average applied force by the two hydraulic jacks as recorded by the load cells. The test was stopped after reaching the maximum stroke of the hydraulic jacks and the maximum recorded average point load was 391 kN for a midspan deflection of 119 mm. The horizontal plateau when reaching about 390 kN is due to pressure losses in the hydraulic jacks when reaching the maximum stroke but is not an indication of failure since no observation of wide crack openings or crushing of concrete was observed. Consequently, the specimen was unloaded and the residual deflection is measured which is equal to 18 mm immediately after unloading and reduced to 10 mm after one hour. Furthermore, the recorded support settlements remained about 0.5% of the midspan deflections, hence no correction of the deflections at the measured points is executed since the difference can be considered negligible. Around 190 kN it is noticeable a change in the slope of the curve which indicates a change of stiffness due to the propagation of cracking.

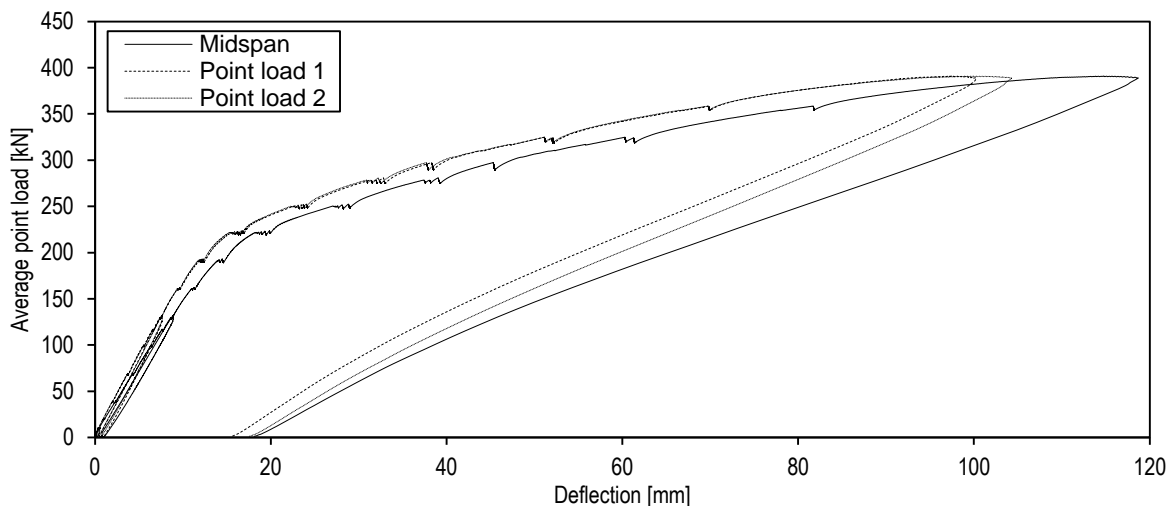


Figure 3.31. Load-deflection diagram (Flexural test)

3.6.3.2 Load – strain behavior at midspan

The concrete strains recorded at midspan by the strain stirrups are given in Figure 3.32. Two of the strain stirrups are at the top and at the bottom of the topping whereas the remaining strain stirrup is at the bottom of the precast girder. The strain stirrups are located at the level of the lower layer of prestressing tendons (bottom girder), bottom longitudinal reinforcement of the topping (bottom topping) and 10 mm from the top of the specimen (top). The first is located in the surface of the precast girder whereas the former two are located in the topping.

The compressive strain in the top layer remains smaller than the crushing strain of concrete according to EN 1992-1-1 [22] (3.5‰) which coincides with the observations that crushing in the top does not occur. Similarly to Figure 3.31, a change of slope around 190 kN is observed in the three curves which indicates cracking of the specimen in the side face. Additionally, at the maximum recorded average point load the strains in the prestressing tendons and longitudinal reinforcement in the topping are 4.1‰ and 2.2‰, respectively. According to 3.4.1, the yield strain of steel B500B and FeP1860 is 2.5‰ and 10‰ (tendons are prestressed to 6‰), respectively. The prestressing tendons are on the verge of yielding if perfect bond between the tendons and the SCGC in the girder is assumed. Furthermore, the cracking strain of SCGC in the precast girder (0.131 ‰) is reached for a load of 70 kN.

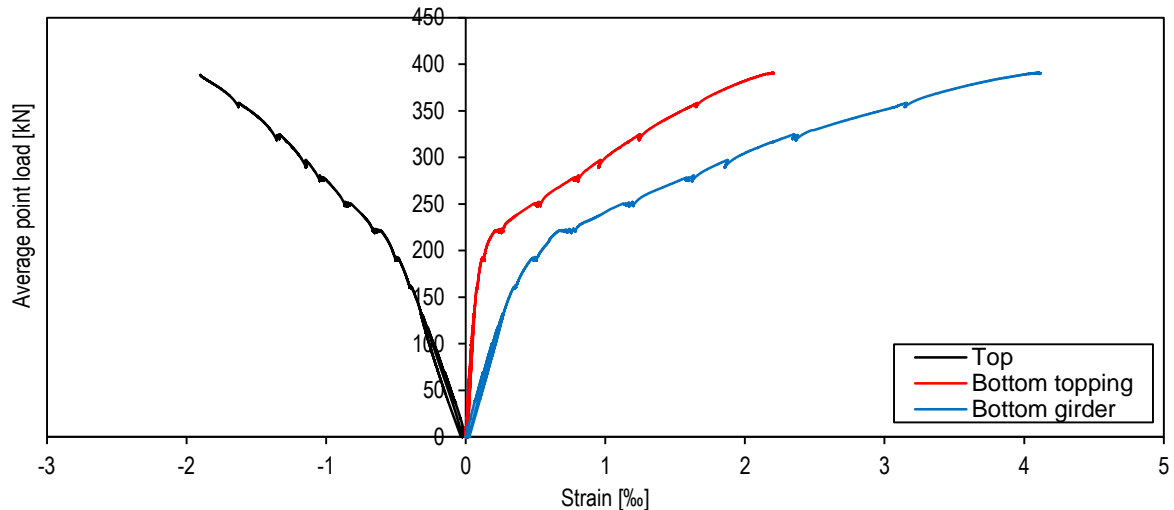


Figure 3.32. Concrete strains at midspan (Flexural test)

3.6.3.3 Cracking behavior

The crack pattern in the constant moment region at different load levels as registered from manual measurements in the LVDT side is illustrated in Figure 3.33. The upper element is the topping whereas the bottom element is the precast girder. Meanwhile, Figure 3.35 depicts the crack pattern and crack width at several load levels to illustrate the development of cracking in the specimen with DIC measurements during testing [60]. Table 3.16 reports the maximum crack width at the load levels as the displayed cracking patterns both from manual and DIC measurements. In the case of manual measurements, the average crack width is obtained from the cracks possible to be measured since cracks close to the strain stirrups could not be measured. On the other hand, the estimation of crack width from DIC is constructed from the measured von Mises strain field where strain concentrations are regarded as crack formation. Strain and displacement resolution for side analysis are 0.217% and 0.008 mm. The following observations were reported from the cracking process:

- 130 kN: minor single first crack in the precast girder at ~100 mm from the midspan.
- 160 kN: occurrence of cracks in the topping.
- 190 kN: cracking extends from the precast girder to the topping.
- 220 kN: propagation of flexural cracks and debond crack between the girder and topping.
- 250 kN: appearance of additional cracks, widening and vertical propagation of cracks.
- 280 kN: cracks outside the constant moment region, flexural shear crack under point load.
- 344 kN: no further appearance of additional cracks.

Table 3.16. Maximum crack width in the constant moment region at different load steps from DIC measurements

Load level [kN]	Topping [mm]	Precast girder [mm]
160	0.04	-
190	0.06	0.03
220	0.10	0.18
250	0.22	0.33
277	0.37	0.50
295	0.46	0.63
323	0.63	0.81
344	0.84	0.87
371	1.08	0.97
390	1.57	1.24

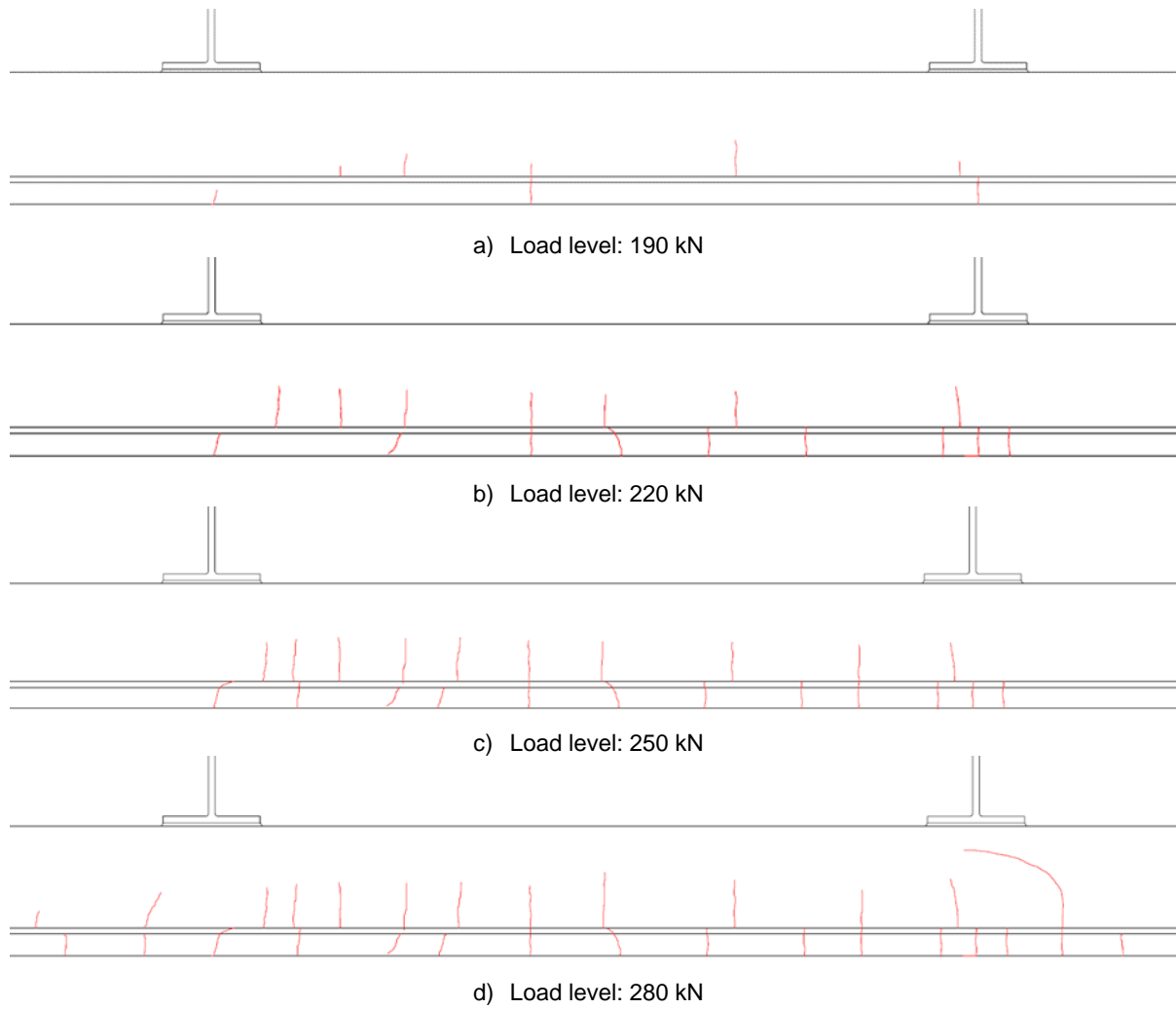


Figure 3.33. Cracking pattern in the constant moment region at different load levels (Flexural test) [61]

3.6.4 Shear test

3.6.4.1 Load – deflection behavior

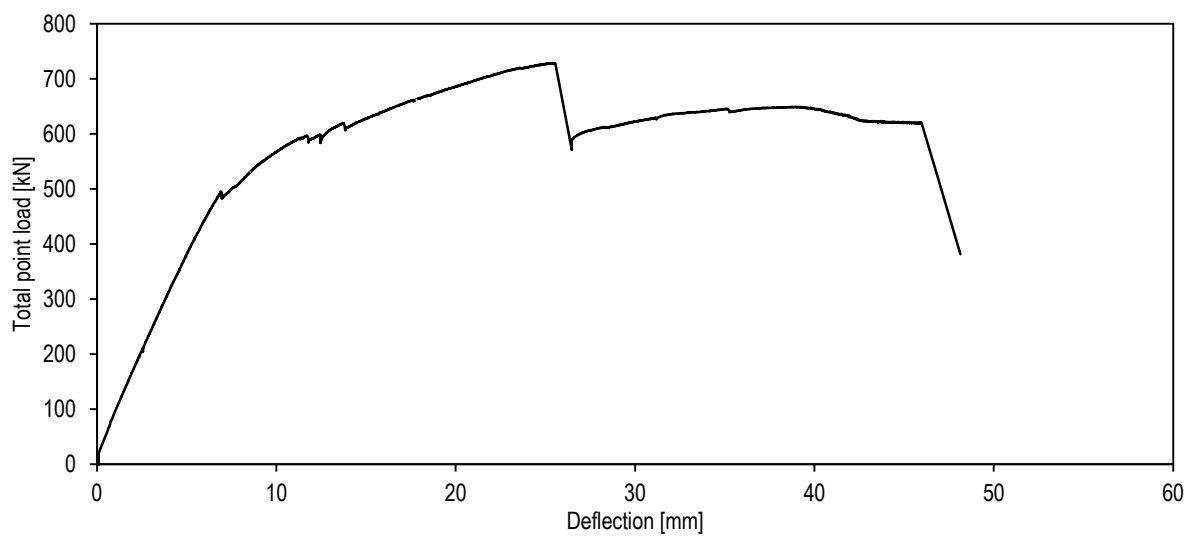


Figure 3.34. Load-deflection diagram (Shear test)

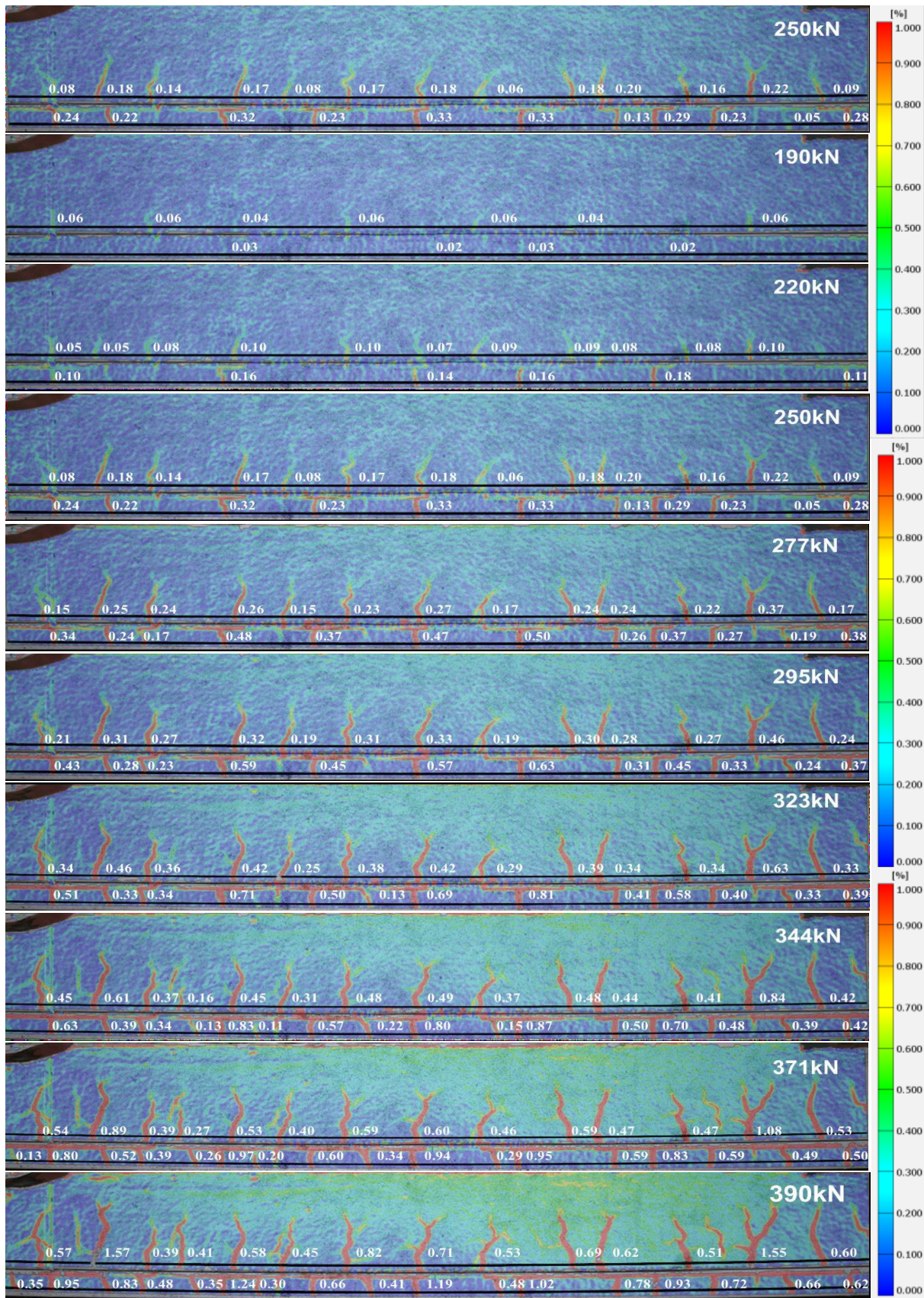


Figure 3.35. Development of cracks and crack width in side surface (Flexural test) [60]

Figure 3.34 displays the measured deflections under the point of application of loading to the total applied force by the two hydraulic jacks as recorded by the load cells. Furthermore, the recorded support settlement at the maximum load level was 1.5% of the deflection under the point of application of loading at the maximum load level, hence no correction of the deflections at the measured points is executed since the difference can be considered negligible. The maximum load is 728 kN for a vertical deformation of 25.5 mm. The failure is principally due a critical shear-flexural crack under the point of application of loading, but also by debonding of the precast girder and cast in-situ topping, slippage of the prestressing tendons and cracking of the flanges of the precast girder near the support.

3.6.4.2 Cracking behavior

The crack pattern in the shear region after failure, as registered by visual inspection, is illustrated in Figure 3.36. The upper element is the topping whereas the bottom element is the precast girder. Meanwhile, Figure 3.37 depicts the crack pattern at several load levels to illustrate the development of cracking in the specimen with DIC measurements during testing [60]. Strain and displacement resolution for side analysis are 0.112% and 0.005 mm. The following observations were reported from the cracking process:

- 140 kN: debond crack between the girder and the topping.
- 344 kN: crack initiation and increasing debond crack opening.
- 480 kN: cracking in the flange of the girder at the end of the specimen.
- 514 kN: inclined cracks in the cast in-situ topping.
- 591 kN: cracking in the precast girder and shear crack in the cast in-situ topping.
- 638 kN: propagation of the shear crack in the cast in-situ topping.
- 728 kN: load drop caused by severe delamination crack in the interface and critical shear crack in the cast in-situ topping.
- After maximum load: load increases slightly in a softening phase caused by widening of existing cracks, further cracking of the flange at the end of the specimen.

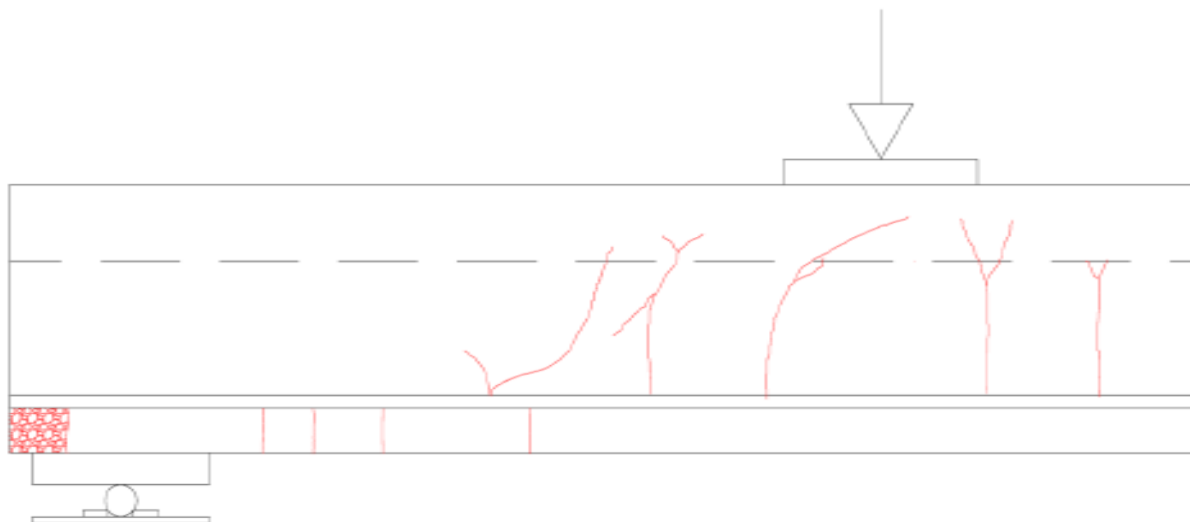


Figure 3.36. Cracking pattern after failure (Shear test) [61]

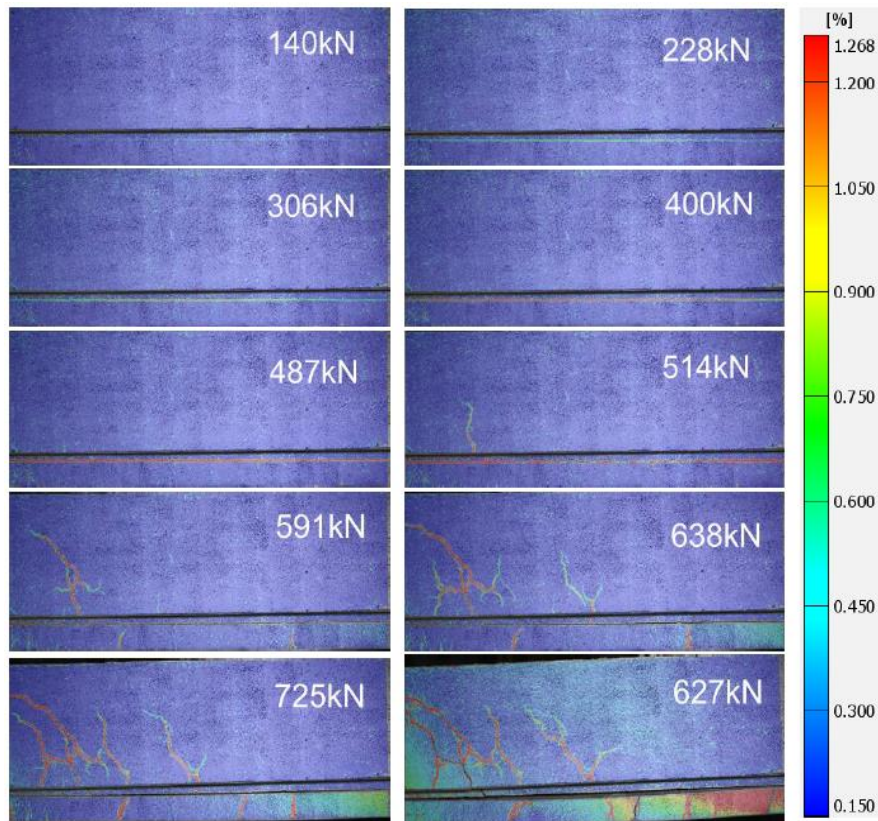


Figure 3.37. Development of cracks in side surface (Shear test) [60]

3.6.5 Flexural test after 9 months

3.6.5.1 Load – deflection behavior

Figure 3.38 displays the measured deflections under the points of application of loading and midspan to the average applied force by the two hydraulic jacks as recorded by the load cells. Furthermore, the recorded support settlement at the maximum load level was 0.5% of the deflection under the point of application of loading at the maximum load level, hence no correction of the deflections at the measured points is executed since the difference can be considered negligible. The maximum load is 381 kN for a vertical deformation of 141 mm.

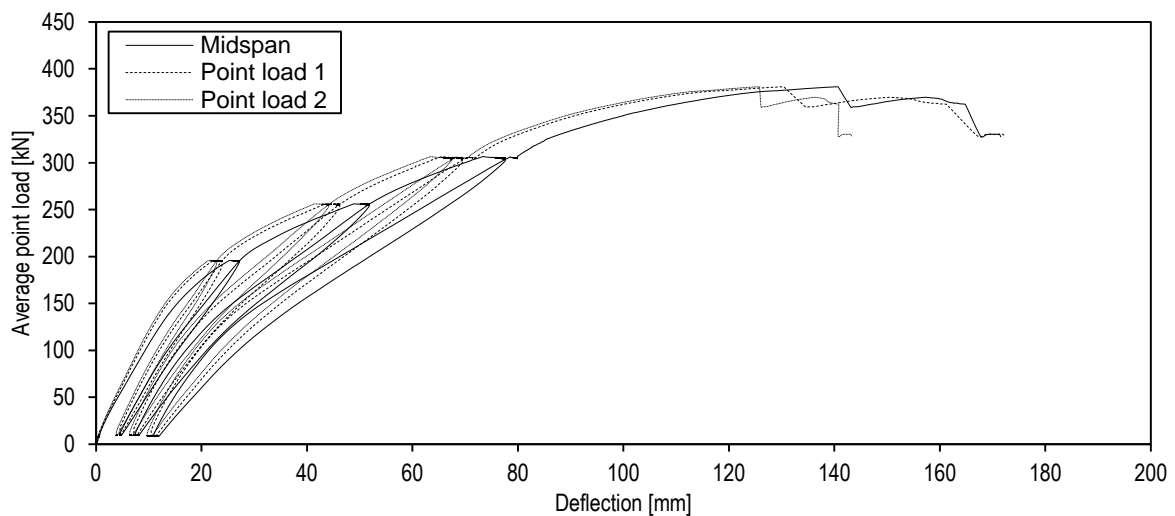


Figure 3.38. Load-deflection diagram (Flexural test after 9 months)

3.6.5.2 State of cracking after 9 months and failure mode after mechanical test

A horizontal debonding crack between the precast girder and cast in-situ topping is observed within the first weeks after casting of the topping and becomes more noticeable towards the end of the 9 months. The specimen showed few flexural cracks on the top, following the upwards deflection caused by prestressing and the creep and shrinkage effects.

The specimen after failure at the end of the flexural test is displayed in Figure 3.39. The failure is principally due anchorage failure resulting in a critical shear-flexural crack and crushing of concrete at the top of the specimen. The failure started at the maximum load of 381 kN and the specimen continued to deform further until fully fractured.



Figure 3.39. Failure of specimen subjected to flexural test after 9 months [61]

4

Flexural and shear capacity by analytical and numerical methods

This chapter describes the analytical analysis, finite element modelling, linear and nonlinear numerical analyses for the specimens subjected to 4-point bending and 3-point load mechanical tests for flexural and shear capacity, respectively. The specimens consist of an individual precast prestressed girder in geopolymer concrete with stirrups and a reinforced topping layer cast in-situ by means of geopolymer concrete delivered by a ready-mix truck.

4.1 Analytical analysis

The analytical model is based upon the design philosophy for conventional concrete structures as described in EN1990 [67] and EN 1992-1-1 [22], implementing the necessary modifications where deviations of the properties of geopolymer and conventional concrete are identified. This section provides an overview of the results, for detailed calculations refer to Appendix C.

The results provided below correspond to the elastic modulus values of scenario 2 of curing conditions with the material properties as defined in 3.3.5.

4.1.1 Principles of prestressing

Flexural members experience sagging bending moments under service loads which causes tensile stresses at the bottom fibre. Normal stresses can reach the tensile strength of concrete at relatively low load levels since the tensile strength of geopolymer concrete, as for OPC concrete, is significantly lower than the compressive strength. Prestressing is a principle to compensate the tensile normal stresses with an initial prestressing compressive force.

Consider the linear elastic response of a simply supported beam in flexure (Figure 4.1). The normal stresses and strains vary linearly over the height of the beam according to Bernoulli's hypothesis (plane sections remain plane) and superposition of actions is applicable. The beam is subjected to its self-weight (q_g) and a variable load (q_q). The stresses are proportional to the sagging bending moment and are maximum at midspan. The top fibre will experience normal stresses significantly lower than the compressive strength but the bottom fibre will start cracking as the normal stresses reach the tensile strength. An eccentric compressive force (P_m) is applied to counteract the tensile stresses in the bottom fibre by generating high compressive stresses at the bottom and small tensile stresses at the top. The resultant stress distribution under service loads is small (or zero) compressive stresses at the bottom fibre which prevents cracking. Nevertheless, the tensile and compressive stresses still need to remain below a limit value during the operation of prestressing and during service.

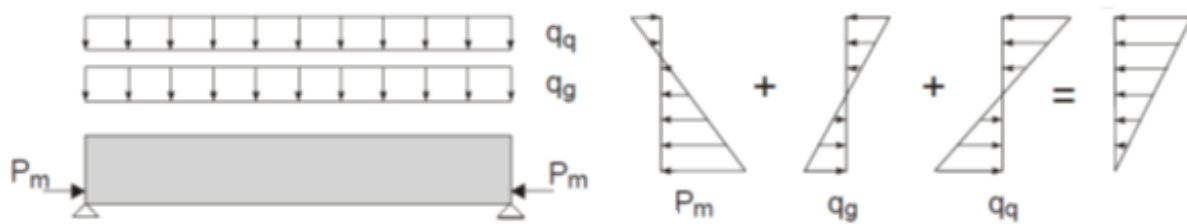
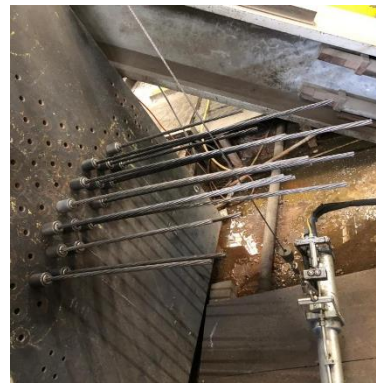


Figure 4.1. Stresses in the midspan of a statically determinate beam subjected to prestressing (P_m), permanent (q_g) and variable loading (q_q) [68]

The prestressing force is applied by pre-tensioned steel (Figure 4.2). High-strength steel tendons are positioned inside the molds, tensioned and anchored at the end, and concrete is poured. Afterwards, when the concrete has hardened and reached a certain strength, the tendons are released from the fixed points and cut at the ends.



a) Tendons inside the molds



b) Tendons anchored at the end



c) Demolding and release of tendons



d) Cutting of tendons at the ends

Figure 4.2. Pre-tensioning process

The prestressing force is transmitted from the tendons to the concrete by bond stresses over a certain distance called transmission length (l_{pt}) which depends on the type of tendons and magnitude of the initial stress. Immediately after prestressing, the element shortens as the force is transmitted to the concrete (Figure 4.3) which changes the stresses in the steel and concrete. The reduction of stresses in the tendons caused by the elastic deformation of concrete at tendon level is called elastic losses.

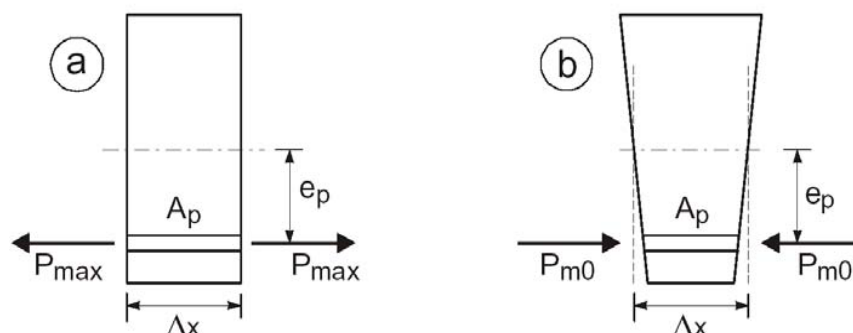


Figure 4.3. Pre-tensioning of concrete: a) before and b) after tensioning [68]

Prestress losses due to deformations and decrease in stresses occurring in the long-term need to be accounted for in the design stage as the prestressing has to limit the tensile stresses during the service lifetime of the structure. The time-dependent prestress losses are:

- Creep of concrete: increase in deformations under sustained loading by the distortion of the gel structure and the pore stresses. The magnitude of the creep deformation $\varepsilon_{cc}(t, t_0)$ is proportional to the elastic deformation by means of the creep function $\phi(t, t_0)$.
- Shrinkage of concrete: is the shortening of concrete caused by moisture loss (drying shrinkage) and under pressure in the pores of the hardened paste (autogenous shrinkage).
- Relaxation of prestressing steel: is the decrease in stresses due to the permanent deformation caused by the high stress levels in the tendons.

4.1.2 Stage I: Prestressing (2.5 days)

The prestressing force is limited by the resulting stresses in concrete from the prestressing force and other loads acting at the time of tensioning or release of prestress and is limited to:

$$\begin{aligned} \text{Maximum prestressing} \quad P_{max} &= (140 \text{ kN/str})(16 \text{ str}) &&= 2240 \text{ kN} \\ \sigma_{max} &= P_{max}/A_p &&= 1400 \text{ MPa} \end{aligned}$$

$$\begin{aligned} \text{No tensile stresses} \\ \text{top fibre} \quad -\frac{P_{m0}}{A_g} + \frac{P_{m0}e_p}{W_{gt}} - \frac{M_{Gc}}{W_{gt}} \leq 0 \end{aligned} \quad P_{m0} \leq 6205 \text{ kN}$$

$$\begin{aligned} \text{Limited compressive} \\ \text{stress bottom fibre} \quad -\frac{P_{m0}}{A_g} - \frac{P_{m0}e_p}{W_{gb}} + \frac{M_{Gc}}{W_{gb}} \geq -0.6f_{cm}(t) \end{aligned} \quad P_{m0} \leq 2499 \text{ kN}$$

4.1.2.1 Immediate prestress losses: elastic deformation and relaxation of the tendons

$$\begin{aligned} \text{Prestressing force} \\ \text{after losses} \quad P_{m0} &= P_{max} + \Delta P_{el} + \Delta P_{pr} &&= 2033.3 \text{ kN} \\ \sigma_{pm0} &= P_{m0}/A_p &&= 1270.81 \text{ MPa} \end{aligned}$$

$$\begin{aligned} \text{Elastic deformation} \\ \sigma_{ps} &= -\frac{P_{m0}}{A_g} - \frac{P_{m0}e_p^2}{I_g} + \frac{M_{Gc}e_p}{I_g} &&= -15.46 \text{ MPa} \end{aligned}$$

	$\varepsilon_{ps} = \sigma_{ps}/E_c$	= -0.618 ‰
	$\Delta_{el} = \varepsilon_{ps}L$	= 4.3 mm
	$\Delta P_{el} = \varepsilon_{ps}E_pA_p$	= -190.5 kN
Relaxation losses	σ_{pi}	= 1400 MPa
	ρ_{1000}	= 2.5 %
	$\mu = \sigma_{pi}/f_p$	= 0.731
	t	= 60 h
	$\Delta\sigma_{pr} = \sigma_{pi}0.66\rho_{1000}e^{9.1\mu}(t/1000)^{0.75(1-\mu)}$	= -10.15 MPa
	$\Delta P_{pr} = A_p\Delta\sigma_{pr}$	= -16.2 kN

4.1.2.2 Maximum prestressing force at the active end during tensioning and transfer

Maximum prestressing in a tendon	$\sigma_{p,max}$	= 1524.60 MPa
	$\sigma_{max} < \sigma_{p,max}$	
Maximum stress in tendon after transfer of prestressing	$\sigma_{pm0}(x)$	= 1436.25 MPa
	$\sigma_{pm0} < \sigma_{pm0}(x)$	
Maximum stress in concrete if longitudinal cracking prevented		= -21 MPa

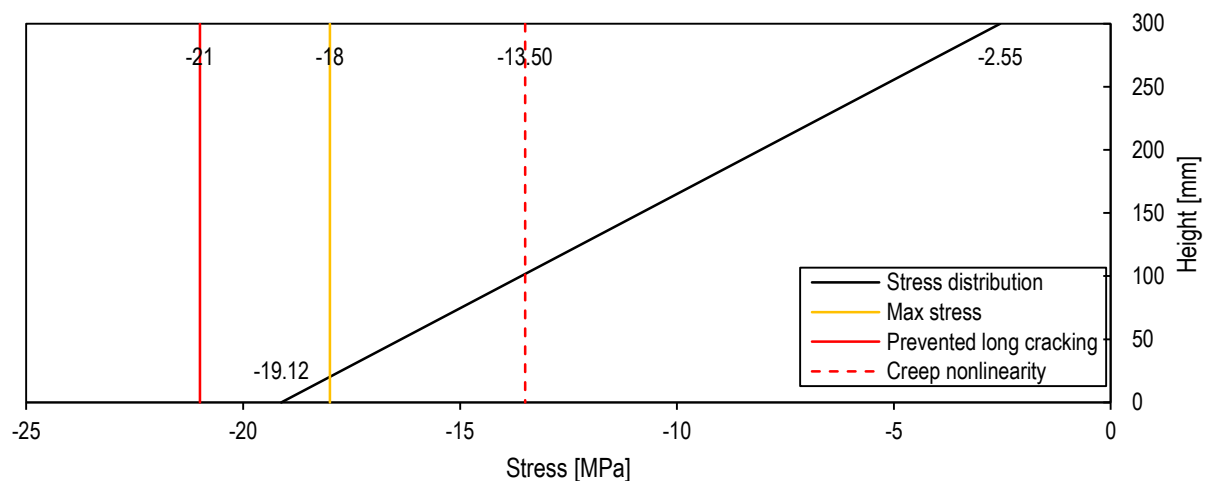


Figure 4.4. Stage I: Stress distribution

The stress distribution at midspan at time of prestressing and the limits in the concrete compressive stress according to EN 1992-1-1 5.10.2.2 [22] are displayed in Figure 4.4. The prestressing force after immediate losses causes slightly larger stresses than allowable in the bottom fibre at midspan based on the characteristic values of the SCGC C30/37 mixture. The stresses in a cross-section closer to the supports is more critical since the stresses caused by the self-weight are considerably lower and higher compressive stresses occur at the bottom fibre. Hence, 4 out of the total 16 prestressing tendons remain unbonded over a length of 1 m at each end to reduce the compressive stresses at the aforementioned cross-sections.

4.1.2.3 Transfer of prestress

Figure 4.5 displays the transfer of prestressing force from the prestressing strands to the surrounding concrete over the transmission length calculated analytically. The prestressing force of the 12 strands is transmitted from the end of the specimen whereas the remaining 4 strands detached at the ends transmit the prestressing force after the first 1 m. The prestressing force is fully transmitted after approximately 1.5 m from the end of the specimen.

Bond stress	η_{p1}	for 7-wire strands	= 3.2
	η_1	for good bond conditions	= 1.0
	$f_{cta}(t) = \alpha_{ct} 0.7 f_{ctm}(t)$		= 1.95 MPa
	$f_{bpt} = \eta_{p1} \eta_1 f_{cta}(t)$		= 6.25 MPa
Transmission length	α_1	for sudden release	= 1.0
	α_2	for 7-wire strands	= 0.19
	$l_{pt} = \alpha_1 \alpha_2 \phi \sigma_{pm0} / f_{bpt}$		= 498 mm

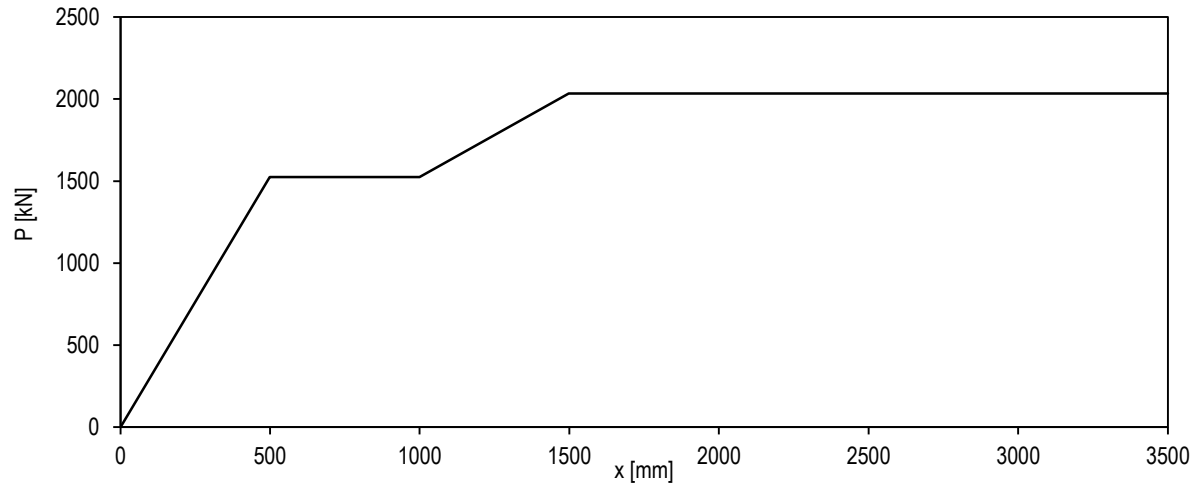


Figure 4.5. Transfer of prestressing force

4.1.2.4 Camber

The constitutive relation of bending in a Euler-Bernoulli beam is: $M = D\kappa \rightarrow \kappa = M/D$. During the stage of prestressing the behavior is linear elastic, therefore the bending stiffness D is equal to EI . In order to solve for the displacement field, the kinematic relation between the deformation and the curvature is considered.

$$\kappa = -\frac{d^2w}{dx^2} \rightarrow \frac{d^2w}{dx^2} = -\frac{M}{EI}$$

The ODE is solved by enforcing the following boundary conditions: $w(0) = w'(L/2) = 0$.

The displacement field over half of the precast girder is displayed in Figure 4.6. The camber after prestressing is equal to 13.7 mm.

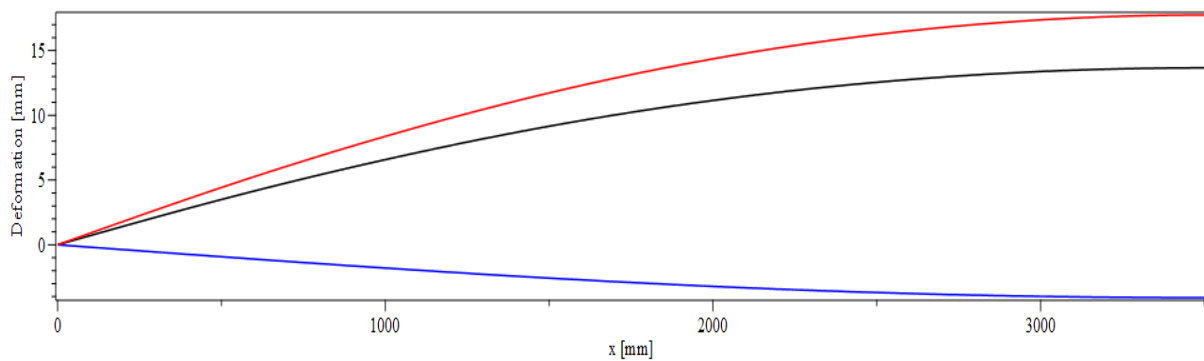


Figure 4.6. Deformation due to prestressing (red), self-weight (blue) and total (black) at 2.5 days

4.1.3 Stage II: Cast in-situ topping (30 days)

4.1.3.1 Immediate prestress losses: elastic deformation and relaxation of the tendons

Elastic losses	ΔP_{el}	= 18.2 kN
Prestressing force after elastic losses	P_{mi}	= 2051.5 kN
Relaxation losses	ΔP_{pr}	= -13.9 kN

4.1.3.2 Time dependent losses: creep and shrinkage

Autogenous shrinkage strain	ε_{ca}	= 550 $\mu\text{m}/\text{m}$
Drying shrinkage strain	$\varepsilon_{cd}(t_{30})$	= 153 $\mu\text{m}/\text{m}$
Total shrinkage strain	ε_{cs}	= 703 $\mu\text{m}/\text{m}$
Creep strain	$\varepsilon_{cc}(t_{30}, t_0)$	= 1028 $\mu\text{m}/\text{m}$

4.1.3.3 Total losses

Shrinkage losses	$\Delta\sigma_s$	= -135.40 MPa
Creep losses	$\Delta\sigma_c$	= -197.89 MPa
Relaxation losses	$\Delta\sigma_{pr}$	= -6.93 MPa
Total losses	$\Delta\sigma$	= -340.23 MPa
	ΔP	= -445.6 kN
Prestress force after losses	P_{m30}	= 1605.9 kN
	σ_{pm30}	= 1003.69 MPa
% prestress force remaining after losses		= 79%

4.1.3.4 Deformation

Creep	$\delta_{\phi, t30}$	= -25.0 mm
Total deformation	δ_{t30}	= -38.6 mm

4.1.4 Stage III: Composite section (60 days)

4.1.4.1 Immediate prestress losses: elastic deformation and relaxation of the tendons

Elastic losses	ΔP_{el}	= 18.2 kN
Prestressing force after elastic losses	P_{mi}	= 2051.5 kN
Relaxation losses	ΔP_{pr}	= -16.6 kN

4.1.4.2 Time dependent losses: creep and shrinkage

Autogenous shrinkage strain	ε_{ca}	= 550 $\mu\text{m}/\text{m}$
Drying shrinkage strain	$\varepsilon_{cd}(t_{60})$	= 332 $\mu\text{m}/\text{m}$
Total shrinkage strain	ε_{cs}	= 882 $\mu\text{m}/\text{m}$
Creep strain	$\varepsilon_{cc}(t_{60}, t_0)$	= 1271 $\mu\text{m}/\text{m}$

4.1.4.3 Total losses

Shrinkage losses	$\Delta\sigma_s$	= -169.78 MPa
Creep losses	$\Delta\sigma_c$	= -244.64 MPa
Relaxation losses	$\Delta\sigma_{pr}$	= -8.28 MPa

Total losses	$\Delta\sigma$	= -422.70 MPa
	ΔP	= -539.8 kN
Prestress force after losses	P_{m60}	= 1511.6 kN
	σ_{pm60}	= 944.78 MPa
% prestress force remaining after losses		= 74%

Figure 4.7 shows the stress distribution in the precast girder after losses. It is noticeable that creep causes the largest prestress losses.

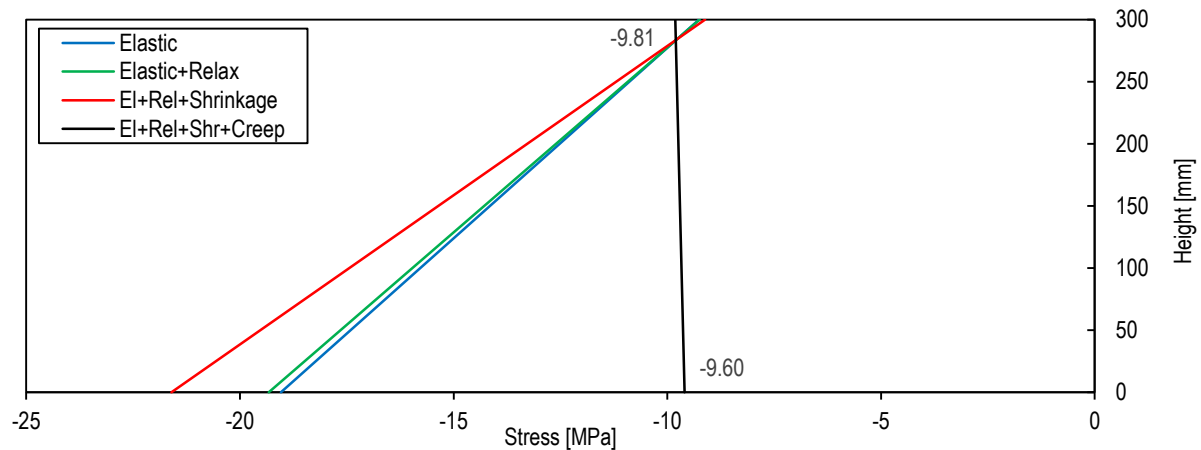


Figure 4.7. Stresses after losses at midspan t_{60}

4.1.4.4 Deformation

Self-weight topping	$\delta_{Gt}(L/2)$	= 6.8 mm
Creep	$\delta_{\phi,t60}$	= -30.9 mm
Total deformation	δ_{t60}	= -37.7 mm

4.1.5 Magnel diagram

The Magnel diagram is a set of two parallelograms constructed from the limiting tensile and compressive stress conditions on the top and bottom of a prestressed member cross section. The analysis is performed for the prestressed girder at the construction stages of prestressing (2.5 days) and in-situ casting of the topping (30 days), and for the composite section at the stage of testing (60 days). The Magnel diagram (Figure 4.8) shows graphically the possible prestress force (P_{m30}) and eccentricity combinations that will satisfy the requirements from the externally applied forces to a given bridge cross-section geometry. The limit value of the eccentricity is 55.5 mm from the construction drawings.

Stage I: Prestressing (2.5 days)

$$\begin{aligned} \text{Top fibre} \quad \mathbf{1.t} \quad & -\frac{P_{m0}}{A_g} + \frac{P_{m0}e_p}{W_{gt}} - \frac{M_{Gc}}{W_{gt}} \leq f_{ctm}(t) \\ \text{Bottom fibre} \quad \mathbf{1.b} \quad & -\frac{P_{m0}}{A_g} - \frac{P_{m0}e_p}{W_{gb}} + \frac{M_{Gc}}{W_{gb}} \geq f_{cm}(t) \end{aligned}$$

Stage II: Cast in-situ topping (30 days)

$$\begin{aligned} \text{Top fibre} \quad \mathbf{2.t} \quad & -\frac{P_{m30}}{A_g} + \frac{P_{m30}e_p}{W_{gt}} - \frac{M_{Gc} + M_{Gt}}{W_{gt}} \geq f_{cm} \\ \text{Bottom fibre} \quad \mathbf{2.b} \quad & -\frac{P_{m30}}{A_g} - \frac{P_{m30}e_p}{W_{gb}} + \frac{M_{Gc} + M_{Gt}}{W_{gb}} \leq f_{ctm} \end{aligned}$$

Stage III: Composite section (60 days)

$$\begin{aligned}
 \text{Top fibre } \mathbf{1.t^{cs}} & -\frac{P_{m60}}{A_g} + \frac{P_{m60}e_p}{W_{gt}} - \frac{M_{Gc} + M_{Gt}}{W_{gt}} - \frac{M_{Gr}}{W_{ct}} \geq f_{cm} \\
 \text{Bottom fibre } \mathbf{1.b^{cs}} & -\frac{P_{m60}}{A_g} - \frac{P_{m60}e_p}{W_{gb}} + \frac{M_{Gc} + M_{Gt}}{W_{gb}} + \frac{M_{Gr}}{W_{cb}} \leq f_{ctm} \\
 \text{Top fibre } \mathbf{2.t^{cs}} & -\frac{P_{m60}}{A_g} + \frac{P_{m60}e_p}{W_{gt}} - \frac{M_{Gc} + M_{Gt}}{W_{gt}} - \frac{M_{Gr}}{W_{ct}} \leq f_{ctm} \\
 \text{Bottom fibre } \mathbf{2.b^{cs}} & -\frac{P_{m60}}{A_g} - \frac{P_{m60}e_p}{W_{gb}} + \frac{M_{Gc} + M_{Gt}}{W_{gb}} + \frac{M_{Gr}}{W_{cb}} \geq f_{cm}
 \end{aligned}$$

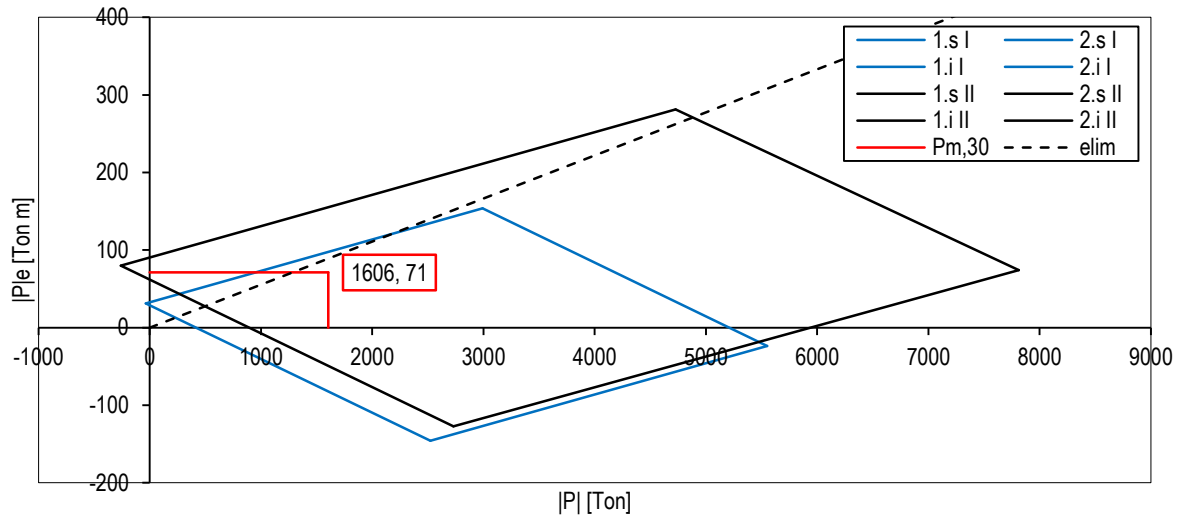


Figure 4.8. Magnel diagram

4.1.6 Flexure

The cross-section becomes composite after the cast in-situ topping has hardened and both the girder and the topping will resist the externally applied loads. The behavior of the flexural member is linear elastic until cracking of concrete after which the structural response is nonlinear due to the material nonlinearity. The stress-strain distributions at midspan and the moment-curvature relations of the composite section of a precast girder with cast in-situ topping are calculated for characteristic stages.

4.1.6.1 Zero external moment

The cross-sectional analysis is performed only considering the stresses caused by the prestressing force, self-weight is excluded.

$$\begin{aligned}
 \text{Curvature} & \kappa & = -2.03 \cdot 10^{-6} \text{ 1/mm} \\
 \text{Moment} & M & = -226 \text{ kN m}
 \end{aligned}$$

4.1.6.2 Decompression of bottom fibre

The decompression moment (M_{dec}) is the externally applied moment that will cause the tensile stresses in the bottom fibre to be equal to zero.

$$-\frac{P_{m60}}{A_g} - \frac{P_{m60}e_p}{W_{gb}} + \frac{M_{Gc} + M_{Gt}}{W_{gb}} + \eta \frac{M_{dec}}{W_{cb}} = 0$$

The stress-strain distributions due to prestressing, self-weight (G) and the externally applied moment are presented in Figure 4.9. The curvature is the slope of the strain profile.

Decompression moment $M_{dec} = 277 \text{ kN m}$
 Curvature $\kappa_{dec} = 1.62 \cdot 10^{-6} \text{ 1/mm}$

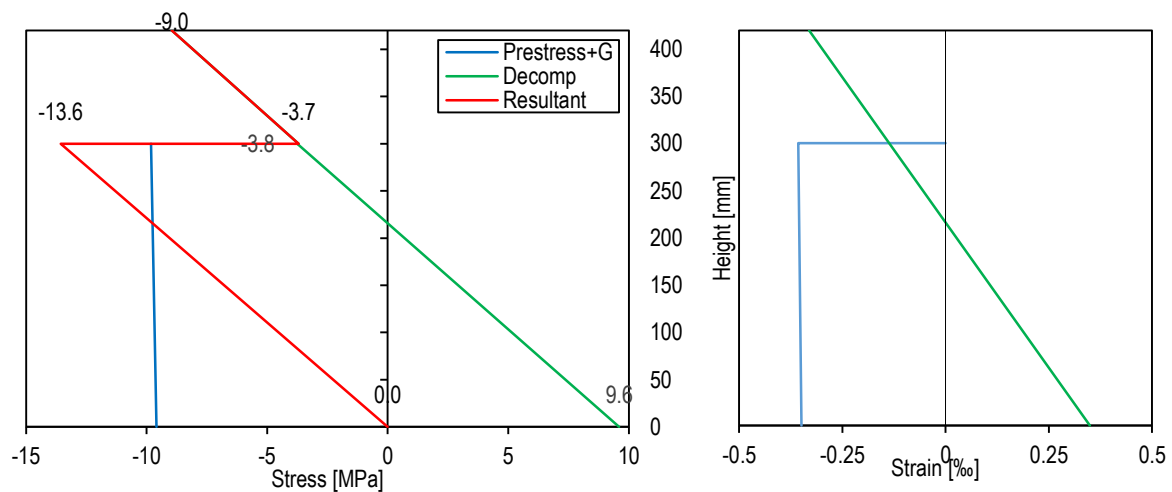


Figure 4.9. Stress and strain distribution at midspan for decompression moment

4.1.6.3 Cracking of bottom fibre

Similarly, the cracking moment (M_{cr}) is the externally applied moment that will cause the tensile stresses in the bottom fibre to be equal to the tensile strength.

$$-\frac{P_{m60}}{A_g} - \frac{P_{m60}e_p}{W_{gb}} + \frac{M_{Gc} + M_{Gt}}{W_{gb}} + \eta \frac{M_{cr}}{W_{cb}} = f_{ctm}$$

The stress-strain distributions due to prestressing, self-weight (G) and the externally applied cracking moment are presented in Figure 4.10. The cracking load is obtained by dividing the moment to the distance to the point of application of loading in the mechanical test.

Cracking moment $M_{cr} = 380 \text{ kN m}$
 Cracking load $Q_{cr} = 165.42 \text{ kN}$
 Curvature $\kappa_{cr} = 2.22 \cdot 10^{-6} \text{ 1/mm}$

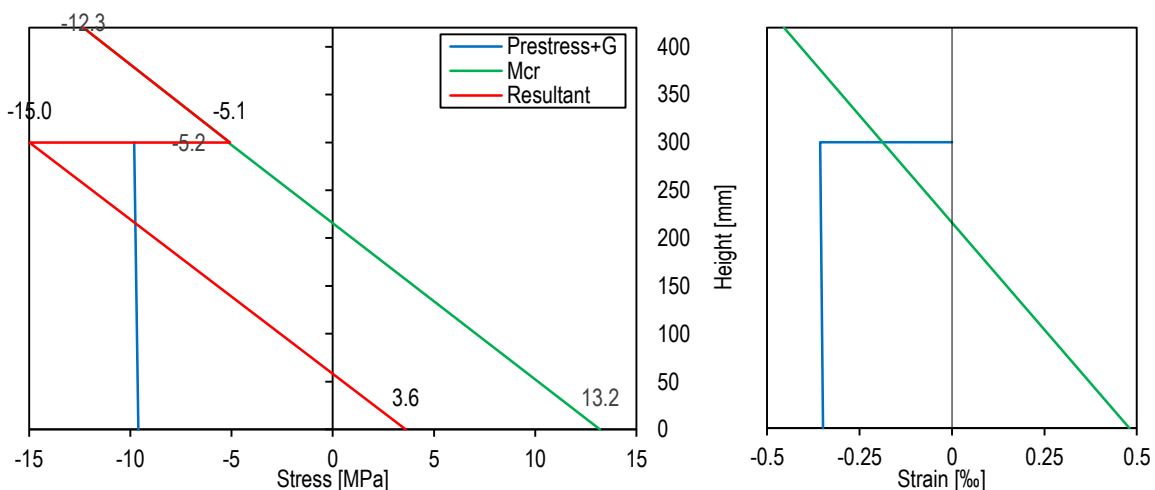


Figure 4.10. Stress and strain distribution at midspan for decompression moment

4.1.6.4 Cracked cross-section

The analysis of the cracked prestressed cross-section is performed with an iterative procedure as described by Mast [69] and Ghali & Elbrady [70].

The composite cross-section of the precast girder with cast in-situ topping is composed of four different materials. The gross transformed cross-sectional properties need to be computed. The areas of the cast in-situ topping, prestressing steel and longitudinal reinforcement are transformed to equivalent areas of precast girder SCGC by use of the modular ratio.

$$\begin{aligned} A_{gt} &= 170845.8 \text{ mm}^2 \\ I_{gt} &= 1.22 \cdot 10^9 \text{ mm}^4 \\ z_{gtb} &= 107.7 \text{ mm} \end{aligned}$$

The properties of the transformed girder cross-section vary slight in comparison to the properties of the girder presented in 3.2.3 because the reinforcement and tendons are taken into account. Next, the stress distribution over the transformed precast girder cross-section, caused by prestressing, self-weight and time-dependent effects, is computed.

$$\begin{aligned} \text{Top fibre} \quad \sigma_{tgt} &= -\frac{P_{m60}}{A_{gt}} + \frac{P_{m60}e_p z_{sgb}}{I_{gt}} - \frac{M_{Gc} + M_{Gt}}{I_{gt}} &= -8.99 \text{ MPa} \\ \text{Bottom fibre} \quad \sigma_{bgt} &= -\frac{P_{m60}}{A_{gt}} - \frac{P_{m60}e_p z_{sgb}}{I_{gt}} + \frac{M_{Gc} + M_{Gt}}{I_{gt}} &= -8.77 \text{ MPa} \end{aligned}$$

The stress gradient in the girder is extended over the full height of the composite section and the fictitious force F is calculated. This is the force that would be in the topping, if it existed, without affecting the stress distribution in the girder. Then the force F is combined with the prestressing force P_{m60} to obtain the equivalent axial force P_e in the composite section. The position of P_e is such that the stress distribution in the girder remains unaltered. Figure 4.11 show the stress distributions in the girder and the fictitious topping, and the forces in the transformed girder and composite sections. The properties of the transformed composite cross-section are calculated, the longitudinal reinforcement in the topping is also included.

$$\begin{aligned} A_{ct} &= 465417.5 \text{ mm}^2 & F &= 2669.5 \text{ kN} \\ I_{ct} &= 6.62 \cdot 10^9 \text{ mm}^4 & P_e &= 4181.1 \text{ kN} \\ z_{ctb} &= 212.7 \text{ mm} & e_{pe} &= -14.6 \text{ mm} \end{aligned}$$

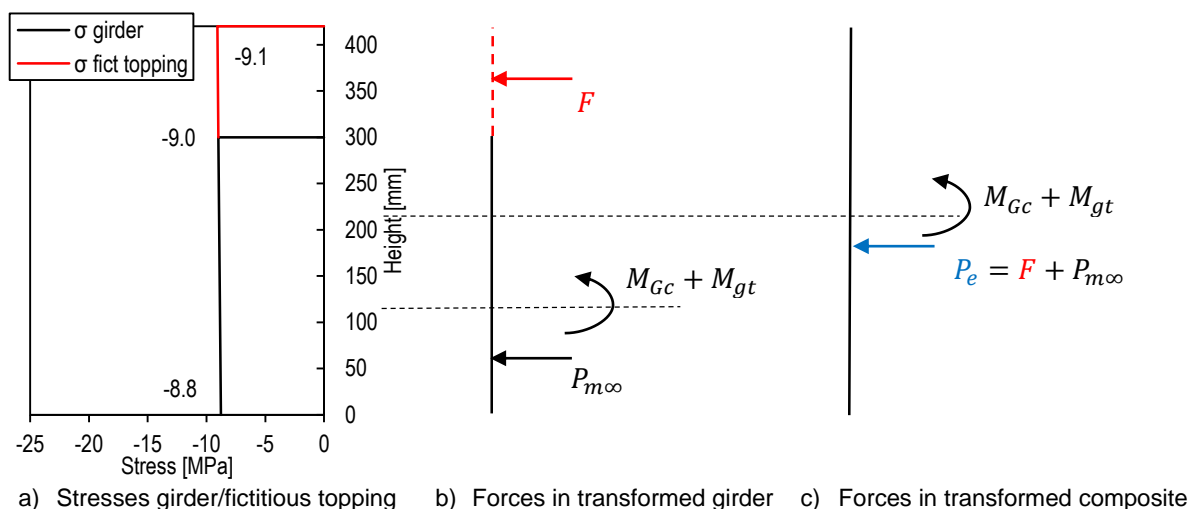


Figure 4.11. Analysis of transformed composite cross-section

The analysis of the cracked composite cross-section is an iterative procedure. An arbitrary depth of the neutral axis c is assumed and the equivalent axial force P_e is moved to the center of gravity of the cracked section by a distance y (Figure 4.12 b)). The net cracked cross-section properties are calculated. The assumed depth of the neutral axis is 332 mm which corresponds to a cracked flange of the precast girder. Instead of solving for c , the variable is the externally applied moment that would cause that depth of the neutral axis and is solved by equilibrium of forces in the cross-section.

$$M_{ext} = M_{Gc} + M_{Gt} - P_e y$$

Finally, the stress distribution in the cracked cross-section is obtained by superposition of the stress state caused by M_{ext} and the fictitious stresses related to the F (Figure 4.12 c)).

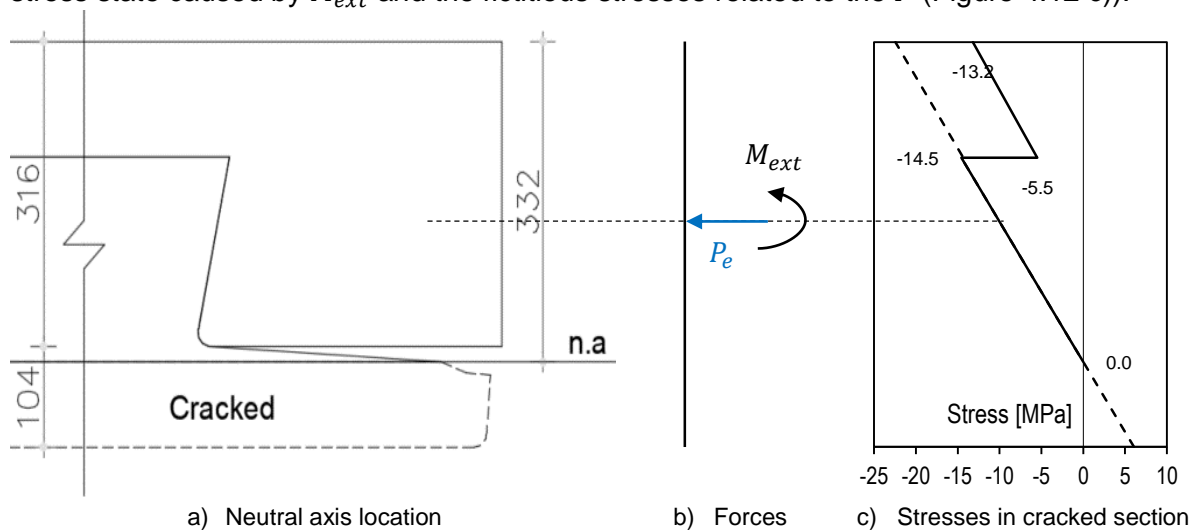


Figure 4.12. Analysis of cracked composite cross-section

$$\begin{aligned}
 A_{g,cr} &= 70695.4 \text{ mm}^2 & A_{c,cr} &= 379893.8 \text{ mm}^2 \\
 I_{g,cr} &= 2.97 \cdot 10^8 \text{ mm}^4 & I_{c,cr} &= 3.57 \cdot 10^9 \text{ mm}^4 \\
 z_{g,cr} &= 191.4 \text{ mm} & z_{c,cr} &= 250.8 \text{ mm} \\
 y &= 38 \text{ mm} \\
 M_{ext} &= 400.8 \text{ kNm} \\
 \kappa_{c,cr} &= 2.46 \cdot 10^{-6} \text{ 1/mm}
 \end{aligned}$$

4.1.6.5 Ultimate Limit State: Flexure

Structures need to meet Ultimate Limit States (ULS) requirements, one of them being the bending moment resistance. According to EN 1992-1-1 6.1 (2)P [22], the following assumptions are made for the determination of the ultimate moment resistance of prestressed and reinforced concrete cross-sections:

- Linear relationship between the strains and the distance of a fibre to the neutral axis (Bernoulli's hypothesis: plane sections remain plane).
- Strains of bonded reinforcement/tendons are equal to those of the surrounding concrete.
- No contribution to the load-carrying capacity of the tensile strength of concrete.
- The influence of prestressing is accounted as an external load acting on the structure. The contribution of prestressing steel to the moment resistance is reduced by the working prestress ($\sigma_{pu} - \sigma_{p\infty}$).
- At least part of the reinforcement steel yields and the strain in the prestressing steel is larger than the 0.1% proof stress.

The moment capacity in the cross-section at midspan is determined by an iterative calculation of equilibrium of the forces caused by the concrete, prestressing and reinforcement steel.

The compressive concrete force arises from the compressive stresses caused by the sagging moments in the top of the flexural member. As mentioned in 2.2.2.1, the stress-strain relationship for geopolymer concrete is qualitatively similar to OPC concrete, with the initial stiffness and peak load increasing with the compressive strength, hence the idealized bi-linear stress-strain relation for OPC concrete is adopted for the compression block for the present analysis (Figure 4.13). The shape of the compression block is determined by the surface factor α and center of gravity factor β , where $\alpha = 0.75$ and $\beta = 7/18$ for concrete with strength class lower or equal to C50/60. The maximum compressive (crushing) strain in concrete is taken equal to 3.5‰.

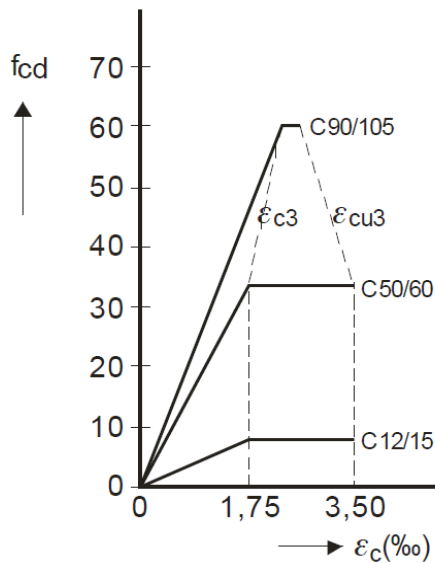


Figure 4.13. Stress-strain relationship in compression (ULS) [68]

The design stress-strain relationships for prestressing and reinforcement steel are idealized bi-linear hardening and ideal plasticity relations (Figure 4.14) as defined in EN 1992-1-1 [22] 3.2.7 and 3.3.6, respectively.

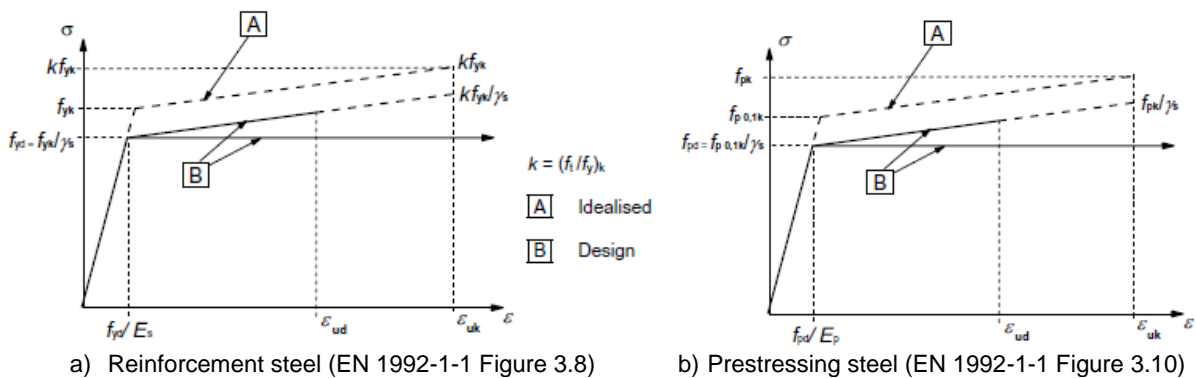


Figure 4.14 Idealized stress-strain relationships in tension and compression [22]

The force and strain distribution over the cross-section are displayed in Figure 4.15. The first step of the iterative procedure consists on assuming the height of the compression zone x_u from equilibrium of horizontal forces. It is assumed that the compression zone is smaller than the height of the cast in-situ topping over the web of the precast girder (120 mm).

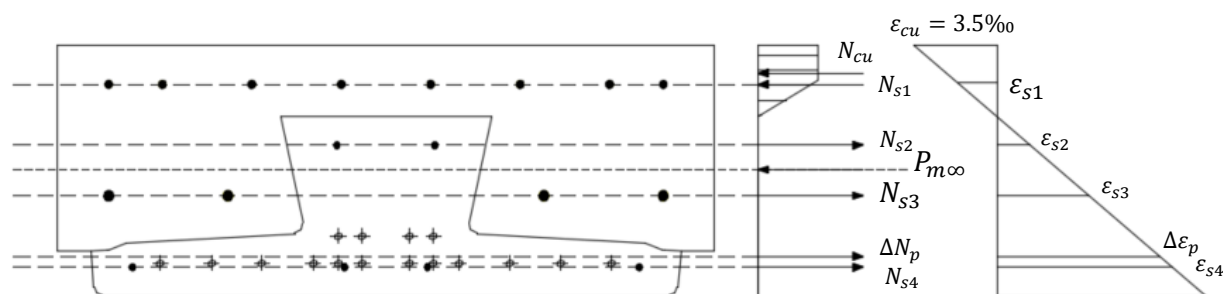


Figure 4.15. Forces and strain distribution (ULS)

$$N_{cu} = P_{m\infty} + \Delta N_p + N_{s1} + N_{s2} + N_{s3} + N_{s4}$$

$$\alpha b x_u f_c = A_p \sigma_{pm\infty} + A_p (f_p - \sigma_{pm\infty}) + A_{s1} f_{s1} + A_{s2} f_{s2} + A_{s3} f_{s3} + A_{s4} f_{s4}$$

The strain in each of reinforcement steel is determined from the geometrical relation with ε_u and x_u with the assumption of plane sections remain plane, where d_{si} is the distance to each layer of reinforcement from the top of the specimen.

$$\frac{\varepsilon_{cu}}{x_u} = \frac{\varepsilon_{cu} + \varepsilon_{si}}{d_{si}}$$

Similarly, the increase in strain in prestressing steel is calculated.

$$\frac{\varepsilon_{cu}}{x_u} = \frac{\varepsilon_{cu} + \Delta\varepsilon_p}{d_{si}} = \frac{\varepsilon_{cu} + \varepsilon_p - \varepsilon_{pm\infty}}{d_{si}}$$

The stresses in the reinforcement and prestressing steel are determined from the strains, and subsequently the forces can be obtained from the relation $N = AE\varepsilon$. The height of the compression zone is adjusted iteratively to satisfy the equilibrium of horizontal forces. Finally, the bending moment capacity is obtained by sum of moments in the cross-section. Table 4.1 displays the results of the horizontal forces for last iteration of the calculation. The height of the compression zone is found to be equal to 86.6 mm which is smaller than the maximum 120 mm. Furthermore, the three bottom layers of reinforcement steel reached the yield strain and according to EN 1992-1-1 3.2.7 b) [22] the strains do not to be checked as the horizontal branch (ideal plasticity relation) of Figure 4.14. On the other hand, the sloped relation (hardening plasticity) is used for the prestressing steel and the strains need to be checked. Figure 4.16 displays the stress and strain in the prestressing steel. The strain limit is not reached and the stress is larger than the 0.1% proof stress, hence the initial assumptions are valid.

Table 4.1. Equilibrium of horizontal forces (ULS)

	A_{si} [mm ²]		d_{si} [mm]	ε_{si} [‰]	σ [MPa]	N [kN]	a [mm]	M [kN m]
A_{s1}	8φ12	905	354	-0.831	-166	-150.4	-20.6	3.1
A_{s2}	2φ10	157	252	3.293	500	78.5	81.4	6.4
A_{s3}	4φ16	804	168	6.689	500	402.1	165.4	66.5
A_{s4}	4φ10	314	48	11.542	500	157.1	285.4	44.8
N_{cu}	--	--	--	--	--	-3213.5	-52.9	170.0
P_{m60}	--	1600	--	4.908	945	1511.6	129.1	195.2
ΔN	--	1600	66.3	10.804	1704	1214.6	267.2	324.5
					$\Sigma =$	0	$\Sigma =$	810.6
						$+P_{m60}e_p - (M_{Gc} + M_{Gt}) =$		967.6

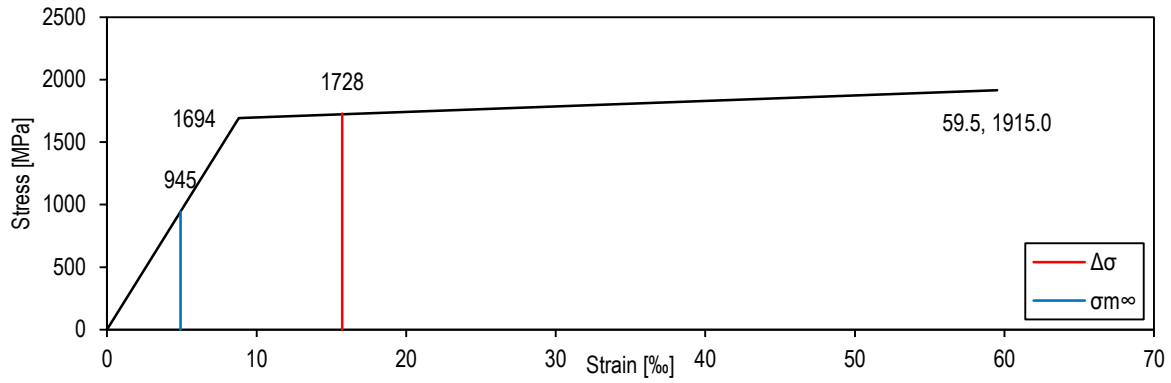


Figure 4.16. Prestressing steel stresses and strains (ULS)

Figure 4.17 displays the stress and strain distributions at midspan for ULS. The curvature is obtained from the slope of the strain diagram ($\kappa_u = 4.62 \cdot 10^{-5} \text{ 1/mm}$) and the maximum external force of the flexural test is obtained by dividing the moment capacity by the distance to the point load in the experiment and is equal to 421 kN.

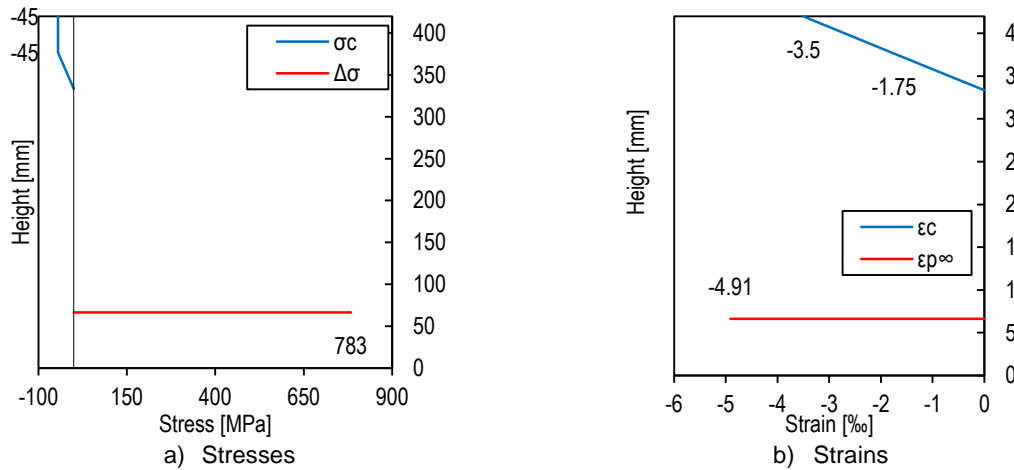


Figure 4.17. Stress and strain distributions at midspan (ULS)

4.1.6.6 Moment curvature diagram

Figure 4.18 summarizes the results of the cross-sectional analysis at decompression, cracking, cracked section and ULS, in terms of bending moment and curvature.

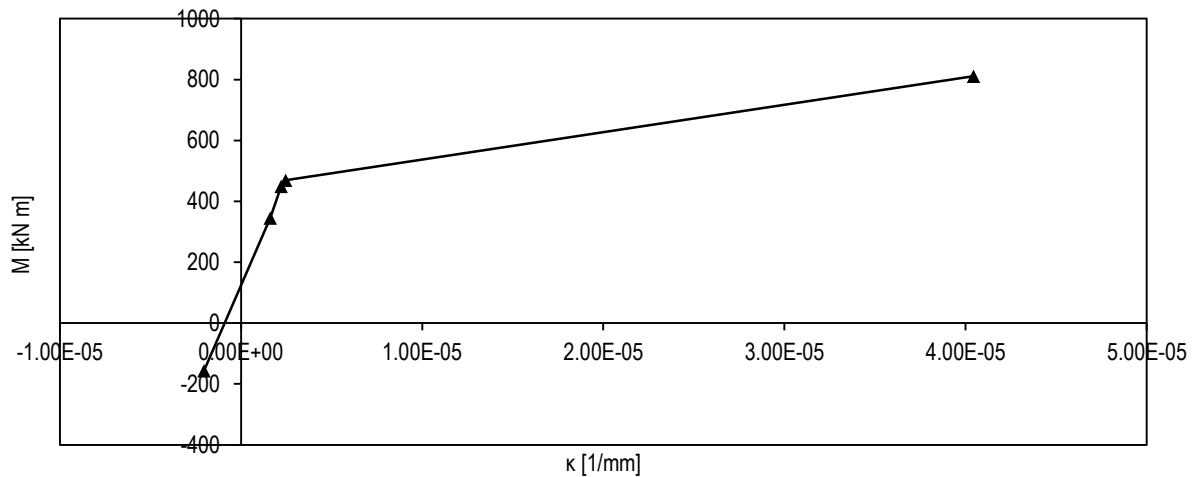


Figure 4.18. Moment curvature diagram

4.1.7 Ultimate Limit State: Shear

Structures need to meet Ultimate Limit States (ULS) requirements, one of them being the shear force resistance.

4.1.7.1 Reinforced concrete member without shear reinforcement

To illustrate the shear behavior of a prestressed member, first consider a member without shear reinforcement subjected to 4-point bending by two symmetrical point loads. The failure mechanism is called flexural-shear failure and occurs when a critical shear crack develops from a flexural crack. The critical shear crack develops over a large distance outside the constant moment region and equilibrium is lost since the concrete in compression is drastically reduced so it can no longer withstand the compressive forces.

The analysis of the capacity of members without shear reinforcement is based on empirically derived relations and in EN 1992-1-1 6.2.2 (1) [22] is given by:

$$V_{Rd,c} = \left(C_{Rd,c} k (\rho_l f_{ck})^{\frac{1}{3}} + k_1 \sigma_{cp} \right) b_w d \geq (v_{min} + k_1 \sigma_{cp}) b_w d$$

The axial stresses (σ_{cp}) in compression contribute to an increase of the shear resistance of the cross-section since the crack opening and propagation is reduced, the opposite effect is caused by tensile stresses.

4.1.7.2 Reinforced concrete member with shear reinforcement

If shear reinforcement is provided, the inclined flexural-shear crack does not result in failure and the load transfer mechanism can be described by a truss model (Figure 4.19). A tensile tie is equivalent to a number of closed stirrups, of cross-sectional area A_{sw} spaced at a distance s , that fit over a distance $z(\cot\theta + \cot\alpha)$. Where z is the internal lever arm, θ is the angle of the compression struts and α is the angle of tensile ties.

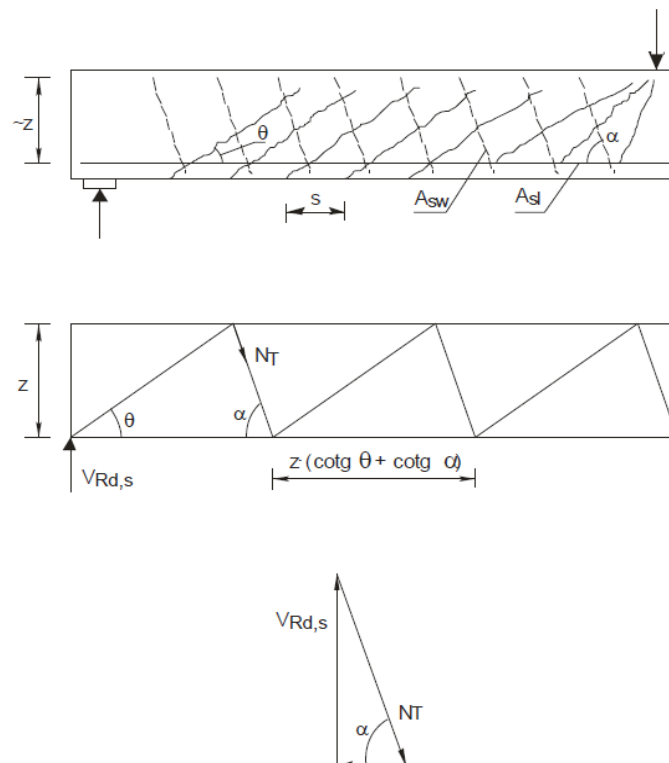


Figure 4.19. Truss model [68]

The shear force resistance is obtained from vertical equilibrium of the compressive strut, which is the same expression as EN 1992-1-1 eqn. (6.13) [22], assuming the shear reinforcement reaches the design yield strength f_{ywd} .

$$V_{Rd,s} = N_T \sin \alpha = \frac{A_{sw}}{s} z (\cot \theta + \cot \alpha) f_{ywd} \sin \alpha$$

According to Walraven & Braam [68], the calculation of the shear capacity with the aforementioned truss model is conservative for several reasons due to the idealization of the model and additional load-carrying mechanisms not accounted for (Table 4.2).

Table 4.2. Conservative assumptions of truss models

Truss model idealization	Additional load-carrying mechanisms
<ul style="list-style-type: none"> ▪ In reality, the connection between the truss elements are not perfect hinges. ▪ The load is transferred directly to the supports. 	<ul style="list-style-type: none"> ▪ Bending of longitudinal reinforcement (dowel action). ▪ Frictional forces in the cracks (aggregate interlock). ▪ Load-carrying capacity of the uncracked concrete in compression.

Two different approaches allow to consider this extra resistance, often referred as concrete capacity.

1. Dutch code NEN 6720: the total shear resistance is the sum of the concrete and steel resistances.

$$V_{Rd} = V_{Rd,c} + V_{Rd,s}$$

2. EN 1992-1-1 [22]: rotation of the compression struts caused by the amount of shear reinforcement. The failure mode is dependent on the amount of shear reinforcement; the first flexural cracks are crossed by a second crack pattern at a different angle with the beam axis which depends on the amount of shear reinforcement. The angle of the second crack pattern is smaller for smaller amounts of shear reinforcement, with a larger amount of stirrups are activated. The angle of the compression struts can be taken between $\theta = 21.8^\circ - 45^\circ$ but the lower value is often chosen for design [68].

The shear resistance of the compression strut ($V_{Rd,max}$) is determined from the dimensions in the truss model and force equilibrium (Figure 4.20).

$$b_D = z (\cot \theta + \cot \alpha) \sin \theta$$

$$V_{Rd,max} = N_D \sin \theta = \sigma_{cD} b_D b_w \sin \theta = \sigma_{cD} b_w z (\cot \theta + \cot \alpha) \sin^2 \theta$$

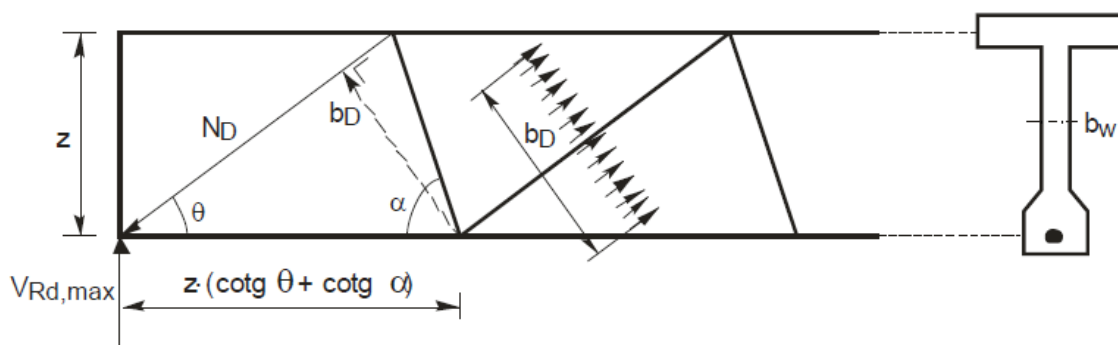


Figure 4.20. Dimensions of compression strut in truss model [68]

Nevertheless, the compressive struts are under biaxial stress conditions as stirrups cross the compressive struts in the web and exert tensile stresses which are transferred by bond stresses between the reinforcement and concrete. The effect of the tensile stresses is a reduction of the maximum compressive stress in the concrete struts as defined in EN 1992-1-1 6.2.3 (3) [22]:

$$\sigma_{cD} = \alpha_{cw} v_1 f_{cd}$$

The strength reduction factor of the concrete cracked in shear v_1 is given in the National Annex EN 1992-1-1 eqn. (6.6 N) [22] and the coefficient for the stress state in the compressive strut α_{cw} is obtained from Figure 4.21 as defined in EN 1992-1-1 6.2.3 (3) [22] where σ_{cp} is the average compressive stress in concrete at a distance less than $0.5d \cot \theta$ from the support.

$$v_1 = 0.6 \left(1 - \frac{f_{ck}}{250} \right)$$

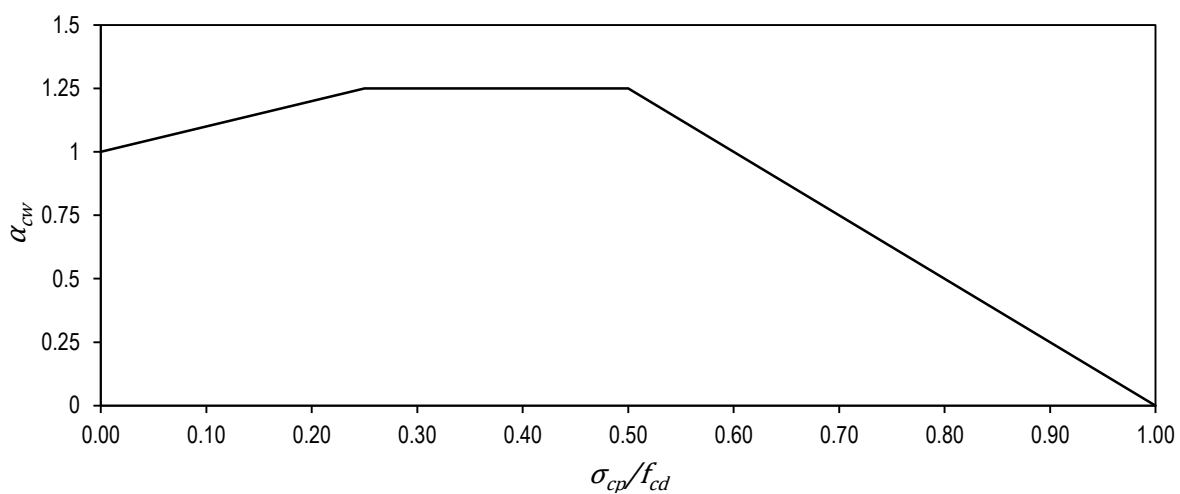


Figure 4.21. Coefficient for the stress state in the compressive strut

Finally, according to EN 1992-1-1 6.2.3 (4) [22], for members with inclined shear reinforcement the shear resistance is the smaller of $V_{Rd,max}$ and $V_{Rd,s}$. For members with vertical shear reinforcement $\cot \alpha = 0$.

4.1.7.3 Prestressed concrete member with straight tendons and without shear reinforcement

As mentioned in 4.1.7.1, the axial compressive stresses contribute to the shear capacity. For a simply supported flexural member (Figure 4.22) subjected to a point load at a distance a from the support, the stresses in the bottom fibre caused by prestressing are:

$$\sigma_b = -\frac{P_m}{A} - \frac{P_m e_p}{W_b}$$

An externally applied moment causing zero stresses in the bottom fibre M_0 is given by:

$$M_0 = \sigma_b W_b$$

The shear force at which $\sigma_b = 0$ is obtained from equilibrium of forces.

$$V_n = M_0/a$$

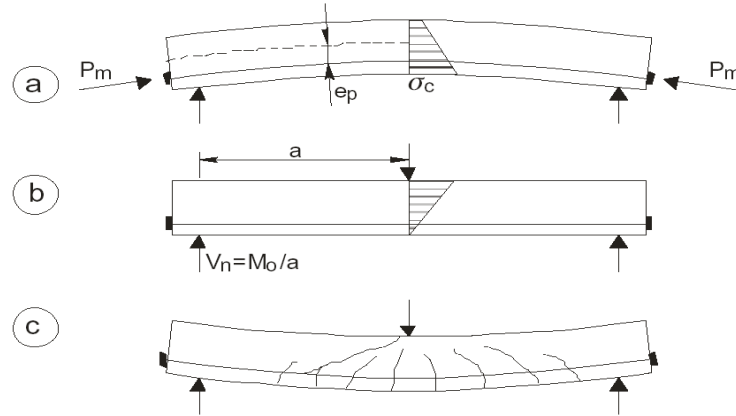


Figure 4.22. Influence of prestressing force in the shear capacity of a prestressed member without shear reinforcement [68]

Figure 4.22 b) is the same situation as a non-prestressed reinforced concrete member without stirrups, hence the shear capacity of prestressed members is increased by V_n due to prestressing [68].

For a rectangular cross-section with $d = 0.85h$ and $e_p = 0.35h$:

$$V_n = \frac{W_b}{a} \left(\frac{P_m}{A} - \frac{P_m e_p}{W_b} \right) = \frac{P_m}{a} \left(\frac{W_b}{A} + e_p \right) = \frac{31}{51} P_m \frac{d}{a} = \begin{cases} 0.15 P_m & \text{for } d/a = 0.25 \\ 0.24 P_m & \text{for } d/a = 0.40 \end{cases}$$

The value of k_1 from EN 1992-1-1 in eqns. (6.2a and b) [22] is equal to 0.15 and represents the lower bound of V_n since P_m is directly proportional to σ_{cp} .

The normal stresses caused by bending of a simply-supported flexural member due to sagging moments from self-weight and superimposed loads are maximum at midspan but are lower closer to the supports. For that reason, the bottom fibre at certain locations will remain uncracked due to the compressive stresses from prestressing compensating the normal stressed from bending. Even if flexural cracks do not occur, these regions can develop shear cracks which originate at the web where the maximum principal stress in concrete reaches the tensile strength and this failure mechanism is called tensile splitting shear failure.

$$\sigma_{1,2} = \frac{\sigma_x + \sigma_y}{2} \pm \sqrt{\left(\frac{\sigma_x - \sigma_y}{2} \right)^2 + \tau_{xy}^2}$$

$$\sigma_1 = \frac{\sigma_x}{2} + \sqrt{\frac{\sigma_x^2}{4} + \tau_{xy}^2} = f_{ctd} \quad \text{for } \sigma_y = 0$$

Consider that the shear stress is given by: $\tau_{xy} = \frac{VS}{bI}$, then:

$$V_{Rd,c} = \frac{b_w I}{S} \sqrt{f_{ctd}^2 - \sigma_x f_{ctd}}$$

EN 1992-1-1 eqn. (6.4) [22] is obtained if the influence of the transmission length is included.

$$V_{Rd,c} = \frac{b_w I}{S} \sqrt{f_{ctd}^2 + \alpha_1 \sigma_{cp} f_{ctd}}$$

The above expression is only applicable where the flexural tensile stress is smaller than $f_{ctk,0.05}/\gamma_c$ (EN 1992-1-1 6.2.2 (2) [22]).

4.1.7.4 Prestressed concrete member with straight tendons and shear reinforcement

For regions with flexural cracking, the calculation is the same as for reinforced concrete with the contribution of σ_{cp} .

For regions without flexural cracking, the uncracked lower flange contributes to the shear resistance. In principle, a lower rotation of the compression diagonal could be used but it is not contemplated in the code and the design requirements is the same as for the uncracked area [68].

4.1.8 Ultimate Limit State: Shear

The shear resistance of the composite section of a precast girder with cast in-situ topping is calculated at a distance of 1.2 m from the support, corresponding to the point of application of loading in the 3-point load mechanical test for shear capacity. Since the cross-section is a composite section, it is divided in two members for the calculation of the shear resistance (Figure 4.23). The middle element is the prestressed girder and the second element is the combination of the two edge reinforced topping elements.

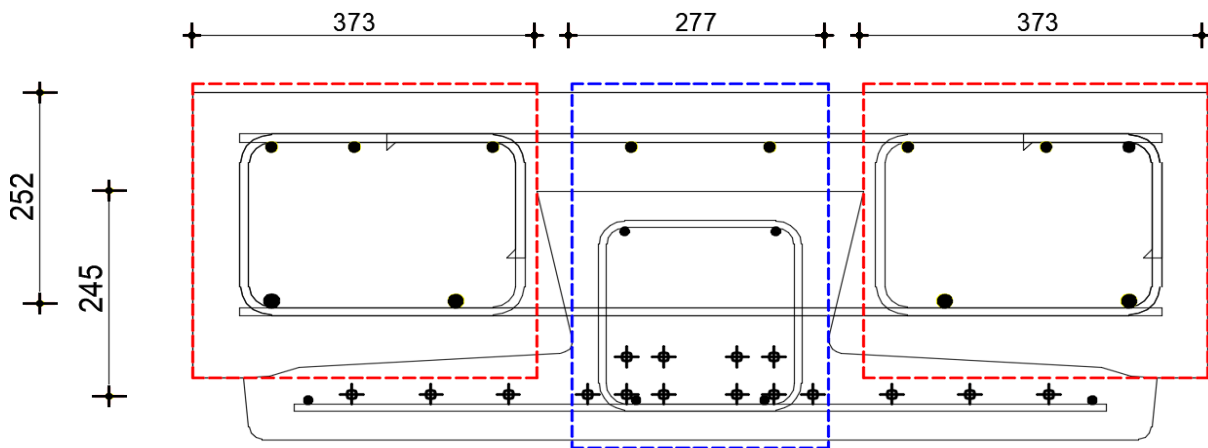


Figure 4.23. Two members for calculation of shear resistance (blue: precast girder, red: cast in-situ topping)

4.1.8.1 Precast girder

Consider that the stirrups are vertical, hence $\cot \alpha = 0$ and $\sin \alpha = 1$. Assume $z = 0.85d = 310$ mm and $\cot \theta = 2.5$. The number of stirrups over a distance of $z(\cot \theta) = 776$ mm are 6 double legged stirrups ($\phi 8$) between $x = 776 - 1551$ mm, at an average spacing of 140 mm (Figure 3.4 and Figure 3.5).

$$V_{Rd,s} = \frac{A_{sw}}{s} z(\cot \theta) f_{ywd}$$

The calculation is performed with mean values of material properties.

$$V_{Rm,s,g} = \frac{A_{sw}}{s} z(\cot \theta) f_{ywm} = \frac{2 \pi (8 \text{ mm})^2}{4 \cdot 140 \text{ mm}} 776 \text{ mm} \cdot 500 \text{ MPa} = 278.5 \text{ kN}$$

Consider that the full prestressing force of the 16 tendons is not fully transmitted to the precast girder over the distance of 1200 mm. The proportion of prestressing force transmitted can be obtained from Figure 4.5 and is equal to 85%.

$$\sigma_{cp} = 0.85 \frac{P_{m60}}{A_g} = 8.2 \text{ MPa} \quad \frac{\sigma_{cp}}{f_{cm}} = 1.5 \frac{8.2}{50} = 0.25 \rightarrow \alpha_{cw} = 1.25 \text{ (Figure 4.21)}$$

$$v_1 = 0.6$$

$$V_{Rd,max,g} = \alpha_{cw} v_1 f_{cd} b_w z (\cot \theta) \sin^2 \theta$$

$$V_{Rm,max,g} = \alpha_{cw} v_1 f_{cm} b_w z (\cot \theta) \sin^2 \theta = 1.25 \cdot 0.6 \cdot 50 \text{ MPa} \cdot 277 \text{ mm} \cdot 776 \text{ mm} \cdot \sin^2(21.8^\circ)$$

$$V_{Rm,max,g} = 1111.1 \text{ kN}$$

Finally, the shear resistance is the minimum between the resistance of the tensile and compressive struts.

$$V_{Rm,g} = \min(V_{Rm,s,g}; V_{Rm,max,g}) = 278.5 \text{ kN}$$

4.1.8.2 Cast in-situ topping

Figure 4.24 displays the inclined stirrups in the cast in-situ topping which are oriented at different angles. According to the convention of Figure 4.20, the stirrups inclined to the left are at an angle of $\alpha_1 = 79.7^\circ$, while the stirrups inclined to the right are at an angle of $\alpha_2 = 100.3^\circ$

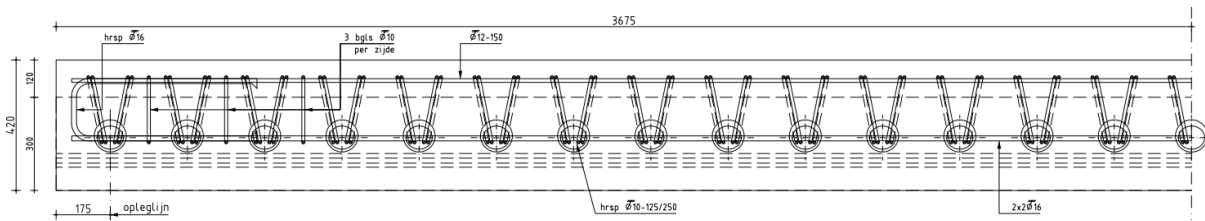


Figure 4.24. Inclined stirrups in cast in-situ topping

Assume $z = 0.85d = 214.2 \text{ mm}$ and $\cot \theta = 2.5$. The number of stirrups over a distance of $z(\cot \theta) = 535.5 \text{ mm}$ are 4 pairs of stirrups ($\phi 10$, 2 oriented to the right and 2 oriented to the left) between $x = 1071 - 1606.5 \text{ mm}$, at an average spacing of 250 mm (Figure 4.24).

$$V_{Rd,s} = \frac{A_{sw}}{s} z (\cot \theta + \cot \alpha) f_{ywd} \sin \alpha$$

The calculation is performed with mean values of material properties.

$$V_{Rm,s,t} = \frac{A_{sw}}{s} z f_{yw} ((\cot \theta + \cot \alpha_1) \sin \alpha_1 + (\cot \theta + \cot \alpha_2) \sin \alpha_2)$$

$$V_{Rm,s,t} = \frac{2\pi(10 \text{ mm})^2}{4 \cdot 250 \text{ mm}} 214.2 \text{ mm} \cdot 500 \text{ MPa} ((2.5 + \cot \alpha_1) \sin \alpha_1 + (2.5 + \cot \alpha_2) \sin \alpha_2)$$

$$V_{Rm,s,t} = 331 \text{ kN}$$

The cast in-situ topping is not prestressed, hence $\sigma_{cp} = 0 \text{ MPa}$ and $\alpha_{cw} = 1$.

$$V_{Rd,max,t} = \alpha_{cw} v_1 f_{cd} b_w z (\cot \theta + \cot \alpha) \sin^2 \theta$$

$$V_{Rm,max,t} = \alpha_{cw} v_1 f_{cm} b_w z (\cot \theta + \cot \alpha) \sin^2 \theta$$

$$V_{Rm,max,t} = 0.6 \cdot 45 \text{ MPa} \cdot 746 \text{ mm} \cdot 252 \text{ mm} (2.5 + \cot 100.3^\circ) \sin^2 100.3^\circ = 11390 \text{ kN}$$

Finally, the shear resistance is the minimum between the resistance of the tensile and compressive struts.

$$V_{Rm,t} = \min(V_{Rm,s,t}; V_{Rm,max,t}) = 331 \text{ kN}$$

Finally the overall shear resistance is the sum of the contributions of the precast girder and the cast in-situ topping: $V_{Rm} = V_{Rm,g} + V_{Rm,t} = 609.5 \text{ kN}$.

4.2 Finite element model

This section describes the linear and nonlinear analysis of the prestressed girder with cast in-situ topping in commercial FE package DIANA [71]. The 2D phased analysis intends to resemble the construction stages and the mechanical tests for flexural and shear capacity. The FE model is an abstraction of the physical structure with several assumptions, generalizations and simplifications [23]. The modelling choices are performed according to the following guidelines to ensure the quality and robustness of the analysis:

- RTD 1016-1 Guidelines for Nonlinear Finite Element Analysis of Concrete Structures [23]
- RTD 1016-3B Validation of the guidelines for NLFEA of RC structures Part Pre-stressed beams [72]
- RTD 1016-3D Validation of the guidelines for NLFEA of RC structures Part Pre-stressed beams 2 [73]

The external load is applied as increasing displacement until failure and the convergence behavior is monitored at each step. The geopolymer concrete members are modelled with plane stress elements. Either a 2D plane stress or full 3D analysis is required to capture shear failure of a concrete structure. The choice of a 2D plane stress analysis reduces the computational costs while still capturing the relevant phenomena. The reinforcement and prestressing tendons are modelled as embedded elements and are perfectly bonded to the geopolymer concrete elements. An impression of the FE model is displayed in Figure 4.25. The sources of nonlinearity are physical as material and contact nonlinearity, as follows:

- Geopolymer concrete: total strain based orthogonal rotating crack model with tension softening and compressive parabolic stress-strain relations.
- Reinforcement steel: ideal plasticity.
- Prestressing tendons: Hardening plasticity.
- Interfaces: bilinear behavior (normal direction) and linear elastic (tangential direction).

The objective is to describe (and compare with the experimental results) the load-deflection response, damage evolution, cracking stages, maximum load that can be resisted in the ultimate limit state and failure mechanism. Additionally, the sensitivity of the results with respect to the long-term material properties (and the level of prestressing force) are analyzed.

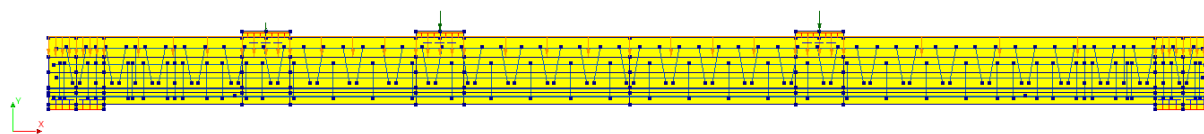


Figure 4.25. Impression of FE model

4.2.1 Geometry

The specimen composed by an individual precast girder and the cast in-situ topping is modelled in plane stress conditions. The finite element model is composed by five parts: 1) Geopolymer concrete members (precast girder and cast in-situ topping), 2) longitudinal and shear reinforcement, 3) prestressing tendons, 4) loading and support plates, and 5) interface between the specimen and the support and loading plates.

Geopolymer concrete members: The dimensions of the precast girder and topping are according Figure 3.6. The geometries of the girder and cast in-situ topping are discretized in four layers to account for the varying out-of-plane thickness and rounded edges (Figure 4.26). The thicknesses of the layers are determined such that the total cross-sectional area and second moment of area are almost equal to the geometry of the real cross-section (Table 4.3).

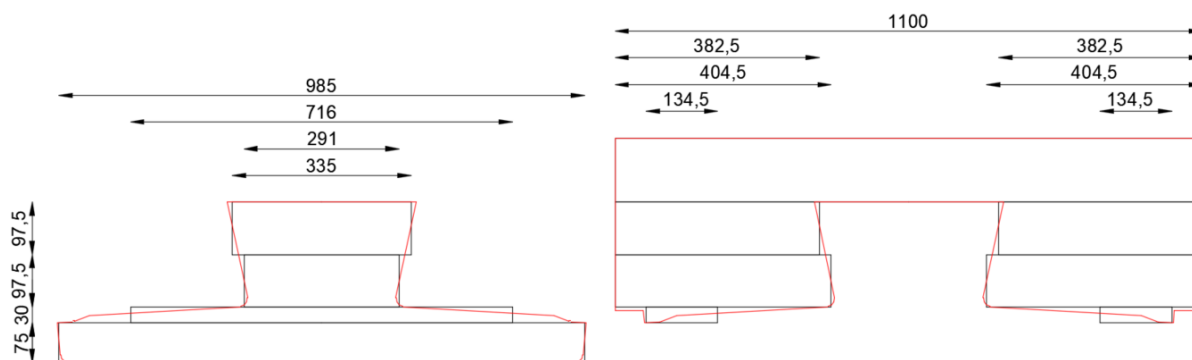


Figure 4.26. Discretization of cross-section

Table 4.3. Discretization of real geometry for plane stress FE model

Quantity	Units	Real geometry	Discretization	Error [%]
A_g	mm ²	156219	156390	0.11
z_{gb}	mm	110.5	110.4	0.05
I_g	mm ⁴	1195891367	1187432446	0.71
A_t	mm ²	294498	293535	0.33
z_{tb}	mm	269.0	269.5	0.19
I_t	mm ⁴	2716741412	2703356568	0.49

The choice for a discretized geometry instead of defining the profile of the precast girder exactly as function is in order to avoid the sharp edges which can cause numerical instability in the stiffness matrix and cause convergence issues during the analysis.

Reinforcement: The longitudinal reinforcement is modelled based on Figure 3.4 and Figure 3.6 in four layers of equivalent area (Table 4.4). The reinforcement spans over the length of the specimen with a cover of 35 and 50 mm at both ends for the precast girder and topping, respectively.

Table 4.4. Longitudinal reinforcement

Element	Layer	Distance from soffit [mm]	Reinforcement layout	Equivalent area [mm ²]
Precast girder	Bottom	252	4 ϕ 10	314.159
	Top	48	2 ϕ 10	157.079
Cast in-situ topping	Bottom	168	4 ϕ 16	804.248
	Top	354	8 ϕ 12	904.779

The shear reinforcement is modelled based on Figure 3.4 to Figure 3.7. The reinforcement is composed by two-legged ϕ 8 mm (precast girder) and pairs of one-legged ϕ 10 mm (topping) stirrups and are incorporated in the model as elements with an equivalent area (100.531 mm² and 157.079 mm², for the precast girder and topping shear reinforcement, respectively) at the corresponding spacing.

Prestressing tendons: The prestressing tendons are modelled in 3 different layers of equivalent area following the layout shown in Figure 3.3. Three layers are considered since four of the tendons in the lower layer are detached over the first 1000 mm. The top layer is at 100 mm from the soffit and is composed by 4 tendons (400 mm²). The two bottom layers are at 55 mm from the soffit and are composed by 4 tendons (400 mm²) and 8 tendons (400 mm²) for the detached and non-detached layers, respectively.

Interface: Zero thickness interface with out-of-plane thickness as the support or loading plates.

Support and loading plates: The length of the support plates is 300 mm and the thickness is 30 mm. The length and thickness of the loading plates is equal to the geometry of the bottom flange of a HEM600 spreader beam (305 mm and 40 mm, respectively). The out-of-plane thickness of the support plates are set 280 mm and the out-of-plane thickness of the loading plate are set to the thickness of the top layer (1100 mm) as the HEM600 spreader beam spans over the full width of the specimen.

4.2.2 Material models and parameters

The finite element model is composed by five different materials: 1) Geopolymer concrete, 2) longitudinal and shear reinforcement bars (B500B), 3) prestressing tendons (FeP1860), 4) interface (mortar layer), and 5) plates (structural steel).

Geopolymer concrete: The mechanical properties are as defined in Table 3.11 for the precast girder at ages 2.5 and 30 days, and the cast in-situ topping at 30 days. Modelled with a total strain based orthogonal rotating crack model. In smeared crack models, the effect of cracking is spread over an area belonging to an integration point. The cracked material is a continuum where the constitutive relations are described in terms of stresses and strains. The constitutive relation of the uncracked material is linear elastic but is replaced by an orthotropic stress-strain law when a tension cutoff is exceeded and the directions of the axes of orthotropy are in accordance to the directions of the principal stresses [74]. In smeared crack models cracks can occur anywhere in the mesh and in any direction. A crack is initiated when the maximum principal stress exceeds the tensile strength and the direction of the crack is perpendicular to the direction of the principal stress. The cracking model is denominated “rotating” because the axes of orthotropy rotate alongside the principal strains during crack propagation. A similar behavior occurs for crushing of concrete when the minimum principal strain exceeds the compressive strength. In smeared crack models, the crack width is the strain of the cracked area corresponding to an integration point over the crack bandwidth.

The parameters for the crack model are as follows. The crack bandwidth estimator according to Govindjee [75]. The fracture energy ($G_F = 0.7 \cdot 0.073 \cdot f_c^{0.18}$) is determined according to fib Model Code 2010 [27] and the compressive fracture energy is taken as ($G_C = 250G_F$) as mentioned in Nakamura [76]. The stress-strain tension softening curve is Hordijk’s relation [77] whereas the compressive relation is parabolic (Figure 4.27).

Table 4.5. Material parameters of geopolymer concrete

Quantity	Units	SCGC girder		Ready-mix topping
		2.5 days	30 days	30 days
ρ	kg/m ³	2550	2550	2550
E_c	MPa	25000	27500	27100
ν	-	0.2	0.2	0.2
f_c	MPa	40	50	45
f_{ct}	MPa	2.8	3.6	3.0
G_F	N/mm	0.0993	0.1033	0.1014
G_C	N/mm	24.82	25.83	25.35

Furthermore, a reduction model due to lateral cracking as described by Vecchio and Collins [78] with a lower bound of 0.6, confinement effects on the compressive strength according to Selby and Vecchio [79] and a reduction of the Poisson ratio dependent on damage are adopted. The material models described originate from research of the behavior of concrete, hence the applicability to the context of geopolymer concrete is to be determined.

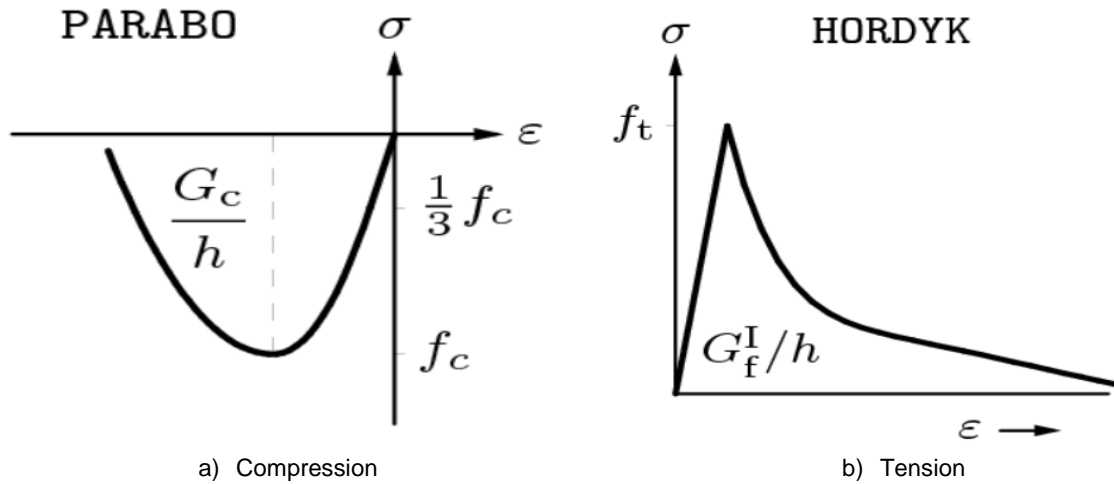


Figure 4.27. Stress-strain curves for geopolymer concrete

B500B: Ideal plasticity with the mechanical properties as defined in 3.4.2 and perfect bond between reinforcement and geopolymer concrete.

FeP1860: Hardening plasticity with mechanical properties as defined in Table 3.13 and perfect bond between reinforcement and geopolymer concrete.

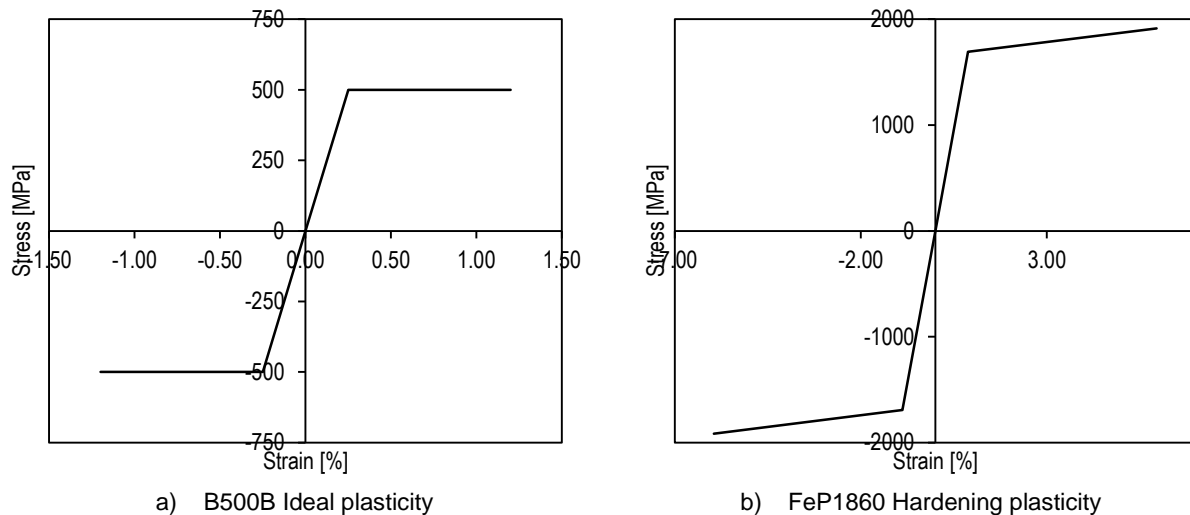


Figure 4.28. Stress-strain curves for reinforcement and prestressing steel

Steel: Linear elasticity with $E_s = 210$ GPa and $\nu = 0.3$.

Interface: The linear elastic material properties are derived from the Elastic modulus of the precast girder SCGC. A bilinear behavior for the interface in the normal direction and a linear elastic relation in the tangential direction are assumed (Figure 4.29). The normal stiffness in tension (to simulate a no tension interface) and the stiffness in tangential direction are taken as almost equal to zero.

$$k_n = \begin{cases} 10^3 \frac{E_c}{l} = 27500 \text{ N/mm}^3 & \text{for compression} \\ 10^{-3} \frac{E_c}{l} = 0.0275 \text{ N/mm}^3 & \text{for tension} \end{cases}$$

$$k_t = 10^{-3} \frac{E_c}{2(1+\nu)l} = 0.0115 \text{ N/mm}^3$$

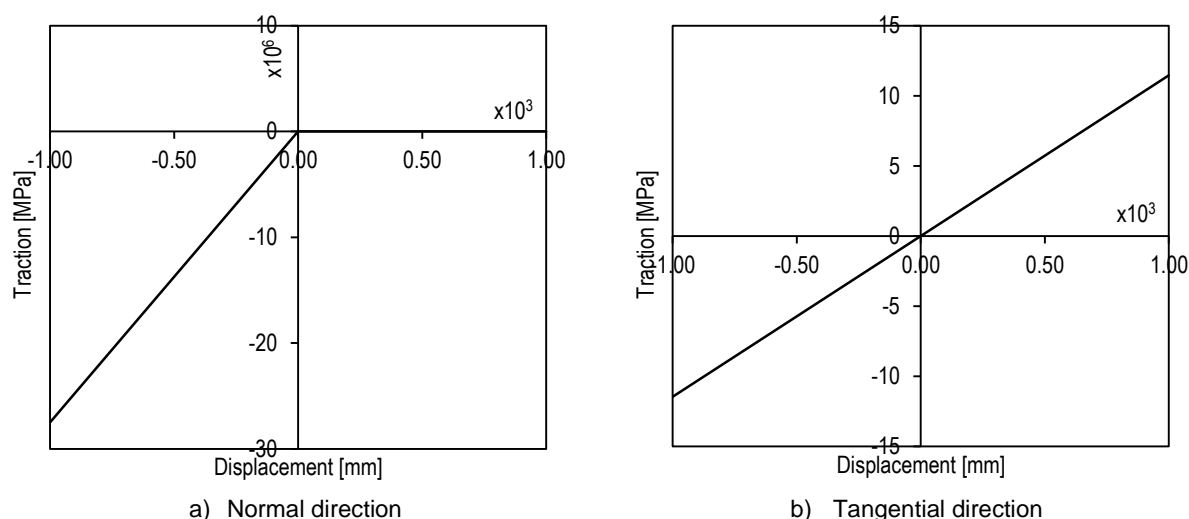


Figure 4.29. Traction-displacement curves for the interface

4.2.3 Element types and finite element mesh

The geopolymer concrete members and steel plates are modelled by a structured mesh (Figure 4.30) of 8-noded quadrilateral plane stress elements (CQ16M) based on a quadratic interpolation scheme and using a full (3x3) Gauss integration scheme. The average element size is 30 mm and the thicknesses are as defined in 4.2.1. A different color scale is used for each of the four discretized layers of both the precast girder and the cast in-situ topping.

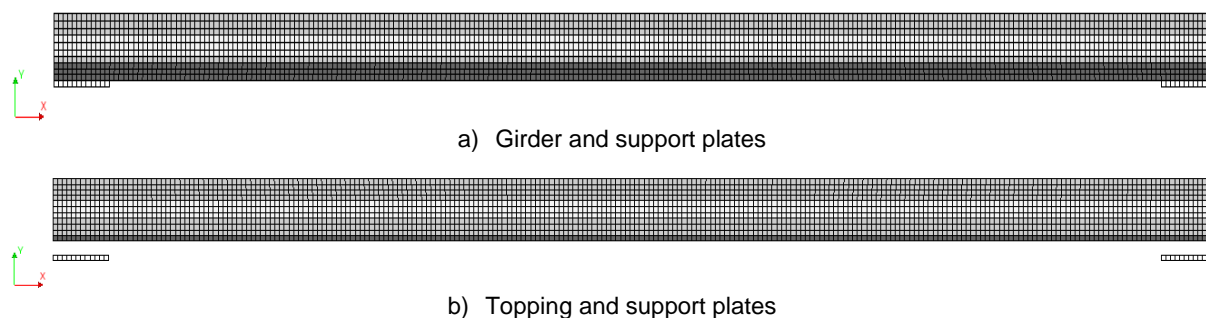


Figure 4.30. Mesh of plane stress elements

The reinforcement bars and prestressing tendons are modelled with embedded truss elements with 2-point Gauss integration along the axis of the element. Figure 4.31 displays the mesh of embedded reinforcements, only half of the beam is shown for visualization purposes. Reinforcements are embedded in the mother elements (structural plane stress elements). The strains are computed from the displacement field of the mother element which implies perfect bond with the geopolymer concrete members. Embedded reinforcements do not have degrees of freedom of their own and only have axial stiffness.

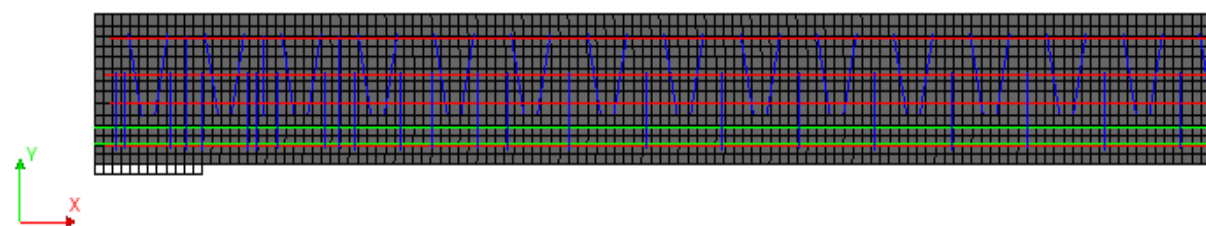


Figure 4.31. Mesh of embedded reinforcement elements longitudinal reinforcement (red), shear reinforcement (blue), prestressing tendons (green)

Table 4.6. Finite element type and mesh details

Finite element type	8-noded quadrilateral plane stress element (CQ16M)	Embedded reinforcement	3+3 nodes interface element (CL12I)
DOFs	u_x, u_y 2 DOFs per node (16 total)	-	$\Delta u_{nx}, \Delta u_{sy}$
Interpolation scheme	Quadratic	-	Quadratic
Integration scheme	Numerical integration 3x3 in plane (Gaussian)	Numerical integration 2-point (Gaussian)	Numerical integration 4-point (Newton-Cotes)
Shape dimension	2D	2D	2D
Topological dimension	2D	1D	1D
Stress components	$\sigma_{xx}, \sigma_{yy}, \sigma_{xy}$	σ_{xx}	t_{nx}, t_{sx}
Average element size [mm]	30x30	-	30
Total number of elements	5220	-	54
Total number of nodes	13445		

4.2.4 Boundary conditions

The bottom mid-nodes of the support plates are constrained vertically and horizontally to resemble the hinge and roller support conditions as shown in Figure 4.32. The translation in x and y directions are constrained in the left node (hinge) and the translation in y direction is constrained in the right node (roller).

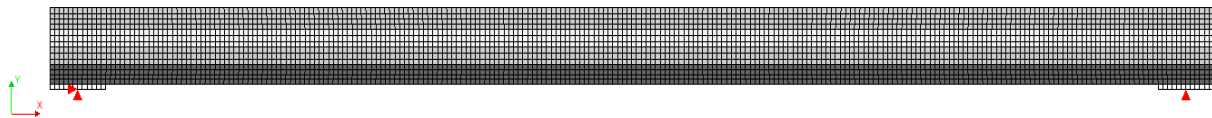


Figure 4.32. Boundary conditions

4.2.5 Phased analysis and loading

Phased analysis is performed in order to simulate the construction stages of the specimen and the varying material properties and loading conditions. At each stage different element sets of the FE model are activated according to Table 4.7 and are illustrated in Figure 4.33. The material properties are according to Table 3.11 for the corresponding age of the specimen.

Three types of loading are considered in the analysis: self-weight, prestressing and mechanical test. The self-weight is applied as a global load except for the construction stage of the cast in-situ topping where a uniformly distributed load is applied to the precast girder to account for the weight of the fresh geopolymer concrete topping. The prestressing force is gradually introduced over the transmission length and is applied simultaneously over 3 layers of tendons from the tendon stress after losses at the corresponding stage.

Table 4.7. Analysis phases

Element	Prestress	Casting of topping	Composite section	Flexural test	Shear test
Age [days]	2.5	30	60	60	60
Prestressed girder	✓	✓	✓	✓	✓
Reinforcement girder	✓	✓	✓	✓	✓
Prestressing tendons	✓	✓	✓	✓	✓
Cast in-situ topping	-	-	✓	✓	✓
Reinforcement topping	-	-	✓	✓	✓
Support plates	✓	✓	✓	✓	✓
Interface support plates	✓	✓	✓	✓	✓
Loading plates flexure	-	-	-	✓	-
Interface plates flexure	-	-	-	✓	-
Loading plate shear	-	-	-	-	✓
Interface plate shear	-	-	-	-	✓

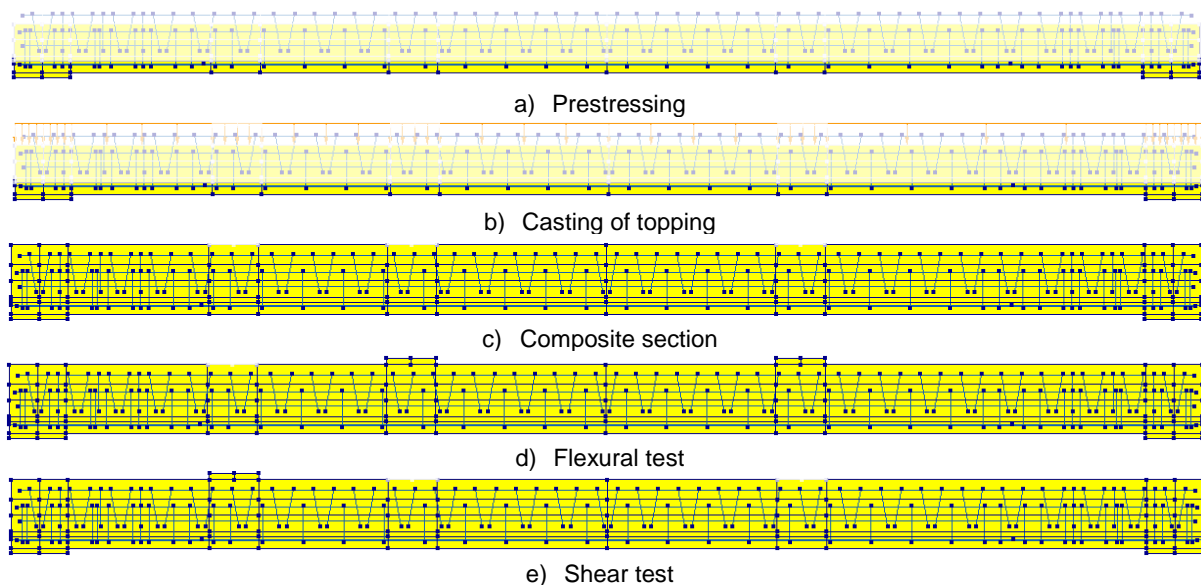


Figure 4.33. Analysis phases

4.2.6 Load increments and convergence criteria

1. Prestressing stage: the prestressed girder is subjected to its own self-weight and the prestressing force after instantaneous losses σ_{pm0} . The loads are applied in one step.
2. Casting of topping: the prestressed girder is subjected to its own self-weight, the weight of the fresh geopolymer concrete topping as uniformly distributed load and the prestressing force after losses at 30 days σ_{pm30} . The loads are applied in one step.
3. Composite section: no further loading is introduced but the stress conditions from previous phase are preserved and the additional elements are activated. This phase is a start step in the analysis to improve the convergence behavior of the model.
4. Flexural test: the load is applied in displacement control with 70 steps of 0.6 mm, 5 steps of 1.2 mm and 40 steps of 1.8 mm.
5. Shear test: the load is applied in displacement control with 200 steps of 0.25 mm.

The iteration procedure is Regular Newton-Raphson method with arc-length control with maximum 100 iterations per load step for the flexural test and 50 iterations per load step for the shear test. Force and energy norms are adopted as convergence criteria (Table 4.8). The analysis requires both norms to be satisfied but is allowed to continue if the convergence criteria are not satisfied within the set number of iterations.

Table 4.8. Convergence criteria

Norm	Tolerance
Relative out of balance force	0.01
Relative energy variation	0.001

4.3 Linear finite element analysis

Linear elastic behavior of the precast girder during prestressing is expected. This section includes the result of the LFEA in terms of deformations, stresses and strains at midspan. Figure 4.34 presents the absolute deformations of the precast girder after application of the prestressing force after immediate elastic losses and its own self-weight. The horizontal deformation includes only elastic shortening and not volume stability effects.

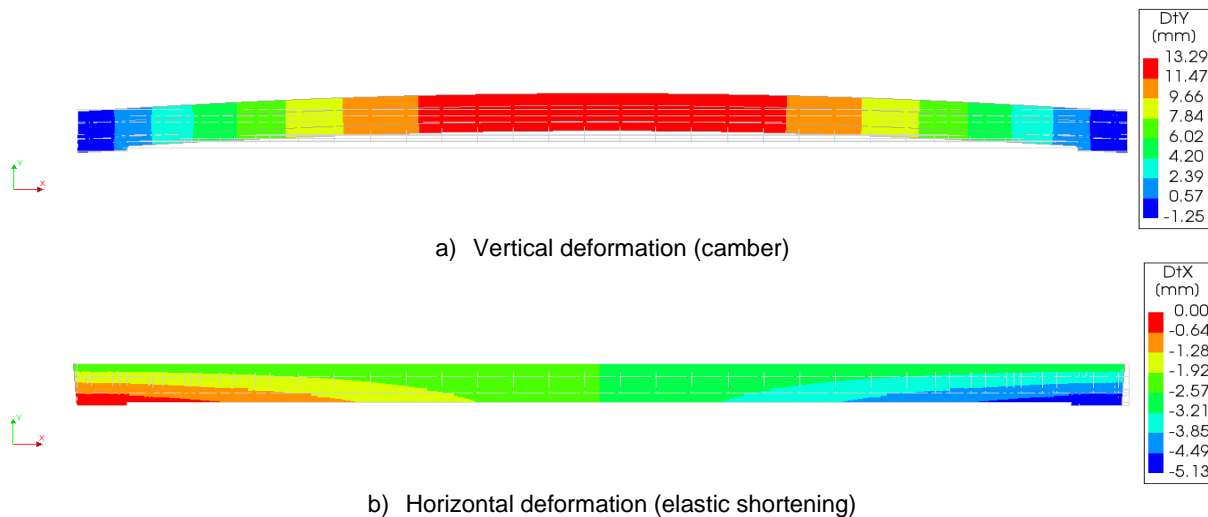


Figure 4.34. Deformation after prestressing (Scale factor: 10)

Figure 4.35 presents the stress and strains distributions of the precast girder at midspan. The labels correspond to the location of the soffit and top of the cross-section and at the centroid of the tendons. The elastic shortening is equal to $0.604‰ \cdot 7350 \text{ mm} = 4.4 \text{ mm}$.

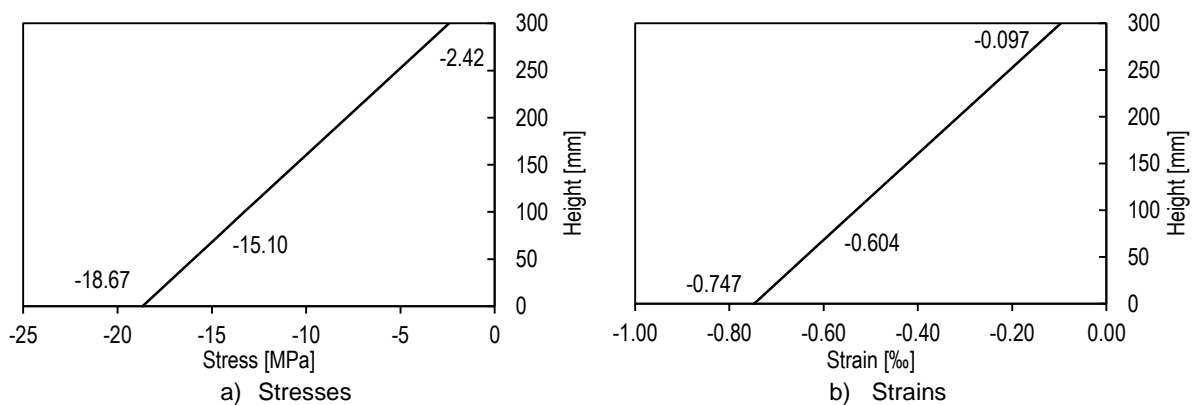


Figure 4.35. Stress and strain distributions after prestressing at midspan

4.4 Nonlinear finite element analysis

This section presents the results of the two nonlinear finite element analyses with particular emphasis in the vertical equilibrium, convergence behavior, load - deflection response, deformed meshes, stresses in the composite section at midspan, crack pattern and principal strains in concrete and strains in steel.

4.4.1 Composite section

The vertical reaction forces are symmetric at both support ends and the value of each reaction force is 40.7 kN. At this stage the applied loads correspond to the self-weight of the precast girder and the topping which adds up to 82.9 kN and 82.7 kN for the exact geometry and the approximate geometry, respectively. The error is 1.8% and 1.6% which is deemed acceptable.

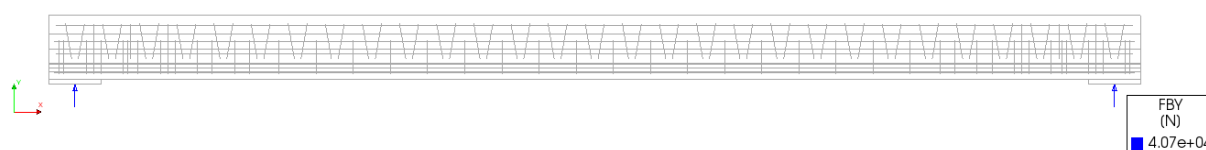


Figure 4.36. Vertical reaction forces

4.4.2 Flexural test

4.4.2.1 Convergence behavior

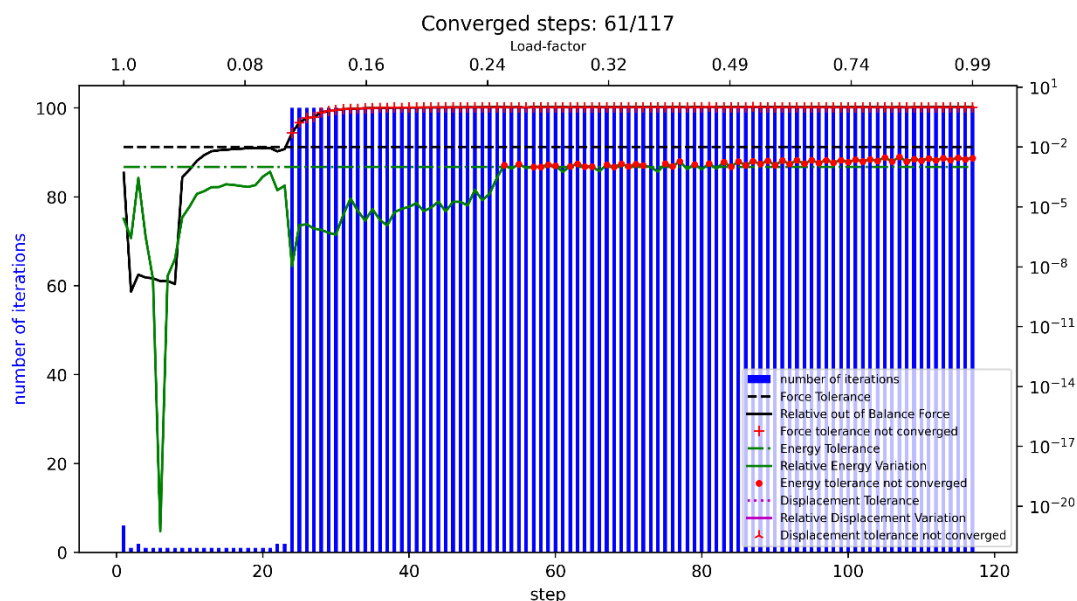


Figure 4.37. Evolution of convergence norms and number of iterations per load step

Figure 4.37 displays the number of iterations and the evolution of the relative out of balance force and relative energy variation during each load step. The dashed green and black lines indicate the energy and force tolerances, correspondingly. The first and second steps corresponds to the casting of topping and composite section phases, respectively. The next 115 steps correspond to the mechanical test phase. From this point onwards the steps mentioned refer only to the 115 steps of the mechanical tests, for global step numeration add the two initial steps. The analysis convergences in terms of both norms until step 21 with only 1 or 2 iterations in each step. At step 9 the force norm approaches the tolerance limit and after step 20 the analysis converges by means of the energy norm exclusively and the force norm no longer satisfies the tolerance for the remainder of the analysis. Between steps 50 and 80

the energy convergence norm oscillates around the tolerance, resulting in converged and non-converged steps (Figure 4.38). The non-converged steps are followed by converged steps and the energy norm is close to the tolerance, hence the results are acceptable. Nevertheless, after step 80 none of the steps converge but the behavior does not show a drastic divergent trend. The energy norm remains smaller than 0.01 which may be considered acceptable.

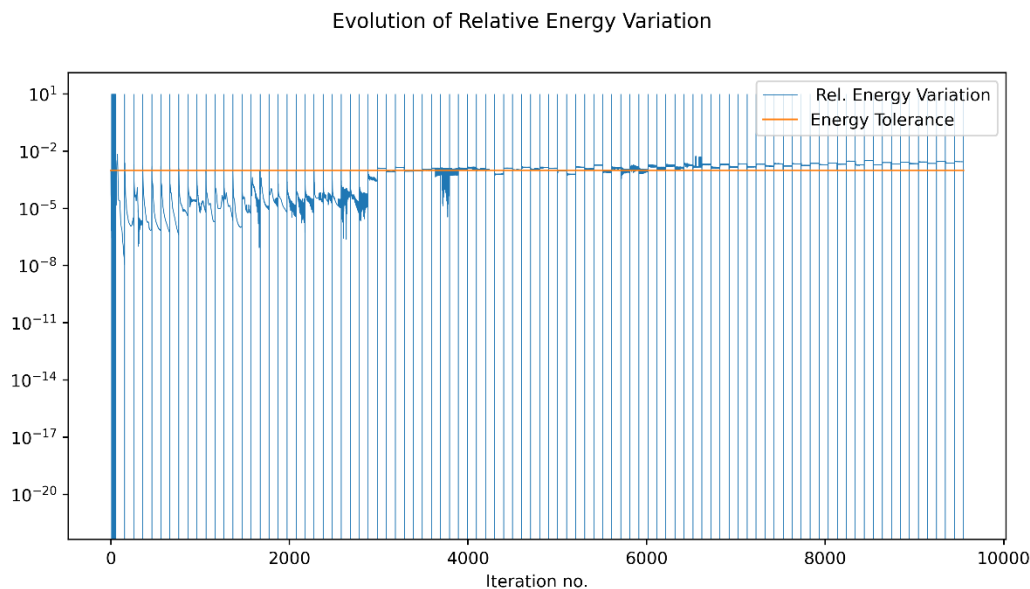


Figure 4.38. Evolution of the relative energy variation

4.4.2.2 Load – deflection

Figure 4.39 displays the load – deflection response of the beam to the prescribed deformation applied during the 4-point bending test. The deflections are obtained at the soffit of the specimen at midspan and the applied load is the average of the two loading plates. The non-converged steps are indicated with red circles. The load – deflection response shows a linear elastic behavior until the tensile strength is reached at the bottom fibre at step 17 (166 kN). Furthermore, at step 22 (199 kN) the first discrete cracks appear in the precast girder and a change of slope is noticeable which indicates a change of stiffness due to the propagation of cracking. The numerically derived load-carrying capacity is 401 kN but the curve reaches a plateau after step 94 at around 96 mm midspan deflection and 392 kN external load where the deflection increases without a significant increase in the load-carrying capacity.

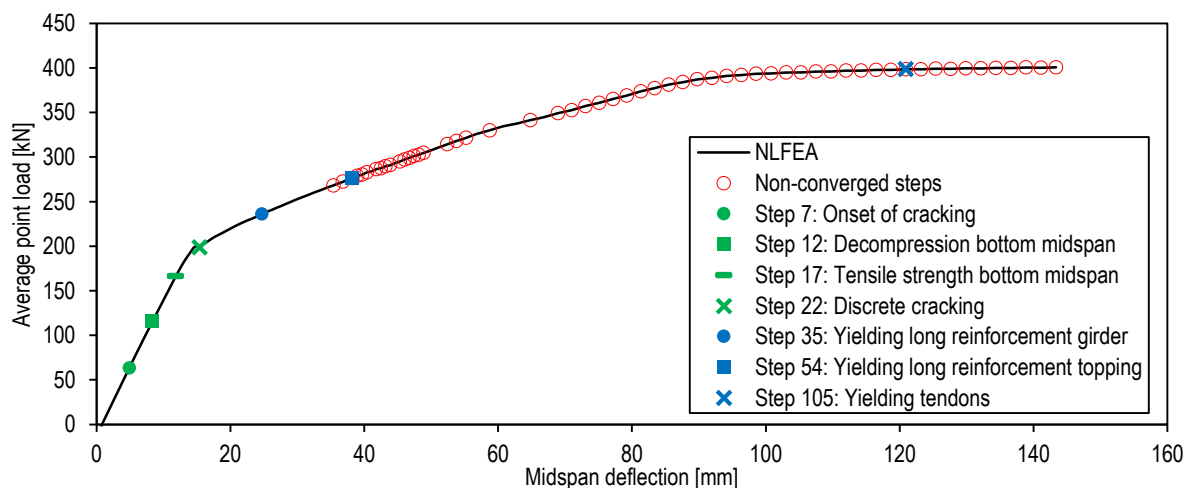


Figure 4.39. Load - deflection curve NLFEA

4.4.2.3 Deformed meshes

Figure 4.40 illustrates the meshes with absolute deformation at load steps 20, 29, 41, 54 and 93. The largest deformation occurs at midspan and local element distortions occur due to cracking both in the precast girder and the topping. The deformed meshes indicate mainly bending deformations. The last step does not show clearly huge distortions of the elements characterizing failure but the equilibrium path at this stage is obtained from non-converged steps.

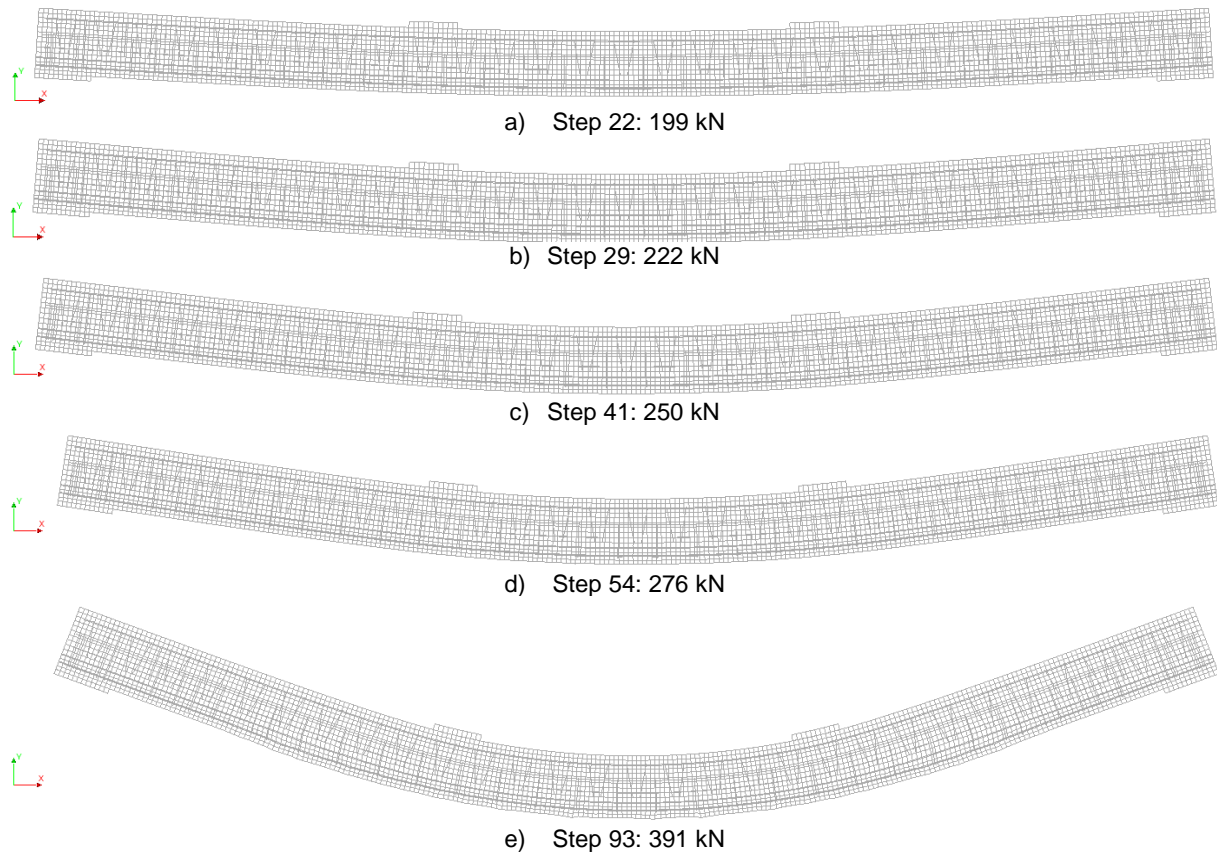


Figure 4.40. Deformed meshes at different load steps (Scale factor: 10)

4.4.2.4 Stresses at midspan

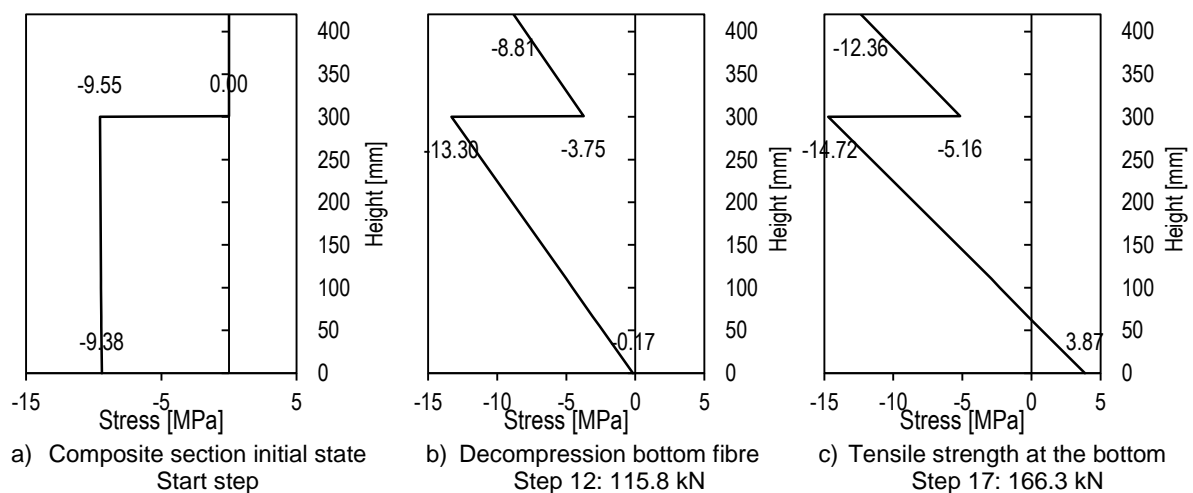


Figure 4.41. Stress distribution at midspan at different load steps

Figure 4.41 indicates the stress distribution at midspan at different load levels. In the start step the stress distribution is characterized by the precast girder subjected to the stresses caused by prestressing and self-weight whereas the topping is stress-free since no external load is applied at this stage. The following two steps show the stress distributions at decompression and when reached the tensile strength at the bottom fibre of the precast girder.

4.4.2.5 Maximum principal strains in concrete and maximum crack width

Figure 4.42 and Figure 4.43 presents the maximum principal strains at load steps 22, 29, 41, 54 and 80 in the topping and precast girder, respectively. The plots illustrate the crack development, starting with a few flexural cracks in the precast girder in load step 22 at 199 kN which coincides with the observation from the load – deflection response. In the next load steps, new flexural cracks appear in the precast girder and the topping and existing cracks in the precast girder widen and propagate in the vertical direction. Vertical cracks propagate from the precast girder to the topping in load step 41 (250 kN). Table 4.9 summarizes maximum crack width in the constant moment region at the same time steps as the presented cracking patterns. After step 41 (250 kN) the precast girder does not develop new cracks and existing cracks widen and propagate vertically, whereas in the topping new cracks appear each step but also existing cracks further propagate. The cracking pattern is widespread over the bottom of both the precast girder and the topping and is symmetrical.

Table 4.9. Maximum crack width in the constant moment region at different load steps from NLFEA

Load step	Load level [kN]	Topping [mm]	Precast girder [mm]
22	199	0.002	0.11
29	222	0.009	0.34
41	250	0.16	0.65
54	276	0.25	1.21
80	345	0.60	2.33

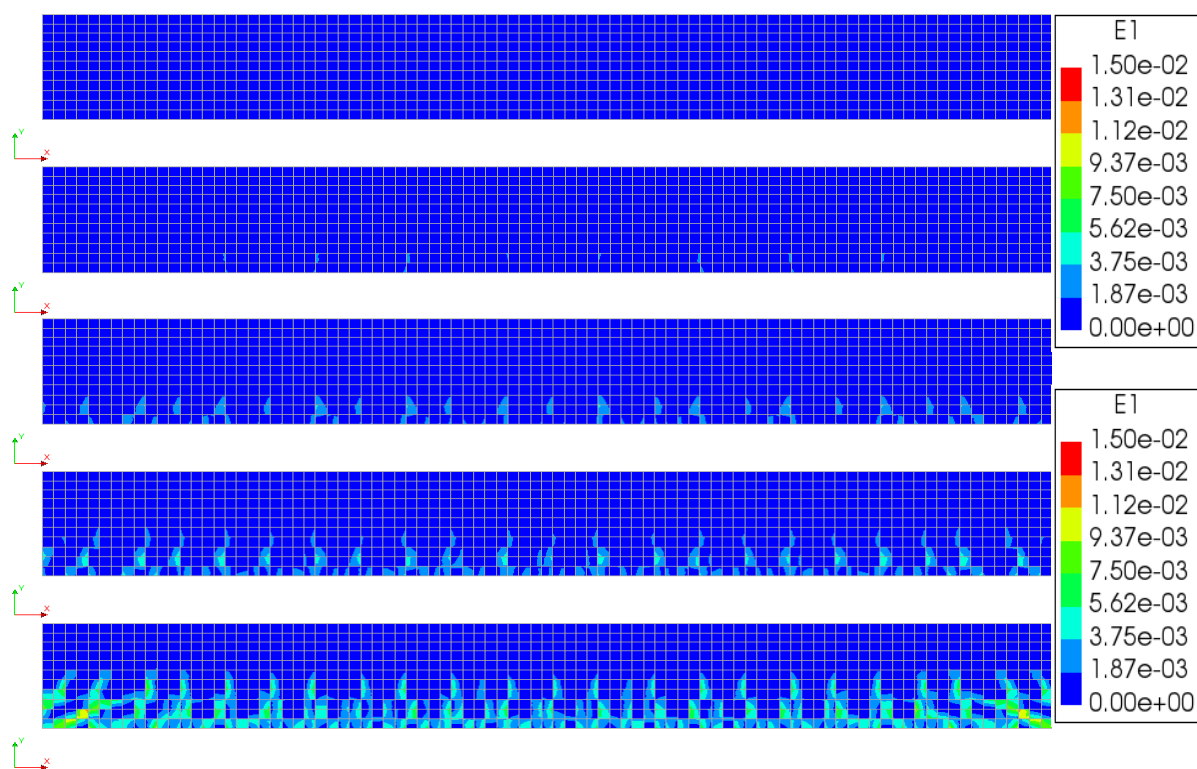


Figure 4.42. Maximum principal strains in the topping at 199, 222, 250, 276 and 345 kN

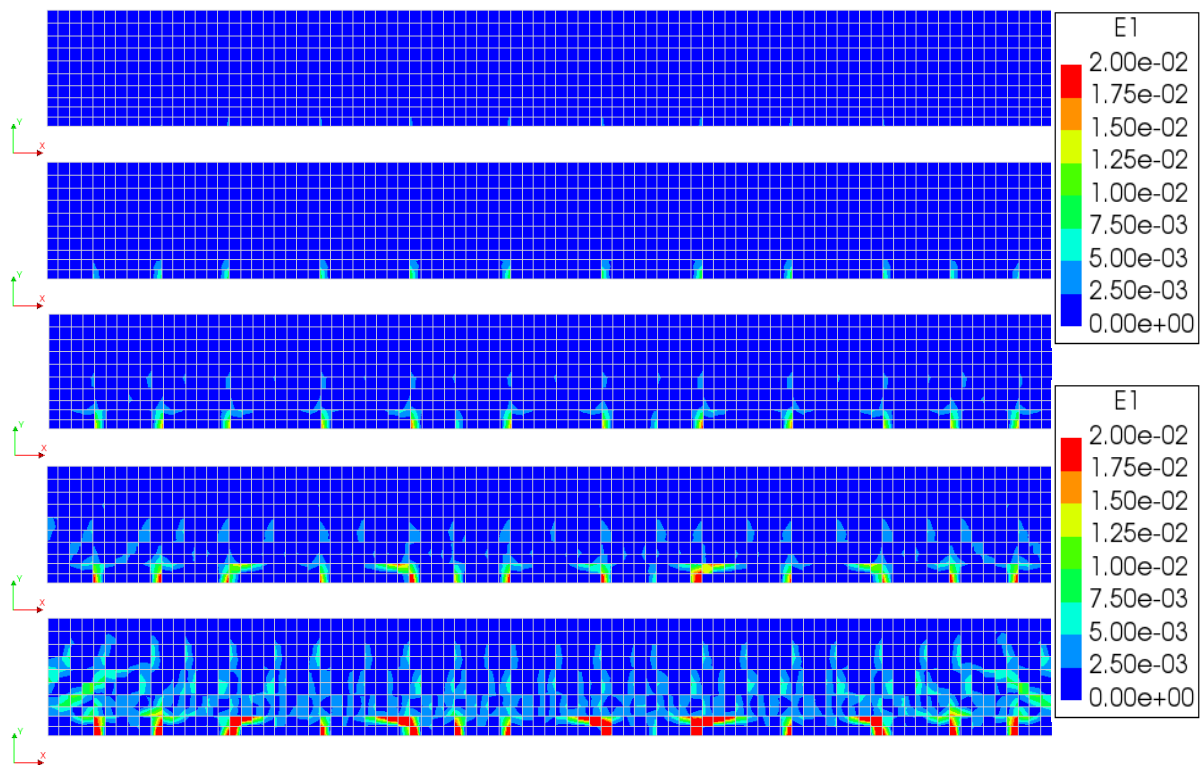


Figure 4.43. Maximum principal strains in the precast girder at 199, 222, 250, 276 and 345 kN

4.4.2.6 Minimum principal strains in concrete

Figure 4.44 displays the minimum principal strains in the precast girder and the topping at load steps 22, 29, 41, 54 and 80. The minimum strains remain lower than the crushing strain of 3.5‰ throughout all the steps.



Figure 4.44. Minimum principal strains at 199, 222, 250, 276 and 345 kN

4.4.2.7 Load – strain behavior at midspan

The concrete strains at midspan are indicated in Figure 4.45. The locations from which the concrete strains are extracted correspond to the nearest nodes to the bottom layer of prestressing tendons (Bottom girder), to the bottom layer of longitudinal reinforcement of the topping (Bottom topping) and 15 mm from the top of the specimen (Top). The latter is located in the precast girder whereas the former two are located in the topping (Figure 4.46).

As inferred from the load – displacement curve in Figure 4.39, also a change of slope around 200 kN is observed in the three curves which indicates cracking in the bottom of the specimen. The compressive strain in the top layer remains smaller than the crushing strain of concrete which coincides with the observations of the minimum principal strains. The prestressing tendons and the longitudinal reinforcement in the topping are past the yield strain as perfect bond between the tendons and the SCGC in the girder is modelled. In particular, the longitudinal reinforcement in the topping reaches the yield strain at load step 91 (2.31‰ at 387 kN) and the prestressing tendons at load step 105 (4.12‰ at 399 kN). The slope of the curve at the location of the longitudinal reinforcement in the topping is flat after reaching the yield strain which corresponds to the ideal plasticity material model adopted for the reinforcement. The behavior at the level of the lower layer of prestressing tendons is similar which indicates redistribution of stresses to neighboring nodes that haven't reached plasticity before hardening occurs.

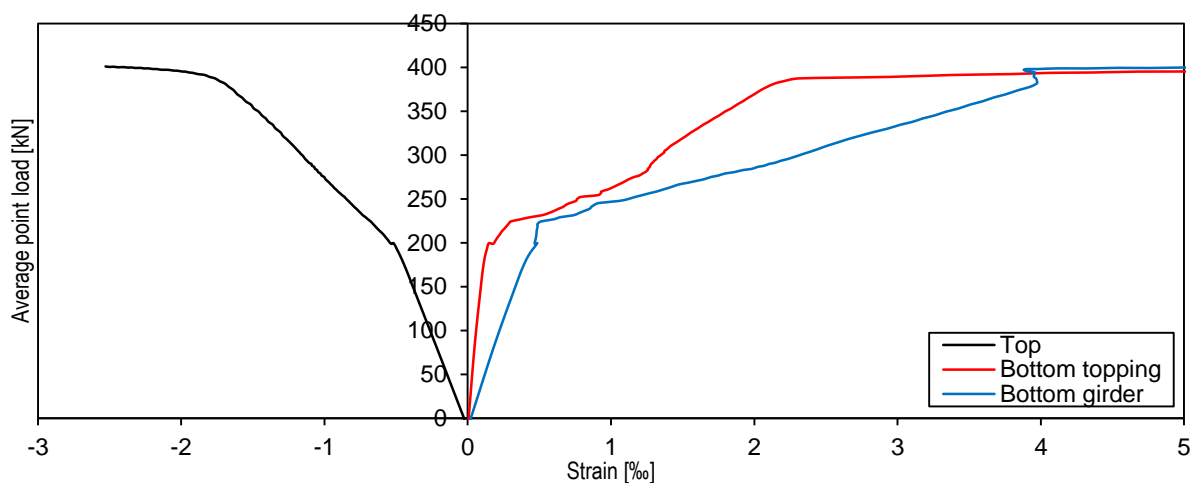


Figure 4.45. Concrete strains at midspan NLFEA

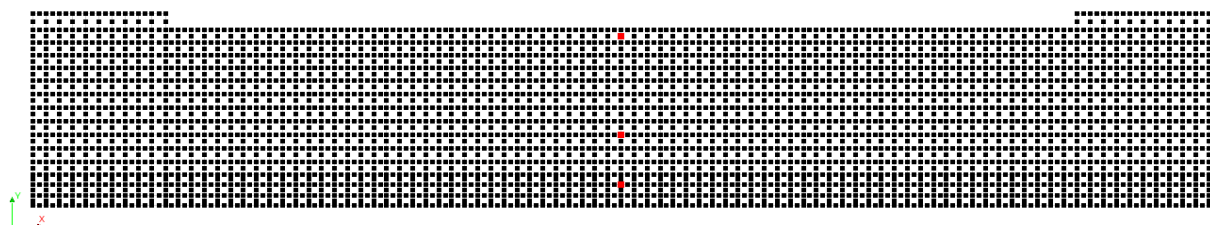


Figure 4.46. Node localization for extraction of concrete strains

4.4.2.8 Strains in steel

Figure 4.47 presents the normal strains in the longitudinal reinforcing bars at load steps 35, 54 and 80. The first yielding is observed at the bottom longitudinal reinforcement of the precast girder at load step 35 (236 kN). The bottom longitudinal reinforcement of the topping first yields at load step 54 (276 kN). Load step 54 coincides with a fully developed crack pattern in the topping and the widening of existing cracks in the precast girder as illustrated in Figure 4.42 and Figure 4.43. Similarly, in step 80 (345 kN) already yielding is widespread in the bottom layers of reinforcement both in the precast girder and the topping and yielding also occurs in the top layer of longitudinal reinforcement in the topping as the cracks propagate vertically. Observe that the yielding of the longitudinal reinforcement in the topping was reported at load step 91 (387 kN) from Figure 4.45, this difference occurs since a crack opening is not present right at the midspan of the specimen.

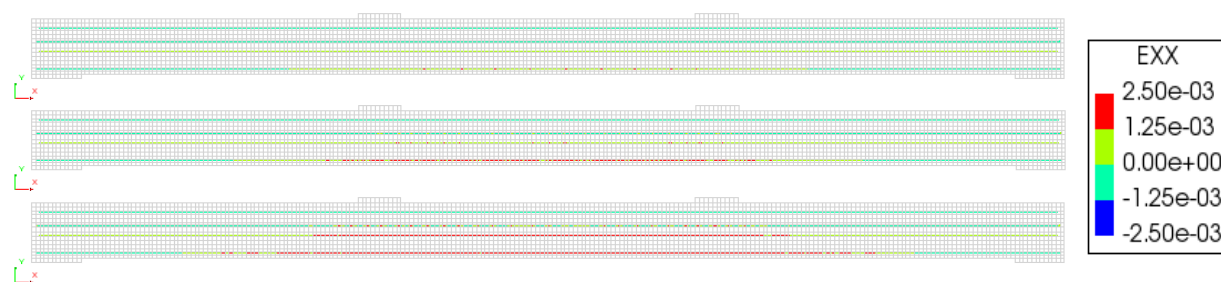


Figure 4.47. Longitudinal reinforcement strains at 236, 276 and 345 kN

Figure 4.48 presents the normal strains in the shear reinforcement at load steps 35, 54 and 80. The stirrups reach the yielding strain in the last steps when flexural-shear cracks develop at the bottom of the specimen next to the loading plates on the side to the supports.

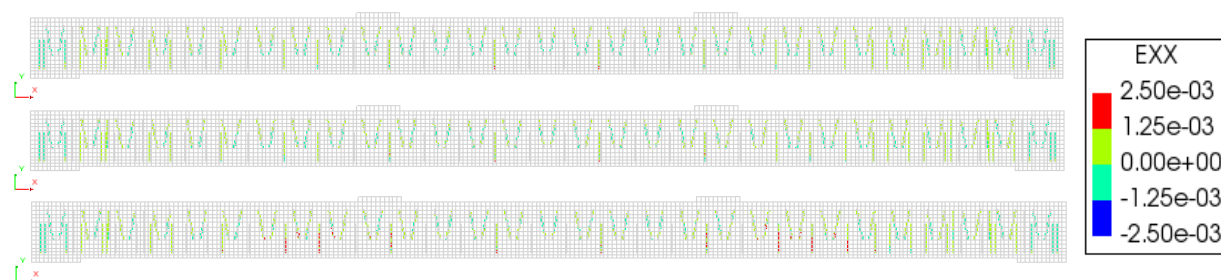


Figure 4.48. Shear reinforcement strains at 236, 276 and 345 kN

Figure 4.49 presents the normal strains in the prestressing tendons of the precast girder. The prestressing tendons in the top and bottom layers reach the yield strain in load step 105 at 399 kN as observed from the strains in concrete from Figure 4.45. Furthermore, it can be noted that the yield strain in the extremes is reached earlier as slippage of the tendons is not accounted for in the model.

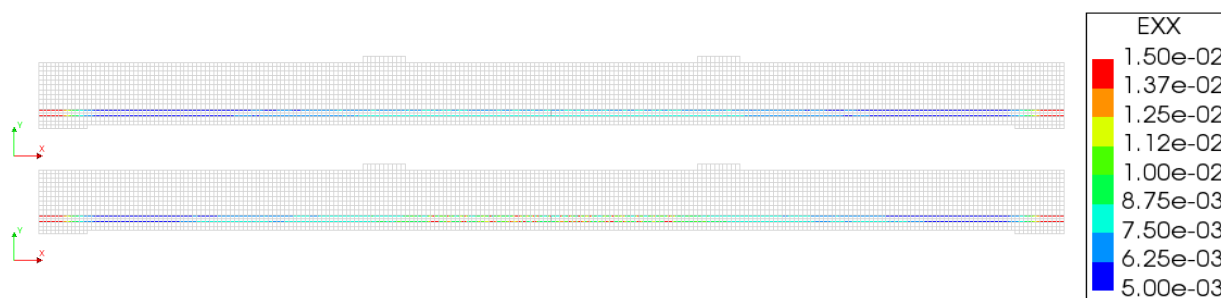


Figure 4.49. Prestressing tendons strains at 345 and 399 kN

4.4.3 Shear test

4.4.3.1 Convergence behavior

Figure 4.50 displays the number of iterations and the evolution of the relative out of balance force and relative energy variation during each load step. The dashed green and black lines indicate the energy and force tolerances, correspondingly. The first and second steps corresponds to the casting of topping and composite section phases, respectively. The next 200 steps correspond to the mechanical test phase. From this point onwards the steps mentioned refer only to the 200 steps of the mechanical tests, for global step numeration add the two initial steps. The analysis convergences in terms of both norms until step 22 with only 1 or 2 iterations in each step. After step 22 the analysis converges by means of the energy norm exclusively and the force norm no longer satisfies the tolerance for the remainder of the analysis.

Between steps 23 and 108 the energy norm remains below the tolerance for most of the steps, resulting in only 5 non-converged steps. The non-converged steps are followed by converged steps and the energy norm is close to the tolerance, hence the results are acceptable. Steps 109 to 125 are non-converged steps with a drastic increase in the energy norm, which is also evident from Figure 4.51, and indicate the post-peak response after failure when equilibrium is no longer fulfilled. Therefore, the maximum load may be expected at step 108. After this non-converged state, a new equilibrium path is found after step 126. Several steps of the analysis converge by means of the energy norm and non-converged steps are followed by converged steps. Nevertheless, the results of these converged steps should be judged carefully as this is a post-peak equilibrium path after several non-converged steps, even though the response after failure is not of particular interest for the present study.

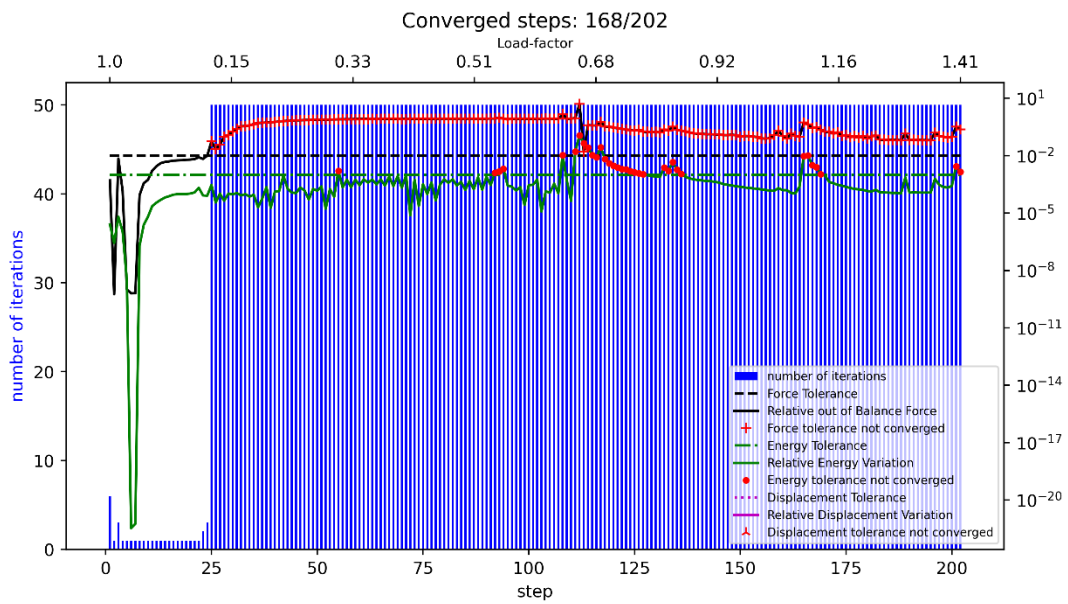


Figure 4.50. Evolution of convergence norms and number of iterations per load step

Evolution of Relative Energy Variation

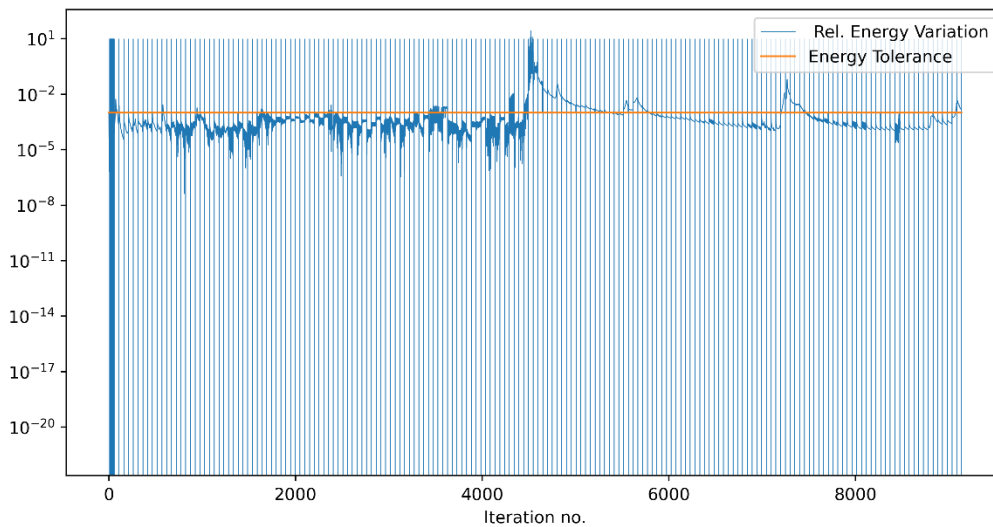


Figure 4.51. Evolution of the relative energy variation

4.4.3.2 Load – deflection

Figure 4.52 displays the load – deflection response of the beam to the prescribed deformation applied during the 3-point load test. The deflections are obtained at the soffit of the specimen under the point of application of loading. The non-converged steps are indicated with red circles. The numerically derived load-carrying capacity is 814 kN at around 36 mm deflection at the soffit of the specimen under the point of application of loading.

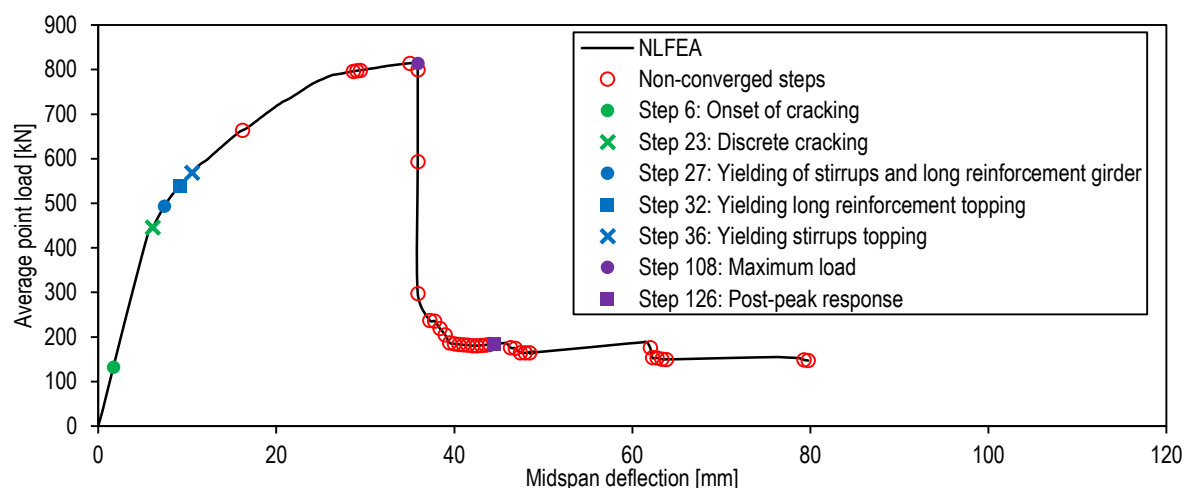


Figure 4.52. Load - deflection curve NLFEA

Seven steps are marked in the load – deflection curve to indicate characteristic stages in the damage evolution of the specimen. The first point corresponds to the onset of cracking i.e. the first appearance of cracks in a finite element. As can be observed the behavior after the onset of cracking is almost linear elastic behavior until the second point (step 23: 446 kN) when discrete cracking first occurs both in the girder and topping. After this point a change of slope is noticeable with a decrease of stiffness caused by the propagation and widening of diagonal cracks. This spread of cracking is accompanied with yielding of the shear and longitudinal reinforcement of both the precast girder and cast in-situ topping within load steps 27 to 36 (493 kN to 568 kN). The deformation continues to increase with the applied load with a decreasing slope caused by the evolution of cracking and yielding of reinforcement. The peak load is attained at step 108 (814 kN), which is followed by a sudden drop in the load-carrying capacity which is caused by the formation of a shear critical crack in both the precast girder and the cast in-situ topping, and crushing of concrete under the bearing plate. At failure, the yielding of shear and longitudinal reinforcement is completely widespread across the localization of the shear critical crack. The following steps do not reach convergence until the system regains equilibrium at step 126. The analysis is allowed to continue to describe post-peak equilibrium path. However, this results are not of much interest to the present analysis as the remaining load-carrying capacity is marginal and several finite elements are completely distorted and lost all stiffness.

4.4.3.3 Deformed meshes

Figure 4.53 illustrates the meshes with absolute deformation at load steps 22, 48, 108 and 126. The main deformations occur under the point of application of loading. Local element distortions start in the bottom of the precast girder and become gradually more pronounced. Step 108 shows the mesh before failure where the distortion is limited to the soffit of the specimen. Meanwhile, step 126 is the post-peak response where the stiffness is entirely vanished from the distorted elements in the soffit but also under the point of loading.

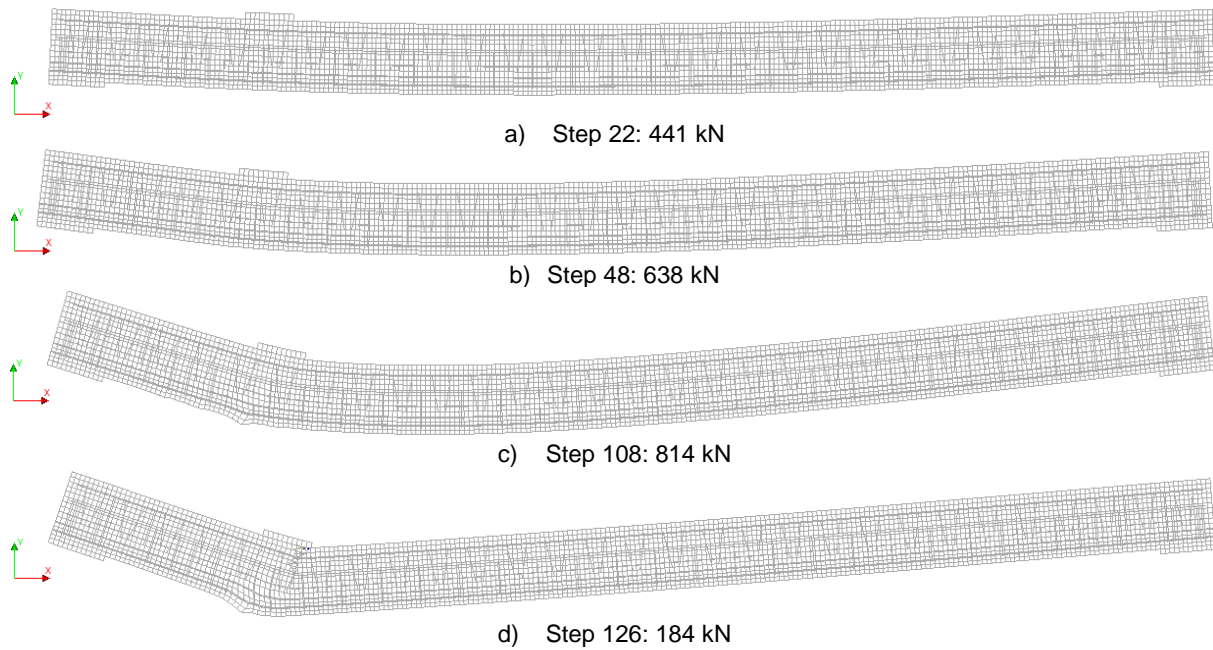
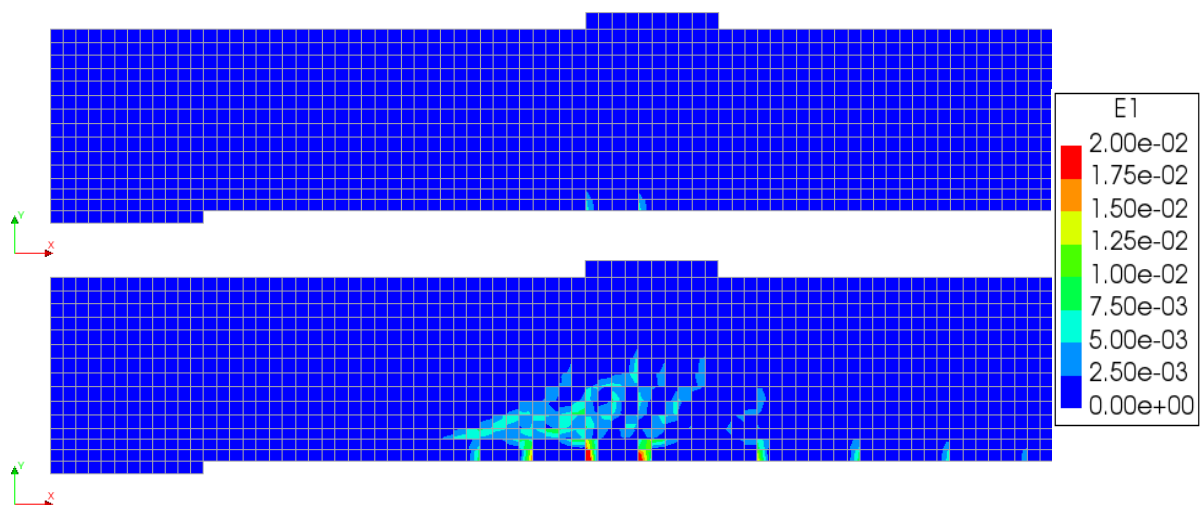


Figure 4.53. Deformed meshes at different load steps (Scale factor: 10)

4.4.3.4 Maximum principal strain in concrete

Figure 4.54 presents the maximum principal strains at load steps 23, 40, 48, 108 and 126 in the shear span. The plots illustrate the crack development, starting with a few vertical cracks in step 23 (446 kN) which coincides with the observation from the load – deflection response. Step 40 (593 kN) already shows the appearance of new diagonal cracks and widening of the existing cracks. This diagonal cracking pattern is accompanied with first yielding of the shear and longitudinal reinforcement of both the precast girder and cast in-situ topping. In the next steps, the diagonal cracks continue to widen and the number of stirrups reaching the yield stress increases, this behavior causes the decrease of the stiffness in the load – deflection diagram. At the maximum load of 814 kN (step 108) is noticeable the shear critical crack which causes failure. The diagonal crack is over the flange of the precast and extends from under the bearing plate in direction to the support. The post-peak behavior shows a fully cracked region without any stiffness at the same position of the distorted elements from Figure 4.53.



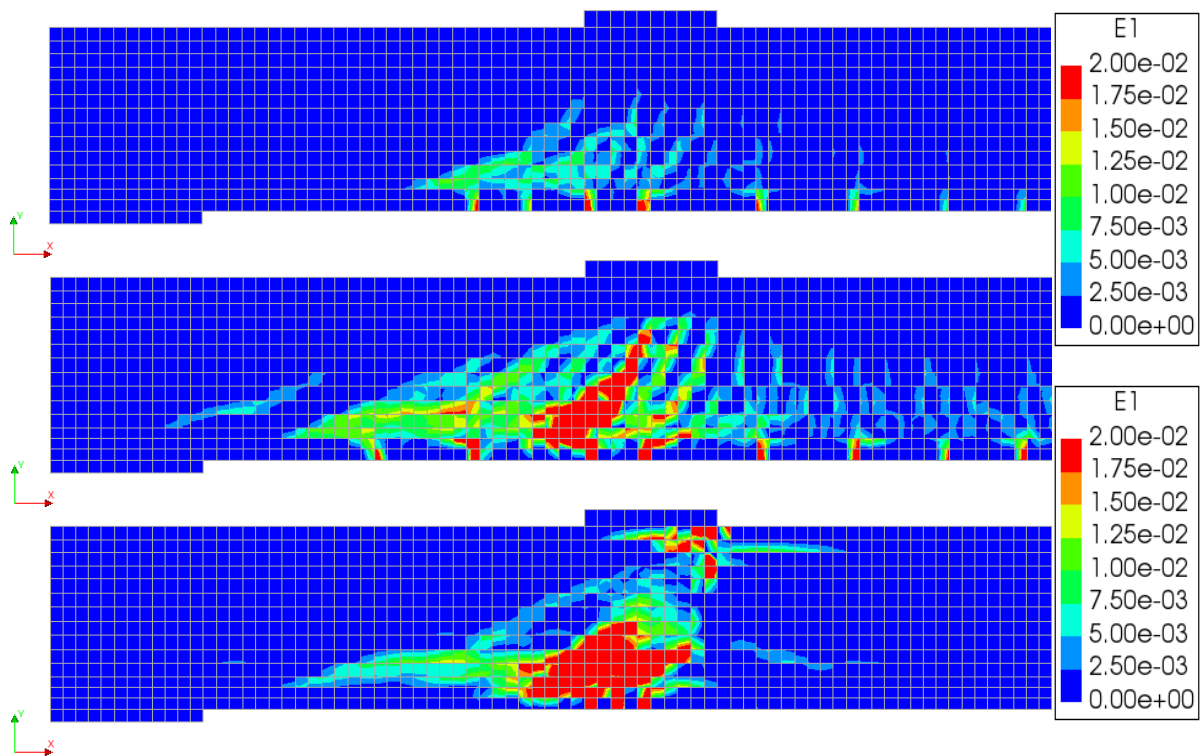
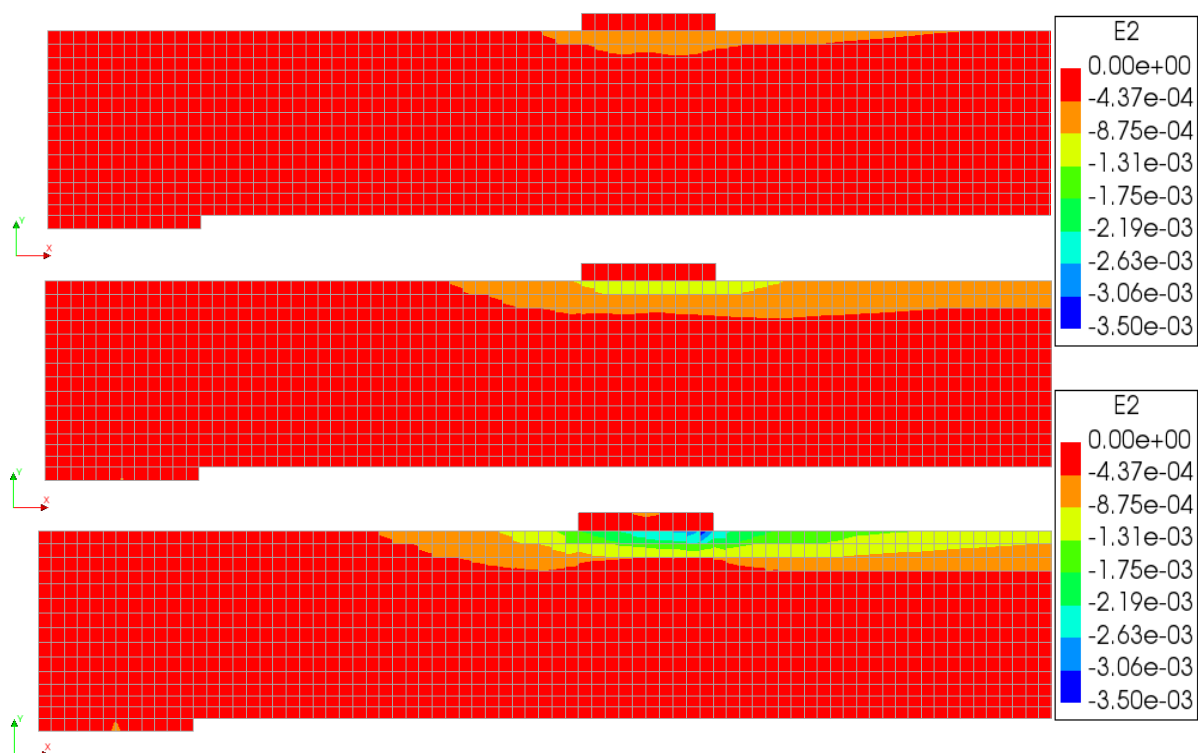


Figure 4.54. Maximum principal strains in concrete at 446, 593, 638, 814 and 184 kN

4.4.3.5 Minimum principal strains in concrete

Figure 4.55 displays the minimum principal strains in the precast girder and the topping at load steps 23, 40, 94, 108 and 126. The minimum strains reach the crushing strain of 3.5‰ at load steps 94 and 108 (801 and 814 kN) near the edge of the loading plate. Finally, the post-peak response shows a region where the crushing strain is surpassed which corresponds to the distorted elements with no stiffness at the edge of the loading plate (Figure 4.53).



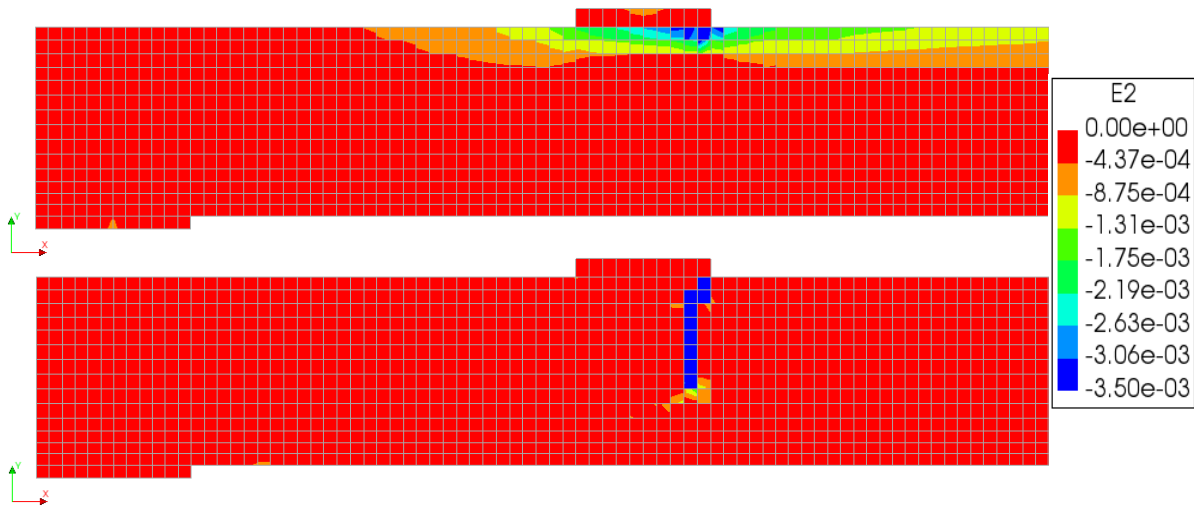


Figure 4.55. Minimum principal strains in concrete at 446, 593, 801, 814 and 184 kN

4.4.3.6 Strains in steel

Figure 4.56 and Figure 4.57 present the normal strains in the shear and longitudinal reinforcement for different load levels.

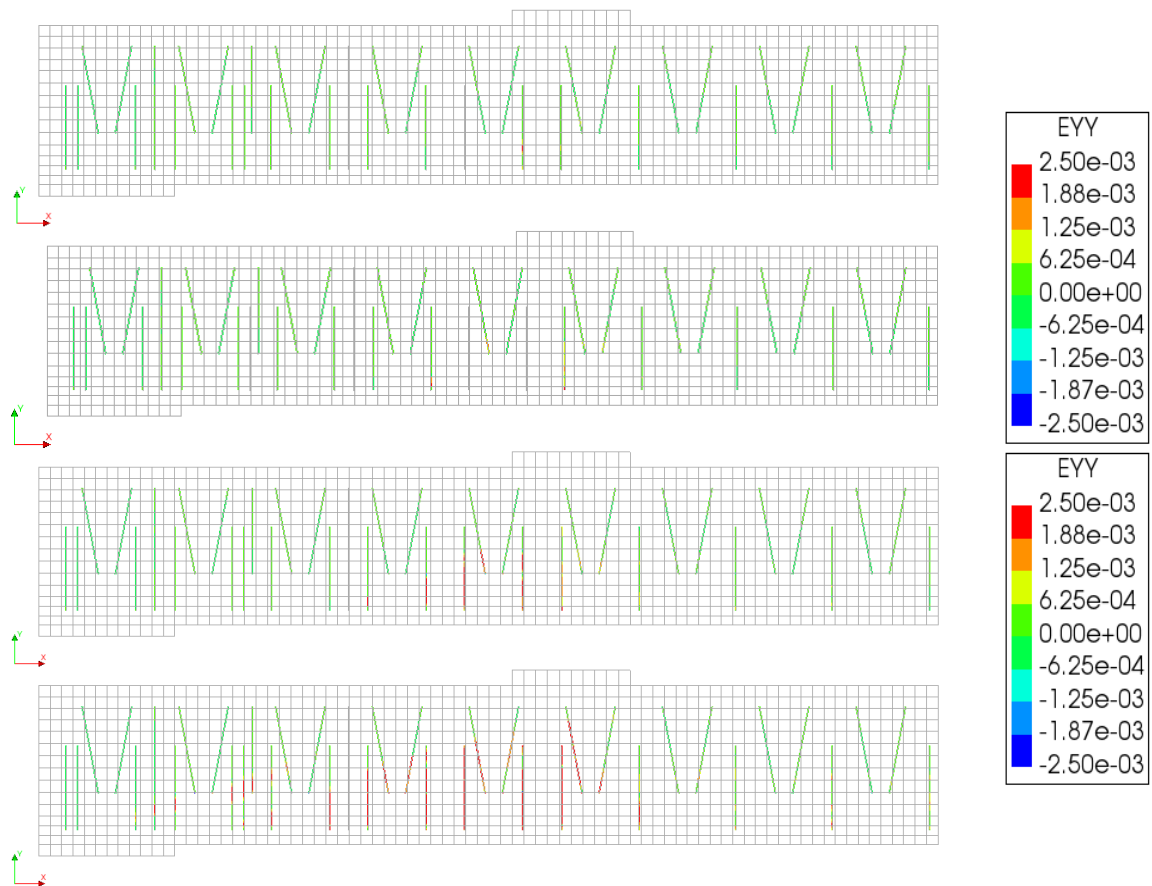


Figure 4.56. Shear reinforcement strains at 493, 568, 638 and 814 kN

The first yielding is observed at load step 27 in the bottom longitudinal and shear reinforcement of the precast girder. In the topping, the bottom longitudinal reinforcement first yields at load step 32 (534 kN) and the shear reinforcement at load step 36 (568 kN). The first yielding of reinforcement is caused by the appearance of diagonal cracks from step 23 to 40, as displayed in Figure 4.54.

The damage evolution until load step 48 (638 kN) is the propagation and widening of the diagonal cracks in both the precast girder and the topping. At this load step the shear and longitudinal reinforcement have an active contribution to the resistance since the elements are yielding at the same positions of the open cracks in Figure 4.54. Finally, at the maximum load level (step 108), the yielding of shear and longitudinal reinforcement is widespread along the critical shear crack.

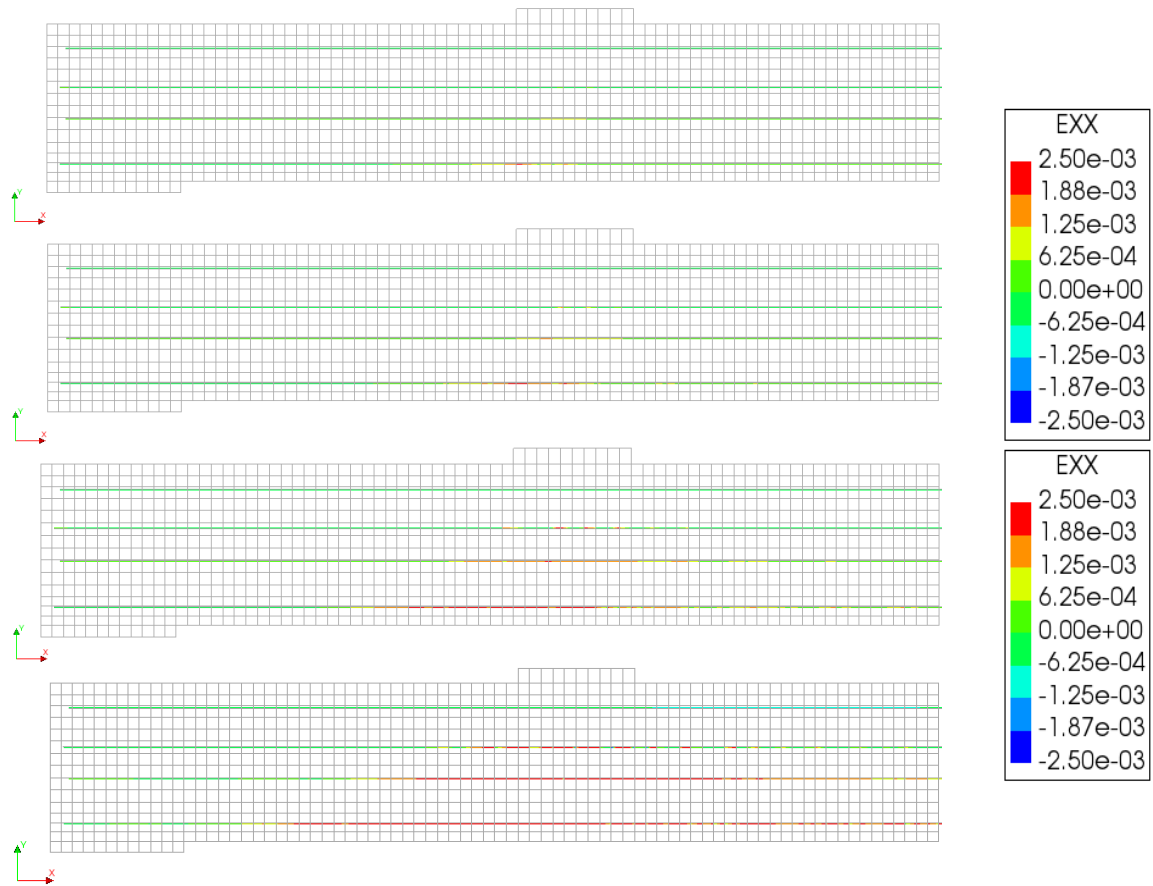


Figure 4.57. Longitudinal reinforcement strains at 493, 540, 638 and 814 kN

5

Comparison of experimental, analytical and FEA results

This Chapter contains a comparative analysis between the experimental, analytical and FEM response of the precast girder with cast in-situ topping to prestressing and the mechanical tests. The comparison is performed on the basis of deformations, concrete strains, stresses, load – deflection curves, evolution of cracking and failure mode. Additionally, NLFEMs are presented to do a sensitivity study to assess the influence of different material parameters in the structural response to the 4-point load test.

5.1 Prestressing

5.1.1 Deformations

Figure 5.1 displays a comparison of the deformations after prestressing calculated by analytical analysis, LFEA and as measured for the SCGC girders. The camber determined analytically is slightly higher than the LFEA results since the second moment of area of the discretized geometry as defined in 4.2.1 is slightly higher than the exact geometry. The analytical calculation is performed for gross cross-sectional properties (i.e. the area of the prestressing tendons and the reinforcement steel are not transformed to equivalent areas of concrete and their contribution to the second moment of area is disregarded), hence the real cross-section is stiffer which leads to a lower measured camber. The OPC bar represents the average camber at 1 day of the precast girders with similar properties produced by Haitsma Beton in OPC concrete C60/75 (Table 3.15) and the difference in camber between SCGC and OPC concrete girders is explained in detail in 3.6.1. The elastic deformation from the analytical model is almost the same as the FE model.

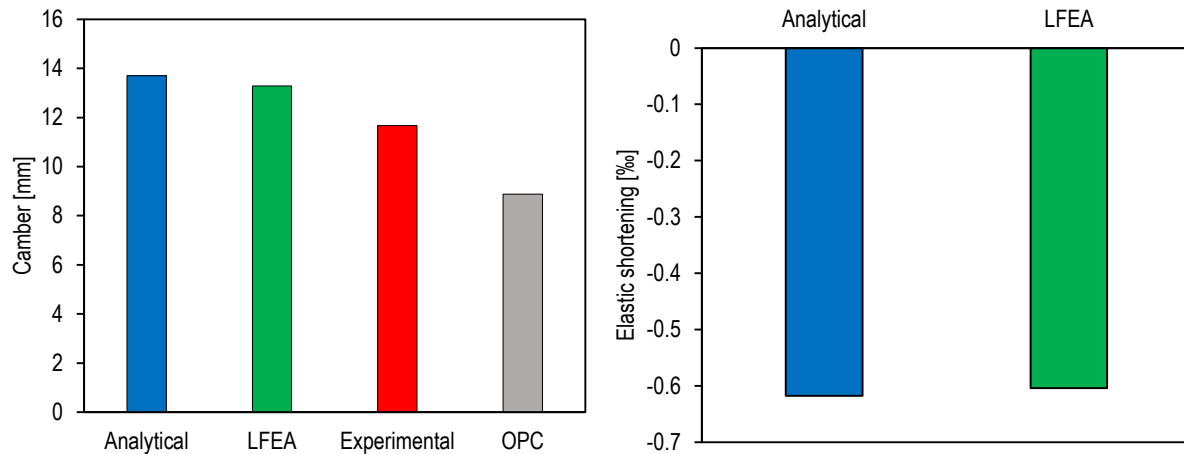


Figure 5.1. Deformations after prestressing (Experimental vs analytical vs LFEA)

5.1.2 Concrete stresses at midspan

Figure 5.2 shows the stress and strain distributions at midspan. The analytical model based on the Euler Bernoulli beam assumptions is almost the same as the plane stress elements that can accurately describe the generalized model for the linear elastic behavior of a beam.

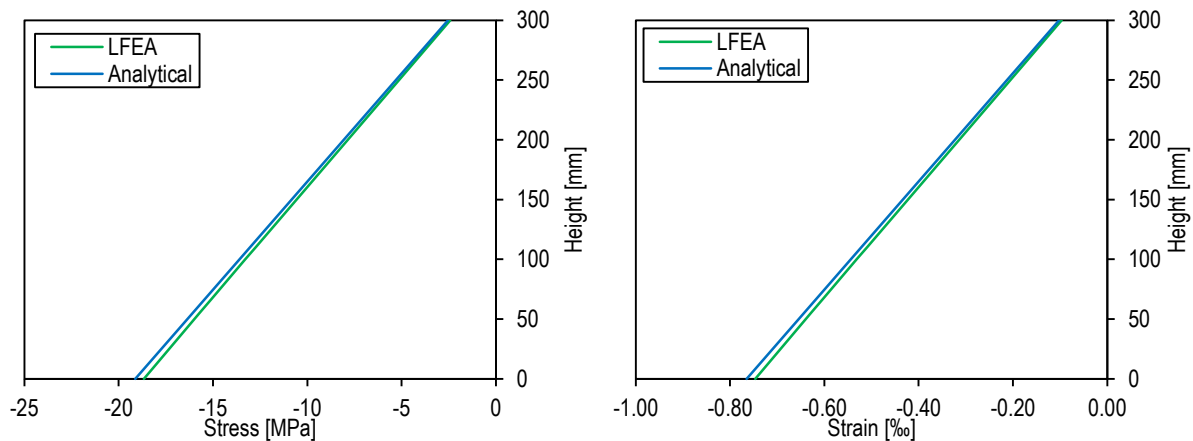


Figure 5.2. Stress and strain distributions after prestressing at midspan (Analytical vs LFEA)

5.1.3 Transmission length

The relative strains measured by the FBG sensors along the length of the specimen for the shear test and the transmission length calculated analytically according to EN 1992-1-1 [22] are displayed in Figure 5.3.

The elastic strain due to prestressing is:

$$\sigma_{ps} = -\frac{P_{m0}}{A_g} - \frac{P_{m0}e_p^2}{I_g} + \frac{M_{Gc}e_p}{I_g} = -15.46 \text{ MPa}$$

$$\varepsilon_{ps} = \sigma_{ps}/E_c = -0.618 \text{ ‰}$$

At the transmission length, the steel and concrete fully coupled and the strains shall be equal. The measured strain at the marked transmission length is close to the elastic strain caused from analytical calculations, even though the measurements are still fluctuating. The calculation model from EN 1992-1-1 [22] seems to be adequate for geopolymer concrete.

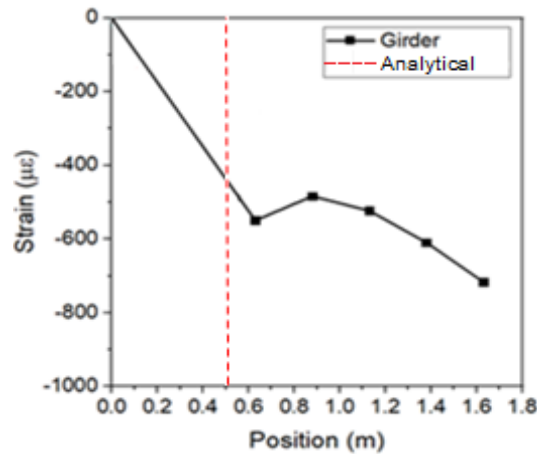


Figure 5.3. Transmission length

5.2 Short-term flexural behavior

5.2.1 Load – deflection

Figure 5.5 presents the load – deflection response as measured from the experiment and the curve obtained numerically by means of the NLFEA for the flexural test. Figure 5.6 displays the load levels during characteristic points in the damage process of the structure as determined analytically, numerically and from the experiment. The load – deflection curve is approximately linear elastic until cracking and the initial slope is almost the same for the NLFEA and the experiment (the unloading cycles in the experiment is the reason why the initial section of the curve is not a single line). The change in slope due to the evolution of cracking occurs at similar load levels. In fact, the cracking load determined analytically and numerically are equal and are only 3% higher than the experiment.

The onset of cracking in the NLFEA is almost the same as the load when the measured strain at the level of the prestressing tendons reach the tensile strength of concrete (Figure 3.32). The load from the experiment is slightly higher (11%) since cracking first occurs at the soffit of the topping layer as reported by the NLFEA, whereas the measured concrete strain from the experiment is at 55 mm from the soffit where cracking will occur later. The onset of cracking in NLFEA is defined as the load step in which first cracking occurs at an integration point after the tensile strength is reached. From the load displacement curve it can be observed that the linear elastic response is practically unaffected after the onset of cracking as the cracks before discrete cracking are microcracks with an order of magnitude of the crack width between 10^{-4} and 10^{-2} mm. This microcracks start in the topping layer (of a lower tensile strength than the precast girder) and are not structural cracks (Figure 5.4), the same is observed from the experiment as cracking is first reported in the topping layer but the NLFEA reports discrete cracks first in the precast girder. Hence the differences in the reported loads at which the onset of cracking, the tensile strength is reached at the bottom of the girder and discrete cracking occur. The development of cracking stage shows a satisfactory correspondence between the experimental and numerical results.

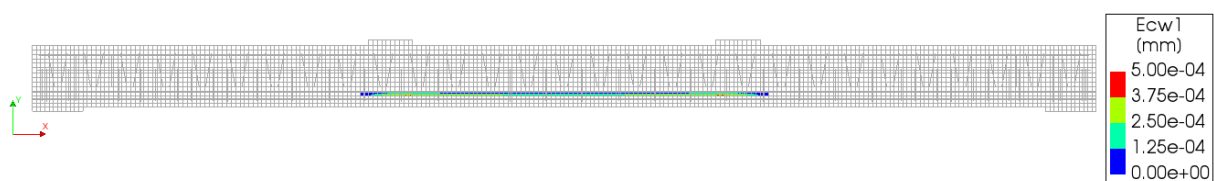


Figure 5.4. Microcracking in the cast in-situ topping at the onset of cracking (Load step 7: 64 kN)

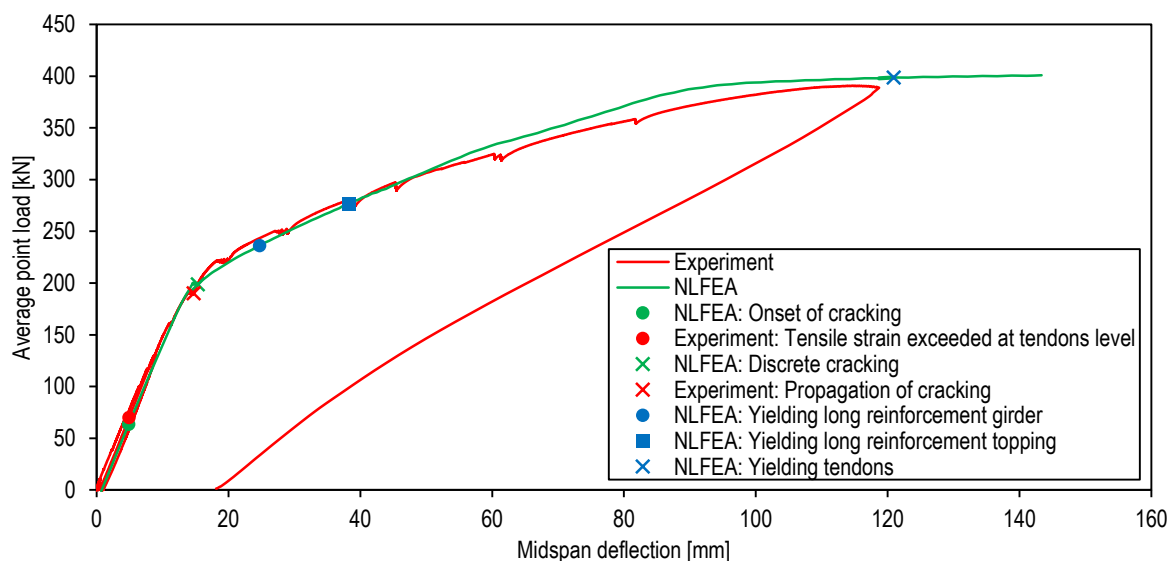


Figure 5.5. Load - deflection curve during flexural test (Experimental vs NLFEA)

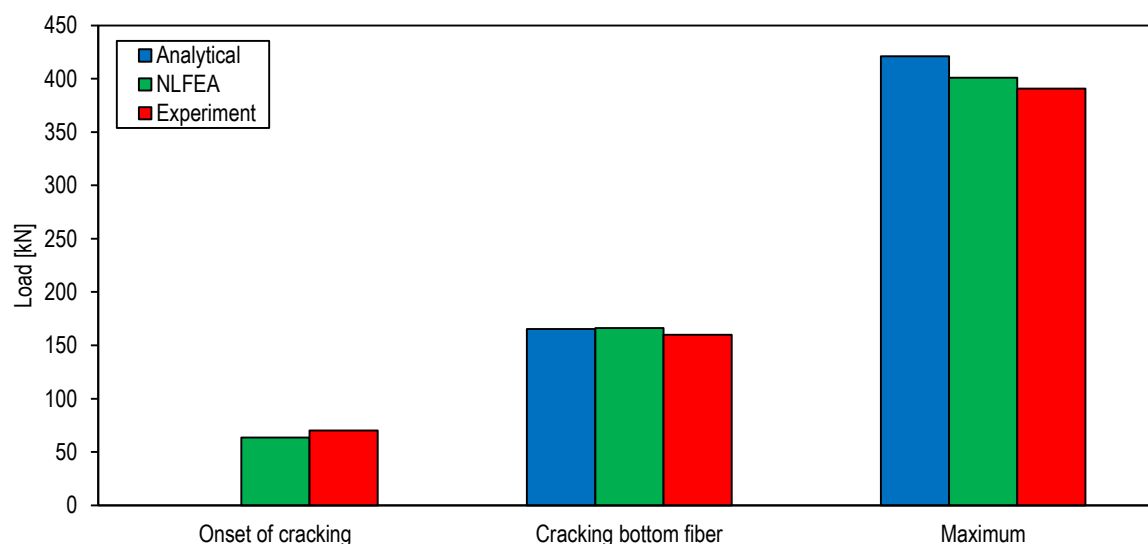


Figure 5.6. Characteristic load levels (Experimental vs analytical vs NLFEA)

Recall that the specimen did not fail during the experiment as the hydraulic jack reached the end of the stroke. Nevertheless, another specimen was tested 9 months later after subjected to self-weight and the load at failure did not reach the maximum load levels as presented in Figure 5.5 as will be seen in the last section of this Chapter. Therefore, the maximum load from the load – deflection curve is assumed to be the resistance force for comparison with the results from the NLFEA and the analytical model. The RTD 1016-3B [72] and RTD 1016-3 [73] present the modelling of seven experimental studies of prestressed concrete girders with and without stirrups and with failure modes in flexure and shear. The modelling is also performed in DIANA FE in plane stress conditions with a total strain based smeared rotating crack model. All but one of the seven models report slightly higher resistances with the NLFEA with no safety format (i.e. without partial factors and mean material properties from testing) than the experiment. From Figure 5.6, this is also the case for the present study as the predicted capacity by NLFEA is slightly higher than the maximum load attained during testing. Figure 5.7 d) displays the stress distribution in concrete at midspan from the NLFEA and the idealized bilinear compressive stress block for the analytical model. The area under both stress

diagrams is almost the same and the analytically determined resistance is slightly higher because the lever arm of the bilinear stress block is slightly higher than the (almost) triangular stress distribution in the NLFEA. Case PB7 from the RTD 1016-3B [72] (I-shaped post-tensioned girder failing in flexure) presents the analytical calculation of the flexural resistance as per EN 1992-1-1 [22] with no safety formats and the result is slightly higher than the NLFEA result, and both a little higher than the experiment which is the case for the present study as well. Therefore, an acceptable prediction of the short-term flexural resistance is possible with the current analytical and numerical models described in this study.

5.2.2 Concrete stresses at midspan

Figure 5.7 presents the stress distributions at midspan at characteristic phases. The start step, decompression and cracking of the bottom fibre show a linear elastic response and correspondence of plane stress and Euler Bernoulli methods of analysis. On the other hand, the bilinear compressive stress block assumed for ULS calculations as per EN 1992-1-1 [22] is not the same stress profile from the NLFEA, nevertheless the area under the stress diagram, hence the compressive forces from both concrete compression zones, are almost equal. Consequently, the idealized bilinear compressive stress block for ULS calculations is adequate for predicting the resistance of the specimen.

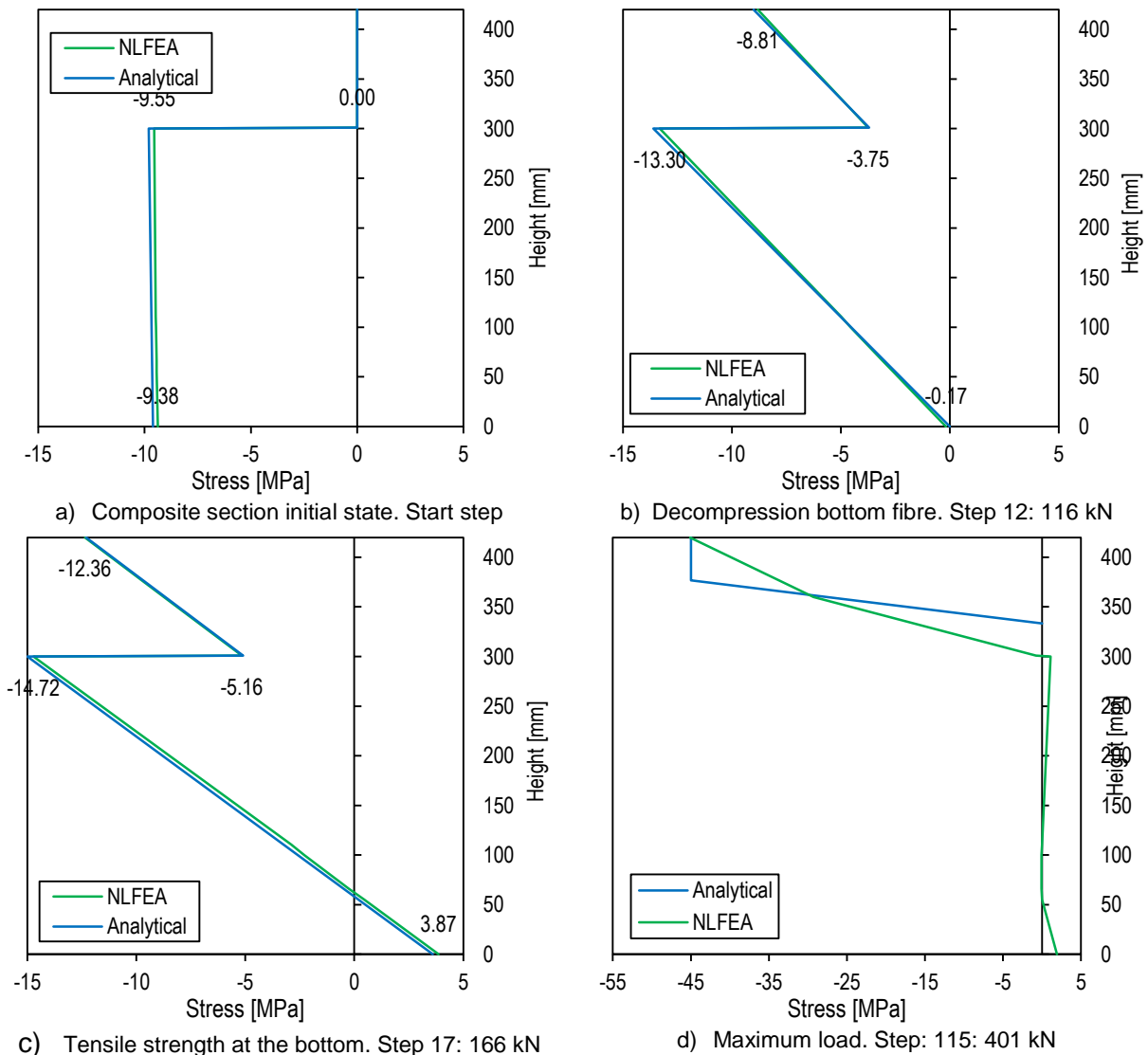


Figure 5.7. Stress distribution at midspan at different load steps (Analytical vs NLFEA)

5.2.3 Load – strains at midspan

Figure 5.8 displays the average point load applied during the flexural test and the corresponding concrete strains at the level of the bottom longitudinal reinforcement in the topping, the lower layer of the prestressing tendons and near the top of the girder as defined in Figure 3.20 and Figure 4.46, for the experiment and the NLFEA, respectively. As mentioned previously for the load – deflection curve, the initial slope is the same both the experiment and the numerical results and a change of slope in the load – strain diagrams occur at around 190 kN which is caused by cracking of the specimen. The numerical results display a satisfactory resemblance to the measured strains, hence the choice of material models for concrete applied to geopolymer concrete appear to be acceptable.

The compressive strain at the top of the girder remains smaller than the crushing strain of concrete (3.5 ‰) according to EN 1992-1-1 [22] for the experiment and the numerical simulation. The measured strains do not reach the yielding strain of the longitudinal reinforcement and the prestressing tendons but in the NLFEA higher loads are attained and yielding occurs. At this stage, concrete is fully cracked and the load – strain behavior resembles the constitutive model of the reinforcement and prestressing steel as the elements are perfectly bonded. Figure 5.8 a) and b) show a plateau after yielding, same as the ideal plasticity model adopted for the reinforcement. The material model of the prestressing tendons is hardening plasticity and the neighboring nodes have to yield before the hardening behavior.

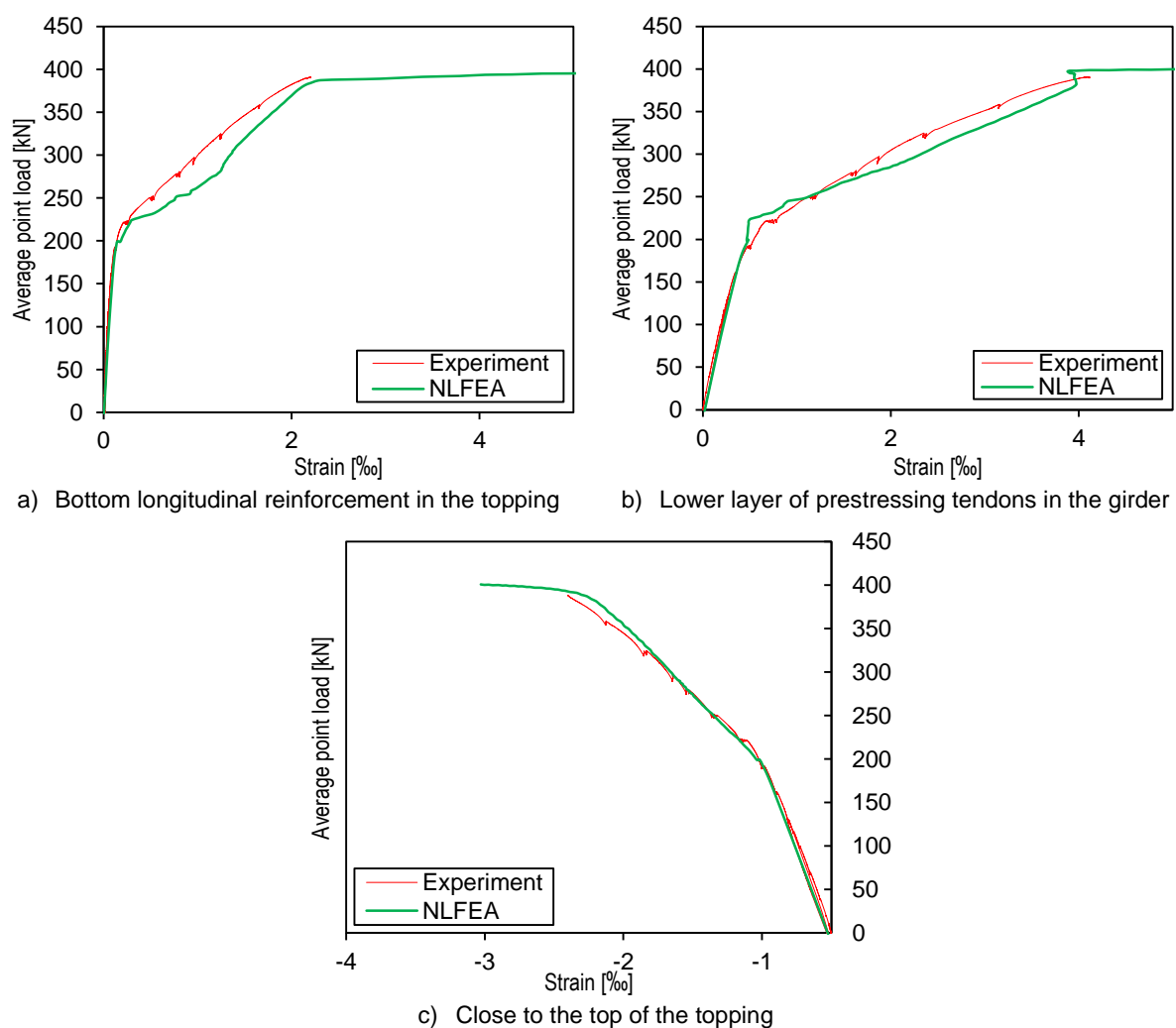


Figure 5.8. Concrete strains at midspan (Experimental vs NLFEA)

5.2.4 Maximum principal strains and crack widths

Figure 5.9 displays the maximum principal strains on the side surface of the specimen in the constant moment region, obtained from the numerical simulation and as measured in the experiment with DIC. The crack widths from DIC measurements are calculated from the measured strain field and for the smeared crack model of the numerical simulation are obtained from the multiplication of the strains with the crack bandwidth. Observe that both methods deduce the crack width from the maximum principal strains. The crack width in the numerical simulation depends on the shape of the tension softening diagram determined by the fracture energy and the crack bandwidth. The fracture energy (Nakamura [76]) is the energy required to open a unit area of crack surface and is a property independent on the element size. The crack bandwidth estimator (Govindjee [75]) considers the crack orientation and is defined as the projected length of the element containing the crack on to the crack plane [71]. Both parameters have been defined by studies for OPC concrete. Figure 5.10 and Figure 5.11 is a comparison of the maximum crack widths measured by DIC and from the NLFEA.

The maximum principal strains exceed the tensile strain of concrete in the precast girder and vertical cracks start to appear. The DIC measurements indicate that at 190 kN few small vertical cracks appear in the precast girder and more in the topping. In contrast, the numerical results at 190 kN display a higher number of evenly spaced cracks in a symmetrical crack pattern exclusively in the precast girder because the normal stresses in the area under consideration are almost equal along the length of the specimen since the prestressing force is fully transmitted, the moment caused by the mechanical test is constant in this region and the moment due to self-weight is maximum at midspan but the effect of this load is less relevant as the load magnitude in the mechanical test increases.

At 220 kN, the numerical results show no new crack formation in the precast girder and the cracking propagates to the topping. The cracking pattern in the topping is similar to the DIC measurements. In the next load steps, the existing cracks widen and propagate in the vertical direction. At 250 kN, additional cracks appear in the precast girder from the numerical simulation and DIC measurements. The cracking pattern in the precast girder with the numerical simulation and DIC measurements is quite similar after this stage of cracking. Nevertheless, Figure 5.10 indicates that the maximum crack width in the precast girder is higher for the numerical simulation as compared to DIC measurements for every load level. The crack width depends on the shape of the tension softening diagram and the tensile strength of geopolymer concrete differs from OPC concrete (2.2.2.2), hence the post-cracking response as described by the fracture energy may also be different for geopolymer concrete. The cracking behavior of geopolymer concrete needs to be investigated, especially with respect to the fracture energy. Larger crack widths in geopolymer concrete girders are also reported in the study by Du, et al. [46]. The following snapshots of the cracking process indicate strain concentrations in the interface between the precast girder and topping both from DIC measurements and the numerical simulation with some cracks in the girder extending horizontally. The interface with the precast girder is modelled as perfect bond hence debonding of the two surfaces is not captured but is reported experimentally, hence cracking starting in the precast girder in the simulation and in the topping in the experiment. The tensile strains in the topping indicate a widespread and fully developed cracking pattern but with lower strains than the DIC measurements. The fully developed crack pattern and smaller spacing between cracks in the topping is explained because higher stresses transfer from the precast girder as the two are perfectly bonded. On the other hand, debonding is reported in the experiment and stresses are not fully transferred in the regions where the two elements are debonded. Figure 5.11 reports higher maximum crack width in the topping as compared to DIC measurements because the numerical simulation shows more cracks at a lower spacing.

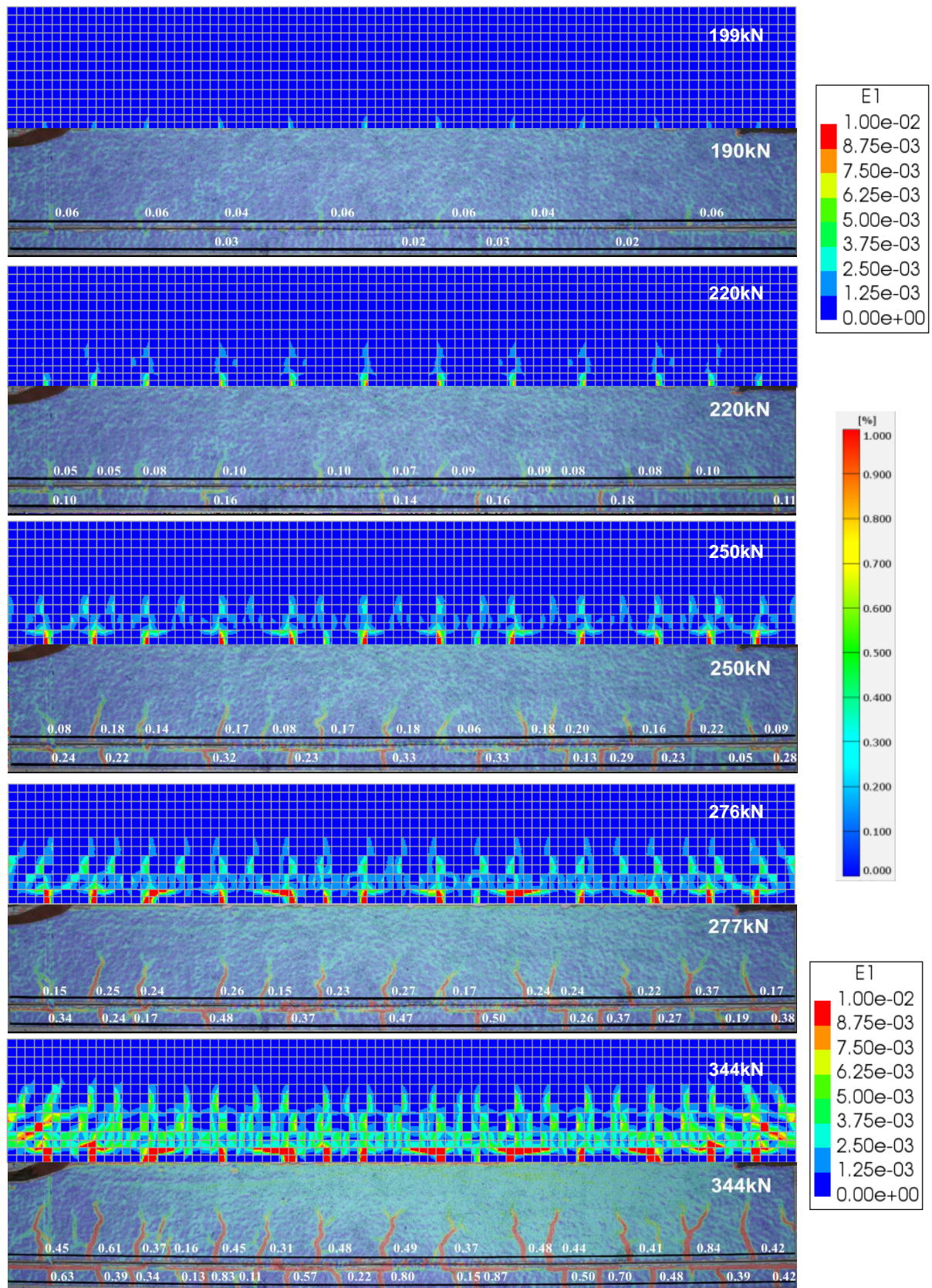


Figure 5.9. Maximum principal strains from DIC measurements and NLFEA at different load levels

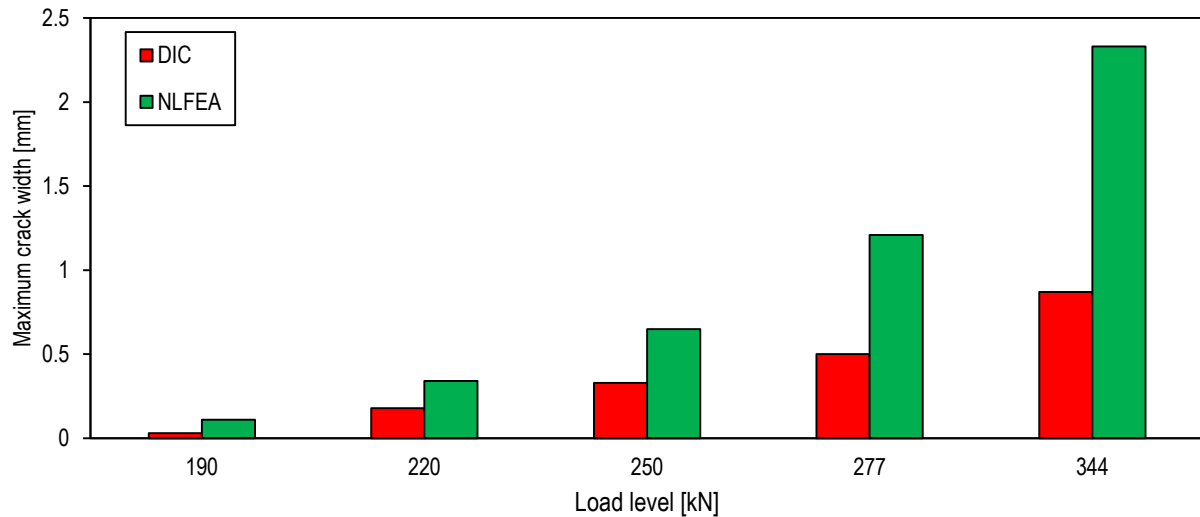


Figure 5.10. Maximum crack widths in precast girder (Experimental vs NLFEA)

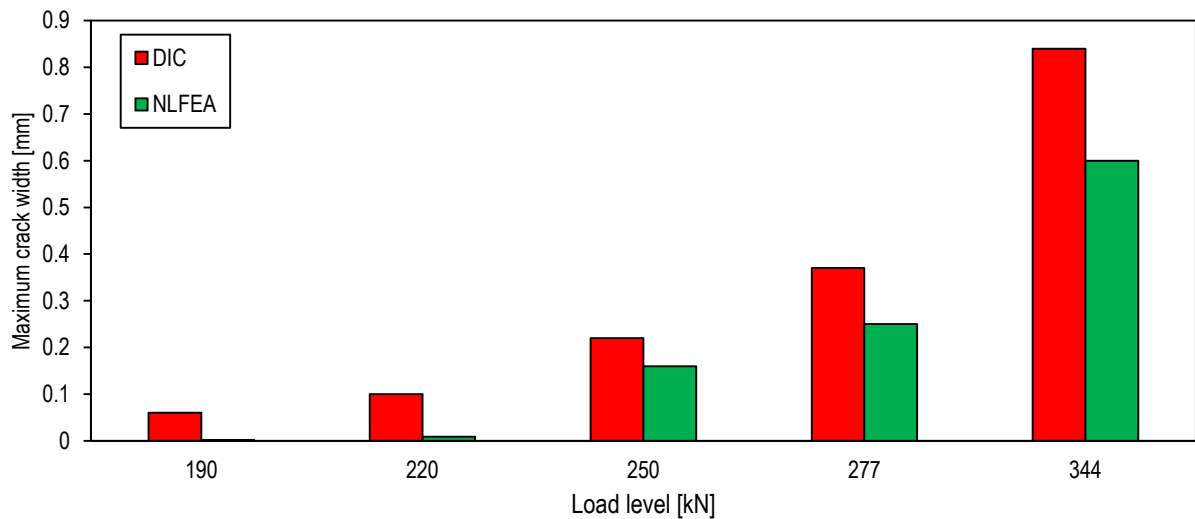


Figure 5.11. Maximum crack widths in cast in-situ topping (Experimental vs NLFEA)

5.3 Sensitivity analysis

A sensitivity analysis is performed to explore the effect of the varying elastic modulus of geopolymer concrete at 28 days cured at different conditions. An additional two NLFEA of the flexural test are performed for the other curing conditions as defined in Table 2.6 (standard curing and drying after 7 days). Furthermore, an extra benchmark NLFEA is performed using material parameters of OPC concrete as input. In the case of the first two analyses, only the elastic modulus (and consequently the prestressing forces) are modified. On the other hand, the benchmark analysis for OPC concrete required the modification of the elastic modulus, tensile strength, transmission length, shrinkage strains and creep coefficient (and consequently the prestressing forces too). The properties for OPC concrete are as calculated in 3.3.3.2 and 3.3.4.2 according to EN 1992-1-1 [22]. An overview of the parameters for the sensitivity analysis are presented in Table 5.1. A comparison of the prestressing of the benchmark analysis, the main analysis and the two extra analyses is displayed in Figure 5.12.

Figure 5.13 presents the load – deflection response to the flexural test of the four NLFEA and the experimental test.

Table 5.1. Parameters sensitivity analysis

Structural member	Age [days]	Parameter	Units	Geopolymer concrete			OPC concrete
				Drying after 7 days	Drying after 14 days	Standard curing	
Precast girder	2.5	E	MPa	25000			33350
		f_{ct}	MPa	2.80			3.00
		l_{pt}	mm	498			470
		σ_{pm0}	MPa	1270.81			1298.60
	30	E	MPa	24900	27500	30650	35650
		f_{ct}	MPa	3.60			3.62
		σ_{pm30}	MPa	993.42	1003.69	1014.23	1172.94
60	σ_{pm60}	MPa	932.90	944.80	957.00	1130.10	
Cast in-situ topping	30	E	MPa	26400	27100	32600	34550
		f_{ct}	MPa	3.00			3.33

The prestressing force at 2.5 days is the same for the three analyses of geopolymer concrete girders since the curing regimes are changed in later stages. On the other hand, the prestressing of the OPC concrete girder is slightly higher since the elastic losses are lower due to the higher elastic modulus at 2.5 days. Furthermore, the same explanation holds for the variation of the prestressing force at 30 and 60 days within the geopolymer concrete members. The prestressing is higher for samples exposed later to drying since the elastic modulus is also higher, hence the elastic and creep losses are lower as both are inversely proportional to the elastic modulus. The prestressing of the OPC concrete girder at 30 and 60 days is significantly higher than the geopolymer concrete counterparts for the same reason but mainly due to lower creep and shrinkage losses.

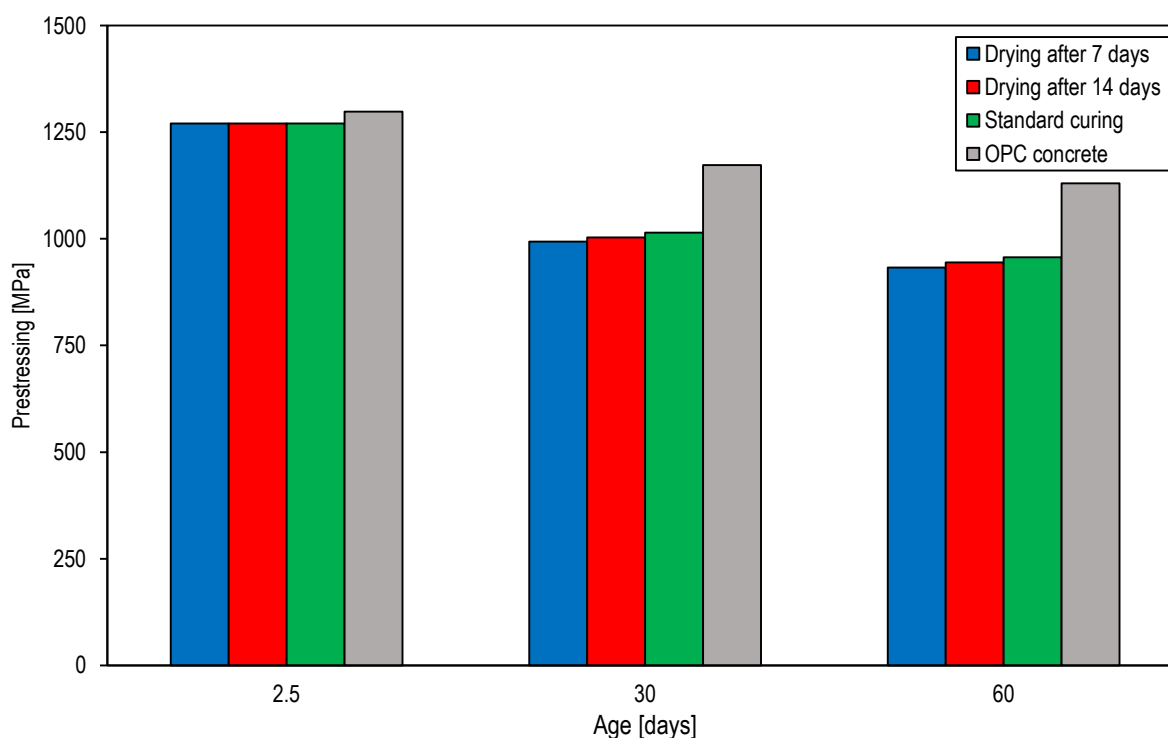


Figure 5.12. Prestressing of precast girders at different ages for geopolymer concrete under different curing conditions and OPC concrete

The four NLFEA and the experimental results have the same qualitative behavior in terms of the load – deflection response, flexural stiffness, cracking load and ultimate load. The results are coincident with the observations of the flexural behavior of reinforced specimens analyzed in 2.3.1.1 which also report similar behavior of geopolymer concrete and OPC concrete girders. The elastic modulus after 30 days is between 14 and 30% lower for geopolymer concrete than OPC concrete for the different curing conditions (Table 5.1). The flexural stiffness is calculated as the slope in the linear part of the load – deflection curve and is equal to 13.2, 14.1, 16.1 and 17.9 kN/mm for the geopolymer (drying after 7, 14 days and standard curing) and OPC concrete girders, respectively. Therefore, the flexural stiffness is 10 to 26% lower for geopolymer than OPC concrete girders. The discrepancy in flexural stiffness is lower than the difference in elastic modulus and coincides to a certain extent with an experimental study [46] presented 2.3.1.1, even though in that case the difference in flexural stiffness for geopolymer and OPC concrete girders was lower. The cracking load of geopolymer concrete girders is independent of the flexural stiffness and only the OPC concrete girder show a higher cracking load since the prestressing losses are lower. The behavior of the geopolymer concrete girders after cracking is similar as the difference in elastic modulus has a marginal effect in the short-term load – deflection response. On the other hand, the load-carrying capacity of the OPC concrete girder is higher than the geopolymer concrete counterparts for the same midspan deformations before reaching the plateau. Therefore, it can be stated that the geopolymer concrete girders undergo higher deformations or have a lower load-carrying capacity. Finally, the maximum load is the same for the four analyses, hence the difference in elastic modulus (between geopolymer concrete under different curing conditions), shrinkage strains and creep coefficient between geopolymer and OPC concrete have a marginal effect in the maximum short-term load-carrying capacity of a flexural member. This is in line with the observation by Prinsse, et al. [34] that describe a negligible effect to the decrease in material properties of geopolymer concrete in the structural behavior of reinforced girders.

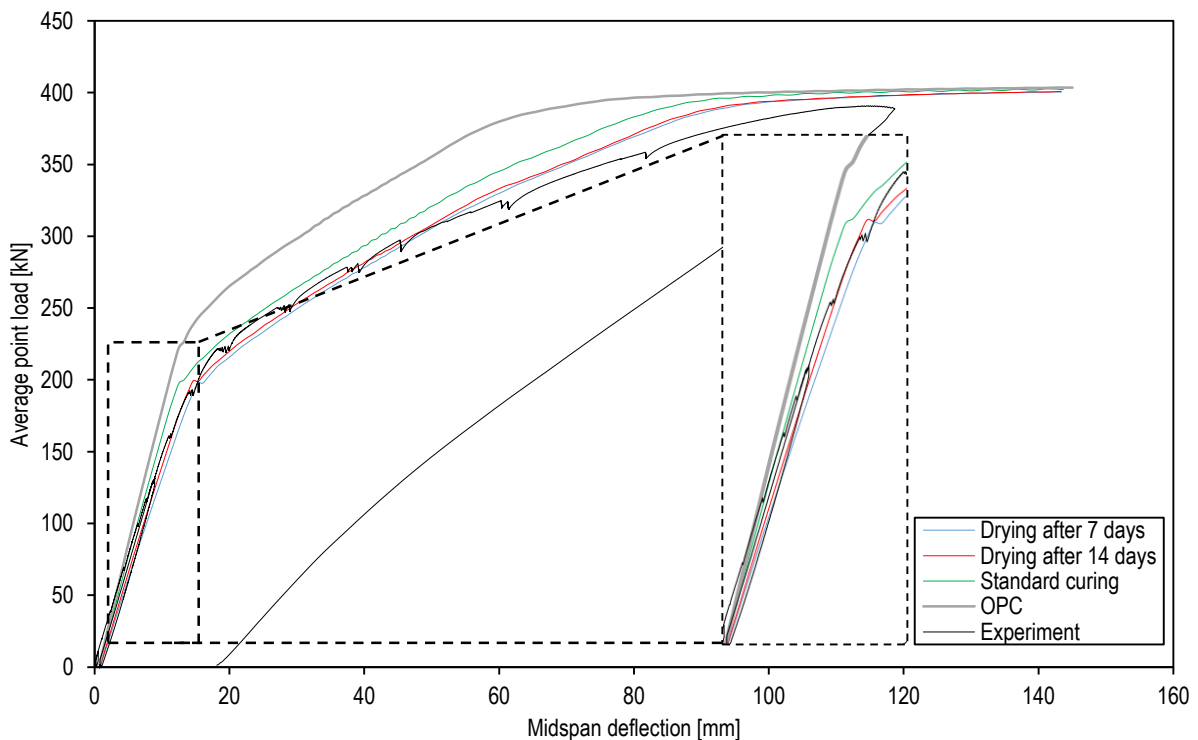


Figure 5.13. Sensitivity analysis Load - deflection curves

5.4 Short-term shear behavior

5.4.1 Load – deflection

Figure 5.14 presents the load – deflection response as measured from the experiment and the curve obtained numerically by means of the NLFEA for the shear test. Figure 5.15 and Figure 5.16 display the maximum deformation and load at failure as determined analytically, numerically and from the experiment.

The load – deflection curve is approximately linear elastic until cracking and the initial slope is almost the same for the NLFEA and the experiment. The change in slope occurs at similar load levels (around 460 kN) and is caused by the propagation and widening of diagonal cracks. The numerical simulation curve starts to separate from the experiment when the shear critical crack starts to propagate to the topping. The response of the NLFEA is stiffer which leads to a higher shear resistance (by 12%) obtained numerically as shown in Figure 5.16. Conversely, the analytically determined shear capacity is 16% lower than the experiment. Additionally, the notable difference is in the ductility displayed by the numerical model which is 35% higher than the experiment. The higher deformations and load carrying capacity are due to a stiffer cross-section in the numerical model caused by the perfect bond between the precast girder and the topping. This condition implies that the cross-section is fully composite, whereas in the experiment debonding is reported in the cross-section and the stresses do not transfer fully as in the numerical model. The fully composite cross-section can attain higher stresses and hence deformations.

As previously described in 5.2.1, the numerical models from RTD 1016-3B [72] and RTD 1016-3 [73] report higher resistances with the NLFEA with no safety format (i.e. without partial factors and mean material properties from testing) than the experiment. Nevertheless, the numerical prediction with perfect bond is not on the safe side as the short-term shear resistance is overestimated. The analytical model as defined in EN 1992-1-1 [22] is conservative as it does not consider the contribution of concrete to the shear strength, aggregate interlock and dowel action of the longitudinal reinforcement. Therefore, a conservative estimate of the short-term shear resistance is possible with the analytical model as described in this study. It is recommended that different loading conditions are performed to analyze the SLS performance where deformations are of principal importance.

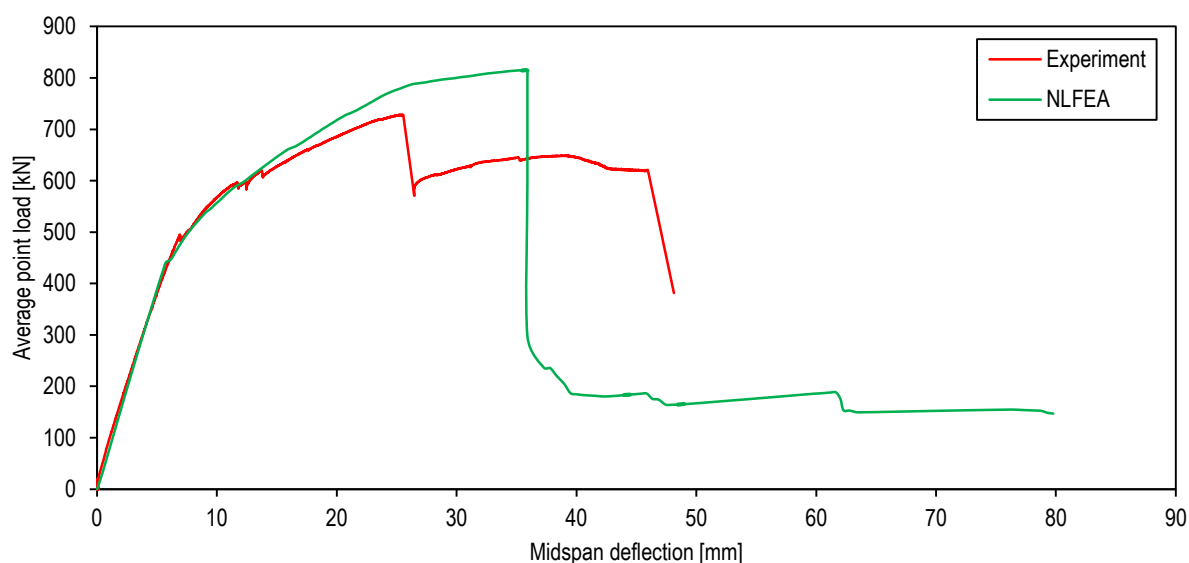


Figure 5.14. Load - deflection curve during shear test (Experimental vs NLFEA)

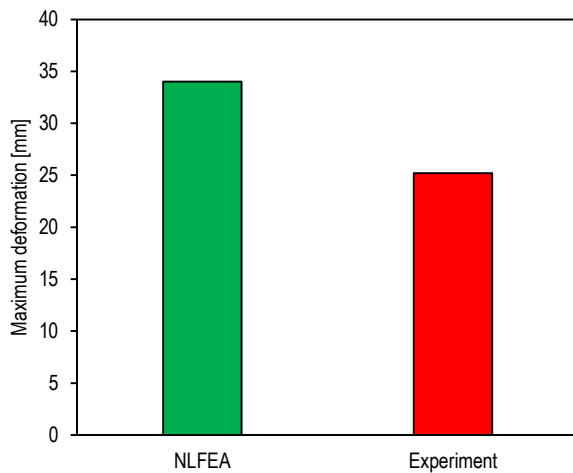


Figure 5.15. Maximum deformation under point of application of loading

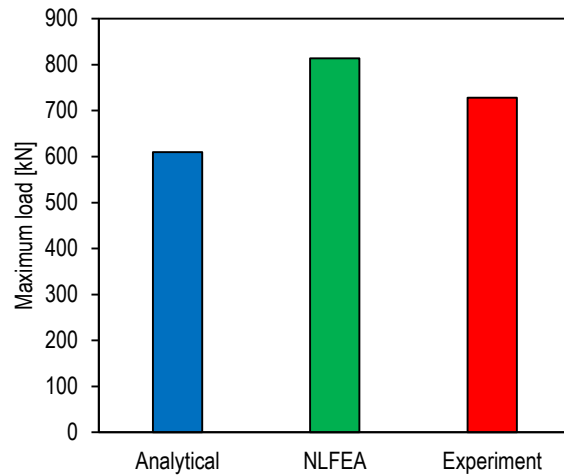


Figure 5.16. Shear capacity

A Mohr-Coulomb interface with tension cutoff was considered to improve the numerical model to more accurately describe the shear behavior by accounting for the debonding between the precast girder and the topping. However, in a 2D plane stress analysis the interface elements are defined as structural line interfaces of a certain thickness. This only allows to apply the interfaces along the horizontal plane (in red) in Figure 5.17, whereas the vertical plane (in blue) is still perfectly bonded. The difference in stiffness between the two planes causes a numerically-ill stiffness matrix and divergence of the solution method for the NLFEA. This is a limitation of the 2D plane stress analysis as a full 3D analysis would be required to define an interface in the horizontal and vertical planes. Observe that the Rijkswaterstaat Guidelines for Nonlinear Finite Element Analysis of Concrete Structures [23] suggest a 2D plane stress analysis and do not define the use of interfaces between elements cast at different stages. Furthermore, initially the debonding crack opening was not a phenomenon to be described by the present numerical model. The particular shape of the cross-section of the specimen makes it difficult to apply interfaces between the precast girders and the topping. For bridges with inverted T girders with a deck on top, the interface could be applied along a single horizontal plane.

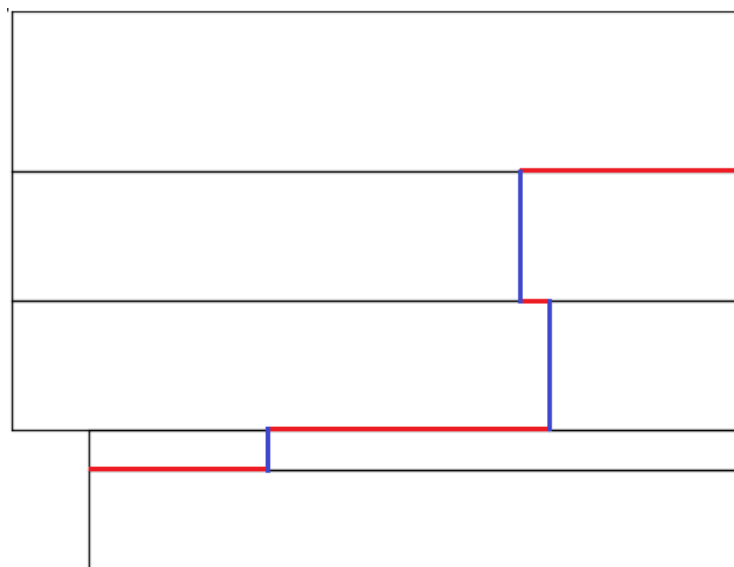


Figure 5.17. Line interfaces in 2D plane stress model

5.4.2 Failure mode

Figure 5.18 displays the maximum principal strains at failure from the numerical simulation and the DIC measurements at the maximum load level before failure by the critical shear crack in the topping. Furthermore, failure in the experiment is also due to the delamination crack in the interface between the precast girder and the topping and slippage of the prestressing tendons. The two latter phenomena are not modelled in the numerical simulation since perfect bond between the geopolymer concrete elements is assumed and the tendons are modelled as embedded reinforcement. The position and orientation of the shear critical crack from the NLFEA is consistent with the DIC observations. Furthermore, the position of the cracks in the bottom of the precast girders are coincident as well.

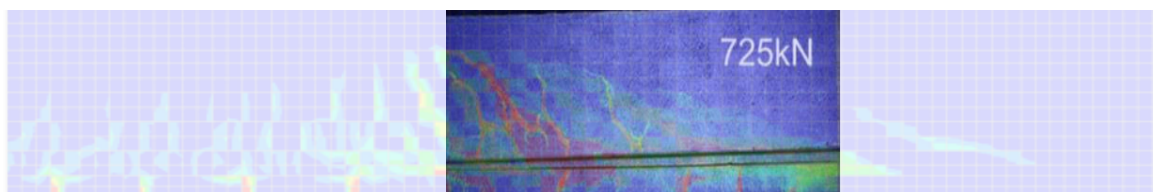


Figure 5.18. Cracking pattern at failure from NLFEA and DIC measurements

5.5 Long-term flexural behavior (after 9 months)

The effect of the long-term material properties (e.g. elastic modulus, creep and shrinkage) of geopolymer concrete is explored by the NLFEA of the specimen tested in flexure by 4-point loading after being subjected to self-weight for 9 months. A comparison of the externally applied loads in the NLFEA of the flexural test and the flexural after 9 months is displayed in Figure 5.19. Figure 5.20 presents the load – deflection response to the flexural test after 9 months of the NLFEA and the experimental test. The analysis of the flexural test after 9 months required the modification of the elastic modulus, shrinkage strains and creep coefficient (and consequently the prestressing forces too). An overview of the parameters for the analysis are presented in Table 5.2.

As stated in 3.2.2, after casting of the in-situ topping the specimens subjected to sustained loading are covered in plastic. The effect of sealed curing conditions on the elastic modulus of the ready-mix geopolymer concrete mixture are explored by material testing as described in 3.3.3.1 and Figure 3.10. As previously discussed, the elastic modulus seemed to be stable after exposed to drying when sealed at early ages, therefore the measurement of the elastic modulus at 60 days is used for the analysis after 9 months as measurements at this age are not available. The elastic modulus of the ready-mix geopolymer concrete mixture is the lowest for this set of curing conditions but degradation of the stiffness due to microcracking is expected so the results shall be analyzed accordingly. On the other hand, the elastic modulus for sealed conditions are not available from the material tests for the SCGC mixture. Therefore, the default selection of curing conditions (drying after 14 days) as the benchmark analysis of the flexural test are used for this analysis. Furthermore, the shrinkage strains and creep coefficients at 270 days (9 months) from the material tests of the SCGC mixture as displayed in Table 3.12 are used to calculate the input of the prestress force after losses in the numerical model of the flexural test after 9 months. From the monitoring results (3.6.2), the total deformation of the specimens is overestimated when scaling the results from material samples at structural level. On the other hand, the scale of effect of shrinkage causes that in smaller samples shrinkage develops and stabilizes faster whereas in larger samples it takes more time to stabilize, hence the shrinkage deformation may not yet be stable after 9 months.

Table 5.2. Parameters analysis flexural test after 9 months

Structural member	Stage	Parameter	Units	Flexural test	Flexural test after 9 months
Precast girder	Prestressing	E	MPa	25000	25000
		σ_{pm0}	MPa	1270.81	1270.81
	Testing	E	MPa	27500	27500
		$\sigma_{pm\infty}$	MPa	944.8	791.6
Cast in-situ topping	Testing	E	MPa	27100	25670

From Figure 5.19 is observed that the effect of the larger shrinkage strains and creep deformations over time of geopolymer concrete is translated in higher prestress losses. The prestress loss at 60 days is 26% whereas it increases to 38% at 270 days.

The linear elastic behavior displayed by the numerical results in Figure 5.20 does not capture accurately the behavior of the specimen. The difference of the slope in the ascending branch between the numerical simulation and experimental results is evident and is caused by the choice of the elastic modulus and the loading scheme in the numerical model. As described in 3.6.5.2, the specimen is cracked before the mechanical test and a decrease of the stiffness over time is expected since the elastic modulus decreases after exposed to drying as indicated from material tests in 3.3.3.1. For such reason, the experimental curve does not display a linear behavior and the degradation of stiffness is already noticeable from the start of the flexural test. Furthermore, the load in the numerical model is not applied with the load cycles with high load levels as in the experiment (Figure 3.26) which cause degradation of the stiffness. Therefore, the elastic modulus measured at 60 days is not appropriate to capture the behavior of the structure in the long-term. Nevertheless, the load – deflection response from the numerical simulation provides an acceptable fit to the experimental results as cracking progresses.

Furthermore, the externally applied load for reaching the tensile strength in the bottom fibre and for discrete cracking of the precast girder decrease in the specimen after 9 months (due to the higher prestress losses) by 17% and 15%, respectively. The cracking resistance in prestressed members is of critical importance (as important as the load carrying capacity) since the full prestressing design assumes the specimen will remain uncracked over the service lifetime. The creep and shrinkage deformations do not appear to stabilize after 9 months, hence the prestress losses will continue to increase over time and the cracking resistance will continue to decrease. The design criteria of conventional concrete structures based on the estimation of material properties from the 28-day compressive strength result in non-conservative estimates of the cracking resistance of prestressed geopolymer concrete members which can lead to an unsafe design.

The maximum load in the flexural test after 9 months is overestimated by 5% in the numerical simulation as compared to the experimental results. The numerical simulation has some intrinsic limitations due to the modelling assumptions which did not allow to fully describe the failure mechanism and the evolution of damage from the experiment. In particular, the perfect bond assumption between geopolymer concrete members and between the prestressing steel and the SCGC girder. The failure mode of the specimen is characterized by anchorage failure of the prestressing tendons and debonding between the precast girder and cast in-situ topping. The two phenomena are not captured in the numerical simulation. Nevertheless, the difference in the maximum load carrying capacity with the experiment may be deemed acceptable and the assumption of perfect bond on the short and long-term flexural resistance has a smaller impact than for the short-term shear resistance.

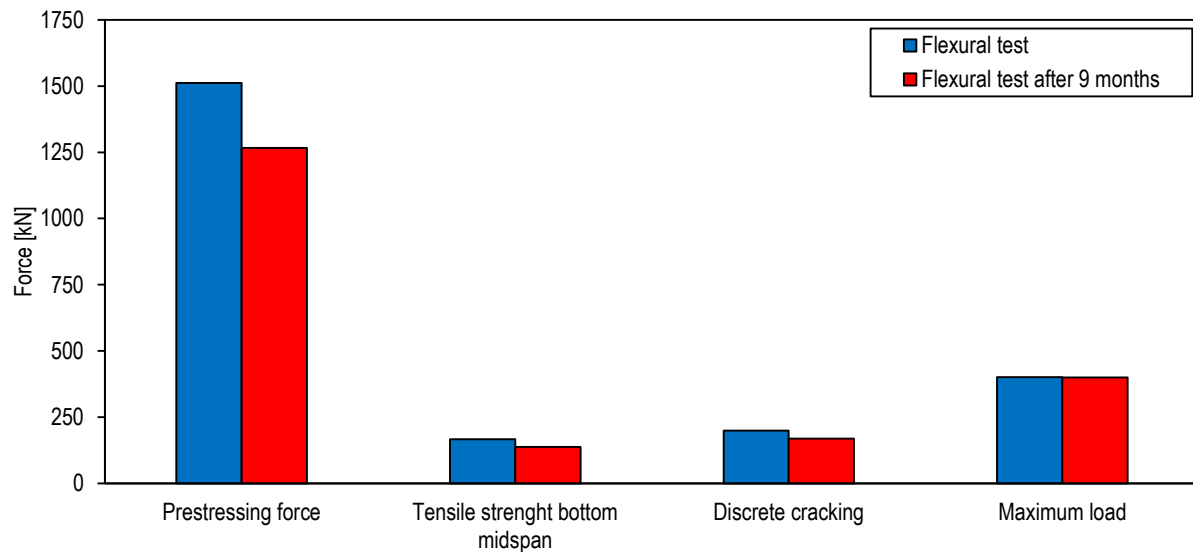


Figure 5.19. Comparison of forces flexural test vs flexural test after 9 months (NLFEA)

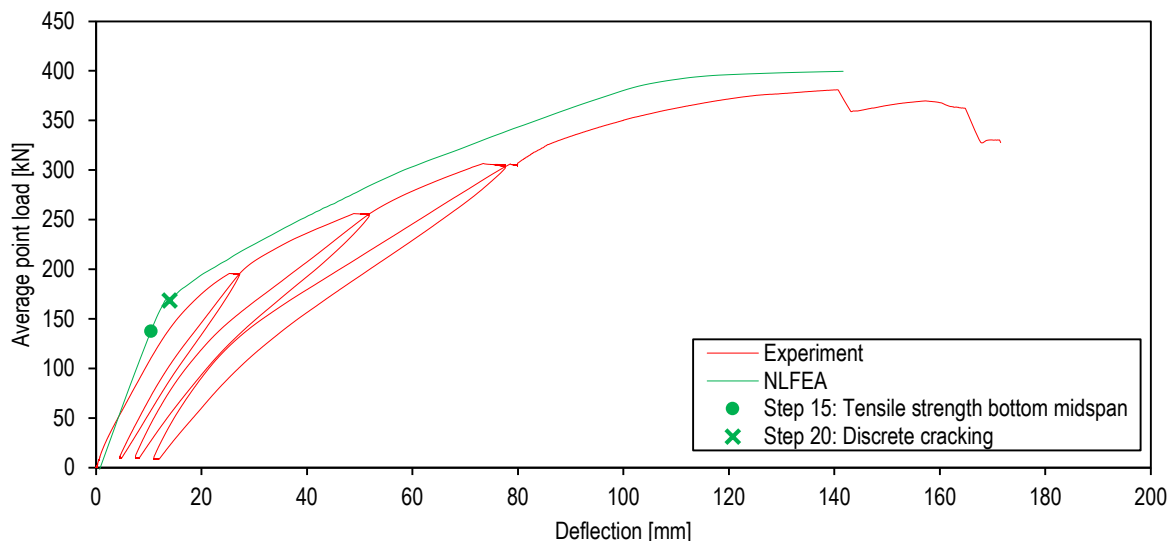


Figure 5.20. Load - deflection curve during flexural test after 9 months (Experimental vs NLFEA)

Figure 5.21 displays the load – deflection response from the numerical simulation and experimental results of both the flexural test and the flexural test after 9 months. The cracking load is decreased by 15% in the specimen after 9 months, and as previously mentioned this is critical for the performance over the service lifetime of the structure. The maximum experimental load (even though the specimen did not reach failure) and the predicted resistance from the numerical analysis of the flexural test are 4% and 5% higher than the maximum load at failure of the flexural test after 9 months, respectively. The maximum load decreases slightly between the NLFEAs of the specimen subjected to the flexural test after 28 days of casting of the topping and the specimen subjected to the flexural test after 9 months. As previously indicated, the size effect will cause shrinkage to develop and stabilize over a longer time span hence the prestress losses can continue to increase even though from the monitoring measurements it appears that the shrinkage and creep deformations from the structure are lower than from the material samples. The numerical model based on the material properties at 28 days can result in non-conservative estimates of the load carrying capacity and the long-term creep and shrinkage deformations shall be monitored for a longer time span to judge the structural performance over the service lifetime.

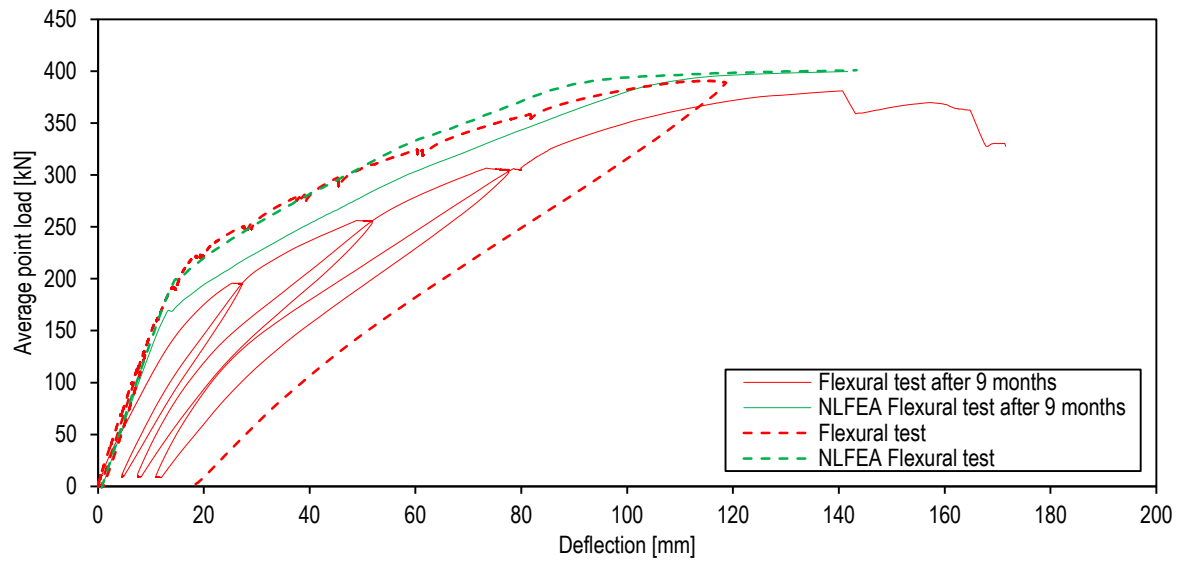


Figure 5.21. Load - deflection curve during flexural test and flexural test after 9 months (Experimental vs NLFEA)

6

Conclusions and future work

This chapter connects the most relevant findings reported in the present study to the research questions. Practical recommendations for the use of geopolymer concrete in engineering practice and directions for further research are suggested.

6.1 Conclusions

The present study focused on the upscaling of two geopolymer concrete mixtures in structural elements consisting of an individual prestressed girder with a compression layer on top. The precursor of the mixture of the precast girder was GGBFS and the activator was a solution of sodium silicate and sodium hydroxide. The first mixture was developed by TU Delft and was used for the construction of a precast geopolymer concrete girder whereas the reinforced topping was cast with a ready-mix geopolymer concrete mixture. Several studies report higher creep and shrinkage, and a decrease of the elastic modulus over time for geopolymer concrete as compared to OPC concrete, which puts in doubt whether the specimens fulfill the criteria for structural performance for conventional prestressed structures. The main objectives of the present study were to determine the impact of these different material properties on the performance of the structural elements subjected to shear and flexure structural tests; the study intended to address how to deal with the material differences for applying the current methods of analysis for conventional concrete structures (EN 1992-1-1 and the Rijkswaterstaat's Guidelines for NLFEA) and to what extent the theoretical foundation, material constitutive models and general practice of design based on the 28 day compressive strength for OPC concrete were applicable for the analysis of geopolymer concrete structures. The study described (and compared with experimental results) the deformations, load-deflection response, principal strains, normal stresses, damage evolution, cracking stages, maximum load and failure mechanism of the specimens subjected to mechanical tests.

RQ1 (1): How different are the time-dependent material properties (e.g. elastic modulus, creep and shrinkage) of the two geopolymer concrete mixtures compared to conventional concrete of similar strength class?

The development of the elastic modulus over time was studied for both geopolymer concrete mixtures as it is reported that the elastic modulus of geopolymer concrete starts to decrease due to microcracking when exposed to drying [30]. The elastic modulus was determined experimentally by testing prismatic samples (100x100x400 mm³) at different ages according to ISO 1920-10:2010 [64] and EN 12390-13 [65]. The samples were kept in standard curing conditions or exposed to drying after 3, 7, 14 or 30 days to assess the influence of curing conditions in the development of stiffness. The elastic modulus of the samples under standard curing conditions slightly increased over time and appeared to be more or less stable. Conversely, the elastic modulus of both mixtures decreased when exposed to drying with a 10% decrease in the elastic modulus at 28 days when exposed to drying after 14 days as compared to standard curing. Moreover, the stiffness of air-exposed samples continued to reduce over time, reporting a decrease of 15-26% at 56 days for the SCGC mixture of the precast girder and 7-19% for the mixture of the topping, when exposed to drying at 28 and 7 days, respectively. Therefore, the reduction of elastic modulus is intrinsically related to the drying process.

The elastic modulus of samples exposed to drying at early ages (≤ 7 days) seemed to stabilize after 30 days, however the initial exposure to drying was accompanied by a lower stiffness as compared to samples exposed to drying at later stages. Consequently, the elastic modulus of geopolymer concrete was compared to estimates for OPC concrete from EN 1992-1-1 [22] as several studies suggest that the elastic modulus of ambient cured geopolymer concrete is lower than OPC concrete of similar strength class and is overestimated by standards and empirical equations from OPC concrete codes [11, 16, 30, 36]. The elastic modulus of both mixtures were consistently lower than the estimates for conventional concrete of the same strength class from EN 1992-1-1 [22], regardless of the curing conditions. The elastic modulus at 30 days of the two mixtures were 22-30% lower when exposed to drying and 6-14% lower for standard curing as compared to OPC concrete estimates. From the literature study in 2.2.2.3, the elastic modulus of geopolymer concrete at 28 and 90 days are 25-30% and 22-31% lower than OPC concrete, respectively. In conclusion, the application of the concrete standard to determine the elastic modulus of geopolymer concrete leads to non-conservative estimates but a rough estimate can be obtained with a reduction of 30% of the elastic modulus of OPC concrete of the same strength class.

Finally, the elastic modulus of the geopolymer concrete mixtures was compared to the estimates from empirical relations from several studies on geopolymer concrete with different choices of precursors, activators and curing conditions [11, 16, 36]. None of the empirical equations gave a satisfactory fit to the experimentally determined elastic modulus of both mixtures. The lowest estimates of elastic modulus were calculated with an equation for fly ash-based geopolymer concrete [11] as the elastic modulus of ambient cured samples increases for higher slag content. The highest estimates were obtained for an equation for GGBFS-based geopolymer concrete with calcium silicate as activator [36] because the high calcium content increases the amount of C-S-H gel in the hardened binder phase and the elastic modulus was closer (but still lower) to OPC regardless of curing conditions. The best fit to the elastic modulus of the geopolymer concrete mixtures was obtained with an equation for heat-cured fly ash-based geopolymer [16]. As a result, a conclusive framework for estimating the elastic modulus from the compressive strength as for OPC concrete is unavailable because the wide variety of choices and combinations of the constituent materials and curing conditions are inherently related to the development of stiffness.

The shrinkage and creep behavior of the SCGC mixture of the precast girder were also studied from prismatic samples [58] since literature suggests that GGBFS-based geopolymer concrete exhibits a considerably larger shrinkage and creep than OPC concrete regardless of the exposure conditions [35, 37]. The drying shrinkage of SCGC at 30 days is 32% higher than the estimate from EN 1992-1-1 [22] for OPC concrete but increases to 73% at 60 days. The creep coefficient of SCGC at 30 days is almost the same as the prediction model from EN 1992-1-1 [22] for OPC concrete but at 60 days the creep coefficient increases for SCGC whereas for OPC it remains constant. The increase of creep and shrinkage between 30 and 60 days suggest a pronounced viscous mechanical response of geopolymer concrete caused by the rearrangement and reorganization of the C-A-S-H gel structure as reported from literature [37], whereas in OPC concrete the volume change is caused by capillary forces arising in the empty voids due to the moisture loss to the environment for OPC concrete. Samples cured at 25°C for 1 day and 20°C until 28 days were tested for autogenous shrinkage in a ADTM [58]. The development of autogenous shrinkage over 28 days was compared to the curve obtained from EN 1992-1-1 3.1.4 (6) [22]. The exponential function to describe the development of autogenous shrinkage of OPC concrete may be suitable to describe the behavior of SCGC but the final autogenous shrinkage of SCGC, obtained by curve-fitting, is significantly higher (an order of magnitude) than the estimate for OPC concrete. The linear prediction of the final autogenous shrinkage $\varepsilon_{ca}(\infty)$ from the compressive strength from EN 1992-1-1 [22] is not applicable for GGBFS-based geopolymer concrete. For such reasons, the isotropic elasticity-based prediction models for OPC concrete appear not to be adequate to predict the visco-elastic/viscoplastic material response both for creep and shrinkage, especially in the long-term, as they both largely underestimate the behavior of geopolymer concrete and lead to unsafe design assumptions.

The prediction models to determine the material properties from the 28-day compressive strength as defined in EN 1992-1-1 [22] for conventional concrete do not capture the long-term material properties (e.g. elastic modulus, creep and shrinkage) of the geopolymer concrete mixtures from this study and result in non-conservative estimates. Therefore, it is advised to only consider the structural application of geopolymer concrete mixtures which have been extensively studied in material scale in terms of constituent materials, curing conditions, microstructure, mechanical properties and volume stability not only at 28 days but more importantly in the long-term. Furthermore, it is advised to further continue testing the material samples from the two geopolymer concrete mixtures used in the present study to determine if the decrease of stiffness and the viscoelastic behavior stabilize at some point.

RQ1 (2): What is their influence in the response of a prestressed girder with reinforced cast in-situ topping to prestressing and mechanical tests?

The insights from the study on the material properties posed a critical impediment for the generalized applicability of geopolymer concrete in a prestressed structure since a lower elastic modulus and higher shrinkage and creep implicate larger deflections and higher prestress losses, thus compromising the structural performance. A comparison of the camber after prestressing of the specimens to OPC concrete C60/75 precast girders with similar geometry and prestressing layout produced by Haitsma Beton, a sensitivity study, consisting on the experimental results, three NLFEA on SCGC and an extra benchmark NLFEA on OPC concrete, and the NLFEA of a specimen tested in flexure after 9 months, were performed to estimate the influence of the varying elastic modulus cured at different conditions and the higher creep coefficient and shrinkage strains as compared to OPC concrete, in the structural response of the prestressed girder after the application of the prestressing force and of the composite section with the cast in-situ topping to the 4-point load flexural test at different ages (28 days and 9 months after casting of the topping).

The camber after prestressing is proportional to the flexural stiffness as the behavior of the structure is elastic and the results showed a higher camber for SCGC girders as the elastic modulus is lower than for OPC concrete of a higher strength class. The decrease of elastic modulus over time and the higher creep deformations due to the visco-elastic/viscoplastic response of geopolymer concrete, explain why the camber of the SCGC girders continues to increase over time (from 2.5 to 7 days) whereas it is stable for OPC concrete girders (from 1 to 28 days). The elastic modulus, creep and shrinkage influence the prestressing force by the elastic, creep and shrinkage losses. The prestressing of the OPC concrete girder at 2.5 days was slightly higher than the SCGC counterparts (lower elastic losses due to higher elastic modulus) and was significantly higher at 30 and 60 days, mainly due to lower creep and shrinkage losses. The prestressing force was lower for SCGC girders modelled with material properties of samples exposed earlier to drying due to the associated decrease of the elastic modulus as exposed beforehand.

The four NLFEA of the short-term flexural test with varying elastic modulus and the experimental results had the same qualitative behavior in terms of the load – deflection response, flexural stiffness, cracking load and ultimate load. The studies on the flexural behavior of reinforced geopolymer specimens (2.3.1.1) also report similar behavior of geopolymer concrete and OPC concrete girders. The load – deflection response was initially linear elastic and the flexural stiffness was 10 to 26% lower for geopolymer concrete than OPC concrete girders. The cracking load of geopolymer concrete girders was independent of the flexural stiffness and only the OPC concrete girder showed a higher cracking load since the prestressing losses are lower. The decrease in elastic modulus in the geopolymer concrete mixtures had a marginal effect in the short-term load – deflection response as the three numerical models and the experimental results display a similar behavior. The load-carrying capacity of the OPC concrete girder was higher than the geopolymer concrete counterparts.

Regarding the long-term flexural behavior, the prestress losses increase from 26% after 28 days to 38% after 270 days due to the larger shrinkage strains and creep deformations over time of geopolymer concrete. The creep and shrinkage deformations do not appear to stabilize after 9 months, hence the prestress losses will continue to increase over time. The effect of the increasing prestress losses is a reduction of the cracking resistance which is of critical importance (as important as the load carrying capacity) in prestressed members since the full prestressing design assumes the specimen will remain uncracked over the service lifetime. The cracking load from the numerical simulation of the flexural test after 9 months is reduced by 15% as compared to the short-term flexural test. The maximum load decreases slightly between the NLFEAs of the specimen subjected to the flexural test after 28 days of casting of the topping and the specimen subjected to the flexural test after 9 months.

RQ2: To what extent are the methods of analysis for conventional concrete structures, from EN 1992-1-1 [22] and the Rijkswaterstaat's Guidelines for NLFEA [23], applicable to estimate the flexural and shear capacity of the test specimen consisting of a prestressed girder with reinforced cast in-situ topping built with geopolymer concrete?

The analysis of the prestressed girder with reinforced cast in-situ topping subject to prestressing and mechanical tests was performed by means of analytical models and numerical simulations. The analytical model was based upon the design philosophy for conventional concrete structures as described in EN 1990 [67] and EN 1992-1-1 [22]. The numerical model was performed in commercial FE software DIANA and consisted in a 2D linear and nonlinear phased analysis in plane stress conditions. The modelling choices were as suggested by the Rijkswaterstaat's Guidelines for NLFEA of Concrete Structures [23] to ensure the quality and robustness of the analysis. The analytical and numerical models were

refined with the input from the material tests on the mechanical properties (compressive strength and elastic modulus) and volume stability properties (creep coefficient, autogenous shrinkage and drying shrinkage) of the geopolymer concrete mixtures as deviations to the properties of OPC concrete were identified, as previously described.

The flexural analytical model was based on the Euler Bernoulli beam theory where plane sections remain plane and normal to the axis of the flexural member, and the strains vary linearly over the height of the cross-section. The normal stresses also vary linearly over the height of the cross-section before cracking when the normal stresses reach the tensile strength of concrete. The resistance of the cracked cross-section was determined from the concrete compressive force (bilinear stress block in the compression zone), the tensile forces in the prestressing steel and the prestressing force. The height of the compression zone was determined by an iterative calculation of equilibrium of forces in the cross-section. The shear analytical model was based on the truss model and the shear resistance is obtained from vertical equilibrium of the concrete compressive strut and the steel tensile tie which is equivalent to a number of closed stirrups over a certain distance. The truss model is conservative as it does not consider the contributions of concrete and the secondary load carrying mechanisms (dowel action and aggregate interlock) to the shear resistance.

The numerical simulation was modelled with 8-noded quadrilateral plane stress elements for the geopolymer concrete members (also the loading and support plates), embedded truss elements for the reinforcement steel and prestressing tendons, and zero-thickness structural interface elements. Perfect bond was assumed between geopolymer concrete members and with the embedded reinforcement and prestressing steel. The geopolymer concrete constitutive model was a total strain based orthogonal rotating crack model with exponential tension softening and parabolic compressive relation, reduction of the compressive strength due to lateral cracking with a lower bound of 0.6, confinement effects on the compressive strength and reduction of the Poisson ratio dependent on damage. The constitutive model for the reinforcement steel was ideal plasticity and for the prestressing steel it was hardening plasticity. The iteration procedure was Regular Newton-Raphson method with arc-length control. Force and energy norms were adopted as convergence criteria. The convergence behavior of the nonlinear analysis for both mechanical tests were satisfactory, hence the solution procedure and the convergence criteria are adequate.

The initial slope of the load – deflection curve was almost the same for the NLFEA and the experiment both for flexural and shear short-term tests. For the flexural test, the stress distributions at characteristic phases in the linear elastic regime (prestressing, decompression and cracking of the bottom fiber) and the cracking load, were practically equal from the analytical and numerical models; the cracking load was 3% higher than the experiment. The change in slope in the load – deflection diagram occurred at similar load levels for the experiment and numerical simulation (190 kN for the flexural test and 460 kN for the shear test) and was caused by the evolution of cracking. Therefore, the linear elastic behavior of the specimen was accurately described both by the analytical model based on the Euler Bernoulli beam theory and the numerical simulation with plane stress elements.

The specimen did not fail during the flexural test but the hydraulic jack reached the maximum stroke. The maximum load attained during testing was considered as the flexural resistance since the specimen was retested months after and the load at failure was lower. In the numerical model, failure was considered as the load – deflection diagram reached a horizontal plateau of increasing deformations for an invariable externally applied load. The predicted flexural resistance was slightly higher (8% by analytical model and 3% for the numerical simulation) than the maximum load attained during testing. The bilinear compressive stress

block assumed for ULS calculations as per EN 1992-1-1 [22] was not the same stress profile from the NLFEA but the areas of the stress diagrams were almost equal. The shear failure was characterized by a shear critical crack in the topping and the position and orientation of the shear critical crack from the NLFEA was consistent with the DIC observations. The predicted shear resistance was 12% higher from the numerical simulation and 16% lower from the analytical model as compared to the experiment. The numerical and analytical models from the validation of the Rijkswaterstaat's Guidelines for NLFEA (RTD 1016-3B [72] and RTD 1016-3 [73]) also report higher resistances with the analytical model and NLFEA with no safety format (i.e. without partial factors and mean material properties from testing).

The numerical models provided more insights of the behavior in the nonlinear regime after cracking and the correspondence with the flexural test in terms of the load – deflection response and concrete strains was satisfactory. The onset of cracking from the numerical simulation was 11% higher than the load at which the measured concrete strain surpasses the tensile strength of concrete. The difference was because the first cracking from the numerical model was reported at the soffit of the topping whereas the concrete strains were measured at the level of the lower layer of prestressing tendons in the experiment. The measured concrete strains at midspan at the levels of steel reinforcement were accurately described by the numerical simulation. The crack widths were deduced from the maximum principal strains both for DIC and NLFEA. The strains in the topping were smaller for the NLFEA due to more cracks appearing at smaller spacing, caused by the higher stresses transferring from the precast girder as the two were perfectly bonded. On the other hand, the strains in the girder for the NLFEA were higher but the cracking pattern is similar, hence the post-cracking response as described by the fracture energy may also be different for geopolymer concrete. Regarding the shear test, the response of the NLFEA was stiffer and the numerically obtained load – deflection curve separated from the experiment when the shear critical crack starts to propagate to the topping. The cross-section of the numerical simulation was stiffer since the perfect bond between the precast girder and the topping implied that the cross-section was fully composite, whereas in the experiment debonding was reported in the cross-section and the stresses did not transfer fully as in the numerical model.

The choice of material constitutive models and the assumption of perfect bond between the reinforcement and prestressing tendons to the geopolymer concrete seem to be acceptable to describe the short-term flexural behavior. On the other hand, the numerical prediction of the short-term shear resistance with perfect bond is not on the safe side and a nonlinear interface to simulate the debonding may allow to describe more accurately the phenomena. Nevertheless, the application of interfaces is only possible in the horizontal plane in a 2D plane stress analysis. A full 3D analysis would be required to define an interface in the horizontal and vertical planes which is also not defined in the Rijkswaterstaat Guidelines for NLFEA of Concrete Structures [23]. Therefore, it must be weighed if the description of this phenomena justifies a more detailed FE model requiring more computational and modelling efforts.

Regarding the flexural test after 9 months, the linear elastic behavior displayed by the numerical model does not capture accurately the experimental results due to the difference in elastic modulus as the specimen was cracked prior to the mechanical test and the stiffness degradation caused by the cyclic application of loading at high load levels in the experiment. The cracking load is decreased significantly (15%) in the specimen after 9 months but the creep and shrinkage deformations do not appear to stabilize after this period, hence the prestress losses will continue to increase over time and the cracking resistance will continue to decrease which is critical for the performance over the service lifetime of the structure. The maximum load in the flexural test after 9 months is overestimated by 5% in the numerical simulation as compared to the experimental results. The perfect bond assumption between

geopolymer concrete members and between the prestressing steel and the SCGC girder did not allow to fully describe the failure mechanism and the evolution of damage from the experiment. The assumption of perfect bond on the short and long-term flexural resistance has a smaller impact than for the short-term shear resistance. The design criteria of conventional concrete structures based on estimating the material properties from the 28-day compressive strength result in non-conservative estimates of the cracking resistance and flexural load carrying capacity of prestressed geopolymer concrete members which can lead to an unsafe design. Nevertheless, the truss model for shear resistance, the bilinear compressive stress block for flexural resistance and the 2D plane stress analysis with total strain based orthogonal rotating crack model with exponential tension softening and parabolic compressive relation can be used to estimate the structural performance of the prestressed girder with reinforced cast in-situ topping built in geopolymer concrete with the adequate long-term material properties as input.

6.2 Future work

Prestressed geopolymer structures are attractive for application in the precast industry. The quality control in the production is ideal for dosage control and safety when handling geopolymer concrete. However, the current production methods are based on mass production with demolding and prestressing after 1 day to speed up the production line. The autogenous shrinkage is significantly higher than OPC concrete, therefore the decision to apply the prestressing force at 2.5 days was adequate since the prestressing losses due to autogenous shrinkage were reduced by approximately half. Nevertheless, a proper economic and technical evaluation is required to determine whether higher shrinkage losses are allowable (which will require higher prestressing forces i.e. more tendons) to speed up the production process.

In order to determine the flexural and shear resistance of prestressed geopolymer concrete structures for engineering practice, the applicability of the current analytical methods from EN 1992-1-1 [32] was determined by comparing the resistance obtained from the analytical and numerical models with the experimental results. In engineering practice, nonlinear finite element analysis is demanding in manpower and computational resources. This type of analysis is a higher approximation level for concrete structures and is justified when significant cost savings can be expected. For example, for developing design codes, assessing existing structures, designing special structures (complex geometries or extreme loading) and forensic failure analysis. The current analytical methods from EN 1992-1-1 [22] can be applied to calculate the short-term flexural and shear resistance of prestressed geopolymer concrete structures. But structures are not designed for short-term lifespan and the development of the material properties over time need to be studied for longer time spans. The warehouse in Poland mentioned in Chapter 2, reports significant increase in the compressive strength and the other projects do not display a loss of performance throughout the years. On the other hand, the present study and literature shows a decrease in the elastic modulus caused by moisture loss and higher creep and shrinkage. The long-term creep and shrinkage deformations shall be monitored for a longer time span to investigate whether they stabilize and judge the structural performance over the service lifetime. Furthermore, it is recommended to study the cracking behavior of geopolymer concrete with regards to the fracture energy.

References

- [1] D. M. Roy, "Alkali-activated cements Opportunities and challenges," *Cement and Concrete Research*, vol. 29, pp. 249-254, 1999.
- [2] J. M. Crow, "The concrete conundrum," *Chemistry World*, pp. 62-66, 2008.
- [3] J. Sanjayan, "Materials technology research to structural design of geopolymer concrete," in *Proceedings of the 24th Australian Conference on the Mechanics of Structures and Materials*, London, 2016.
- [4] J. L. Provis and J. van Deventer, *Alkali Activated Materials State-of-the-Art Report*, RILEM TC 224-AAM, vol. 13, Dordrecht: Springer, 2014.
- [5] R. M. Andrew, "Global CO₂ emissions from cement production, 1928–2017," *Earth System Science Data*, vol. 10, no. 4, pp. 2213-2239, 2018.
- [6] European Committee for Standardization, *EN 197-1 Cement - Part 1 Composition, specifications and conformity for common cements*, Brussels, 2011.
- [7] G. Habert and C. Ouellet-Plamondon, "Recent update on the environmental impact of geopolymers," *RILEM Techn Lett*, vol. 1, pp. 17-23, 2016.
- [8] J. Aldred and J. Day, "Is geopolymer concrete a suitable alternative to traditional concrete?," in *37th Conference on Our World in Concrete & Structures*, Singapore, 2012.
- [9] T. Glasby, J. Day, R. Genrich and M. Kemp, "Commercial Scale Geopolymer Concrete Construction," in *The Saudi International Building and Constructions Technology Conference*, 2015.
- [10] J. L. Provis, "Alkali-activated materials," *Cement and Concrete Research*, vol. 114, pp. 40-48, 2018.
- [11] P. Nath and P. K. Sarker, "Flexural strength and elastic modulus of ambient-cured blended low-calcium fly ash geopolymer concrete," *Construction and Building Materials*, vol. 130, pp. 22-31, 2017.
- [12] F. G. Collins and J. G. Sanjayan, "Microcracking and strength development of alkali activated slag concrete," *Cement Concrete Composites*, vol. 23, no. 4-5, pp. 345-352, 2001.
- [13] Rijkswaterstaat, "Circular Economy," 2021. [Online]. Available: <https://www.rijkswaterstaat.nl/en/environment/circular-economy>. [Accessed January 2022].
- [14] Government of the Netherlands, "Circular Dutch economy by 2050," 2021. [Online]. Available: <https://www.government.nl/topics/circular-economy/circular-dutch-economy-by-2050>. [Accessed January 2022].
- [15] M. Sofi, J. Van Deventer, P. Mendis and G. Lukey, "Engineering properties of inorganic polymer concretes (IPCs)," *Cement and Concrete Research*, vol. 37, no. 2, pp. 251-257, 2007.
- [16] A. Hassan, M. Arif and M. Shariq, "Effect of curing condition on the mechanical properties of fly ash-based geopolymer concrete," *SN Applied Sciences*, vol. 1, no. 1694, 2019.
- [17] H. Ye, C. Cartwright, F. Rajabipour and A. Radlinska, "Understanding the drying shrinkage performance of alkali-activated slag mortars," *Cement and Concrete Composites*, vol. 76, pp. 13-24, 2017.

- [18] F. Collins and J. Sanjayan, "Effect of pore size distribution on drying shrinkage of alkali activated slag concrete," *Cement and Concrete Research*, vol. 30, no. 9, pp. 1401-1406, 2000.
- [19] C.-K. Ma, A. Z. Awang and W. Omar, "Structural and material performance of geopolymer concrete: A review," *Construction and Building Materials*, vol. 186, pp. 90-102, 2018.
- [20] T. Sonal, D. Urmil and B. Darshan, "Behaviour of ambient cured prestressed and non-prestressed geopolymer concrete beams," *Case Studies in Construction Materials*, vol. 16, 2022.
- [21] K. H. Mo, U. J. Alengaram and M. Z. Jumaat, "Structural performance of reinforced geopolymer concrete members: A review," *Construction and Building Materials*, vol. 120, pp. 251-264, 2016.
- [22] European Committee for Standardization, *EN 1992-1-1 Eurocode 2: Design of concrete structures - Part 1-1: General rules and rules for buildings*, Brussels, 2005.
- [23] M. Hendriks and M. Roosen, *Guidelines for Nonlinear Finite Element Analysis of Concrete Structures*, Rijkswaterstaat Centre for Infrastructure, 2019.
- [24] P. Krivenko, "Alkaline cements: terminology classification, aspects of durability," in *Proceedings of the 10th International Congress on the Chemistry of Cement*, Gothenburg, 1997.
- [25] The Portland Cement Association, "Aggregates," The Portland Cement Association, 2019. [Online]. Available: <https://www.cement.org/cement-concrete/concrete-materials/aggregates>. [Accessed March 2022].
- [26] A. Fernandez-Jimenez, P. Krivenko and A. Palomo, "Classification and Characteristics of Alkali-Activated Cements," *Journal of the Chinese Ceramic Society*, vol. 40, no. 1, pp. 69-75, 2012.
- [27] CEB/fib, *Model Code 2010 - Final draft, Volume 2. fib Bulletin No. 66*, Ernst & Sohn, 2012.
- [28] A. Castel, S. J. Foster, T. Ng, J. G. Sanjayan and R. I. Gillbert, "Creep and drying shrinkage of a blended slag and low calcium fly ash geopolymer Concrete," *Materials and Structures*, vol. 49, pp. 1619-1628, 2016.
- [29] A. M. Humad, J. L. Provis, K. Habermehl-Cwirzen, M. Rajczakowska and A. Cwirzen, "Creep and Long-Term Properties of Alkali-Activated Swedish-Slag Concrete," *Jorunal of Materials in Civil Engineering*, vol. 33, no. 2, 2021.
- [30] Z. Li, B. Del saute, T. Lu, A. Kostiuchenko, S. Staquet and G. Ye, "A comparative study on the mechanical properties, autogenous shrinkage and cracking proneness of alkali-activated concrete and ordinary Portland cement concrete," *Construction and Building Materials*, vol. 292, 2021.
- [31] Z. Li, T. Lu, X. Liang, H. Dong and G. Ye, "Mechanisms of autogenous shrinkage of alkali-activated slag and fly ash," *Cement and Concrete Research*, vol. 135, 2020.
- [32] J. Ma and F. Dehn, "Shrinkage and creep behavior of an alkali-activated slag concrete," *Structural Concrete*, vol. 18, pp. 801-810, 2017.
- [33] K. Parthiban, K. Saravanaramohan, S. Shobana and A. Anchal Bhaskar, "Effect of Replacement of Slag on the Mechanical Properties of Fly ash Based Geopolymer Concrete," *International Journal of Engineering and Technology*, vol. 5, no. 3, pp. 2555-2559, 2013.

- [34] S. Prinsse, D. A. Hordijk, G. Ye, P. Lagendijk and M. Lukovic, "Time-dependent material properties and reinforced beams behavior of two alkali-activated types of concrete," *Structural COncrete*, pp. 1-17, 2019.
- [35] F. Puertas, S. Martinez-Ramirez, S. Alonso and T. Vazquez, "Alkali-activated fly ash/slag cement: strength behaviour and hydration products," *Cement and Concrete Research*, vol. 30, no. 10, pp. 1625-1632, 2000.
- [36] K.-H. Yang, A.-R. Cho and J.-K. Song, "Effect of water–binder ratio on the mechanical properties of calcium hydroxide-based alkali-activated slag concrete," *Construction and Building Materials*, vol. 29, pp. 504-511, 2012.
- [37] H. Ye and A. Radlinska, "Shrinkage mechanisms of alkali-activated slag," *Cement and Concrete Research*, vol. 88, pp. 126-135, 2016.
- [38] F. Collins and J. Sanjayan, "Workability and mechanical properties of alkali activated slag concrete," *Cement and Concrete Research*, vol. 29, no. 3, pp. 455-458, 1999.
- [39] K. Neupane, A. Hadigheh and D. Dias da Costa, "Numerical Study on the Structural Behaviour of a Geopolymer Prestressed Concrete Beam," in *Biennial Conference of the Concrete Institute of Australia (Concrete 2019)*, Sydney, 2019.
- [40] ACI Committee 318, *Building Code Requirements for Structural Concrete (ACI 318-19) and Commentary*, American Concrete Institute, 2019.
- [41] F. Puertas, T. Amat, A. Fernandez-Jimenez and T. Vazquez, "Mechanical and durable behaviour of alkaline cement mortars reinforced with polypropylene fibres," *Cement and Concrete Research*, vol. 33, pp. 2031-2036, 2003.
- [42] G. Ye, C. Cartwright, F. Rajabipour and A. Radlinska, "Effect of drying rate on shrinkage of alkali-activated slag cements," in *Proceedings of the 4th International Conference on the Durability of Concrete Structures (ICDCS)*, Purdue University, West Lafayette, 2014.
- [43] M. Mastali, P. Kinnunen, A. Dalvand, R. Mohammadi Firouz and M. Illikainen, "Drying shrinkage in alkali-activated binders – A critical review," *Construction and Building Materials*, vol. 190, pp. 533-550, 2018.
- [44] P. Awoyera and A. Adesina, "A critical review on application of alkali activated slag as a sustainable composite binder," *Case Studies in Construction Materials*, vol. 11, pp. 1-13, 2019.
- [45] D. Sumajouw, H. Djwantoro, V. Rangan and S. Wallah, "Behaviour and Strength of Reinforced Fly Ash-Based Geopolymer Concrete Beams," in *Proceedings of Australian Engineering Conference*, Newcastle, 2005.
- [46] Y. Du, J. Wang, C. Shi, H.-J. Hwang and N. Li, "Flexural behavior of alkali-activated slag-based concrete beams," *Engineering Structures*, vol. 229, 2021.
- [47] J. R. Yost, A. Radlinska, S. Ernst, M. Salera and N. J. Martignetti, "Structural behavior of alkali activated fly ash concrete. Part 2: structural testing and experimental findings," *Materials and Structures*, vol. 46, pp. 449-462, 2013.
- [48] P. Visintin, M. S. Mohamed Ali, M. Albitar and W. Lucas, "Shear behaviour of geopolymer concrete beams without stirrups," *Construction and Building Materials*, vol. 148, pp. 10-21, 2017.
- [49] C. Wu, H.-J. Hwang, C. Shi, N. Li and Y. Du, "Shear tests on reinforced slag-based geopolymer concrete beams with transverse reinforcement," *Engineering Structures*, vol. 219, 2020.
- [50] K. T. Nguyen, T. A. Le and K. Lee, "Experimental study on flexural strength of reinforced geopolymer concrete beams," *International Journal of Civil and Environmental Engineering*, vol. 10, no. 4, pp. 516-520, 2016.

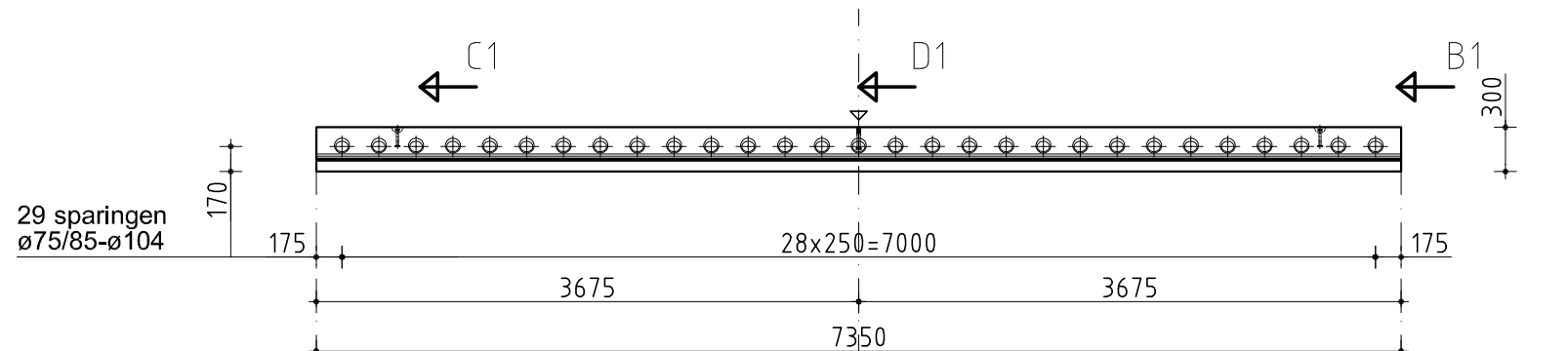
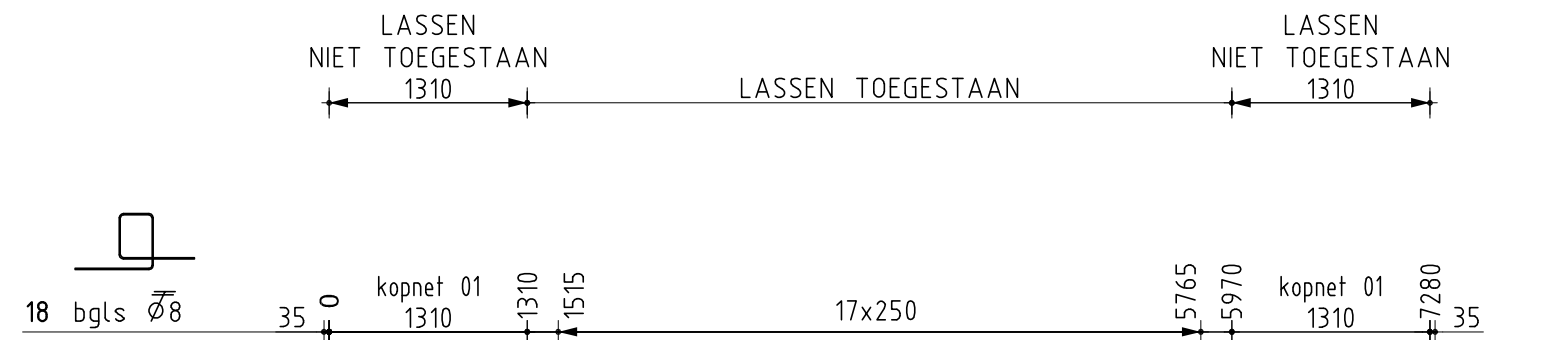
- [51] T. El-Sayed and Y. Algash, "Flexural behavior of ultra-high performance geopolymer RC beams reinforced with GFRP bars," *Case Studies in COstruction Materials*, vol. 15, pp. 1-24, 2021.
- [52] Dassault Systèmes, "Abaqus 6.13 Abaqus Analysis User's Guide," 2013. [Online]. Available: <http://130.149.89.49:2080/v6.14/books/usb/default.htm>. [Accessed 12 July 2022].
- [53] ANSYS, "SOLID65 3-D Reinforced Concrete Solid," 15 July 2017. [Online]. Available: https://www.mm.bme.hu/~gyebro/files/ans_help_v182/ans_elem/. [Accessed 12 July 2022].
- [54] American Society for Testing and Materials, "ASTM WK68966 New Specification for Alkali Activated Cementitious Materials," ASTM, 7 March 2019. [Online]. [Accessed June 2022].
- [55] E. Gartner, "Industrially interesting approaches to "low-CO₂" cements," *Cement and Concrete Research*, vol. 34, no. 9, pp. 1489-1498, 2004.
- [56] G. Habert, J. B. d'Espinose de Lacaillerie and N. Roussel, "An environmental evaluation of geopolymer based concrete production: reviewing current research trends," *J Cleaner Prod*, vol. 19, no. 11, pp. 1229-1238, 2011.
- [57] Microlab Section Materials and Environment, "Testing Report on Phase I - Part 1: Development of a self-compacting geopolymer," Delft University of Technology, Delft, 2021.
- [58] Microlab Section Materials and Environment, "Testing Report on Phase I – Part 2: Durability and volume stability of the selfcompacting," Delft University of Technology, Delft, 2021.
- [59] Microlab Section Materials and Environment, "Testing Report on Phase II – Industrial production of pre-cast bridge girders using the self-compacting geopolymer concrete (C45/55)," Delft University of Technology, Delft, 2021.
- [60] Section of Concrete Structures, "Testing Report on Phase III - Part 1: Additional Analysis of Structural Tests including DIC measurements," Delft University of Technology, Delft, 2022.
- [61] S. Matthys and A. Proia, "Test Report Jul '22: Loading tests on prestressed precast bridge deck members in AAM concrete," Ghent University, Ghent, 2022.
- [62] Section of Concrete Structures, "Monitoring of Prestressed Geopolymer Concrete Girders using Smart Aggregates and Fibre Optic Sensors," Delft University of Technology, Delft, 2022.
- [63] European Committee for Standarization, *EN 12390-3 Testing hardened concrete - Part 3 Compressive strength of test specimens*, Brussels, 2019.
- [64] International Organization for Standardization, *ISO 1920-10:2010 Testing of concrete - Part 10: Determination of static modulus of elasticity in compression*, 2010.
- [65] European Committee for Standarization, *EN 12390-13 Testing hardened concrete - Part 13: Determination of secant modulus of elasticity in compression*, Brussels, 2013.
- [66] European Committee for Standarization, *EN 12390-17 Testing hardened concrete - Part 17: Determination of creep of concrete in compression*, Brussels, 2019.
- [67] European Committee for Standarization, *EN 1990 Eurocode 0: Basis of structural design*, Brussels, 2002.
- [68] J. C. Walraven and R. Braam, *Prestressed concrete*, Delft: TU Delft, 2019.

- [69] R. F. Mast, "Analysis of Cracked Prestressed Concrete Sections: A Practical Approach," *PCI Journal*, vol. 43, no. 4, pp. 80-91, 1998.
- [70] A. Ghali and M. M. Elbrady, "Cracking of composite prestressed concrete sections," *Canadian Journal of Civil Engineering*, vol. 14, no. 3, pp. 314-319, 1987.
- [71] DIANA FEA, "User's Manual 10.5," 24 January 2022. [Online]. Available: <https://manuals.dianafea.com/d105/Diana.html>. [Accessed February 2022].
- [72] Rijkswaterstaat, *Validation of the Guidelines for Nonlinear Finite Element Analysis of Concrete Structures Part: Prestressed beams*, Rijkswaterstaat Centre for Infrastructure, 2017.
- [73] A. Slobbe and A. Bigaj-van Vliet, *Validating the guidelines for nonlinear finite element analysis of three prestressed concrete beams - blind predictions*, Delft: TNO, 2018, p. 107.
- [74] P. H. Feenstra, R. de Borst and J. G. Rots, "A Comparison of different crack models applied to plain and reinforced concrete," in *Fracture processes in Concrete, Rock and Ceramics*, London, E. & F.N., 1991, pp. 629-638.
- [75] S. Govindjee, G. Kay and J. Simo, "Anisotropic modelling and numerical simulation of brittle damage in concrete," *International Journal for Numerical Methods in Engineering*, vol. 38, pp. 3611-3633, 1995.
- [76] H. Nakamura and T. Higai, "Compressive Fracture Energy and Fracture Zone Length of Concrete," in *Modelling of inelastic behavior of RC structures under seismic loads*, Tokyo, 2001.
- [77] D. A. Hordijk, *Local approach to fatigue of concrete (Doctoral thesis)*, Delft: Delft University of Technology, 1991.
- [78] F. Vecchio and M. Collins, "Compression Response of Cracked Reinforced Concrete," *Journal of Structural Engineering*, vol. 119, no. 12, pp. 3590-3610, 1993.
- [79] R. G. Selby and F. Vecchio, *Three-dimensional Constitutive Relations for Reinforced Concrete*, Toronto: University of Toronto, 1993.

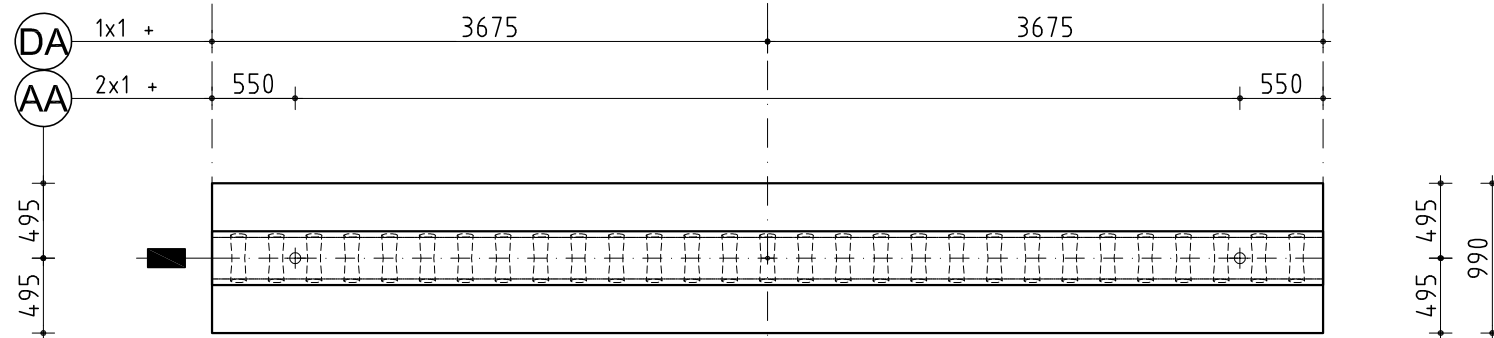
Appendix A: Construction drawings

List of construction drawings

Code	Description	Date	Paper size
KO-01	Element Drawing KO-01	24/06/2021	A3
KO-D1	Section B + ribs detail	23/07/2021	A3
KO-D2	Section C1 and D1	23/07/2021	A3
KO-D3	Detail beam end	24/06/2021	A3
DR-02	Reinforcement topping	23/07/2021	A3



AANZICHT A
(1:50)

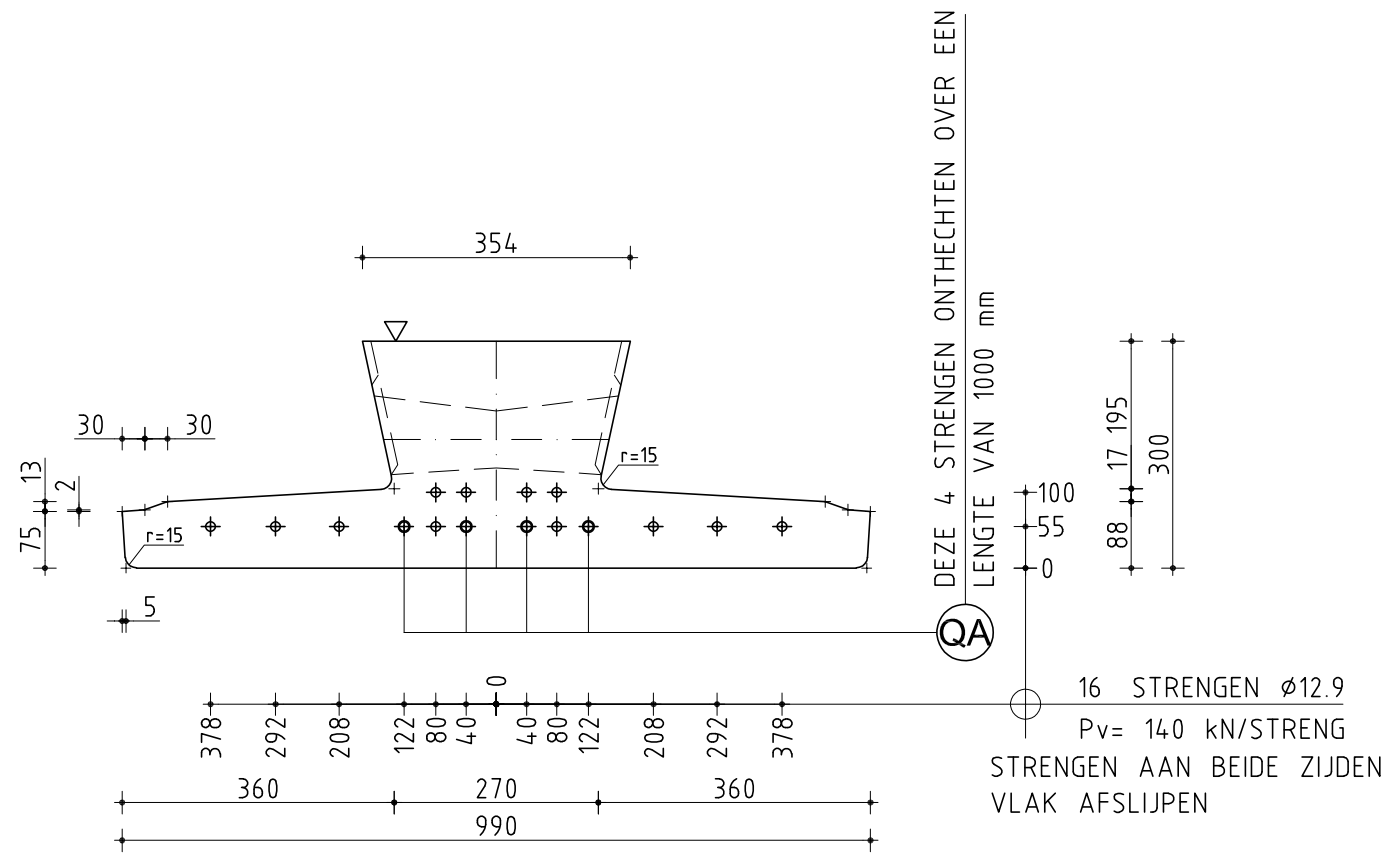


AFWERKZIJDE
(1:50)

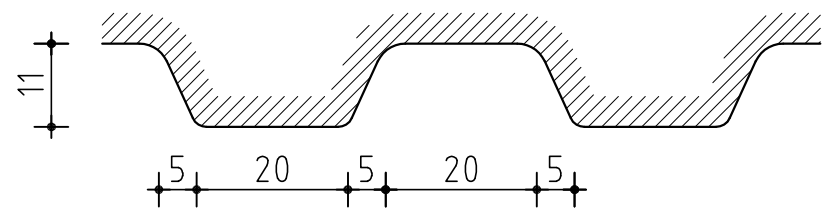
24-06-21	A
Datum:	Uitg.:
Schaal:	1:50

Tekeningnummer: 3089 KO-01





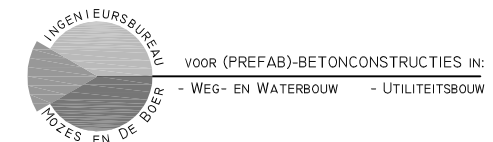
AANZICHT B1
(1:10)

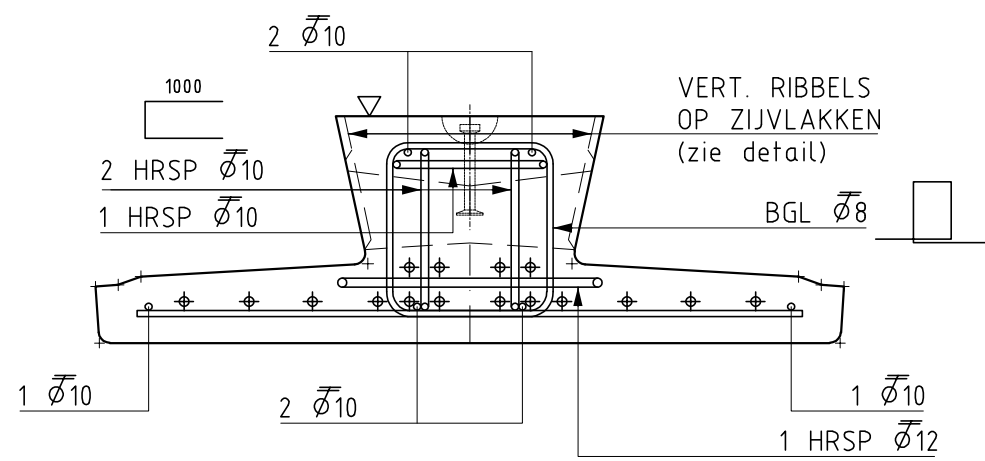


Detail ribbels

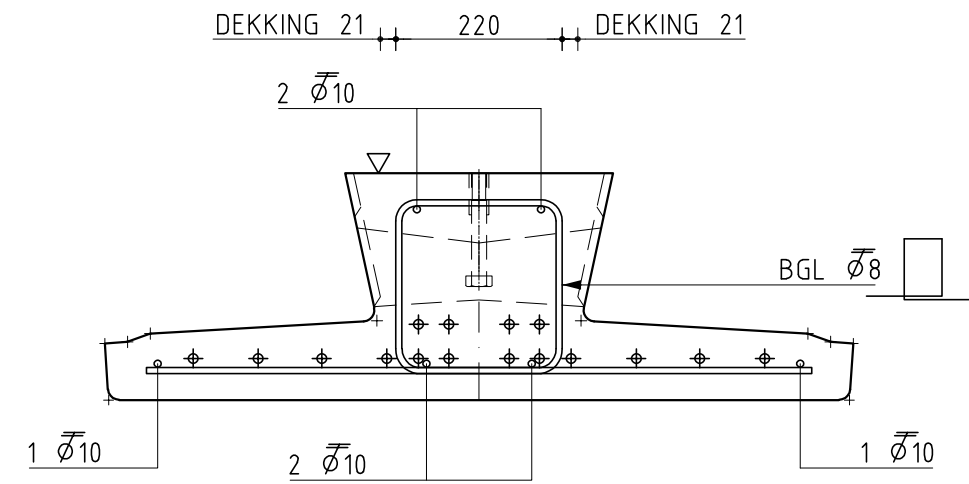
23-07-21	B
24-06-21	A
Datum:	Uitg.:
Schaal:	1:10

Tekeningnummer: 3089 KO-D1





DOORSNEDE C1
(1:10)



DOORSNEDE D1
(1:10)

23-07-21	B
24-06-21	A
Datum:	Uitg.:
Schaal:	1:10

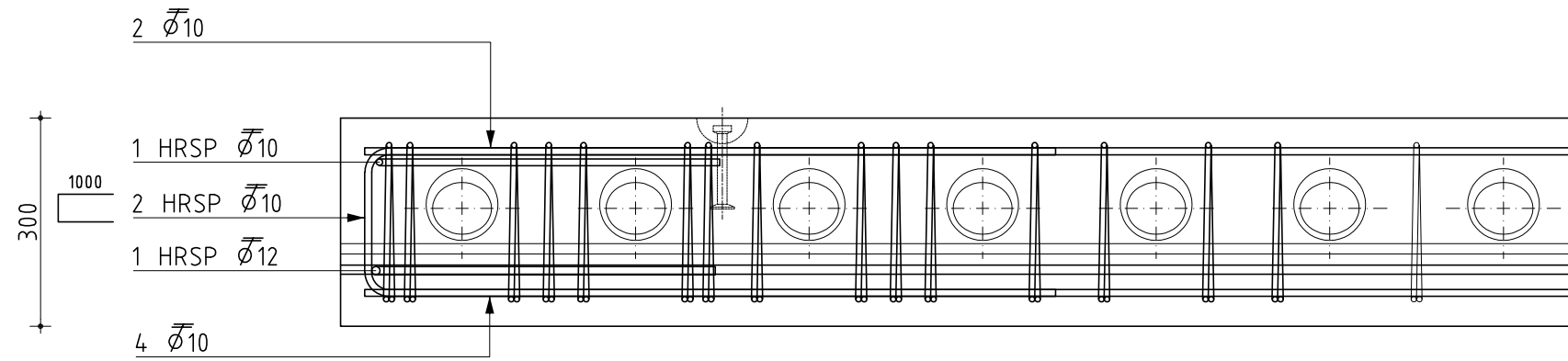
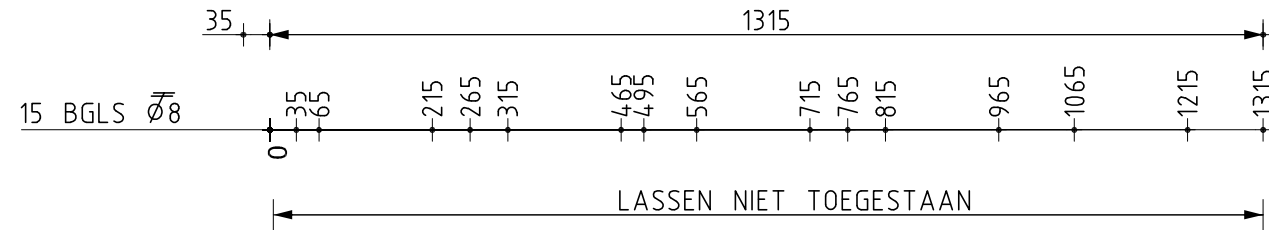
Tekeningnummer: 3089 KO-D2



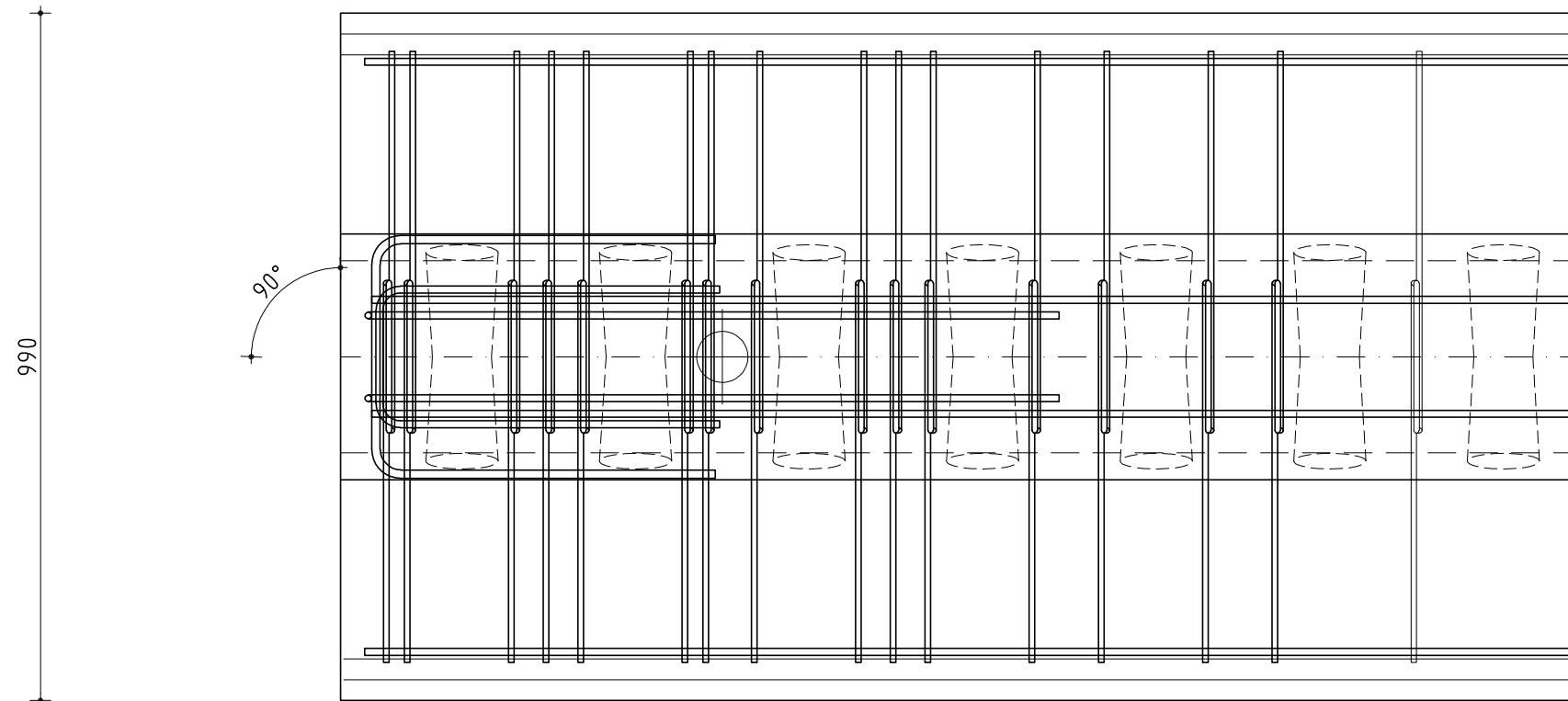
VOOR (PREFAB)-BETONCONSTRUCTIES IN:
- WEG- EN WATERBOUW - UTILITEITSBOUW



KOPNET 01



ZIJAANZICHT



AFWERKZIJDE

DETAIL BALKEINDE KO-01

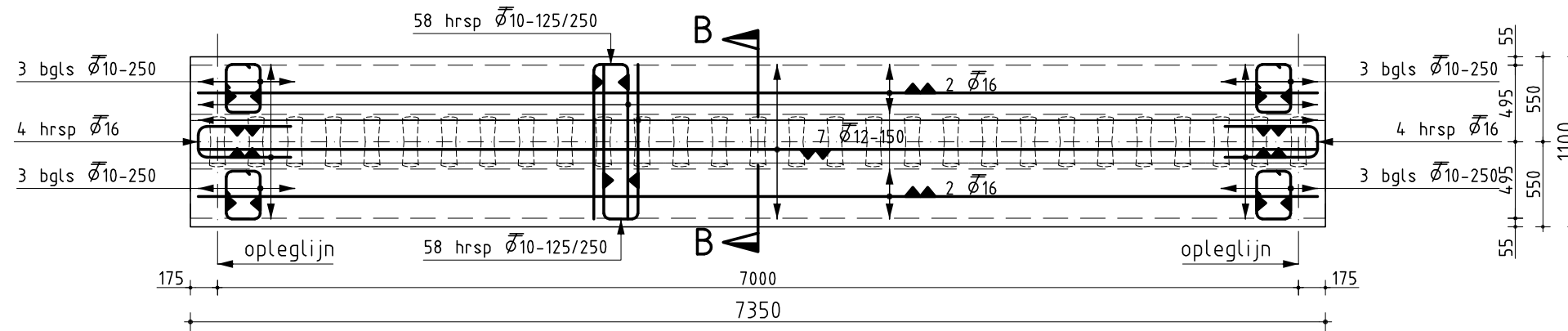
24-06-21	A
Datum:	Uitg.:
Schaal:	1:10

Tekeningnummer: 3089 KO-D3



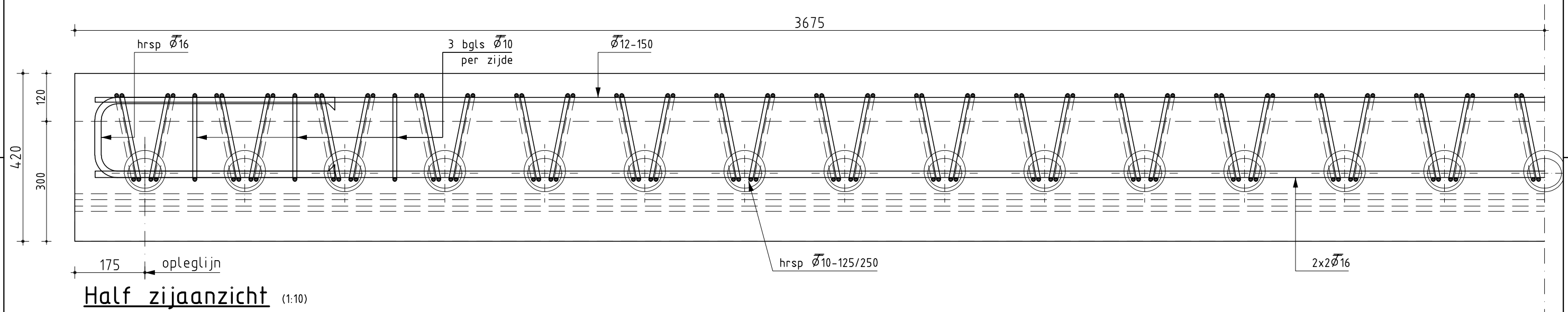
VOOR (PREFAB)-BETONCONSTRUCTIES IN:
- WEG- EN WATERBOUW - UTILITEITSBOUW

haitsma
B E T O N

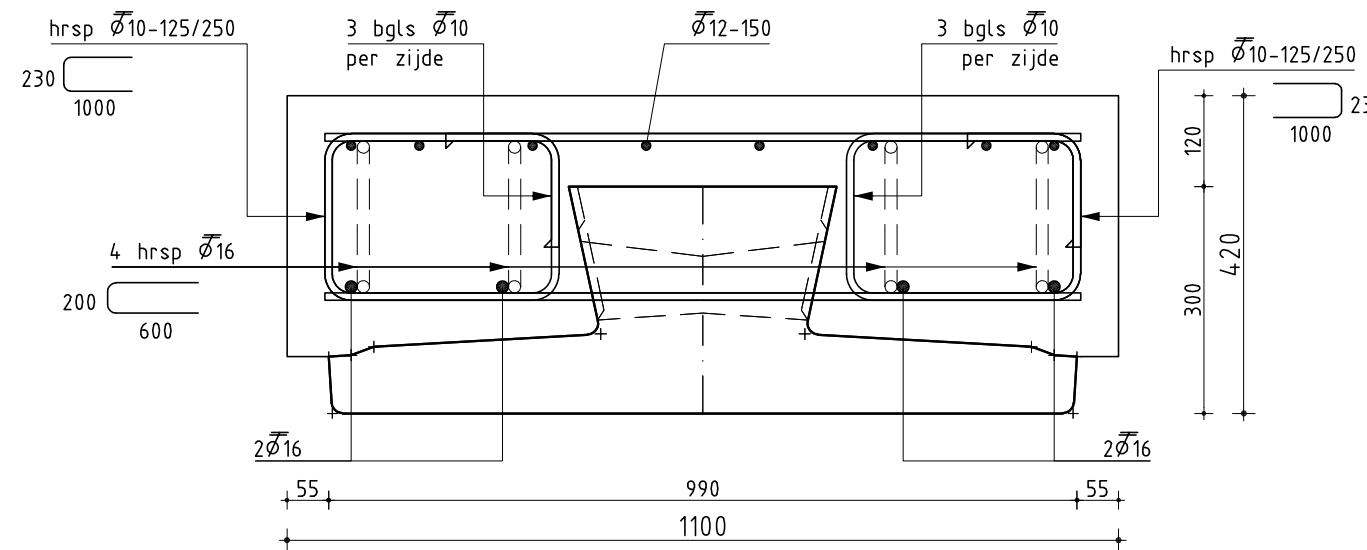


Bovenaanzicht (1:40)
(druklaag met 1 ligger)

DEK KING = 50 mm



Half zijaanzicht (1:10)



Doorsnede B-B (1:10)

23-07-21 A
Datum: Uitg.:
Schaal: 1:40/10


Tekeningnummer: 3089 DR-02



VOOR (PREFAB)-BETONCONSTRUCTIES IN:
WEG- EN WATERBOUW - UTILITEITSBOUW



Appendix B: Inspection certificates of prestressing strands



D&D DRÓTÁRU ZRT.

Inspection Certificate
Abnahmeprüfzeugnis

MSZ EN 10204:2004 "3.1"

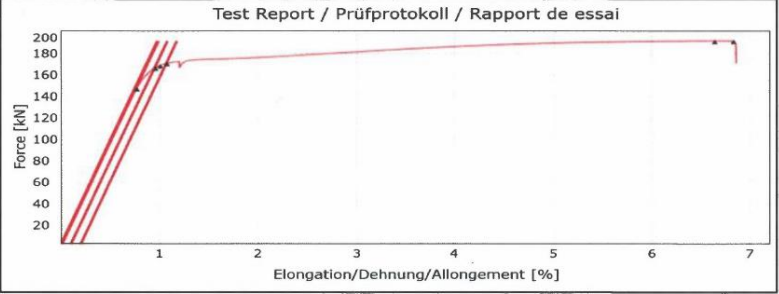
Number:
17 663

Testing machine \ Prüfmaschine	INSTRON 600KN, serial nr: J9906
Testing standard \ Prüfstandard	MSZ EN ISO 15630-3:2011
Serial nr. of load cell \ Wägezelle nr	51983
Serial nr. of extensometer \ Serial nr. of extensometer	E101656

Client \ Käufer	Haitsma Beton BV p/a Ballast Nedam Cent. Financ. Diensten
Order No. \ Auftrags-Nr	30005456;
Designation \ Genorm Benennung	NEN 3868:2001 FeP-1860-12,9-7S (Y1860S7-12,9-R1-F1-C1) left hand lay / St 1660/1860 Z-12.3-109 linksgängig

Diameter \ Durchmesser	12,9
Nom. area \ Nennquerschnitt	100,00 mm ²
Construction \ Konstruktion	4,40+6*4,25 mm
Coil No. \ Ring Nr	21D 4062
Heat No. \ Schmelze Nr	57103
Length \ Länge	5085
Netweight \ Nettogewicht	3956
Coil dimens \ Ringabmess.	900X710

Test Report / Prüfprotokoll / Rapport de essai



Measured data \ Messdaten

M (g/m)	Sn (mm ²)	Fm (kN)	Rm (MPa)	Fp0,01 (kN)	Rp0.01 (MPa)	Fp0.1 (kN)	Rp0.1 (MPa)	Fp0.2 (kN)	Rp0.2 (MPa)
777,92	99,61	191,89	1927	147,48	1481	166,82	1675	171,01	1717

Ft1% (kN)	Rt1% (MPa)	Em (GPa)	Agt (%)	Ratio Fp0,1/Fm	Ratio Fm/Fp02
168,81	1688	192,88	6,64	0,87	


On basis of the measured and calculated data, the product corresponds to the contractual requirements. \ Auf Grund der gemessenen und gerechneten Angaben entspricht das Produkt den Vorschriften des Vertrages.

Chemical composition: \ chemische Zusammensetzung


Heat	C	Mn	Si	P	S
57103	0,8400	0,6700	0,2000	0,0120	0,0090

Heat	C	Mn	Si	P	S
T57103-MI	0,8400	0,6700	0,2000	0,0120	0,0090

This document has been made by the informatic system of D&D Drótáru Zrt and valid without signature
Dieses Dokument wurde von der Informatiksystem von D & D Drótáru Zrt und ohne Unterschrift gültig gemacht worden



K7517



Lehóczki Zoltán
Head of Quality Control Department
Leiter der Qualitätskontrolabteilung

2021. július. 19.

D&D Drótáru Zrt. Magyarország 3527 Miskolc, Sajószigeti u. 4. Telefon: +36 46 519 100, Telefax: +36 46 519 115, web: www.drotaru.hu, e-mail: contact@drotaru.hu

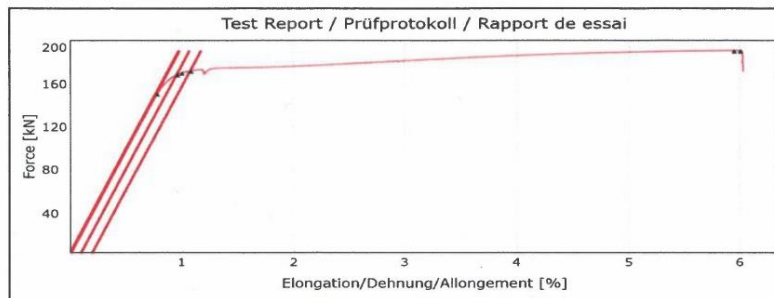


**Inspection Certificate
Abnahmeprüfzeugnis**

Number:
17 663

MSZ EN 10204:2004 "3.1"

Testing machine \ Prüfmaschine	INSTRON 600KN, serial nr: J9906
Testing standard \ Prüfstandard	MSZ EN ISO 15630-3:2011
Serial nr. of load cell \ Wägezelle nr	51983
Serial nr. of extensometer \ Serial nr. of extensometer	E101656
Client \ Käufer	Haitsma Beton BV p/a Ballast Nedam Cent. Financ. Diensten
Order No. \ Auftrags-Nr	30005456;
Designation \ Genorm.Benennung	NEN 3868:2001 FeP-1860-12,9-7S (Y1860S7-12,9-R1-F1-C1) left hand lay / St 1660/1860 Z-12.3-109 linksgängig
Diameter \ Durchmesser	12,9
Nom. area \ Nennquerschnitt	100,00 mm ²
Construction \ Konstruktion	4,40+6*4,25 mm
Coil No. \ Ring Nr	21D 4061
Heat No. \ Schmelze Nr	57103
Length \ Länge	5075
Netweight \ Nettogewicht	3956
Coil dimens \ Ringabmess.	900X710



Measured data \ Messdaten

M (g/m)	Sn (mm ²)	Fm (kN)	Rm (MPa)	Fp0,01 (kN)	Rp0.01 (MPa)	Fp0.1 (kN)	Rp0.1 (MPa)	Fp0.2 (kN)	Rp0.2 (MPa)
779,39	99,79	191,14	1915	151,31	1516	169,04	1694	172,43	1728
Ft1% (kN)	Rt1% (MPa)	Em (GPa)	Agf (%)	Ratio Fp0.1/Fm		Ratio Fm/Fp02			
170,49	1705	192,49	5,95	0,88					

On basis of the measured and calculated data, the product corresponds to the contractual requirements. \ Auf Grund der gemessenen und gerechneten Angaben entspricht das Produkt den Vorschriften des Vertrages.

Chemical composition: \ chemische Zusammensetzung

Heat	C	Mn	Si	P	S
57103	0,8400	0,6700	0,2000	0,0120	0,0090

Heat	C	Mn	Si	P	S
T57103-MI	0,8400	0,6700	0,2000	0,0120	0,0090

This document has been made by the informatic system of D&D Drótáru Zrt and valid without signature
Dieses Dokument wurde von der Informatiksystem von D & D Drótáru Zrt und ohne Unterschrift gültig gemacht worden



Lehóczki Zoltán
Head of Quality Control Department
Leiter der Qualitätskontrolleabteilung

2021.július.19.

D&D Drótáru Zrt. Magyarország 3527 Miskolc, Sajtószigeti u. 4. Telefon: +36 46 519 100, Telefax: +36 46 519 115, web: www.drotaru.hu, e-mail: contact@drotaru.hu

Appendix C: Analytical calculations

Calculations according EN 1990 and EN 1992-1-1 (clauses referenced in left hand side).

1. Stage I: Prestressing (2.5 days)

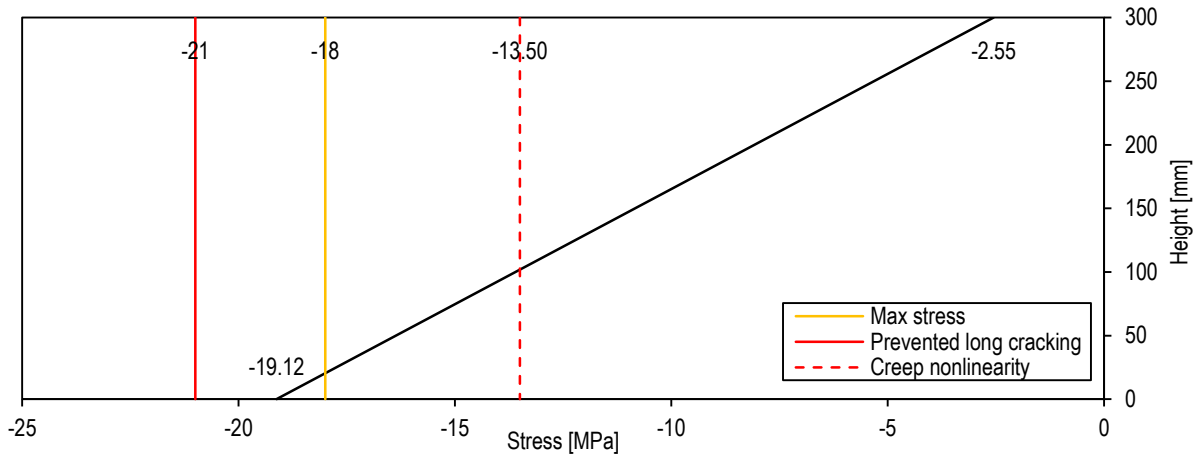
5.10.2.1	$P_{max} = (140 \text{ kN/str})(16 \text{ str})$	= 2240 kN
Maximum prestressing	$\sigma_{max} = P_{max}/A_p$	= 1400 MPa
No tensile stresses top fibre	$-\frac{P_{m0}}{A_g} + \frac{P_{m0}e_p}{W_{gt}} - \frac{M_{Gc}}{W_{gt}} \leq 0$	
	$P_{m0} \leq \frac{M_{Gc}A_c}{A_g e_p - W_{gt}}$	≤ 6205 kN
5.10.2.2 (5)	$-\frac{P_{m0}}{A_g} - \frac{P_{m0}e_p}{W_{gb}} + \frac{M_{Gc}}{W_{gb}} \geq -0.6f_{cm}(t)$	
Limited compressive stress bottom fibre	$P_{m0} \leq \frac{M_{Gc}A_g + 0.6f_{cm}(t)W_{gb}A_g}{A_g e_p + W_{gb}}$	≤ 2499 kN

1.1 Immediate prestress losses: elastic deformation and relaxation of the tendons

Prestressing force after losses	$P_{m0} = P_{max} + \Delta P_{el} + \Delta P_{pr}$	= 2033.3 kN
	$\sigma_{pm0} = P_{m0}/A_p$	= 1270.81 MPa
5.10.4 (1)	$\sigma_{ps} = -\frac{P_{m0}}{A_g} - \frac{P_{m0}e_p^2}{I_g} + \frac{M_{Gc}e_p}{I_g}$	= -15.46 MPa
Elastic deformation	$\varepsilon_{ps} = \sigma_{ps}/E_c$	= -0.618 ‰
	$\Delta_{el} = \varepsilon_{ps}L$	= 4.3 mm
	$\Delta P_{el} = \varepsilon_{ps}E_pA_p$	= -190.5 kN
5.10.4 (1) & 3.3.2 (7)	σ_{pi}	= 1400 MPa
Relaxation loss (Class 2: low relaxation tendons)	ρ_{1000}	= 2.5 %
	$\mu = \sigma_{pi}/f_p$	= 0.731
	t	= 60 h
	$\Delta\sigma_{pr} = \sigma_{pi}0.66\rho_{1000}e^{9.1\mu}(t/1000)^{0.75(1-\mu)}$	= -10.15 MPa
	$\Delta P_{pr} = A_p\Delta\sigma_{pr}$	= -16.2 kN

1.2 Maximum prestressing force at the active end during tensioning and transfer

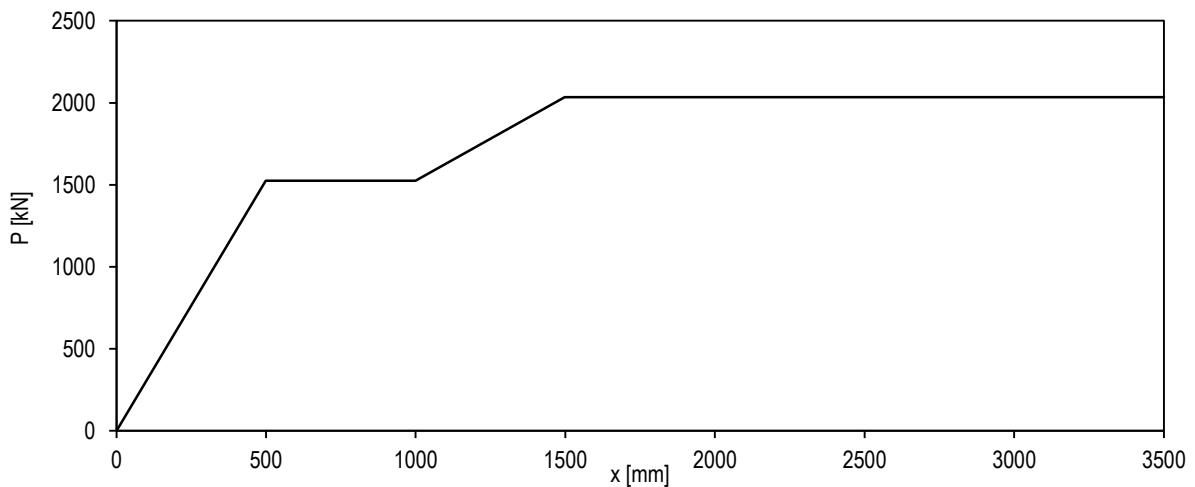
5.10.2.1 (1)	$\sigma_{p,max} = \min(k_1f_p, k_2f_{p0.1})$	= 1524.60 MPa
Maximum prestressing in a tendon	$k_1 = 0.8$	
	$k_2 = 0.9$	$\sigma_{max} < \sigma_{p,max}$
5.10.3 (2)	$\sigma_{pm0}(x) = \min(k_7f_p, k_8f_{p0.1})$	= 1436.25 MPa
Maximum stress in tendon after transfer of prestressing	$k_7 = 0.75$	
	$k_8 = 0.85$	$\sigma_{m0} < \sigma_{pm0}(x)$
5.10.2.2 (5)	$k_6f_{ck}(t)$	= -21 MPa
Maximum stress in concrete if longitudinal cracking prevented	$k_6 = 0.7$	



Stage I: Stress distribution

1.3 Transfer of prestress

8.10.2.2 (1)	η_{p1}	for 7-wire strands	= 3.2
Bond stress	η_1	for good bond conditions	= 1.0
	$f_{cta}(t) = \alpha_{ct} 0.7 f_{ctm}(t)$		= 1.95 MPa
	$f_{bpt} = \eta_{p1} \eta_1 f_{cta}(t)$		= 6.25 MPa
8.10.2.2 (2)	α_1	for sudden release	= 1.0
Transmission length	α_2	for 7-wire strands	= 0.19
	$l_{pt} = \alpha_1 \alpha_2 \phi \sigma_{pm0} / f_{bpt}$		= 498 mm



Transfer of prestressing force

1.4 Camber

$$\kappa = -\frac{d^2 w}{dx^2} \rightarrow \frac{d^2 w}{dx^2} = -\frac{M}{EI}$$

Boundary conditions: $w(0) = w'(L/2) = 0$

$$\kappa_{Gc}(x) = \frac{q_{Gc} x(L-x)}{2E_c I_g}$$

$$\kappa_{Gc}(L/2) = \frac{q_{Gc} L^2}{8E_c I_g} = 8.00 \cdot 10^{-7} \text{ 1/mm}$$

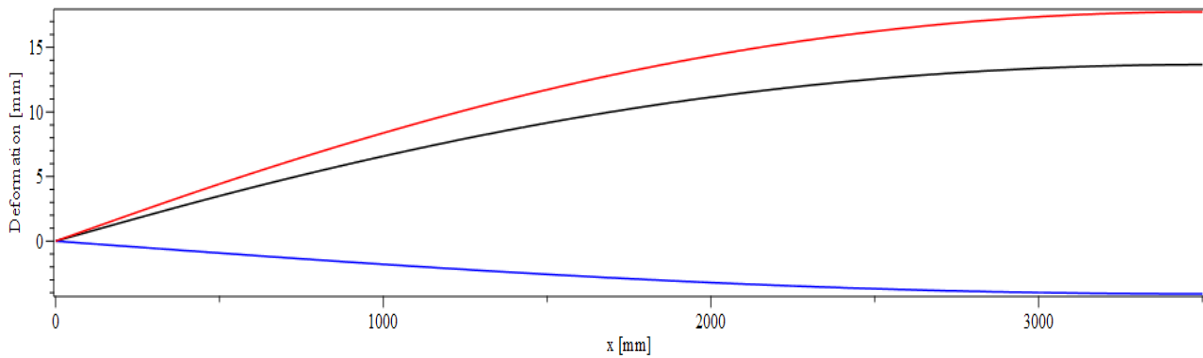
$$\delta_{Gc}(L/2) = \frac{5}{48} \kappa_{Gc}(L/2)L^2 = 4.1 \text{ mm}$$

$$\kappa_P(x) = -\frac{P_{m0}e_p}{E_c I_g} \begin{cases} \frac{3x}{4l_{pt}} & 0 \leq x < l_{pt} \\ \frac{3}{4} & l_{pt} \leq x < 1000 \text{ mm} \\ \frac{1}{4} \left(3 + \frac{x - 1000 \text{ mm}}{l_{pt}} \right) & 1000 \text{ mm} \leq x < 1 + l_{pt} \\ 1 & 1000 \text{ mm} + l_{pt} \leq x \leq L/2 \end{cases}$$

$$\delta_P(x) = -\frac{P_{m0}e_p}{2E_c I_g} \begin{cases} \frac{x}{l_{pt}} \left(-l_{pt}^2 + (L - 500)l_{pt} - \frac{x^2}{4} \right) & 0 \leq x < l_{pt} \\ -\frac{3x^2}{4} + \left(L - \frac{l_{pt}}{4} - 500 \right) x - \frac{l_{pt}^2}{4} & l_{pt} \leq x < 1000 \text{ mm} \\ \frac{1}{l_{pt}} \left(-\frac{x^3}{12} + \left(-\frac{3l_{pt}}{4} + 250 \right) x^2 + \dots \right) & 1000 \text{ mm} \leq x < 1 + l_{pt} \\ xL - x^2 - \frac{l_{pt}^2}{3} - 250l_{pt} - 250000 & 1000 \text{ mm} + l_{pt} \leq x \leq L/2 \end{cases}$$

$$\delta_P(L/2) = -17.7 \text{ mm}$$

$$\delta_{Pt_0}(L/2) = \delta_{Gc}(L/2) + \delta_P(L/2) = -13.7 \text{ mm}$$



Deformation due prestressing (red), self-weight (blue) and total (black)

2. Stage II: Cast in-situ topping (30 days)

2.1 Immediate prestress losses: elastic deformation and relaxation of the tendons

Elastic deformation	$\sigma_{Gt} = \frac{M_{Gt}e_p}{I_g}$	= 1.62 MPa
	$\Delta P_{el} = \sigma_{Gt}E_pA_p/E_c$	= 18.2 kN
Prestressing force after elastic losses	$P_{mi} = P_{m0} + \Delta P_{el}$	= 2051.5 kN
	$\sigma_{pmi} = P_{mi}/A_p$	= 1282.17 MPa
5.10.4 (1) & 3.3.2 (7)	ρ_{1000}	= 2.5 %
Relaxation loss (Class 2: low relaxation tendons)	$\mu = \sigma_{pmi}/f_{pm}$	= 0.670
	t	= 732 h
	$\Delta\sigma_{pr} = \sigma_{pi}0.66\rho_{1000}e^{9.1\mu}(t/1000)^{0.75(1-\mu)}$	= -8.67 MPa
	$\Delta P_{pr} = A_p\Delta\sigma_{pr}$	= -13.9 kN

2.2 Time dependent losses: creep and shrinkage

Autogenous shrinkage	$\varepsilon_{ca}(t_{2.5})$	= 590 $\mu\text{m/m}$
	$\varepsilon_{ca}(t_{30})$	= 1140 $\mu\text{m/m}$
	$\varepsilon_{ca} = \varepsilon_{ca}(t_{30}) - \varepsilon_{ca}(t_{2.5})$	= 550 $\mu\text{m/m}$
Drying shrinkage	$\varepsilon_{cd}(t_{30})$	= 153 $\mu\text{m/m}$
Total shrinkage	$\varepsilon_{cs} = \varepsilon_{ca} + \varepsilon_{cd}$	= 703 $\mu\text{m/m}$
Creep	$\phi(t_{30}, t_0)$	= 1.83
	$\varepsilon_{cc}(t_{30}, t_0) = \phi(t_{30}, t_0)\sigma_{ps}/E_c$	= -1028 $\mu\text{m/m}$

2.3 Total losses

Shrinkage losses	$\Delta\sigma_s = \varepsilon_{ca}E_p$	= -135.40 MPa
Creep losses	$\Delta\sigma_c = \varepsilon_{cc}(t_{30}, t_0)E_p$	= -197.89 MPa
Relaxation losses	$\Delta\sigma_{pr} = 0.8\Delta\sigma_{pr}$	= -6.93 MPa
Total losses	$\Delta\sigma = \Delta\sigma_s + \Delta\sigma_c + \Delta\sigma_r$	= -340.23 MPa
Prestress after losses 5.10.6 (2)	$\Delta P = \frac{\Delta\sigma A_p}{\left(1 + \frac{E_p A_p}{E_c A_g} \left(1 + \frac{e_p^2 A_g}{I_g}\right) (1 + 0.8\phi(t, t_0))\right)}$	= -445.6 kN
	$P_{m30} = P_{mi} + \Delta P$	= 1605.9 kN
	$\sigma_{pm30} = P_{m30}/A_p$	= 1003.69 MPa
	$p = P_{m30}/P_{m0}$	= 0.79

2.4 Deformation

Creep	$\delta_{\phi, t30} = \phi(t_{30}, t_0)\delta_{Pt_0}(L/2)$	= -25.0 mm
Total deformation	$\delta_{t30} = \delta_{Pt_0} + \delta_{\phi, t30}$	= -38.6 mm

3. Stage III: Composite section (60 days)

3.1 Immediate prestress losses: elastic deformation and relaxation of the tendons

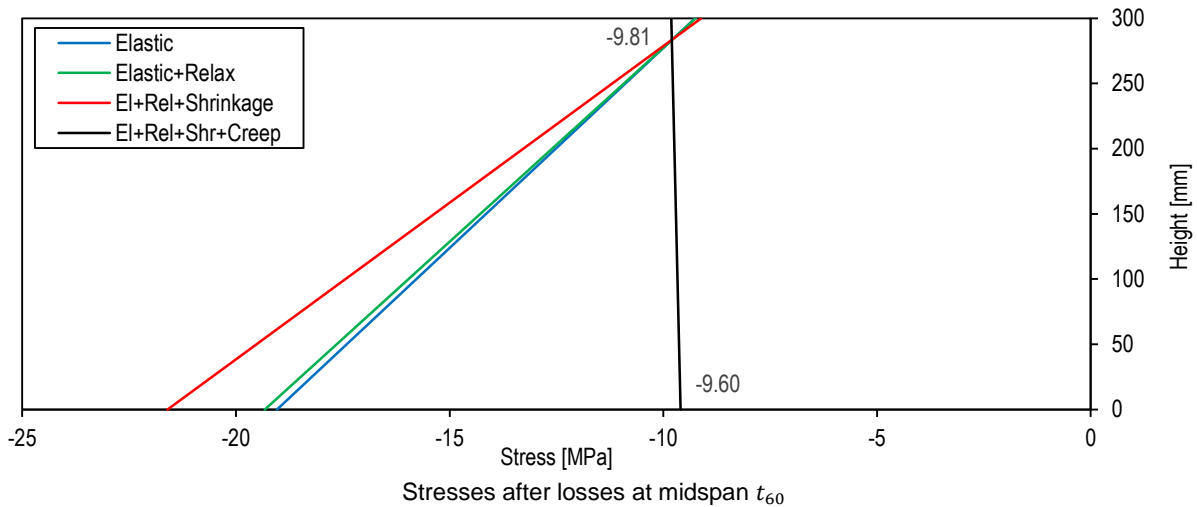
Elastic deformation	$\sigma_{Gt} = \frac{M_{Gt}e_p}{A_g}$	= 1.62 MPa
	$\Delta P_{el} = \sigma_{Gt}E_p A_p/E_c$	= 18.2 kN
Prestressing force after elastic losses	$P_{mi} = P_{m0} + \Delta P_{el}$	= 2051.5 kN
	$\sigma_{pmi} = P_{mi}/A_p$	= 1282.17 MPa
5.10.4 (1) & 3.3.2 (7)	ρ_{1000}	= 2.5 %
Relaxation loss (Class 2: low relaxation tendons)	$\mu = \sigma_{pmi}/f_{pm}$	= 0.670
	t	= 1500 h
	$\Delta\sigma_{pr} = \sigma_{pi}0.66\rho_{1000}e^{9.1\mu}(t/1000)^{0.75(1-\mu)}$	= -10.35 MPa
	$\Delta P_{pr} = A_p\Delta\sigma_{pr}$	= -16.6 kN

3.2 Time dependent losses: creep and shrinkage

Autogenous shrinkage	$\varepsilon_{ca}(t_{2.5})$	= 590 $\mu\text{m/m}$
	$\varepsilon_{ca}(t_{\infty})$	= 1140 $\mu\text{m/m}$
	$\varepsilon_{ca} = \varepsilon_{ca}(t_{\infty}) - \varepsilon_{ca}(t_{2.5})$	= 550 $\mu\text{m/m}$
Drying shrinkage	$\varepsilon_{cd}(t_{60})$	= 332 $\mu\text{m/m}$
Total shrinkage	$\varepsilon_{cs} = \varepsilon_{ca} + \varepsilon_{cd}$	= 882 $\mu\text{m/m}$
Creep	$\phi(t_{60}, t_0)$	= 2.26
	$\varepsilon_{cc}(t_{60}, t_0) = \phi(t_{60}, t_0)\sigma_{ps}/E_c$	= -1271 $\mu\text{m/m}$

3.3 Total losses

Shrinkage losses	$\Delta\sigma_s = \varepsilon_{ca}E_p$	= -169.78 MPa
Creep losses	$\Delta\sigma_c = \varepsilon_{cc}(t_{60}, t_0)E_p$	= -244.64 MPa
Relaxation losses	$\Delta\sigma_r = 0.8\Delta\sigma_{pr}$	= -8.28 MPa
Total losses	$\Delta\sigma = \Delta\sigma_s + \Delta\sigma_c + \Delta\sigma_r$	= -422.70 MPa
Prestress after losses 5.10.6 (2)	$\Delta P = \frac{\Delta\sigma A_p}{\left(1 + \frac{E_p A_p}{E_c A_g} \left(1 + \frac{e_p^2 A_g}{I_g}\right) (1 + 0.8\phi(t, t_0))\right)}$	= -539.8 kN
	$P_{m60} = P_{mi} + \Delta P$	= 1511.6 kN
	$\sigma_{p60} = P_{m60}/A_p$	= 944.78 MPa
	$p = P_{m60}/P_{m0}$	= 0.74



3.4 Deformation

Self-weight topping	$\kappa_{Gt}(L/2) = \frac{q_{Gt}L^2}{8E_c I_g}$	= $1.33 \cdot 10^{-6}$ 1/mm
	$\delta_{Gt}(L/2) = \frac{5}{48}\kappa_{Gt}(L/2)L^2$	= 6.8 mm
Creep	$\delta_{\phi, t60} = \phi(t_{60}, t_0)\delta_{Pt_0}(L/2)$	= -30.9 mm
Total deformation	$\delta_{t60} = \delta_{Pt_0} + \delta_{Gt} + \delta_{\phi, t60}$	= -37.7 mm

4. Magnel diagram

Stage I: Prestressing (2.5 days)

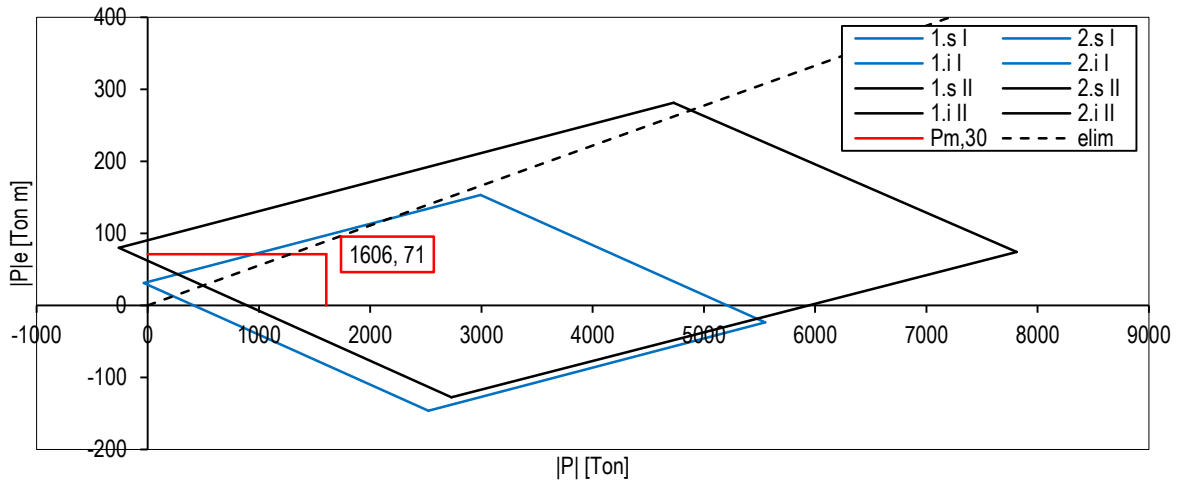
Top fibre	1.t	$-\frac{P_{m0}}{A_g} + \frac{P_{m0}e_p}{W_{gt}} - \frac{M_{Gc}}{W_{gt}} \leq f_{ctm}(t)$
Bottom fibre	1.b	$-\frac{P_{m0}}{A_g} - \frac{P_{m0}e_p}{W_{gb}} + \frac{M_{Gc}}{W_{gb}} \geq f_{cm}(t)$

Stage II: Cast in-situ topping (30 days)

Top fibre	2.t	$-\frac{P_{m30}}{A_g} + \frac{P_{m30}e_p}{W_{gt}} - \frac{M_{Gc} + M_{Gt}}{W_{gt}} \geq f_{cm}$
Bottom fibre	2.b	$-\frac{P_{m30}}{A_g} - \frac{P_{m30}e_p}{W_{gb}} + \frac{M_{Gc} + M_{Gt}}{W_{gb}} \leq f_{ctm}$

Stage III: Composite section (60 days)

$$\begin{aligned}
 \text{Top fibre } \mathbf{1.t^{cs}} \quad & -\frac{P_{m60}}{A_g} + \frac{P_{m60}e_p}{W_{gt}} - \frac{M_{Gc} + M_{Gt}}{W_{gt}} - \frac{M_{Gr}}{W_{ct}} \geq f_{cm} \\
 \text{Bottom fibre } \mathbf{1.b^{cs}} \quad & -\frac{P_{m60}}{A_g} - \frac{P_{m60}e_p}{W_{gb}} + \frac{M_{Gc} + M_{Gt}}{W_{gb}} + \frac{M_{Gr}}{W_{cb}} \leq f_{ctm} \\
 \text{Top fibre } \mathbf{2.t^{cs}} \quad & -\frac{P_{m60}}{A_g} + \frac{P_{m60}e_p}{W_{gt}} - \frac{M_{Gc} + M_{Gt}}{W_{gt}} - \frac{M_{Gr}}{W_{ct}} \leq f_{ctm} \\
 \text{Bottom fibre } \mathbf{2.b^{cs}} \quad & -\frac{P_{m60}}{A_g} - \frac{P_{m60}e_p}{W_{gb}} + \frac{M_{Gc} + M_{Gt}}{W_{gb}} + \frac{M_{Gr}}{W_{cb}} \geq f_{cm}
 \end{aligned}$$



Magnet diagram

Vortices Magnet diagram

Vertex	Stages I and II			Stage III		
	P e [kN m]	P [kN]	e [mm]	P e [kN m]	P [kN]	e [mm]
A	-145.9	2521.9	-58	-127.2	2729.7	-47
B	-23.6	5548.9	-4	74.3	7810.9	10
C	31.3	-36.5	-1	80.0	-260.8	0
D	153.6	2990.6	0	281.4	4726.7	0

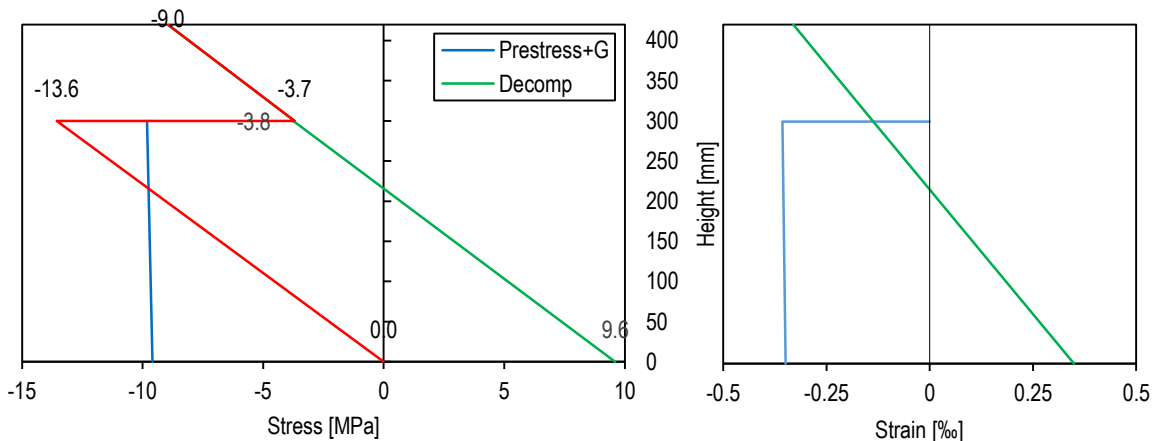
5. Flexure

5.1 Zero external moment

$$\begin{aligned}
 \text{Bottom fibre} \quad & \sigma_b = -\frac{P_{m60}}{A_c} - \frac{P_{m60}e_p}{W_{cb}} = -15.86 \text{ MPa} \\
 & \varepsilon_b = \sigma_b/E_{cm} = -0.58 \text{ ‰} \\
 \text{Top fibre} \quad & \sigma_t = -\frac{P_{m60}}{A_c} + \frac{P_{m60}e_p}{W_{ct}} = 0.92 \text{ MPa} \\
 & \varepsilon_t = \sigma_t/E_c = 0.03 \text{ ‰} \\
 \text{Cross-section analysis} \quad & x_u = h_c \left(1 - \frac{\varepsilon_t}{\varepsilon_t - \varepsilon_b}\right) = 283 \text{ mm} \\
 & \kappa = \varepsilon_b/x_u = -2.03 \cdot 10^{-6} \text{ 1/mm} \\
 & M = -P_{m60}e_p = -226 \text{ kN m}
 \end{aligned}$$

5.2 Decompression of bottom fibre

Decompression bottom fibre	$-\frac{P_{m60}}{A_g} - \frac{P_{m60}e_p}{W_{gb}} + \frac{M_{Gc} + M_{Gt}}{W_{gb}} + \eta \frac{M_{dec}}{W_{cb}} = 0$	
	$M_{dec} = \left(\frac{P_{m60}}{A_g} + \frac{P_{m60}e_p}{W_{gb}} - \frac{M_{Gc} + M_{Gt}}{W_{gb}} \right) \frac{W_{cb}}{\eta}$	= 277 kN m
Stress bottom fibre girder P_{m60} and M_G	$\sigma_{gb} = -\frac{P_{m60}}{A_g} - \frac{P_{m60}e_p}{W_{gb}} + \frac{M_{Gc} + M_{Gt}}{W_{gb}}$	= -9.60 MPa
Stress top fibre girder P_{m60} and M_G	$\sigma_{gt} = -\frac{P_{m60}}{A_g} + \frac{P_{m60}e_p}{W_{gt}} - \frac{M_{Gc} + M_{Gt}}{W_{gt}}$	= -9.81 MPa
Stress bottom fibre girder M_{dec}	$\sigma_{gb,dec} = \frac{\eta M_{dec}}{W_{cb}}$	= 9.60 MPa
Stress top fibre girder M_{dec}	$\sigma_{gt,dec} = -\frac{\eta M_{dec}(h_c - z_{cb})}{I_c}$	= -3.75 MPa
Stress bottom fibre topping M_{dec}	$\sigma_{tb,dec} = -\frac{M_{dec}(h_c - z_{cb})}{I_c}$	= -3.70 MPa
Stress top fibre topping M_{dec}	$\sigma_{tt,dec} = -\frac{M_{dec}}{W_{ct}}$	= -8.96 MPa
Resulting stress girder at interface	$\sigma_t = \sigma_{gt} + \sigma_{gt,dec}$	= -13.56 MPa
Resulting stress bottom fibre	$\sigma_b = \sigma_{gb} + \sigma_{gb,dec}$	= 0.00 MPa
Cross-section analysis	$x_u = h_c - z_{cb} \left(\frac{\sigma_b}{\sigma_b - \sigma_t} \right)$	= 420 mm
	$\kappa_{dec} = \frac{\sigma_{gb,dec} - \eta \sigma_{tt,dec}}{E_c h_c}$	= $1.62 \cdot 10^{-6}$ 1/mm

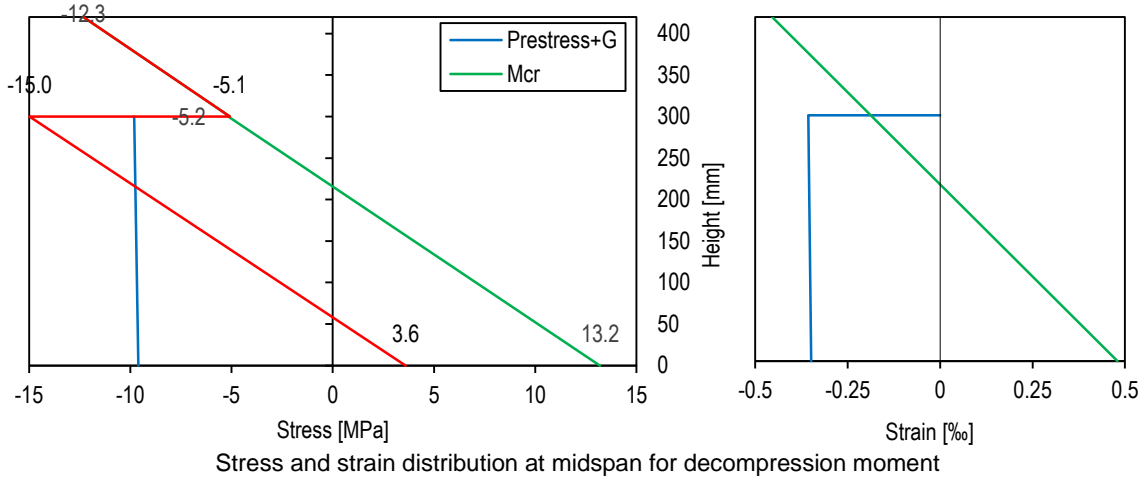


Stress and strain distribution at midspan for decompression moment

5.3 Cracking of bottom fibre

Cracking bottom fibre	$-\frac{P_{m60}}{A_g} - \frac{P_{m60}e_p}{W_{gb}} + \frac{M_{Gc} + M_{Gt}}{W_{gb}} + \eta \frac{M_{cr}}{W_{cb}} = f_{ctm}$	
	$M_{cr} = \left(f_{ctm} + \frac{P_{m60}}{A_g} + \frac{P_{m60}e_p}{W_{gb}} - \frac{M_{Gc} + M_{Gt}}{W_{gb}} \right) \frac{W_{cb}}{\eta}$	= 380 kN m
Stress bottom fibre girder P_{m60} and M_G	$\sigma_{gb} = -\frac{P_{m60}}{A_g} - \frac{P_{m60}e_p}{W_{gb}} + \frac{M_{Gc} + M_{Gt}}{W_{gb}}$	= -9.60 MPa

Stress top fibre girder P_{m60} and M_G	$\sigma_{gt} = -\frac{P_{m60}}{A_g} + \frac{P_{m60}e_p}{W_{gt}} - \frac{M_{Gc} + M_{Gt}}{W_{gt}}$	= -9.81 MPa
Stress bottom fibre girder M_{cr}	$\sigma_{gb,cr} = \frac{\eta M_{cr}}{W_{cb}}$	= 13.20 MPa
Stress top fibre girder M_{cr}	$\sigma_{gt,cr} = -\frac{\eta M_{cr}(h_c - z_{cb})}{I_c}$	= -5.16 MPa
Stress bottom fibre topping M_{cr}	$\sigma_{tb,cr} = -\frac{M_{cr}(h_c - z_{cb})}{I_c}$	= -5.08 MPa
Stress top fibre topping M_{cr}	$\sigma_{tt,cr} = -\frac{M_{cr}}{W_{ct}}$	= -12.32 MPa
Resulting stress girder at interface	$\sigma_t = \sigma_{gt} + \sigma_{gt,cr}$	= -14.97 MPa
Resulting stress bottom fibre	$\sigma_b = \sigma_{gb} + \sigma_{gb,cr}$	= 3.60 MPa
Cross-section analysis	$x_u = h - h_g \left(\frac{\sigma_b}{\sigma_b - \sigma_t} \right)$	= 362 mm
	$\kappa_{cr} = \frac{\sigma_{gb,cr} - \eta \sigma_{tt,cr}}{E_c h_c}$	= $2.22 \cdot 10^{-6}$ 1/mm



5.4 Cracked cross-section

Transformed cross-sectional properties of the precast girder:

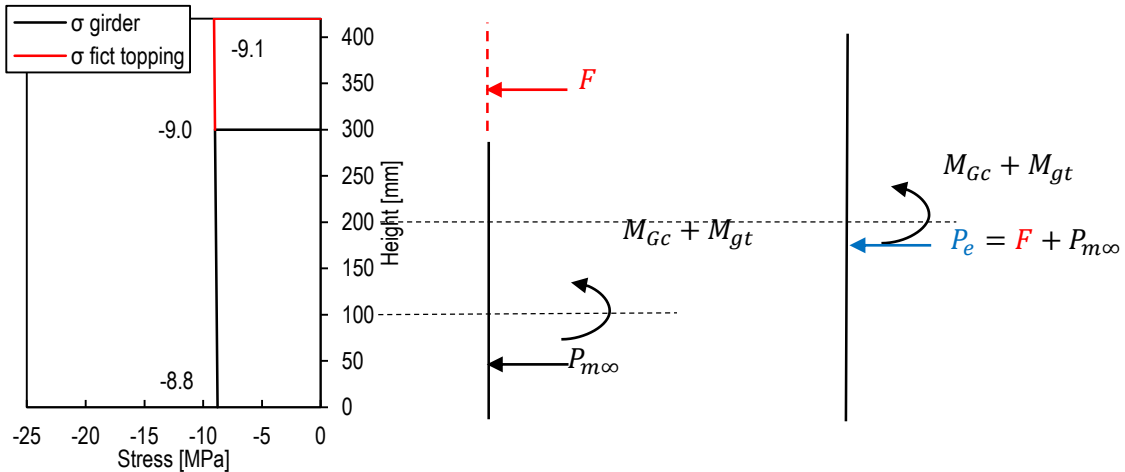
$\eta_p = E_p/E_c = 7.00$	$z_{sgb} = 116.0$ mm
$A_{pt} = A_p \eta_p = 11199$ mm ²	$A_{gt} = 170845.8$ mm ²
$\eta_s = E_s/E_c = 7.27$	$I_{gt} = 1.22 \cdot 10^9$ mm ⁴
$A_{sgt} = A_{sg} \eta_s = 3427$ mm ²	$z_{gtb} = 107.7$ mm

Top fibre $\sigma_{tgt} = -\frac{P_{m60}}{A_{gt}} + \frac{P_{m60}e_p z_{sgb}}{I_{gt}} - \frac{M_{Gc} + M_{Gt}}{I_{gt}} = -8.99$ MPa

Bottom fibre $\sigma_{bgt} = -\frac{P_{m60}}{A_{gt}} - \frac{P_{m60}e_p z_{sgb}}{I_{gt}} + \frac{M_{Gc} + M_{Gt}}{I_{gt}} = -8.77$ MPa

Transformed cross-sectional properties of the composite section:

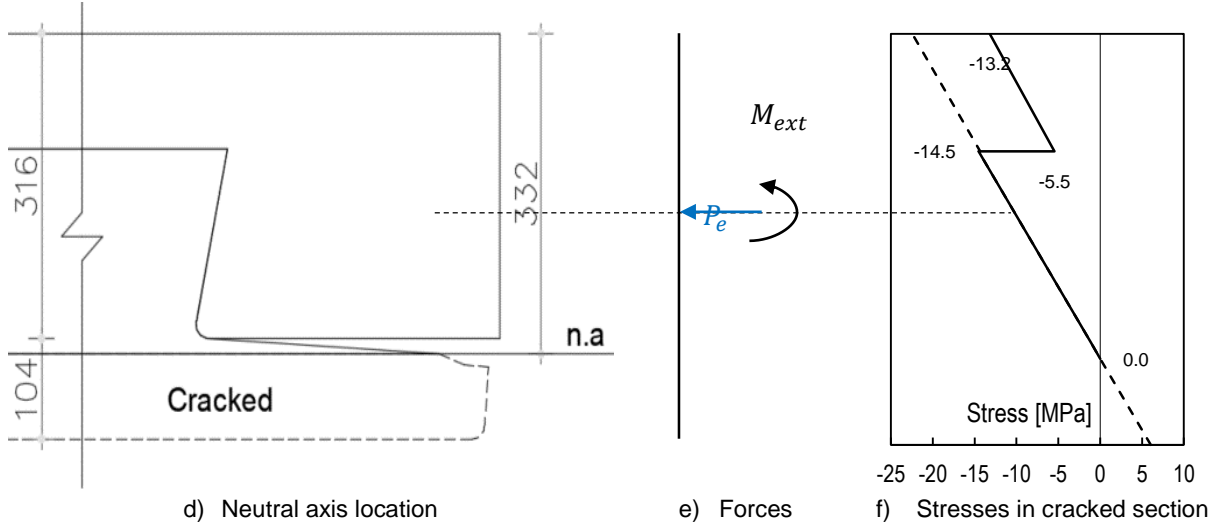
$\eta_t = E_t/E_c = 0.985$	$I_{ct} = 6.62 \cdot 10^9$ mm ⁴
$A_{tt} = A_t \eta_p = 282142.5$ mm ²	$z_{ctb} = 212.7$ mm
$A_{stt} = A_{st} \eta_s = 12429$ mm ²	$F = 2669.5$ kN
$z_{scb} = 266.5$ mm	$P_e = 4181.1$ kN
$A_{ct} = 465417.5$ mm ²	$e_{pe} = -14.6$ mm



a) Stresses girder/fictitious topping b) Forces in transformed girder c) Forces in transformed composite

Analysis of transformed composite cross-section

Analysis of the cracked composite cross-section



d) Neutral axis location

e) Forces

f) Stresses in cracked section

Analysis of cracked composite cross-section

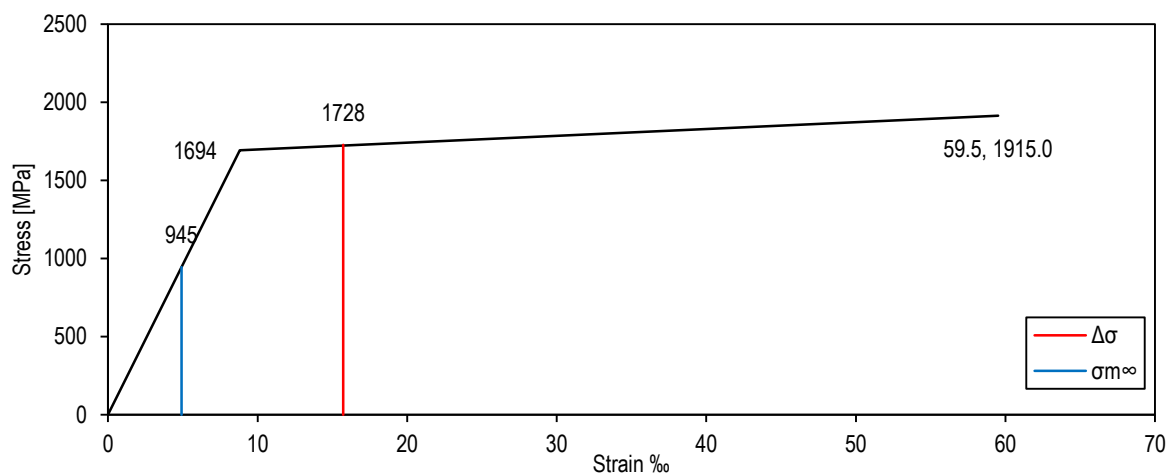
$$\begin{aligned}
 A_{g,cr} &= 70695.4 \text{ mm}^2 \\
 I_{g,cr} &= 2.97 \cdot 10^8 \text{ mm}^4 \\
 z_{g,cr} &= 191.4 \text{ mm} \\
 y &= 38 \text{ mm} \\
 M_{ext} &= 400.8 \text{ kNm} \\
 \kappa_{c,cr} &= 2.46 \cdot 10^{-6}
 \end{aligned}$$

$$\begin{aligned}
 A_{c,cr} &= 379893.8 \text{ mm}^2 \\
 I_{c,cr} &= 3.57 \cdot 10^9 \text{ mm}^4 \\
 z_{c,cr} &= 250.8 \text{ mm}
 \end{aligned}$$

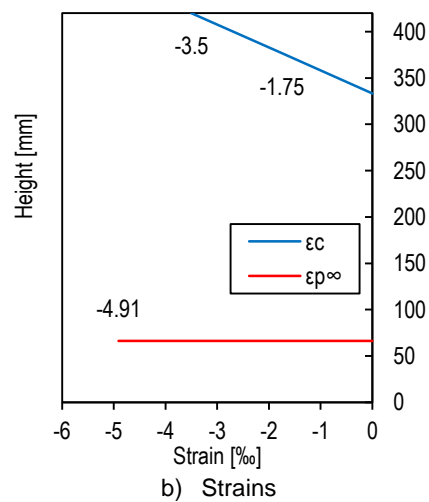
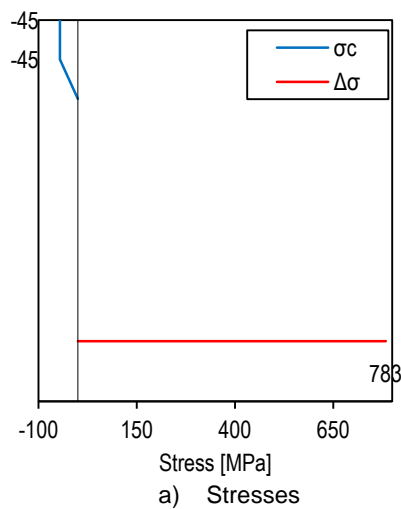
5.5 Ultimate Limit State

Equilibrium of horizontal forces (ULS)

	A_{si} [mm ²]	d_{si} [mm]	ϵ_{si} [‰]	σ [MPa]	N [kN]	a [mm]	M [kN m]
A_{s1}	8 ϕ 12	905	354	-0.831	-166	-20.6	3.1
A_{s2}	2 ϕ 10	157	252	3.293	500	81.4	6.4
A_{s3}	4 ϕ 16	804	168	6.689	500	165.4	66.5
A_{s4}	4 ϕ 10	314	48	11.542	500	285.4	44.8
N_{cu}	--	--	--	--	--	-52.9	170.0
P_{m60}	--	1600	--	4.908	945	129.1	195.2
ΔN	--	1600	66.3	10.804	1704	267.2	324.5
				$\Sigma =$	0	$\Sigma =$	810.6
				$+P_{m60}e_p - (M_{Gc} + M_{Gt}) =$			967.6



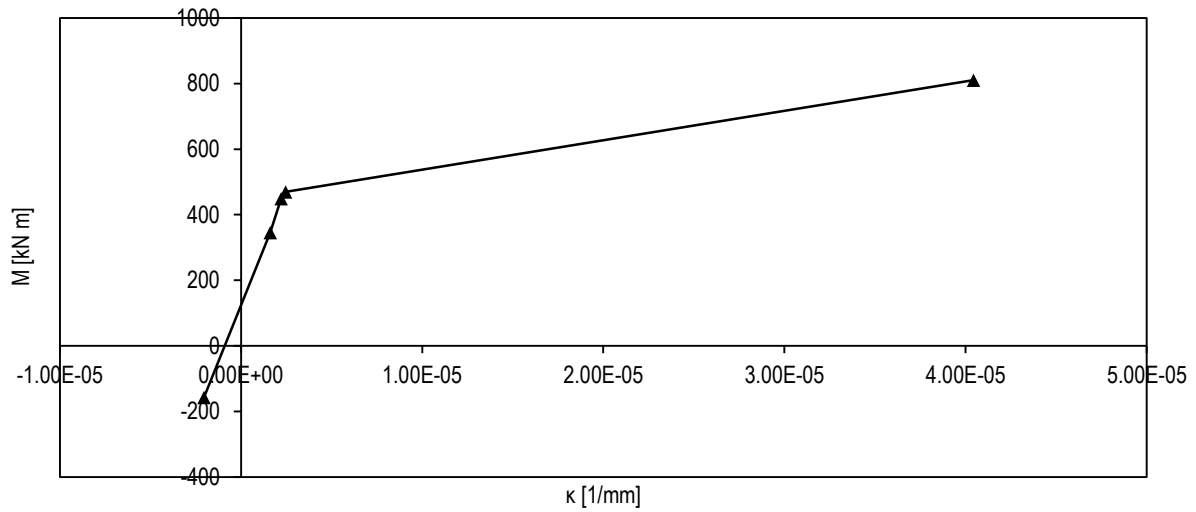
Prestressing steel stresses and strains (ULS)



Stress and strain distributions at midspan (ULS)

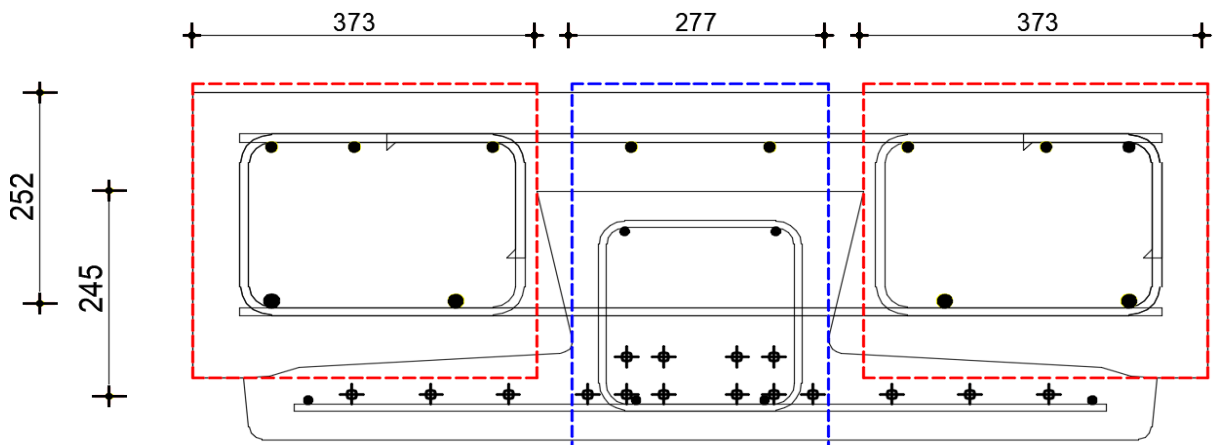
$$\begin{aligned}
 x_u &= 86.6 \text{ mm} \\
 Q_{ext} &= 421 \text{ kN} \\
 \kappa_u &= 4.04 \cdot 10^{-5}
 \end{aligned}$$

5.6 Moment curvature diagram



Moment curvature diagram

6. Ultimate Limit State: Shear



Two members for calculation of shear resistance (blue: precast girder, red: cast in-situ topping)

6.1 Precast girder

$$\cot \alpha = 0 \text{ and } \sin \alpha = 1 \quad z = 0.85d = 310 \text{ mm} \quad \cot \theta = 2.5.$$

6 double legged stirrups ($\phi 8$) over a distance $z(\cot \theta) = 776 \text{ mm}$ between $x = 776 - 1551 \text{ mm}$, at an average spacing of 140 mm .

$$V_{Rd,s} = \frac{A_{sw}}{s} z(\cot \theta) f_{ywd}$$

$$V_{Rm,s,g} = \frac{A_{sw}}{s} z(\cot \theta) f_{yw} = \frac{2 \pi (8 \text{ mm})^2}{4 \cdot 140 \text{ mm}} 776 \text{ mm} \cdot 500 \text{ MPa} = 278.5 \text{ kN}$$

The proportion of the prestressing force transmitted over the distance of 1200 is equal to 85%.

$$\sigma_{cp} = 0.85 \frac{P_{m60}}{A_g} = 8.2 \text{ MPa} \quad \frac{\sigma_{cp}}{f_{cm}} = 1.5 \frac{8.2}{50} = 0.25 \rightarrow \alpha_{cw} = 1.25$$

$$v_1 = 0.6$$

$$V_{Rd,max,g} = \alpha_{cw} v_1 f_{cd} b_w z (\cot \theta) \sin^2 \theta$$

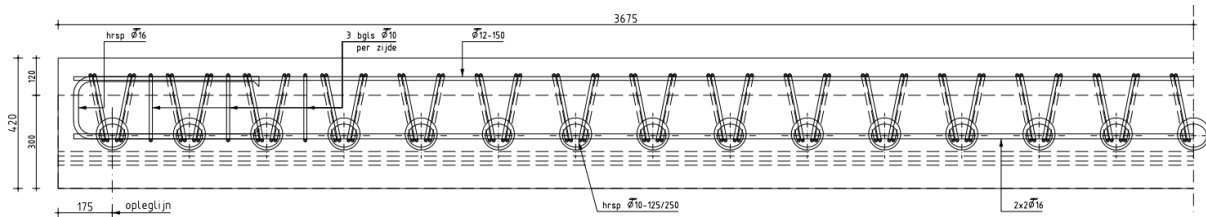
$$V_{Rm,max,g} = \alpha_{cw} v_1 f_{cm} b_w z (\cot \theta) \sin^2 \theta = 1.25 \cdot 0.6 \cdot 50 \text{ MPa} \cdot 277 \text{ mm} \cdot 776 \text{ mm} \cdot \sin^2(21.8^\circ)$$

$$V_{Rm,max,g} = 1111.1 \text{ kN}$$

$$V_{Rm,g} = \min(V_{Rm,s,g}; V_{Rm,max,g}) = 278.5 \text{ kN}$$

6.2 Cast in-situ topping

Stirrups inclined to the left are at an angle of $\alpha_1 = 79.7^\circ$, while the stirrups inclined to the right are at an angle of $\alpha_2 = 100.3^\circ$



Inclined stirrups in cast in-situ topping

$$z = 0.85d = 214.2 \text{ mm}$$

$$\cot \theta = 2.5$$

4 pairs of stirrups ($\phi 10$, 2 oriented to the right and 2 oriented to the left) over a distance of $z(\cot \theta) = 535.5 \text{ mm}$ between $x = 1071 - 1606.5 \text{ mm}$, at an average spacing of 250 mm.

$$V_{Rd,s} = \frac{A_{sw}}{s} z (\cot \theta + \cot \alpha) f_{ywd} \sin \alpha$$

$$V_{Rm,s,t} = \frac{A_{sw}}{s} z f_{yw} m ((\cot \theta + \cot \alpha_1) \sin \alpha_1 + (\cot \theta + \cot \alpha_2) \sin \alpha_2)$$

$$V_{Rm,s,t} = \frac{2\pi(10 \text{ mm})^2}{4 \cdot 250 \text{ mm}} 214.2 \text{ mm} \cdot 500 \text{ MPa} ((2.5 + \cot \alpha_1) \sin \alpha_1 + (2.5 + \cot \alpha_2) \sin \alpha_2)$$

$$V_{Rm,s,t} = 331 \text{ kN}$$

The cast in-situ topping is not prestressed, hence $\sigma_{cp} = 0 \text{ MPa}$ and $\alpha_{cw} = 1$.

$$V_{Rd,max,t} = \alpha_{cw} v_1 f_{cd} b_w z (\cot \theta + \cot \alpha) \sin^2 \theta$$

$$V_{Rm,max,t} = \alpha_{cw} v_1 f_{cm} b_w z (\cot \theta + \cot \alpha) \sin^2 \theta$$

$$V_{Rm,max,t} = 0.6 \cdot 45 \text{ MPa} \cdot 746 \text{ mm} \cdot 252 \text{ mm} (2.5 + \cot 100.3^\circ) \sin^2 100.3^\circ = 11390 \text{ kN}$$

$$V_{Rm,t} = \min(V_{Rm,s,t}; V_{Rm,max,t}) = 331 \text{ kN}$$

Finally the overall shear resistance is the sum of the contributions of the precast girder and the cast in-situ topping: $V_{Rm} = V_{Rm,g} + V_{Rm,t} = 609.5 \text{ kN}$.



**Master of Science Civil Engineering
Structural Engineering – Concrete Structures
DELFT UNIVERSITY OF TECHNOLOGY**